A Study of the Forward-Backward Charge Asymmetry in Hadronic Z^o Decays

Andrew William Halley

Department of Physics and Astronomy
The University of Glasgow
Glasgow Scotland

Thesis submitted for the degree of
Doctor of Philosophy

May 1991

Abstract

This thesis concerns a study of the forward-backward charge asymmetry observed in hadronic events using the ALEPH detector at the LEP e^+e^- collider. The asymmetry is interpreted as arising from electroweak effects during quark production in Z^o decays.

Particle charges and momenta are measured using information from the time projection and inner tracking chambers of ALEPH while the effects of charge retention are investigated and used to tag the charge and direction of quarks from particles detected after parton fragmentation. The data were recorded over a range of energies around the Z^o resonance and represent an integrated luminosity of $8.7 \pm 0.2\,\mathrm{pb}^{-1}$.

The asymmetry is expressed as the mean difference between momentum weighted charges in the forward and backward hemispheres and is found to be :

$$\langle \text{Forward Charge} - \text{Backward Charge} \rangle = -0.0084 \quad \underbrace{\pm \ 0.0014}_{\text{(statistical)}} \ \underbrace{\pm \ 0.0004}_{\text{(expt. syst.)}}$$

Fragmentation models are used to estimate the degree of charge retention for each quark flavour so that their contributions to the observed asymmetry can be determined. In the context of the Standard Model, the asymmetry may be interpreted in terms of the coupling strength of fermions to the Z^o and so as a measure of the effective electroweak mixing angle :

$$sin^2\theta_w(M_Z^2) = 0.2303 \ \underbrace{\pm 0.0036}_{\text{(stat.)}} \ \underbrace{\pm 0.0009}_{\text{(expt.syst.)}} \ \underbrace{\pm 0.0038}_{\text{(theor.syst.)}}$$

When taken in conjunction with previously extracted quark coupling constants from neutrino-nucleon scattering measurements, the ratio of lepton couplings is found to be :

$$\frac{v_e}{a_e} = +0.072 \ \pm 0.025$$

combining both statistical and systematic uncertainties. This measurement establishes that the axial and vector lepton couplings have the same sign.

Preface

This thesis describes a study of the forward-backward asymmetry of quark jets in the ALEPH detector at the LEP collider near CERN, Geneva. The data were recorded during the period following the successful commissioning of the accelerator. The motivation for the asymmetry study is to provide a measure of the strength of fermion couplings to the intermediate Z^o boson.

The work of a collaboration depends directly and indirectly on the participation of many people over a long period of time. The authors individual contributions to the experiment include the development and running of a remote laser calibration system for the time projection chamber. This was combined with analyses of the subdetector performance and studies of distortions close to the edges of the tracking chambers. The author was also involved in the preliminary scanning of events at the commencement of LEP operation and took part in data taking shifts. The material presented in this thesis reflects the individual work of the author, developed within a small team at CERN. The results depend on the work of several people although the analysis presented here is my own.

No portion of the work referred to in this thesis has been submitted in support of an application for another degree or qualification in this, or any other, institution of learning.

Acknowledgements

It is hard to express my thanks and appreciation of the many people who have helped me over the last three years so I hope that any omissions will be forgiven. Firstly, I thank my family, for their encouragement and support throughout my studies, who put up with me and helped me through many of the rough patches.

It is a pleasure to thank my supervisor, Ken Smith, for his advice, good humoured support and arrangment of my extended stay at CERN. I thank the Physics and Astronomy Department of the University of Glasgow, under the direction of Professors Hughes and Ferrier, for providing me with the opportunity to undertake this research, and the SERC for financial support. I am indebted to Catherine for her kind help and interest over the last few years and for keeping my finances from total chaos.

I very much enjoyed the company and friendship of Rob, Steve and Jonathan from the beginning of my time in Geneva who later contributed to my knowledge of mainframe computing, physics-analysis, religion and how to define a weirdo[1]. Their continuing friendship is something I value greatly. The trips were made bearable by the company of Marion and her family for which I am very grateful. I would like to thank the members of the TPC group who made a lone Scotsman welcome from the beginning, including Werner who warned me about the dangers of *bricolage*, Jo and the laser team of Thomas, Frank, Reiner and Steffen who shared with me the delights of frisbee by the lake and international partygoing. Thanks for the voyages across Germany and the hospitality of friends and families in Mainz. Cheers to Mad Max and Hartmut for the exhausting squash games and good beer. Sanity was preserved and sometimes weakened with the company of Mark, Jols and Dazbob in the ghetto, with Andy, Steve, Mary and Dave's late night bottle of *Laphroig*. Many thanks to them for attacks on mountains, ski-slopes and the Mexican. Thanks also to Andrew, Nigel and Christine for showing the posh side of Geneva, bad films and worse food, while sharing the swimming pool and letting me away with trying to kill them on the glacier. Back in Glasgow, I have enjoyed the company and help of Denis, Butrus, Stuart and Big Stan. Thanks for the generation of hideous amounts of Monte Carlo tapes and conversations in the pub on a Friday night. Best regards to the members of the Western Hillwalking Club for mountain days and bothy nights. Most important to me, is the Dutch lass who convinced me that it *could* work; and made sure that it did.

I would like to express my respect and gratitude to Alain Blondel for his stimulus and interest in our analysis and for his repeated, patient explanations of (frequently simple) concepts. It was a pleasure to work with the analysis team of asymmetrics, Ingrid ten Have and Lee Sawyer. Thanks for all the hard work, explanations, ideas, crazy discussions and the most amazing meetings. In this regard I also thank Witold Wkozanec and the members of the ALEPH collaboration for their valued advice, ideas and sheer effort when bringing the analysis towards publication. I am further indebted to the colleagues who ended up reading draft copies of this document, for their comments, suggestions and concern.

Lastly, I would like to thank my parents for their unfailing interest and patient help from beginning to end; for their thoughts whilst I was in Geneva, and for their support back in Glasgow. This document is dedicated to them.

[1] "When the going gets weird, the weird turn pro" (Raol Duke).

Even now
I mind that I loved cypress and roses, clear,
The great blue mountains and the small grey hills,
The sounding of the sea. Upon a day
I saw strange eyes and hands like butterflies;
For me at morning larks flew from the thyme
And children came to bathe in little streams.

Even now
I know that I have savoured the hot taste of life
Lifting green cups and gold at the great feast.
Just for a small and forgotten time
I have had full in my eyes from off my girl
The whitest pouring of eternal light...

"Black Marigolds". translated from the Sanskrit by E. Powys Mathers.

Contents

Chapter 1

The Standard Model and Quark Asymmetries

Experimental Particle Physics concerns itself with the study of fundamental particles and the manner in which they behave. A combination of theory and experiment has given rise to a conceptual framework, the so-called "Standard Model", which is used to test our understanding as new discoveries appear. It has evolved from studies of the behaviour of matter over increasingly smaller distance scales using high energy particle interactions.

The science of elementary particles has its roots in the discoveries of the electron and nucleus by Thomson and Rutherford. Combined with Maxwell's unification of the theories of electricity and magnetism, these led to the *Classical* concepts of matter made from "fundamental" particles moving in electric and magnetic fields with an as yet unknown "strong" force holding the nucleus together. Later discoveries of the proton and neutron added to an elegant picture of a world consisting of three particle types.

This picture was drastically modified by the theories of Planck and Einstein which described the quantisation of light into photons, which was finally verified by Compton in 1923. The uncovering of many new particles and antiparticles led to a proliferation which belied the word "fundamental". Properties of the new particles gave rise to principles of a new, more profound, structure which led ultimately to the relative simplicity of the quark parton model. In a similar period, the development of quantum mechanics by Heisenberg and Schrodinger, with Einstein's theory of relativity, laid the foundations of quantum field theory.

The intimate link between particles and their forces has illuminated the path from the electron, proton and neutron interacting via classical fields to the ideas of quarks and leptons under the influences of quantum gauge fields.

1.1 The Standard Model

The Standard Model (SM) [1] encompasses our current knowledge concerning particles and the fields with which they interact. The particles of the model consist of two families of fermions; the quarks and leptons. Quarks are fractionally charged and help to explain underlying symmetries in the quantum numbers of the plethora of particles found in the latter half of this century. The original *parton model* envisaged "quarks" to explain the

decays of such particles as the baryons (Λ, Ξ etc.) and mesons (π, K, ρ, η etc.). Evidence that the partons are physical entities (quarks) came about in a similar manner to the discovery of nuclei. Deep inelastic scattering of electrons off protons showed the typical behaviour of scattering angles larger than would be expected from a uniformly distributed charge within the proton. When taken into consideration with jet-like structures observed in e^+e^- annihilation, the support for a model containing quarks as physical particles has become established.

The lepton family consists of the e, μ and τ particles, together with their associated neutrinos. The muon was initially discovered in cosmic ray experiments during the 1940's while the tau remained undiscovered until 1975. Neutrinos were first postulated to account for the continuous energy spectra of electrons in β-decay. The discovery that separate ν_e and ν_μ neutrinos were required, to account for the rates of leptons produced in lepton-nucleon collisions in 1962, gave rise to the current model containing three neutrino types with their corresponding antiparticles.

The symmetry of three generations of quarks and leptons, shown in table 1.1, is marred only by the absence of the top (or "truth") quark which remains to be discovered. Current

Particle Name	Symbol	Spin	Charge	Baryon Number	Lepton Number
Quarks					
up, charm, top	u, c, t	$\frac{1}{2}$	$+\frac{2}{3}$	$\frac{1}{3}$	0
down, strange, beauty	d, s, b	$\frac{1}{2}$	$-\frac{1}{3}$	$\frac{1}{3}$	0
Leptons					
electron, muon, tau	e, μ, τ	$\frac{1}{2}$	-1	0	1
lepton neutrinos	ν_e, ν_μ, ν_τ	$\frac{1}{2}$	0	0	1
Gauge Bosons					
photon	γ	1	0	0	0
weak bosons	$W^\pm, Z^o$	1	$\pm 1, 0$	0	0
gluons	$g_i\ (i = 1 \ldots 8)$	1	0	0	0
Higgs Boson					
Higgs	H	0	0	0	0

Table 1.1: Summary of the elementary particle in the Standard Model.

estimates point to a mass of $120\,(\pm 45)$ GeV [2] which accounts for its non-appearance to date. The latest LEP results indicate that the number of light neutrinos is limited to the three generations found so far.

Prior to the Standard Model it was thought that all particles behaved under the influences of four basic forces: the *electromagnetic* force for charged particles, the ***strong force*** binding protons and neutrons in nuclei, the *gravitational* force and the ***weak*** force responsible for effects such as the β-decay of nuclei.

The Maxwellian idea of charged particles interacting with each other through electromagnetic fields was incorporated into the modern field theory of *Quantum Electro-Dynamics* (QED). This envisages interactions between charges mediated by a stream of photons passing between them. QED is an example of a *gauge theory* and, due to its great success in describing precision measurements of the magnetic moments of electrons and muons, has been used as a model to construct theories describing other forces.

The theory of strong interactions is based on such a model and contains *coloured* quarks which act as "charges" of *Quantum Chromo-Dynamics* (QCD). The concept of colour was first introduced to solve the puzzle of the assumed three-parton state, the Δ^{++}. At first sight, the particle violates the Exclusion Principle, whereas addition of an extra, coloured degree of freedom distinguishes the three states from each other so that the situation is avoided. QCD is based on the theory of QED where the photon is supplanted by eight coloured gluons. The analogy between QED and QCD contains major differences however, as gluons carry the colour charge while the photon of QED remains neutral. This allows gluons to interact, not only with quarks, but amongst themselves. QCD has a coupling strength, α_s, greater than the fine structure constant, α, of QED. The coupling strength rapidly increases with separation and is thought to explain the confinement of quarks within hadrons.

Gravity remains the weakest of known forces, even though its long range effects on large masses are responsible for much of the observed structure of the Universe. The small masses of elementary particles however, mean that its contribution is generally negligible when they are considered in isolation.

The presence of an additional weak force was first postulated to explain the process of β-decay in nuclei and the long lifetimes of particles such as pions and the muon. The theory, developed by Fermi, was based upon the idea of a current interaction similar to QED and, although able to describe some experimental observations, it was unable to incorporate non-conservation of parity, observed in the decay of polarised Cobalt-60 nuclei, and proved later to be non-renormalizable.

The Standard Model unifies the theories of QED, QCD and weak interactions by revealing that a single gauge theory can be used to describe them. The following sections describe how the model of weak interactions was developed and unified with QED to form the *eletroweak* theory. The prediction of the existence, masses and subsequent discovery of the gauge bosons of the theory at CERN have made the electroweak model the basis upon which the SM is built.

1.2 Weak Interactions

The original weak interaction theory (due to Fermi) envisaged the β-decay of nuclei :

$$n \rightarrow p e^- \bar{\nu}_e \tag{1.1}$$

as a vector current reaction based upon the ideas of QED with a coupling, G_F. The observation of parity violating effects led to a generalisation of this theory by Feynman and Gell-Mann to treat the reaction as a vector/axial-vector (V-A) interaction. In such a theory, it is the left-handed projection of the neutrino which interacts, coupled to left-handed electron components. Interactions are between the *chiral* fermion states made up from the left and right-handed states projected using the operator $\frac{1}{2}(1 \pm \gamma^5)$. This accounts for the fact that only left-handed neutrinos are observed. This theory is non-renormalizable however, and the cross-section diverges at high energies.

A solution to remove such divergencies is to destroy the gauge invariance by introducing *massive* force carriers with a dimensionless coupling, as advocated by Glashow [3]. The successful V-A structure is retained, and masses of the required charged bosons (W^+, W^-) are responsible for the short range nature of the interaction. However, such a theory still remains non-renormalizable as cross-sections, such as $\nu\overline{\nu} \rightarrow W^+W + -$, diverge at high energies.

The success of QED as a renormalizable gauge theory, based on exchange of massless bosons, led to a search for a similar structure for weak interactions in an attempt to incorporate gauge invariance from first principles.

1.2.1 Local Gauge Invariance in QED

The Lagrangian approach to particle dynamics is based upon the Euler-Lagrange method of Classical Dynamics where the invariance of the Lagrangian under specific transformations gives rise to conserved quantities. The Dirac equation for a free, spin $\frac{1}{2}$ particle :

$$(i\gamma^\mu\partial_\mu - m)\psi = 0 \tag{1.2}$$

may be derived from the Euler-Lagrange equation if its Lagrangian is defined as :

$$\mathcal{L}_o = i\bar{\psi}\gamma^\mu\partial_\mu\psi - m\bar{\psi}\psi \tag{1.3}$$

Such an equation can be shown to be invariant under changes to ψ of the form :

$$\psi(x) \rightarrow e^{i\theta}\psi(x) \tag{1.4}$$

Any real number, or phase θ, has no effect on the Lagrangian. This is referred to as a *global* gauge transformation, as θ is the same for all points in space and time. $U(\theta) = e^{i\theta}$ form an *Abelian* unitary group, as individual transformations commute with each other. Invariance of the Lagragian under such infinitesimal transformations implies the existence of a conserved quantity, in this case the current :

$$\partial_\mu j^\mu = 0 \quad \text{where} \quad j^\mu = -e\bar{\psi}\gamma^\mu\psi \tag{1.5}$$

Global gauge invariance may be generalised so that conservation rules are also obeyed *locally*. ie. the phase θ may depend on position, so that $\theta \rightarrow \theta(x)$. Under this change, $\mathcal{L}_o$ transforms as :

$$\mathcal{L}_o \rightarrow \mathcal{L}_o - \bar{\psi}\gamma^\mu\psi\partial_\mu\theta \tag{1.6}$$

As it stands, $\mathcal{L}_o$ is not invariant unless additional terms are included. This is done by adding another term into (1.3) :

$$\mathcal{L}_1 = \mathcal{L}_o + e\bar{\psi}\gamma^\mu A_\mu \psi \tag{1.7}$$

where A_μ is a *gauge field* and transforms as :

$$A_\mu \rightarrow A_\mu + \frac{1}{e}\partial_\mu \theta \tag{1.8}$$

The new term in (1.7) represents the *interaction* of the current j^μ with the field A_μ. The Lagrangian is not complete as, though the field A_μ can interact, it has no "free" term for it to exist as a particle its own right. An additional gauge invariant term can be added to represent its kinetic energy. The Lagrangian for such a vector field contains the gauge invariant field tensor :

$$F_{\mu\nu} = \partial_\mu A_\nu - \partial_\nu A_\mu \tag{1.9}$$

and additional kinetic energy terms of the form : $\frac{1}{2}m^2 A_\mu A^\mu$. Invariance of the entire Lagrangian is broken by the latter terms and so the vector field A_μ *must* be massless. The full QED Lagrangian is then given by :

$$\mathcal{L}_{QED} = \bar{\psi}(i\gamma^\mu \partial_\mu - m)\psi + e\bar{\psi}\gamma^\mu A_\mu \psi - \frac{1}{4}F_{\mu\nu}F^{\mu\nu} \tag{1.10}$$

Generally, local gauge invariance introduces extra phase derivative terms $\partial_\mu \theta$ in (1.6). These may be avoided in principle by replacing all derivatives in the free Lagrangian by their covariant equivalents :

$$\mathcal{D}_\mu = \partial_\mu - ieA_\mu \tag{1.11}$$

The massless quantum of the electromagnetic field is associated with the photon of QED. The important point is that imposition of local gauge invariance on a free particle Lagrangian leads to an interacting field theory containing massless vector fields. Such a principle, found to be successful for QED, can be applied to the generalised case of the electroweak model.

1.2.2 Extension of QED to Weak Interactions

The success of QED in creating a renormalizable theory is applicable to the V-A theory of the weak interaction. However there remain important differences. The $U(1)$ group of QED contains a single, massless photon, while an analogous gauge group for an electroweak theory must be found including massive bosons to account for the short range of the weak force.

The gauge group which successfully describes the weak interaction was developed by Glashow who based it upon an $SU(2)_L \times U(1)_Y$ symmetry. The $SU(2)_L$ group contains a boson triplet, where the L denotes that the couplings of the weak bosons are left-handed only and preserve the parity violating V – A structure. The triplet contains two charged

bosons and a third neutral member. This cannot be the photon as it couples to all charged particles, right or left-handed. Thus the $U(1)_Y$ group is introduced. The $U(1)$ symmetry of QED is based upon the charge of the fermions. The *generators* of the $SU(2)_L$ and $U(1)_Y$ groups are the weak isospin, T_3, and weak hypercharge, Y, respectively. In this model the electromagnetic charge, Q, is :

$$Q = T_3 + \frac{Y}{3} \tag{1.12}$$

When local gauge invariance is imposed on such a Lagrangian, the gauge fields manifest themselves as 4 different vector fields. Two members of the $SU(2)_L$ triplet form the charged vector bosons (the W^+, W^-) whereas the $U(1)_Y$ gauge boson and remaining member of the $SU(2)_L$ triplet are *mixed* to form the Z^o and the photon.

All such considerations are independent of the fact that the massive nature of the $W^{\pm}$ and Z^o violate the gauge invariance of the model. The model avoids gauge dependence of the mass terms by invoking the idea of "spontaneous symmetry breaking".

Spontaneous symmetry breaking occurs when gauge invariance is applied to a field with a potential minimum corresponding to a non-vanishing vacuum expectation value. The symmetry, evident in the Lagrangian, still exists but is "hidden" by the choice of a particular ground state which itself does not share the symmetry. The coupling between the vacuum state and gauge fields generates mass-like terms for the gauge bosons in the Lagrangian. This is the *Higgs Mechanism* when applied to a complex isospin doublet with four degrees of freedom. The mechanism exploits the presence of such terms by "absorbing" massless scalars into the three longitudinal states of the massive gauge bosons. The fourth state of the auxiliary vacuum field is the Higgs boson which still remains to be discovered.

Using the concepts of Glashows local gauge symmetry and the Higgs mechanism enables the electroweak model to describe much of the behaviour of known particles and their interactions.

1.2.3 The Electroweak Model

The V-A structure of the weak interaction makes it clear that right and left-handed chiral components transform differently under $SU(2)_L \times U(1)_Y$ local gauge transformations :

$$\begin{aligned} \chi_L \quad &\rightarrow \quad \chi'_L = e^{i\theta(x)\mathbf{T} + i\phi(x)\mathbf{Y}} \chi_L \\ \chi_R \quad &\rightarrow \quad \chi'_R = e^{i\phi(x)\mathbf{Y}} \chi_R \end{aligned} \tag{1.13}$$

where $\mathbf{T}$ and $\mathbf{Y}$ are the generators of the two gauge groups respectively. Left-handed fermions are organised into the weak isospin doublets :

$$\chi_L = \begin{pmatrix} e^- \\ \nu_e \end{pmatrix}_L, \begin{pmatrix} \mu^- \\ \nu_\mu \end{pmatrix}_L, \begin{pmatrix} \tau^- \\ \nu_\tau \end{pmatrix}_L, \begin{pmatrix} u \\ d \end{pmatrix}_L, \begin{pmatrix} c \\ s \end{pmatrix}_L, \begin{pmatrix} t \\ b \end{pmatrix}_L . \tag{1.14}$$

while right-handed fermions form the isosinglets :

$$\psi_R = e_R^-,\ \mu_R^-,\ \tau_R^-,\ u_R,\ d_R,\ s_R,\ c_R,\ b_R,\ t_R. \tag{1.15}$$

When local gauge invariance is invoked, three weak isospin currents, j_μ are created together with a single weak hypercharge current, j_μ^Y. This leads to an electroweak Lagrangian of the form :

$$\begin{aligned}\mathcal{L} = \ & \bar{\chi}_L \gamma^\mu \left[i\partial_\mu - g\tfrac{1}{2}\mathbf{T}\cdot\mathbf{W}_\mu - g'\tfrac{Y}{2}B_\mu \right] \chi_L \quad + \bar{\psi}_R \gamma^\mu \left[i\partial_\mu - g'\frac{Y}{2}B_\mu \right] \psi_R \\ & - \tfrac{1}{4}\mathbf{W}_{\mu\nu}\cdot\mathbf{W}^{\mu\nu} - \tfrac{1}{4}\mathbf{B}_{\mu\nu}\cdot\mathbf{B}^{\mu\nu}\end{aligned} \tag{1.16}$$

The last two terms concern the dynamics of the vector fields. The tensor $B_{\mu\nu}$ has a similar structure to the tensor $F_{\mu\nu}$ of (1.9) since the fields B_μ, like A_μ, are Abelian. However, the W_μ fields do not commute and the corresponding tensor is more complex :

$$W_{\mu\nu} = \partial_\mu W_\nu - \partial_\nu W_\mu - g\, W_\mu \times W_\nu \tag{1.17}$$

to retain the gauge invariance.

g and g' are the fermion couplings to the W_μ and B_μ fields respectively. Application of the Higgs mechanism spontaneously breaks the symmetry by selecting a non-zero vacuum state as the Lagrangian potential minimum. This is done by introducing the complex doublet :

$$\phi = \begin{pmatrix} \phi^+ \\ \phi^o \end{pmatrix} = \frac{1}{\sqrt{2}} \begin{pmatrix} \phi_1 + i\phi_2 \\ \phi_3 + i\phi_4 \end{pmatrix} \quad \text{where} \quad \phi_{vac} = \begin{pmatrix} 0 \\ \frac{v}{\sqrt{2}} \end{pmatrix} \tag{1.18}$$

When additional Higgs terms are added to the Lagrangian of (1.16) the symmetry is broken giving the bosons mass while the substitution of (1.18) yields :

$$\begin{aligned} W^+ &= \frac{1}{\sqrt{2}}\left(W_\mu^1 + iW_\mu^2\right) \\ W^- &= \frac{1}{\sqrt{2}}\left(W_\mu^1 - iW_\mu^2\right) \end{aligned} \tag{1.19}$$

and the neutral fields :

$$\begin{aligned} A_\mu &= cos\theta_W\, B_\mu \quad + \quad sin\theta_W\, W_\mu^3 \\ Z_\mu &= cos\theta_W\, W_\mu^3 \quad - \quad sin\theta_W\, B_\mu \end{aligned} \tag{1.20}$$

where Z_μ and A_μ are identified with the Z^o and photon fields respectively. The ***weak mixing angle***, θ_W, can be written as :

$$g\, sin\,\theta_W = g'\, cos\,\theta_W = e \tag{1.21}$$

relating the strength of weak interactions to the electromagnetic coupling of QED.

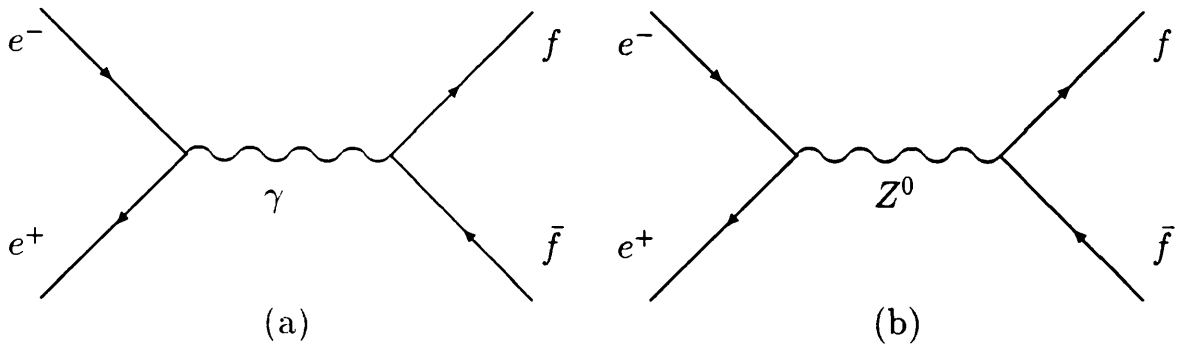

Figure 1.1: Lowest order Feynman graphs for the reaction $e^+e^- \rightarrow f\bar{f}$.

1.3 Asymmetries in e^+e^- Collisions

The reaction $e^+e^- \rightarrow f\bar{f}$ proceeds in lowest order via either of the two diagrams in figure 1.1. In lower energy collisions, the dominant contribution is that from the QED process (a) whereas in the region close to the Z^o resonance (b) increases dramatically and dominates by over two orders of magnitude. Kinematics conventions are shown in figure 1.2 where θ is the scattering angle between the incoming electron and outgoing *fermion*. The angular distribution of the total cross-section, at centre-of-mass energy $\sqrt{s}$,

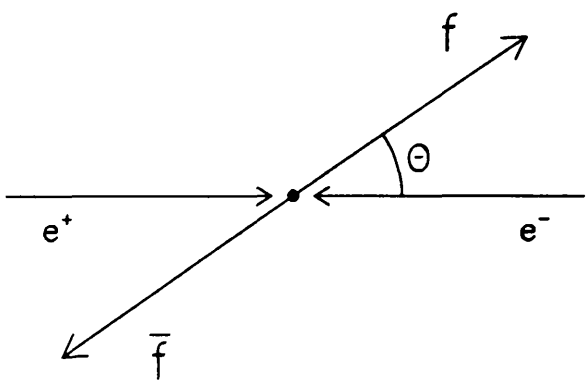

Figure 1.2: Particle kinematics conventions.

may be written as :

$$\frac{d\sigma}{d\Omega} = \frac{\alpha^2}{4s} N_c \left[G_1(s) \left(1 + cos^2\theta\right) + G_2(s) cos\theta \right] \qquad (1.22)$$

neglecting the small effects of fermion masses ie. terms including $\mu_f = m_f^2/s$ which are close to zero [4]. This is derived from the diagrams of figure 1.1 where :

$$\begin{aligned} G_1(s) &= Q_e^2 Q_f^2 + 2Q_e Q_f v_e v_f \mathrm{Re}(\chi_0) + \left(a_e^2 + v_e^2\right)\left(a_f^2 + v_f^2\right) \mid \chi_0^2 \mid \\ G_2(s) &= 4Q_e Q_f a_e a_f \mathrm{Re}(\chi_0) + 8 a_e a_f v_e v_f \mid \chi_0^2 \mid \end{aligned} \tag{1.23}$$

The s dependence is contained in the propagator, χ_0. Q_e and Q_f are the charges of the electron and fermion respectively while a_f, v_f and N_c are the axial and vector couplings to the intermediate boson and the number of QCD colour degrees of freedom respectively. The form and estimated values of the couplings are shown in table 1.2 assuming a $sin^2\theta_w$ value of 0.230. The $G_2(s)\,cos\theta$ term in (1.22) leads to an asymmetry between forward and

Particle	T_3^f	Q^f	a_f	v_f	$a_f^2 + v_f^2$	$\mathcal{A}_f$
ν_e, ν_μ, ν_τ	$+\frac{1}{2}$	0	+1	+1.00	+2.00	+0.50
e, μ, τ	$-\frac{1}{2}$	−1	−1	−0.08	+1.01	+0.16
u, c, t	$+\frac{1}{2}$	$+\frac{2}{3}$	+1	+0.39	+1.15	+0.67
d, s, b	$-\frac{1}{2}$	$-\frac{1}{3}$	−1	−0.69	+1.48	+0.94

The Standard Model form of axial couplings are $a_f = 2T_3^f$ while vector couplings may be written as $v_f = a_f - 4Q_f sin^2\theta_w$.

Table 1.2: Summary of SM couplings assuming a $sin^2\theta_w$ of 0.230.

backward regions where the difference in cross-sections may be expressed as a *forward-backward asymmetry* :

$$A_{FB} = \frac{\int_0^{+1} \frac{d\sigma}{d\Omega}\, d\,cos\theta - \int_{-1}^{0} \frac{d\sigma}{d\Omega}\, d\,cos\theta}{\int_{-1}^{+1} \frac{d\sigma}{d\Omega}\, d\,cos\theta} \tag{1.24}$$

Using equations (1.22) and (1.23) this may be written as :

$$A_{FB} = \frac{3}{4}\frac{G_2(s)}{G_1(s)} \tag{1.25}$$

At lower energies of PEP and PETRA experiments [5] [6], the asymmetric component is due to interference between the vector and axial-vector couplings of the γ and Z^o to the fermions. The small magnitude of the propagator and vector couplings relative to the axial couplings leads to an asymmetry insensitive to $sin^2\theta_w$ and proportional to the axial couplings :

$$(A_{FB})_{low\ energy} = \frac{3}{2} a_e\, a_f\, \mathrm{Re}(\chi) \tag{1.26}$$

Close to the Z^o peak the situation changes dramatically as the propagator increases in size and vector couplings become significant. On resonance, the asymmetry of equation (1.25) becomes :

$$A_{FB} = \frac{3}{4}\mathcal{A}_e \mathcal{A}_f \quad \text{where} \quad \mathcal{A}_f = \frac{2v_f a_f}{a_f^2 + v_f^2} \tag{1.27}$$

$\mathcal{A}_e$ is the polarisation of the Z^o due to electroweak couplings. The vector and axial couplings can be expressed in terms of the weak *left* and *right* couplings using :

$$g_L^f = v_f + a_f \quad \text{and} \quad g_R^f = v_f - a_f \tag{1.28}$$

and so :

$$\mathcal{A}_f = \frac{\left(g_L^f\right)^2 - \left(g_R^f\right)^2}{\left(g_L^f\right)^2 + \left(g_R^f\right)^2} \tag{1.29}$$

This forward-backward asymmetry arises from the difference between left and right-handed couplings of fermions to the weak neutral current. The couplings in table 1.2 make it clear that, for quarks, $\mathcal{A}_f$ is large and relatively insensitive to $sin^2\theta_w$ while $\mathcal{A}_e$ is the difference between $sin^2\theta_w$ and $\frac{1}{4}$ and is *highly* sensitive to this parameter. Thus an asymmetry measurement on the Z^o peak proves to be a sensitive test of the *lepton* couplings. If the outgoing fermions are also leptons then (assuming universality) it is $\mathcal{A}_e^2$ which is measured. In quark channels the sign of $\mathcal{A}_e$, and hence the relative signs of v_e and a_e, can be determined.

The assumption that fermion masses are negligible in equation (1.23) is valid at the level of 10^{-4} for the worst case of b quarks [4]. Similarly, contributions from γ exchange remain small on the peak so that the on-resonance asymmetry is essentially determined completely by $sin^2\theta_w$.

1.3.1 Radiative Corrections

Formulae for the asymmetry in section 1.3 represent Born level derivations and must be corrected for effects of radiation at LEP energies. Radiative effects remove the dependence of A_{FB} on a single parameter by including higher order contributions. Studies have shown that these contributions are large and must be treated carefully [4]. Several sources must be considered :

- **QED Corrections** : These arise from inclusion of higher order Feynman diagrams where a photon is radiated from a fermion line in the lowest order graphs. Corrections are independent of the details of the underlying theory and apply to the exchange of any neutral boson. The corrections depend on the fermion charges and the global parameters of Z^o exchange such as M_Z, Γ_Z and the couplings of table 1.2.
- **Weak Corrections** : These arise from higher order loop corrections to the $\gamma - Z^o$ propagator and vertices with inclusion of complex box diagrams. They depend on the precise structure of the underlying theory since undiscovered particles give virtual contributions. Weak corrections depend upon m_t, M_H and M_W. The dependence on M_W can be avoided using the SM relation :

$$M_W^2\left(1 - \frac{M_W^2}{M_Z^2}\right) = \frac{\pi\alpha}{G_\mu\sqrt{2}}\frac{1}{1 - \Delta r} \tag{1.30}$$

where G_μ is the precisely measured Fermi constant from muon decay. Δr includes corrections to the fine structure constant, α, and depends on m_t and M_H.

- **QCD Corrections** : These have a similar structure to QED corrections from the effects of *gluon* bremsstrahlung and loops replacing the photon of QED. Modifications to A_{FB} are of the form [4] :

$$A_{FB} \rightarrow A_{FB}\left[1 - \frac{\alpha_s}{\pi}\left(1 - \frac{2\pi}{3}\mu\right)\right] \tag{1.31}$$

where $\mu = \frac{2m_f}{\sqrt{s}}$ and remains small for all light flavours of fermion.

The corrections alter the observable asymmetry and introduce uncertainties in its interpretation in terms of $sin^2\theta_w$.

The dominant contribution is from initial state QED radiation which acts to lower the effective centre-of-mass energy at which the e^+e^- reaction occurs. Higher order corrections, to $O(\alpha^2)$, are required as $O(\alpha)$ corrections are of the same order as the asymmetry itself. The $O(\alpha^2)$ corrections lower peak asymmetries by $\sim$ 1.5%. Final state radiation effects are negligible to first order, as are contributions from interference terms [4].

Weak corrections depend upon model parameters, including the unknown quantities m_t and M_H. Propagator corrections can be safely absorbed by a redefinition of the weak "charges". This uses the idea of an *Effective Lagrangian* [7] so that the measurable value of $sin^2\theta_w$ is the *effective* value, $sin^2\theta_w(M_Z^2)$, and includes weak corrections. As a result it becomes both s and (m_t, M_H) dependent. Similarly, all dependent quantities must be replaced by their *running* equivalents which vary with energy. This technique retains the renormalizability of the theory while allowing weak effects to be summed to a high degree of accuracy.

Weak vertex and box corrections are absorbed in the same way but include dependencies on the characteristics of the external fermions. For light flavours the effects are dependent upon M_W and M_Z. For b quarks, the top quark also makes an appearance. The corrections are calculable, but use of the SM relation (1.30) between M_W and G_μ means that such terms depend on m_t.

QCD corrections are seen to be small throughout due to the small fermion masses. In the worst case of the b channel, the correction to the on-resonance asymmetry is of the order of $\sim$ 0.4% [8].

To summarise : an effective Lagrangian allows a measured value of $sin^2\theta_w(M_Z^2)$ to be interpreted as a model dependent measure of weak couplings, including inherent m_t and (small) M_H contributions by definition. Additional corrections from initial state QED are known to $O(\alpha^2)$ and are calculable to an accuracy of $\sim 10^{-4}$.

1.3.2 Energy Dependence

The energy dependence of the forward-backward asymmetry is contained within the propagator in (1.23). At energies around the Z^o resonance the asymmetry changes both as a

result of the propagator and from radiative corrections. The latter change substantially across the resonance as radiation attempts to "step back" onto the peak.

The energy dependence of weak corrections is included in the running couplings and infers that the effective mixing angle changes slowly across the resonance. The asymmetry variation is different for u and d-type quarks and leptons due to the relative sizes of couplings and is shown in figure 1.3 taking into account radiative corrections.[1] c, s and b quark contributions are indistinguishable, with mass effects remaining negli-

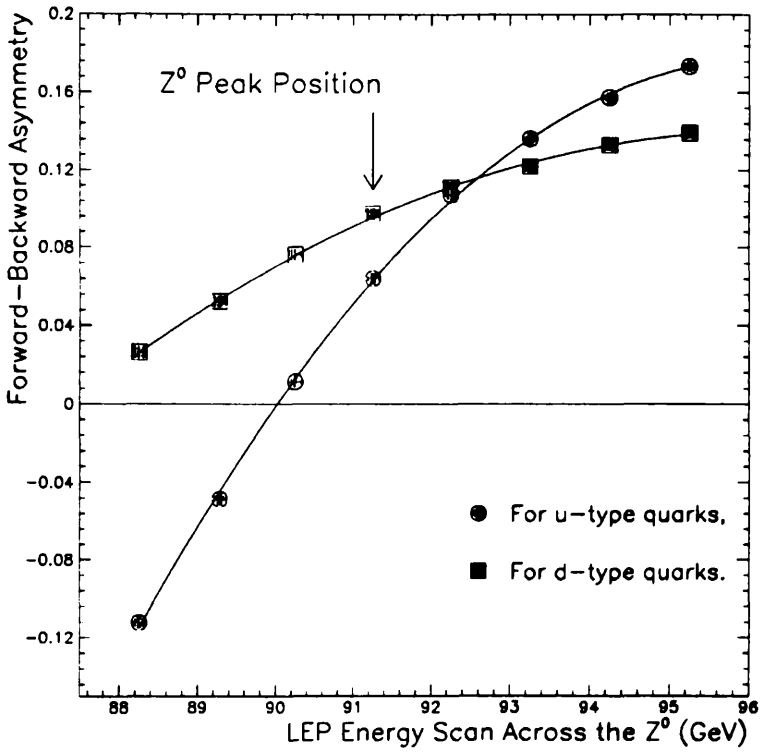

Calculations carried out [9] using the EXPOSTAR program assuming a top mass of 150 GeV and a Higgs mass of 100 GeV. The fitted curves represent quadratic polynomials.

Figure 1.3: Energy variation of the u and d-type asymmetry contributions.

gible to within $\sim 0.05\%$ for the extreme case of A_{FB}^{b}. A measurement of $sin^2\theta_w(M_Z^2)$ at the peak represents the effective value *at that energy* and allows a set of electroweak measurements at the Z° to be combined using the same formalism. The effect of a shift in $sin^2\theta_w(M_Z^2)$ to the curves of figure 1.3 is to change the overall magnitude of the asymmetries with little change to their gradient. Running couplings allow $sin^2\theta_w(M_Z^2)$ to be used as an indicator of unknown SM parameters as the asymmetries change slowly under the influence of radiative corrections.

In combined quark asymmetry measurements [10], the asymmetry is detected using the quark *charge* so that the measured combined asymmetry is the ***difference*** between the

[1] Calculated using EXPOSTAR which *excludes* the small effects of final state QED radiation.

curves of figure 1.3. Thus, (u,d) and (c,s) contributions cancel to a large extent while the b quark enters alone. The latter accounts for $\sim$ 40% of the combined, asymmetry[2] which is shown in figure 1.4 as a function of energy for different m_t assumptions. The

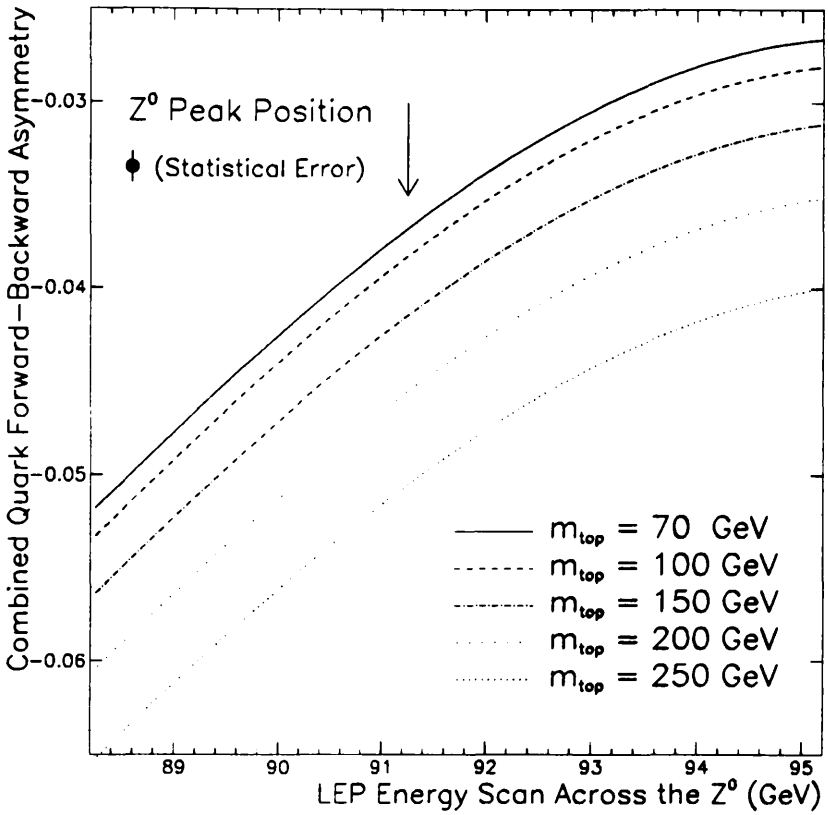

Calculations carried out [9] using the EXPOSTAR program assuming a Higgs mass of 100 GeV. The fitted curves represent quadratic polynomials with an inherent statistical uncertainty of ±0.0009 on each curve.

Figure 1.4: Energy variation of the combined quark asymmetry indicating the radiative effects of different m_t expectations.

gradient is of the same sign as that of u and $d-$type flavours as the difference between them *decreases* with energy. Corresponding changes to the effective value of $sin^2\theta_w(M_Z^2)$ with m_t as it runs across the peak are shown in figure 1.5.

1.4 Summary

Interactions at LEP energies, leading to the formation of hadronic events, are predicted by the Standard Model. Electroweak effects, due to the difference between left and right-handed couplings of fermions to the intermediate Z^o, are expected to induce an asymmetry between forward and backward regions of a detector. If the combined asymmetry of all

[2] At the peak of the Z^0 resonance.

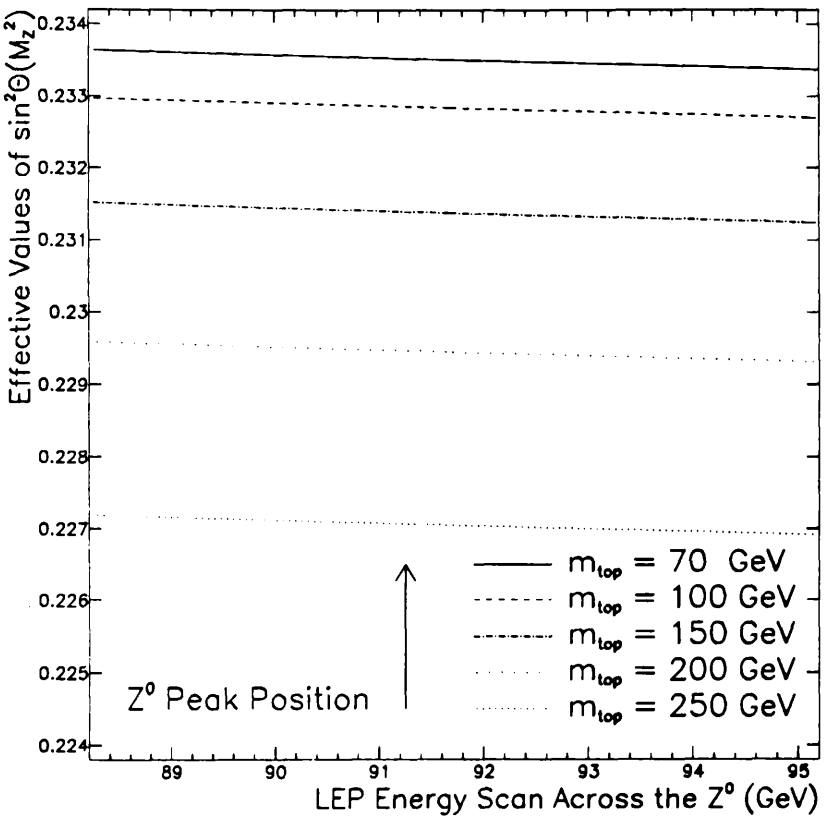

Calculations carried out [9] using the EXPOSTAR program assuming a Higgs mass of 100 GeV. The fitted curves represent quadratic polynomials.

Figure 1.5: Predicted values of the effective $sin^2\theta_w(M_Z^2)$ as a function of energy for different values of m_t.

flavours is measured, by tagging the charge and direction of quarks with perfect efficiency, then an asymmetry of the order of $\sim 4\%$ is expected on the peak. Radiative effects must be considered so that an asymmetry measurement is interpretable as a sensitive test of the effective value of fermion couplings and $sin^2\theta_w(M_Z^2)$ at the Z^o peak.

Chapter 2

The Experiment

2.1 Introduction

The detector discussed here is the ALEPH experiment for electron-positron annihilation at the LEP collider in CERN near Geneva. The experiment is housed in an underground cavern near the village of Echenevex on a straight section of the 27 km long LEP tunnel. It surrounds a vertex where two counter-circulating beams of electrons and positrons are brought into collision at high energies. In the current phase of LEP operations, the centre-of-mass energies at which collisions take place are around the nominal Z^o mass of 91 GeV. This gives a relatively high rate of interactions, which are detected and analysed by ALEPH. The purpose of LEP and ALEPH (during phase I) is to provide detailed studies of the type and rate of Z^o interactions. These are used to test predictions of the theory discussed in chapter 1 while searching for evidence of new phenomena.

Z^o interactions vary from low multiplicity events containing particles with large energies to complex events with many lower energy particles. A general purpose detector with power to separate particles of different types, position and energies, is best suited to such an environment. The rate of physics interactions allows fast electronics to be exploited to yield large quantities of information about the characteristics of each event.

Due to the complexity and volume of information available, it is necessary to limit the discussion presented here. Detailed information about the LEP accelerator is available in [11] while the ALEPH handbook [12] and [13] represents the definitive specifications of the detector itself.

The purpose of this chapter is to highlight aspects of the experiment which are of importance to the analysis presented later and to which the author contributed directly.

2.2 The LEP Collider

LEP lies within a tunnel of average diameter 8.5 km. The shape is roughly circular but uses eight straight sections (each 0.5 km long) connected by curved sections of length 2.8 km. The tunnel contains the elements necessary to bend, focus and accelerate electrons and positrons travelling close to the speed of light. This is done using a series of 3400 bending magnets, 1902 focussing and correction magnets and an RF system of 128 copper-coupled cavity units respectively [11]. The accelerator and detector, shown in figure 2.1,

are tilted at 1.42% to the horizontal for geophysical reasons. The +Z direction follows

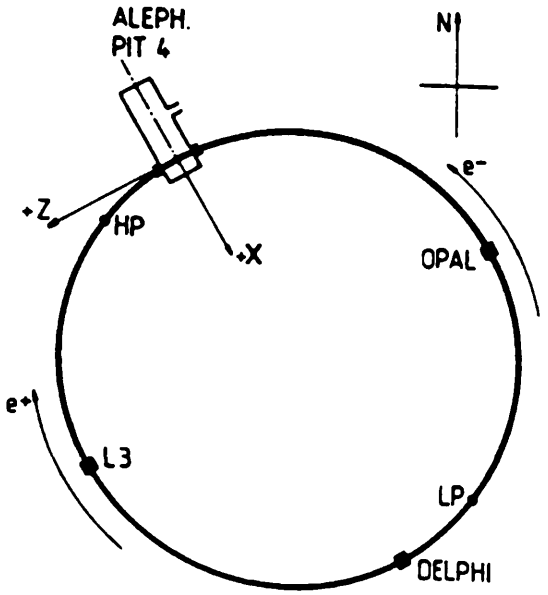

Figure 2.1: Schematic illustration of the LEP Collider.

that of the electrons (e^-) while +X points towards the centre of the ring and +Y points vertically upwards.

The machine was originally conceived [14] as an accelerator operating at centre-of-mass energies between 90 and 200 GeV with luminosities of the order of $10^{31}\,cm^{-2}s^{-1}$ around the Z^o peak. The first of these regimes is reached by LEP I using conventional copper cavity RF technology while Phase II will be reached by use of superconducting cavities. The event rate, R, is defined by the relation :

$$R = \sigma L \tag{2.1}$$

where σ is the total cross-section for $e^+e^- \rightarrow f\bar{f}$ and L is the luminosity. The event rate during the 1989→1990 period has been roughly one hadronic event every 15→20 s during a fill on the peak. The luminosity depends on the number of bunches, beam intensities and focussed sizes as they collide. The nominal luminosity of $10^{31}\,cm^{-2}s^{-1}$ has yet to be realised[1] due to problems of commissioning such a large and complex device. Typical luminosity in 1989→90 has been of the order of $2\rightarrow5 \times 10^{30}\,cm^{-2}s^{-1}$.

The beams circulate within a pipe of ellipsoidal cross-section under a vacuum of design pressure 3×10^{-9} Torr throughout. The pipe is narrowed around interaction regions, allowing detectors to come closer to the vertex. As they collide, bunches have widths of a few hundred microns and lengths of a few centimetres.

[1]The design luminosity assumes currents of 3 mA *per beam* while the amount of current delivered never exceeded this in the whole machine.

Creation of particles for LEP is carried out using a high intensity electron gun pulsed at 100 Hz. Positrons are created by accelerating electrons from the gun through a 200 MeV linear accelerator (LINAC) onto a tungsten converter where they are created in $e^{\pm}$ pair production from shower photons. These are accelerated by a further 600 MeV LINAC and transferred into the Electron-Positron Accumulation Ring (EPA). This process is repeated over a period of 11 s. A similar procedure is carried out for electrons but with the gun current reduced and converter removed so that particles are fed directly into the EPA. Nominal intensities of 1.6×10^{12} particles can be achieved at this stage [11]. After each accumulation cycle, the contents of the EPA are injected into the Proton Synchroton (PS) and the Super Proton Synchroton (SPS) which accelerates them to energies of 3.5 GeV and 20 GeV respectively.

Injection into LEP is carried out at 20 GeV using the SPS which injects into particle bunches repeatedly until each is of roughly equal intensity and contains $\sim 2 \times 10^{12}$ particles per beam. The design period of the injection cycle was approximately 15 minutes, although during 1989→90 this was significantly longer. Inside LEP, the two beams are accelerated to their nominal fill energy. After stable beams are achieved, orbit corrections and adjustments are made before introducing final collimator settings and data-taking commences.

During the period of a fill, the beams are allowed to *coast* around the ring, producing hundreds of Z^{o} collisions over a period of several hours. Intensities of the beams fall slowly over this time mainly due to losses from synchrotron radiation.

2.3 The ALEPH Detector

The ALEPH detector is designed and built to study collision products emanating from a vertex at the centre of the apparatus. A cylindrical approach is employed to detect particles over as large a solid angle as possible. This results in a largely *hermetic* detector, capable of detecting the 20 or so charged particles, and roughly equivalent number of neutrals, in each event.

As event rates at LEP are relatively low in comparison with ep and $p\bar{p}$ colliders, ALEPH is designed to gather as much information as possible about any given event. This relies upon a fast, structured and efficient online system to handle large amounts of information while performing data reduction. Thus ALEPH is characterised by large, high resolution devices exploiting their granularity with large numbers of fast readout channels. Its general features are :

- A comprehensive tracking system from the region immediately surrounding the vertex out to a radius of 1.8 m while immersed in a strong magnetic field of 1.5 T.
- A highly granular electromagnetic calorimeter *inside* the superconducting coil allowing uniform energy measurements combined with shower profile and position

information. This is supplemented by a large hadronic calorimeter inside the magnetic return yoke.

- High precision, combined luminosity calorimeters and tracking chambers allowing accurate measurements of absolute and relative luminosities.

At the time of writing, the final integration of a silicon strip vertex detector into the online readout and offline reconstruction is almost complete. The vertex detector is not discussed in detail beyond the effect of its presence on the present analysis.

Primary components of the detector are outlined below with their positions indicated in figure 2.2. ALEPH subdetectors are labelled using three or four letter abbreviations

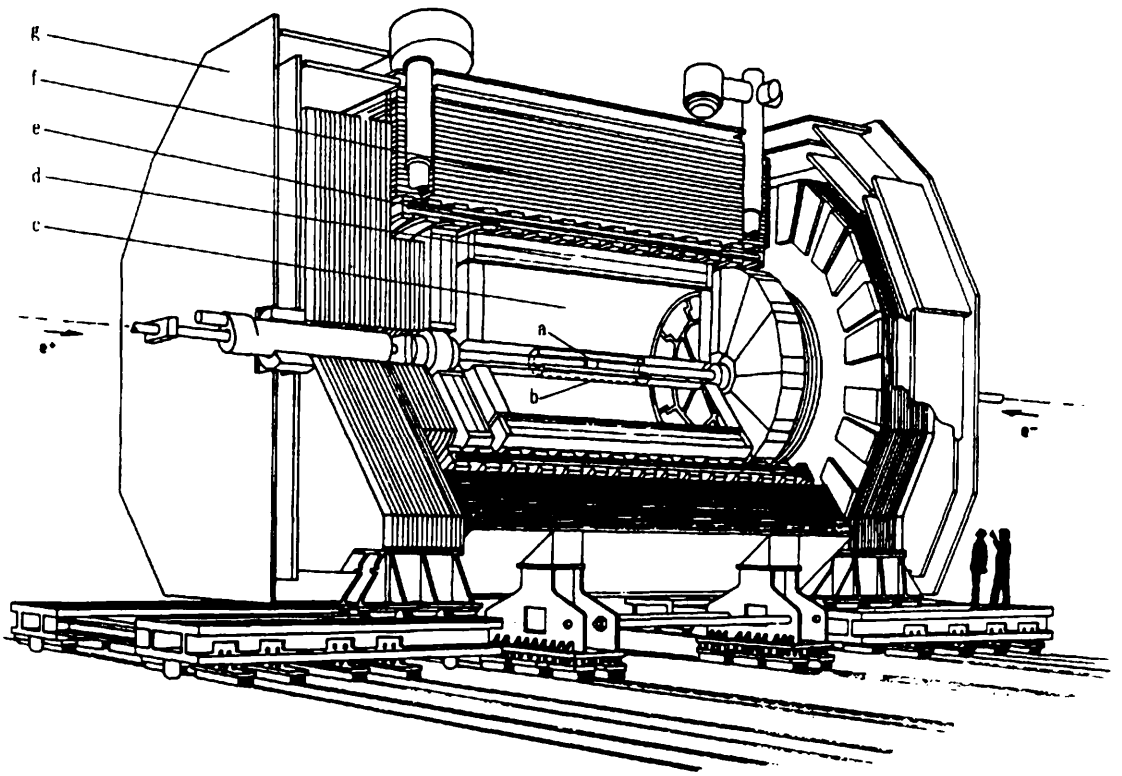

Components are labelled as follows : (a) the vertex detector, VDET, (b) the inner tracking chamber, ITC, (c) the time projection chamber, TPC, (d) the electromagnetic calorimeter, ECAL, (e) the superconducting coil, (f) the hadron calorimeter, HCAL and (g) the muon chambers, MUON.

Figure 2.2: Cut-away section through the ALEPH detector.

and are used throughout this document for brevity.

1. **Tracking Detectors**; These consist of the Vertex Detector (VDET), the Inner Tracking Chamber (ITC) and the Time Projection Chamber (TPC). They are used to track charged particles from the interaction point to the calorimeters. The TPC acts as the central tracking chamber with the ITC also providing a fast trigger. VDET will eventually be used to tag secondary decay vertices and to extrapolate

TPC-ITC tracks more accurately to the interaction point.

2. **Calorimeters and Muon Detectors**; These are the Electromagnetic Calorimeter (ECAL), the Hadron Calorimeter (HCAL) and the Muon Chambers (MUON). They are granular devices, offering good energy and position resolutions combined with electron and muon identification properties. Electrons, photons and muons passing through ECAL have distinctively different shower characteristics which are used offline for particle identification. Hadronic particles are seen in HCAL which uses the return yoke iron with limited streamer tubes. The penetration depth in this material is used to identify muons. Muon chambers lie outside HCAL, depending on the iron yoke to screen them from other particle types.

3. **Luminosity Monitors**; These are the Luminosity Calorimeter (LCAL), the Small Angle Tracker (SATR) and the Bhabha Calorimeter (BCAL). They determine the ALEPH luminosity from Bhabha events detected close to the beam. LCAL is of a similar design to ECAL, and is supplemented by SATR, positioned directly in front, to track the incoming leptons. BCAL provides an online luminosity measure using tungsten converter sheets combined with sampling layers of plastic scintillator and silicon strips.

ALEPH uses a superconducting NbTi solenoid to immerse the tracking chambers and electromagnetic calorimeter within a strong magnetic field. The total current circulating around the coil is just below 5000 A including subsidiary currents within *compensation coils*. These reduce field distortions from non-uniform magnetic characteristics of the external return-yoke (HCAL) and from imperfections in the winding of the main coil. Using the compensation coils in conjunction with field-map corrections keeps sagitta distortions in the TPC below the expected tolerance of 0.22 mm [13].

For the measurement of forward-backward asymmetries, several details are of some importance. The direction defined as being the +Z axis is the direction of electron travel, ie. the primary *fermion*, around the ring. The detector is manufactured, to a first approximation, as a symmetric device in both polar and azimuthal angles. As physics asymmetries represent a ratio of cross-sections, the systematics and statistical errors involved in measurements of the *absolute* luminosity cancel.

The following sections represent an overview of the major detector components relevant to this thesis.

2.4 Data Acquisition

The ALEPH Data Acquisition System (DAQ) is an important component, reflecting the modular design of the detector and data structures used for physics analyses. It exists as a collection of nodes running software modules with the aim of :

- Reducing a raw $\sim 500\,\mathrm{Mbs}^{-1}$ data rate to the order of $100\,\mathrm{Kbs}^{-1}$ suitable for offline processing and storage.

- Formatting raw data from the detector digitisations into the standard offline format.
- Performing consistency checks and error logging as data arrive.
- Allowing independent subdetector development and calibration.

To date, with the addition of the Slow Control detector monitoring system, all of the above goals have been realised. This is done using a rigid tree-like structure connecting high-level computers to the front-end subdetector electronics. The system is almost entirely digital from the front-end electronics up. Analogue signals from a particle's passage exist only for a fraction of a second before they are digitised and fed into the first processing elements.

The DAQ structure [15] has a "strong hierarchy" meaning that components on the same level do not communicate with each other but merely feed information either *upstream* or *downstream*. The architecture uses a 32 bit FASTBUS data acquisition chain linked to a local-area VAXcluster of minicomputers and multiple workstations. Both synchronous and asynchronous techniques are employed to optimise data flow and to reduce the time when a fresh event cannot be accepted (this is referred to as the experiment *deadtime*).

2.4.1 Flow of Information

The flow of data from the front-end electronics changes raw digitisations, produced at a speed governed by the nature of the detector, to a stream of formatted "tables" passing onto disk. The protocol for this flow is synchronised by a trigger which activates the readout process. As each subdetector reads out at its own speed, data is allowed to flow asynchronously up each branch of the tree. The flow can pass through several stages before arriving at the Main Event Builder (MEB). Here events are assembled from their constituent parts with synchronous flow reasserted by demanding that all parts refer to the same event. This data flow is achieved by allocating memory at intermediate readout stages to buffer data from several events. Each stage acts according to a protocol using an event buffer.

Tasks run in parallel where a *producer* can be reading data from the next event while the present one is being formatted and the previous is being either transmitted or studied by *consumer* tasks. The structure of producers and consumers is used throughout the DAQ with data transfers also handled by rigid protocols.

The ability of a single subdetector to run in *standalone* mode is inherent in the above system of data flow. Several independent calibration or debugging activities can take place concurrently, reading data into several versions of the DAQ in separate software *partitions*. The concept of partitions ensures that data flow through the DAQ from several sources to various destinations is possible.

2.4.2 Hardware and Software Implementation

The FASTBUS standard [15] is used exclusively for the DAQ with occasional NIM or CAMAC units providing specialised external functions. The ALEPH event builder is a general purpose FASTBUS unit and is used throughout the DAQ in the guise of trigger supervisors (TS), Service Request Handlers (SR), FASTBUS→VAX interfaces and for both local and main EBs.

DAQ control signals are passed throughout the readout tree by dedicated Fan-In-Fan-Out modules (FIO) which are essentially programmable logic arrays. System timing commences with the T0 module which synchronises readout electronics to the LEP bunch crossing. Several signals are provided before and during the crossing, based on a fixed delay from the previous one. The signal is passed through a chain of local trigger supervisor modules (TS) controlled by the Main TS.

The network of readout controllers, (ROCs), feed subdetector data into local event builders and ultimately into the MEB. The DAQ reduces the data flow largely by *zero-suppression* which prevents readout of channels unaffected by the particle collision. Prior to arriving at event builders, data are formatted into the ALEPH data standard, BOS [16]. This memory management program is the underlying data structure used throughout ALEPH. Data are represented as banks in a superficially linear order but organised into tables using header information.

Consumer tasks make monitoring of the data quality and the compilation of statistics etc. an integral part of the DAQ. In many cases, if an error is detected, diagnostic banks are inserted into the BOS event and passed offline. This technique is used by the Slow Control System which switches hardware on and off and provides information on voltages, currents and temperatures etc. Databases are used throughout the DAQ to provide access to routing tables, addresses etc. and booking of system resources.

2.4.3 System Performance

The ALEPH DAQ allows flexible use of various subdetectors for individual development and a coherent structure for full data-taking. With the luminosity and scan strategy employed during 1989→1990, the system handled the incoming data rate while introducing a relatively small deadtime of $\sim$ 2%. The data volume for accepted events varies from between 30 Kb to several 100 Kb for large hadronic events while the detector "up-time" has been over $\sim$ 80%. Data integrity is ensured throughout by automatic FASTBUS parity checking of data transfers. Combined with the ability to rapidly start and stop data taking, the system has allowed ALEPH to amass a total of $\sim 2 \times 10^5$ events; a substantially higher total than any other LEP experiment.

2.5 The Trigger

The ALEPH Trigger is an integral part of the online system and synchronises the DAQ using the Trigger Protocol Unit (TPU) and MTS. It is used mainly to reduce backgrounds to a manageable level. Expected event rates from known physics processes are such that acceptance of any significant charged or neutral energy anywhere in the detector is permissible as a trigger. This contrasts with higher rate experiments where physics algorithms searching for correlations between tracks or energy deposits are used to accept events passing a preconceived criterion. In this way, the ALEPH scheme incorporates sensitivity to new physics processes.

2.5.1 Constraints and Implementation

ALEPH introduces several constraints upon the timing and speed which can be maintained by the trigger. Important considerations are : (a) the bunch crossing rate of 40.5 KHz resulting in a $\sim$ 1 Hz rate of physics events and (b) the limitations of gating, refresh and readout of subdetectors such as the TPC and ECAL. These are satisfied by the three level trigger scheme shown below :

- **Trigger Level 1:** The trigger delivers its decision within 5.5 μs of the bunch crossing and informs the TPC of whether the gate should remain open to accept already drifting tracks or be closed to prevent the build up of space charge.
- **Trigger Level 2 :** This corresponds to the full TPC drift time so that information from trigger pads may be used in subsequent decisions. This reduces the rate to below 10 Hz.
- **Trigger Level 3 :** The third level aims to verify that the triggered event is a genuine e^+e^- interaction and occurs after a full readout of the detector. This performs partial *reconstruction* of tracks and energies and reduces the rate to roughly 1 Hz.

Expected and observed rates after each level are given in table 2.1.

Trigger Level	Expected Rate (Hz)	Observed Rate in 1989 → 90 (Hz)
Level 1	$\sim$ 500	7.0
Level 2	$\sim$ 10	1.5
Level 3	$\sim$ 1.5	0.6

The disparity between expected and observed values is indicative of the lower luminosities delivered combined with the unexpectedly low backgrounds.

Table 2.1: Expected and observed trigger rates during the 1989 → 90 run period.

Trigger levels 1 and 2 are based on the signals from *segments* of four detectors; HCAL, ECAL, ITC and TPC. Each subdetector is sectioned into $\sim$ 60 segments which are cabled

through mixer units, summed and fed into discriminators to yield four YES/NO signals per segment. These are the primary signals available for physics triggers and form a total of 32 possible decisions.

Triggers are masked onto a one word register, passed through a veto and sent to the TPU and MTS which informs various subdetectors of whether they should ready themselves for the next fresh event or continue with readout of the current one. The level 3 trigger is based upon a small farm of KA800 processors on the same bus as the main VAX computers. These run in parallel looking at the entire information of each event, performing cross-checks and verifying the level 2 YES decision.

2.5.2 Available Triggers and Performance

Physics triggers depend on general characteristics of the different types of expected events and aim to detect every $e^+e^- \rightarrow Z^o$ interaction. There is a large degree of redundancy so that several triggers often "fire" at once. A general list of triggers is shown in table 2.2 while additional specialised triggers are also used, specifically for neutral electromagnetic and hadronic energy depositions. Generally, events are triggered by more than one of

Trigger Inputs	General Trigger Description
ECAL and ITC	Total energy greater than 6.5 GeV in the ECAL barrel. Total energy greater than 3.8 GeV in either of the ECAL endcaps . Total energy greater than 1.6 GeV in both end caps in coincidence. Track candidate in the ITC and at least 1.3 GeV in ECAL.
HCAL and ITC	Track candidate in the ITC and four out of 12 HCAL planes fired.
LCAL	A coincidence of 20 GeV on one side with 16 GeV on the other. A single arm deposition of 31 GeV on either side. Lower energy requirement single arm triggers for background tests.

Table 2.2: General description of the available triggers.

these combinations. This gives rise to measured efficiencies of 100% for hadronic and lepton pair events with 99.7% for Bhabha events. From experience in 1989 [13], roughly 20% of level 1 triggers involve tracks only while level 2 removes about 75% of these[2]. Level 3 reduces the rate of single neutral electromagnetic events brought about due to sparks, cosmics rays or noise fluctuations in ECAL.

[2]These are primarily beam gas interactions.

2.6 The Inner Tracking Chamber

The purpose of the ITC is twofold; providing a fast input to the level 1 trigger while detecting tracks close to the beam. Information is available 2 to 3 μs after the bunch crossing and is the only tracking used to make the first level decision. The subdetector is shown in figure 2.3. Loss of low-momentum particles is small as the inner wall of the

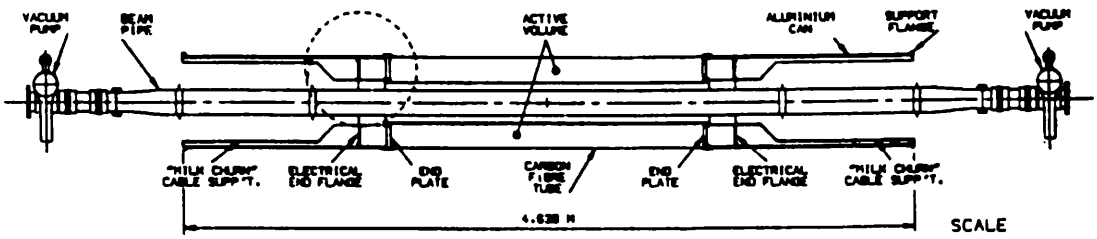

Figure 2.3: Cross-sectional diagram of the ITC.

chamber represents only 0.002 radiation lengths. It is a multi-wire proportional drift counter (MWPC) with active wires 2 m long, parallel to the beam line. The response time is limited by the drift time in the hexagonal "cell" arrangement of the wires shown in figure 2.4. Sense wires are held at a voltage of between 2 and 2.5 kV, surrounded by

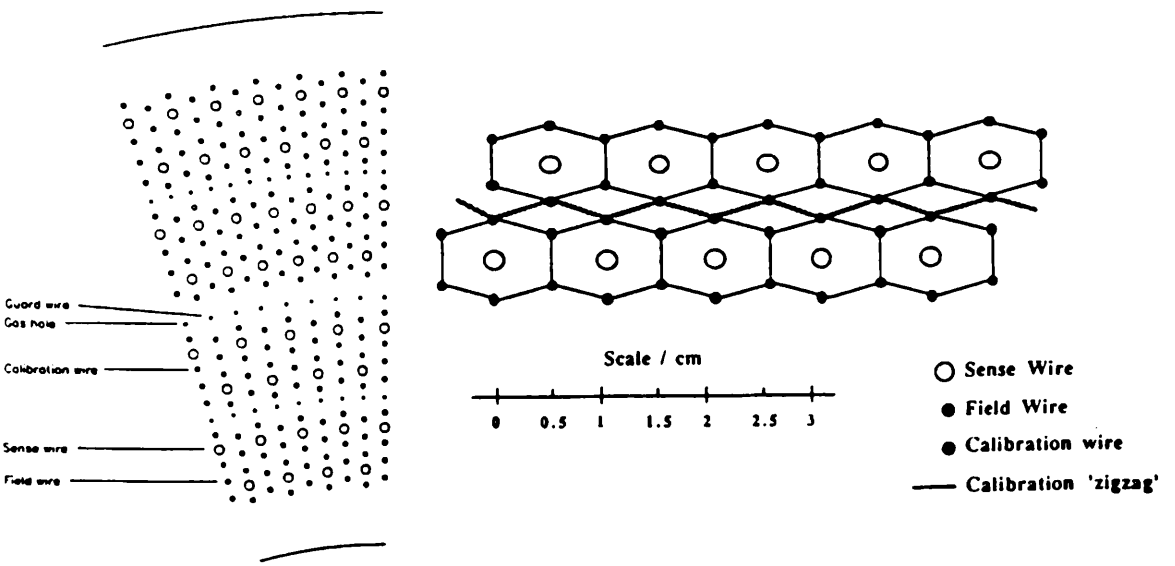

Figure 2.4: Wire cell structure of the ITC.

six field wires at earth potential. Cells are staggered to remove the left-right ambiguity while increasing radially in size as the hit density decreases. The nominal $r\phi$ coordinate is given by the position of the wire at the centre of the cell, with the Z coordinate derived from the difference in arrival times of pulses at either end of the wire. Signals from the analogue-to-digital (ADC) converters are fed into a primary $r\phi$ processor which searches

for tracks in the $r\phi$ plane. A second $r\phi z$ processor will eventually be responsible for associating hits to tracks in 3 dimensions using Z information. Much of the speed of the ITC readout electronics is due to its *single-hit* design. This means that once a channel has detected the passage of a particle, then further particles can pass unnoticed by that channel.

The ITC allows tracking to be performed in the region between 160 mm and 260 mm in radius and over a total length of 2 m in Z around the vertex. This corresponds to an angular acceptance of $-0.97 < cos\theta < 0.97$ for tracks crossing all eight layers of the chamber. The resolution of hits in $r\phi$ varies slightly with radius but is, on average, 120 μm. The Z resolution is 3 cm, including a small Z dependence due to signal attenuation effects. Trigger information is available in 500 ns and 2.5 μs for the $r\phi$ and Z coordinates respectively.

During the August 1989→August 1990 period, Z information of the ITC was not used. The lack of the less accurate Z coordinate does not degrade the quality of tracking in ALEPH because of the greater accuracy of tracks from the TPC. Problems associated with this loss of information only appear as a decrease in the track finding efficiency at low angles. This occurs below the 15° angle at which the TPC can track in Z efficiently since reconstruction requires a minimum of 4 TPC space points to extrapolate into the ITC. When ITC Z coordinate finding is available, this limit may be circumvented by inverting the method to extrapolate "tracklets" in the ITC to the low angle region of the TPC, recovering unassociated hits in the larger detector [17].

Offline coordinate finding in $r\phi$ is carried out using hit wire numbers to find the nominal position after correcting for the sag of the wires. The time difference between the hit and the beam crossing is calculated using a time-to-digital (TDC) converter and combined with the drift velocity to calculate the displacement from the wire. Further corrections are necessary so that the ITC does not degrade the track fit from the larger and more accurate TPC. These involve the relative alignment between the TPC-ITC and angular corrections for non-radial or low momentum tracks.

2.7 The Time Projection Chamber

The time projection chamber is the central subdetector of ALEPH, providing accurate tracking over a long lever-arm from the ITC out to the calorimeters. In addition, it provides information for identifying particles using $\frac{dE}{dx}$ as they pass through the drift volume. The chamber has two parallel fields; magnetic and electric, to bend a track and transport its ionisation to sensitive endcap regions. The chamber is cylindrical in shape (as shown in figure 2.5) with axis parallel to the ($\overline{E}$ and $\overline{B}$) fields and the colliding beams. Traversing particles leave a trail of ionisation behind them which drifts onto the endcaps. The $r\phi$ position at which ionisation is detected is combined with the measured drift time and velocity to form a fully three-dimensional coordinate. Tracking benefits from the uniformity of the drift volume which interferes little with the particle's passage.

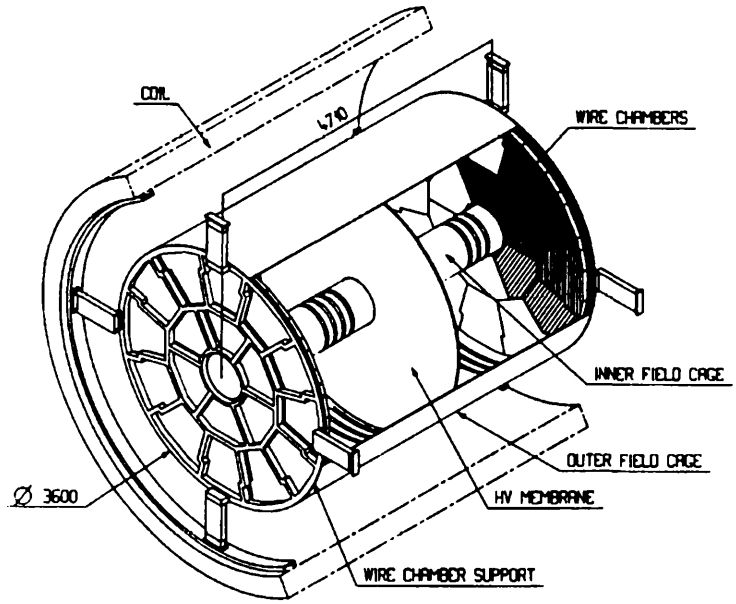

Figure 2.5: An overall view of the time projection chamber (TPC).

This allows smooth parameterisations and accurate simulation of geometrical effects to be used when fitting track helices to the 21 possible space points. Such consideration are discussed in detail in section 2.7.2.

The ALEPH TPC is the largest chamber of its kind to date and incorporates several solutions to problems noted by its predecessors. Previous experiments discovered that field distortions limited the achievable resolution while build-up of space charges within the drift volume led to further inhomogeneities. These problems are countered in ALEPH using a combination of laser calibration[3] and *gating* of the sensitive wire chambers. After reconstruction of coordinates and tracks, resolutions of 160→400 μm per coordinate are found depending on the track position and angle. The chamber measures the track's transverse momentum (relative to the beam axis) with a resolution given by :

$$\frac{\Delta p_t}{p_t} = 0.027\, p_t \frac{\Delta s}{l^2 B} \tag{2.2}$$

where Δs is the sagitta resolution, B the absolute magnetic field and l, the lever-arm over which the track is measured. Discussion of the resolution and its dependence on momentum and geometry is given in section 2.7.2 while the chamber's performance is described in section 2.7.3.

2.7.1 Design Considerations and Construction

The TPC consists of inner and outer field cages, a central membrane and two endplates. The subdetector is essentially a homogeneous gas-filled volume with composition 91%

[3]This is described in Appendix B.

Argon and 9% Methane held slightly above atmospheric pressure. The gas is slowly cycled from a larger buffer volume held on the surface. The mixture is selected due to its favourable gas amplification, low attenuation, and high value of $\omega\tau$. The latter[4] ensures that drifting electrons spiral *tightly* along the field lines. The gas system is optimised for maximum stability so that changes to drift velocity and gas gain are small and develop slowly with time.

The field cages are responsible for maintaining uniformity of the electric field and prevent distortions as electrons drift along. This is done by placing the central membrane at a large negative voltage (typically -27,000 V) while each endplate is held at just below ground potential. The gradient between these surfaces is then "guided" by a potential divider of high-precision resistors on both field cages. The alignment of the TPC structure, with respect to the remainder of the detector, is crucial to the parallel nature of the two fields. Alignment is maintained at the levels shown in table 2.3 ensuring that field directions are as parallel as possible. Use of composite materials results in radiation

Component	Alignment Accuracy and Method
Sector Positions	$\sim 50\,\mu$ from mechanical positioning.
Endplate to Endplate	$\sim 500\,\mu$ from optical surveys.
Inter-subdetector Position	$\sim 1000\,\mu$ from optical surveys.

Table 2.3: The accuracy and method of aligning the major TPC components.

lengths of only $0.023X_o$ and $0.048X_o$ for the inner and outer field cages respectively. The central membrane is made from a $25\,\mu$ thick mylar sheet coated with graphite paint. It is placed close to the LEP vertex position at Z=0 and perpendicular to the beam axes. It represents negligible material to passing particles while maintaining a field gradient of $125\ \mathrm{Vcm}^{-1}$ between Z=0 and the endplates. This gives an electron drift velocity of $5.2\,cm\,\mu s^{-1}$ which lies on the parabolic maximum of the relation between drift velocity and applied voltage [18]. The velocity vector is determined experimentally using a laser system described in Appendix B.

Sector Construction and Gating

The large lever-arm of the TPC leads to a need for large, uniform and sensitive endplates. This is achieved using a set of 36 (2 x 18) wire chambers with "zig-zag" boundaries segmenting the endcaps into independent modules. These are arranged as shown in figure 2.6. Each sector contains between 900 and 1400 sensitive cathode pads arranged in concentric rings around the beam. The staggered method of placing inner and outer sectors, combined with the "zig-zag" sector boundaries, ensures that all particles cross a

[4] ω represents the cyclotron frequency of the electrons in the magnetic field while τ is the mean time between collisions with gas molecules.

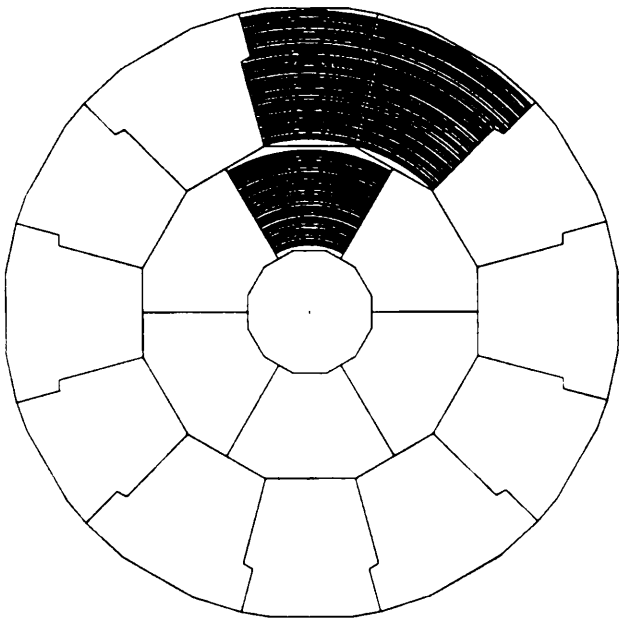

Figure 2.6: Overall geometry of the TPC endplate.

large number of padrows. The pads have dimensions 5.202 × 30.0 mm with the longer radial sides separated by a distance of 5 mm. The wire grids shown in figure 2.7, consist of 3 individual layers serving different purposes. These are, in order of height above the

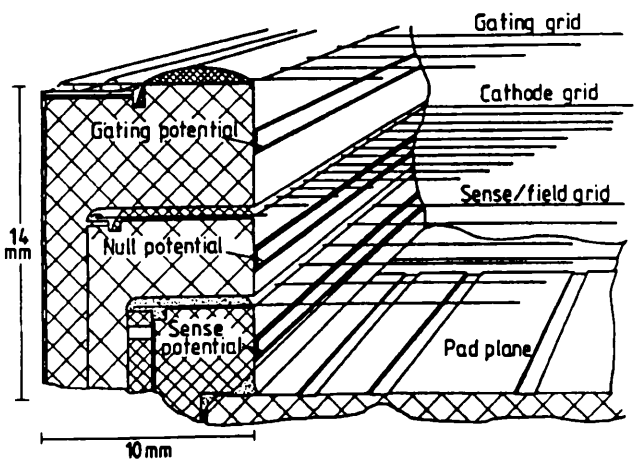

Figure 2.7: Schematic of the sector edge region showing wire grids and potential strips.

cathode pads :

1. **The Sense and Field Wire Grid** uses either 148 or 196 sense wires per sector, held at over 1000 V, to provide $\frac{dE}{dx}$ and Z measurements from avalanches which form around them. These are interleaved with field wires to shape the electric field and direct electrons to the avalanche region.

2. **The Cathode Grid** is held at the same voltage as the pads. This separates the drift and sense fields and prevents deflection of incoming electrons when close to the endplate. The delineation between field regions is shown in figure 2.8.

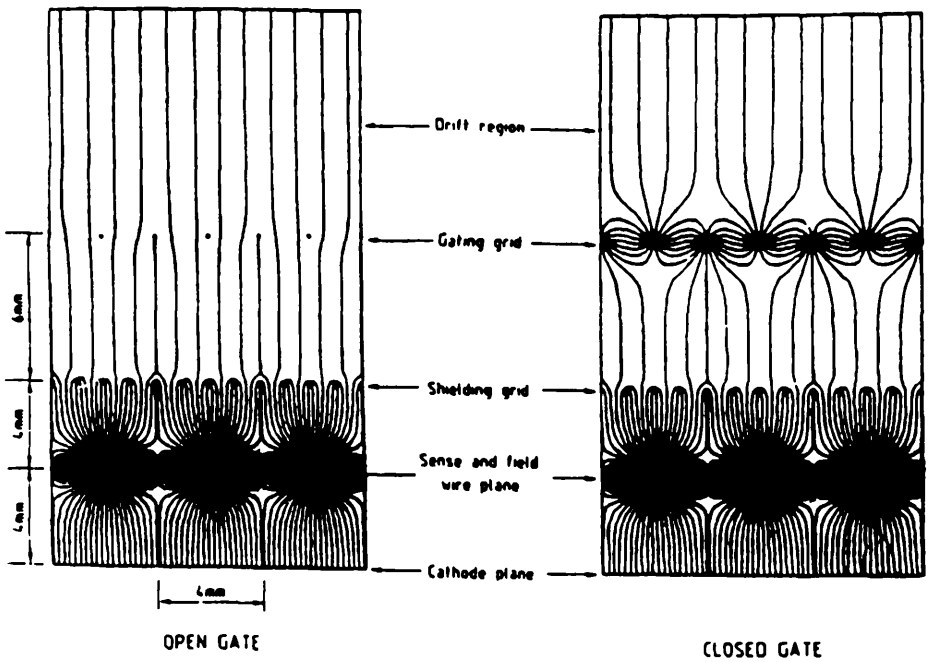

Figure 2.8: Electric fields around the wire grids above the endplate sectors when the gating grid is open and closed.

3. **The Gating Grid** serves the twofold purposes of reducing the build-up of space charge in the drift region while inhibiting chamber ageing. This is achieved by being able to *open* or *close* the sensitive region at will and is done by setting alternate wires to opposite differences in voltage from the null cathode value. The effect on the field above the shielding grid is also shown in figure 2.8

Potential strips are arranged around the perimeter of the sector and adjusted so that uniformity of the various fields is maintained close to the edges. At positions where the circular pad rows meet a sector edge, full cathode pads are split into half-pads as shown in figure 2.7. These are intended to decrease distortions and allow particle tracking as close to sector boundaries as possible.

The *transparency* of the gating grid is a function of the differential voltage applied between alternate grid wires. The gate is opened upon warning of an imminent bunch crossing (EGBX) and allows electrons to start drifting into the sense region. After a delay, it is left open or closed depending on the level 1 trigger decision. If the event is rejected then the gate is closed until the next EGBX while with a YES decision the gate remains open for the full drift period. The loss of track segments close to the endcap is prevented while leaving the gate open only for $\sim \frac{1}{3}$ of the time on average.

Calibration and Readout

The large volume of the TPC results in a vast number of readout channels, and data, as summarised in table 2.4. The 45 μs drift of the chamber is scanned with a time resolution

Type	Channels	Boards	TPDs	TPPs
Pads	41004	2568	660	36
Wires	6336	408	108	36

The number of channels for both pads and wires are different for the three different types of sector. The above values are totals for the whole TPC including both endplates. Each channel is sampled every ~100 ns during a full drift time of ~ 45 μs yielding ~450 samples per channel.

Table 2.4: Total number of readout channels for the TPC.

sufficient to separate pulses from tracks lying close together in Z or crossing each other. FASTBUS time projection digitisers (TPD) are used to sample incoming data from wires and pads at a rate of 11.2 MHz using flash analogue-to-digital-converters (ADC). Each TPD scans 64 channels with sufficient memory to buffer 4 events. The TPD scans the samples searching for values above threshold which are formed into complete pulses. An address table HITLIST is compiled and sent to the next level, the time projection processors (TPP), which transfer data using FASTBUS block exchanges. At all times, any incoming event has priority over such transfers and is buffered before transfers restart. A number of *pre* and *post-samples* are also transferred to the TPP allowing the complete pulse shape to be analysed .

The TPP is used to control and receive data from one sector of pad and/or wire TPD modules while performing the following tasks :

- Transferring data from the TPD to free event buffers.
- Renumbering channels and formatting data into BOS banks.
- Standalone channel calibration.
- Long term monitoring and data compression.

After these have been completed, BOS banks are passed to the event builder allocated to each TPC endcap before being transferred to the MEB. Uniform calibration of wire and pad channels is essential to provide accurate, unbiased $\frac{dE}{dx}$ and coordinate measurements. This is performed by the TPP and can be done in under 30 minutes. Calibration is performed using programmable generators for each sector to pulse the field wires and induce signals on both sense wires and cathode pads in a similar way to a passing particle. An iterative process is followed of applying a known pulse, adjusting the FADC ladder tap voltages via programmable DACs and measuring the channel response before the required degree of linearity is found. This is done for all channels, measuring the response slope (gain) and intercept (pedestal), to arrive at a calibration error of 1% in pulse height or 6 ns on

a time measurement. This keeps position errors below 70 μm in $r\phi$ and less than 0.5 mm in Z from calibration effects alone.

2.7.2 Creation of Coordinates and Track Reconstruction

The TPC reconstructs coordinates and tracks of charged particles traversing the gas-filled chamber. As clouds of ionisation drift through the chamber, they are affected by collisions with gas molecules and electromagnetic fields. These are described by the *Langevin* equation [18] where the interplay between the two types of field depends critically on their relative strengths[5]. This is shown in equation (2.3).

$$\overline{v_D} = \frac{\mu}{1+(\omega\tau)^2}\left[\overline{E} + \omega\tau\frac{\overline{E}\times\overline{B}}{\mid\overline{B}\mid} + (\omega\tau)^2\frac{\overline{B}\left(\overline{E}.\overline{B}\right)}{\overline{B}^2}\right] \tag{2.3}$$

The behaviour of electrons during drift is dependent on the magnitude of the quantities $\mid\overline{E}\mid$, $\mid\overline{B}\mid$ and $\omega\tau$. With the current TPC gas mixture $\frac{\omega\tau}{\mid\overline{B}\mid}$ has been measured to be $5.9\,(\pm 0.2)\,\mathrm{T}^{-1}$ [18]. At low magnetic fields (low $\omega\tau$) the first term in (2.3) dominates, and the drift is largely parallel to the $\overline{E}$ field, while at large magnetic fields (large $\omega\tau$) the opposite is true. The TPC is normally run at 1.5 T where electrons spiral tightly around the $\overline{B}$ field lines, reducing transverse diffusion and deviations due to electric field distortions. The decrease of coordinate residuals as a function of the magnetic field, shown in figure 2.9, is expected from contributions of the second term in equation (2.3). As the drift length increases, the electron cloud grows longitudinally due to collisions with the gas. A similar effect is apparent when tracks are at low angles relative to the beam, so that a long projected track segment in Z creates an extended cloud of ionisation.

The cloud drifts through the chamber with an attenuation of less than 5% for the full drift length before being measured twice on arrival using the sense wires and cathode pads. The amount of charge deposited, as well as the time of drift, is measured by both pads and wires and used to determine the *mean* arrival time and ϕ position on the pads. Pads use the time of arrival and distribution of charges along the padrow to form a precise three-dimensional coordinate while the wires measure the time of arrival. Coordinates are measured in terms of (r, ϕ, Z) where r is determined by the radial pad or wire position.

Reconstruction

Tracks in the TPC are fitted using *coordinates* formed from *clusters* of associated *pulses* induced on cathode pads. The TPD readout gives pulses consisting of digitised samples which lie above threshold. A fixed pedestal is then subtracted. The readout of such pulses contains *pre* and *post* samples which can be used to define a *dynamic* pedestal different from the constant value determined by the TPP calibration. Tests indicate that such a

[5]The various quantities are as follows : $\overline{v_D}$ is the drift velocity vector, μ is the electron mobility, ω and τ are defined previously while $\overline{E}$ and $\overline{B}$ are the electric and magnetic field vectors respectively.

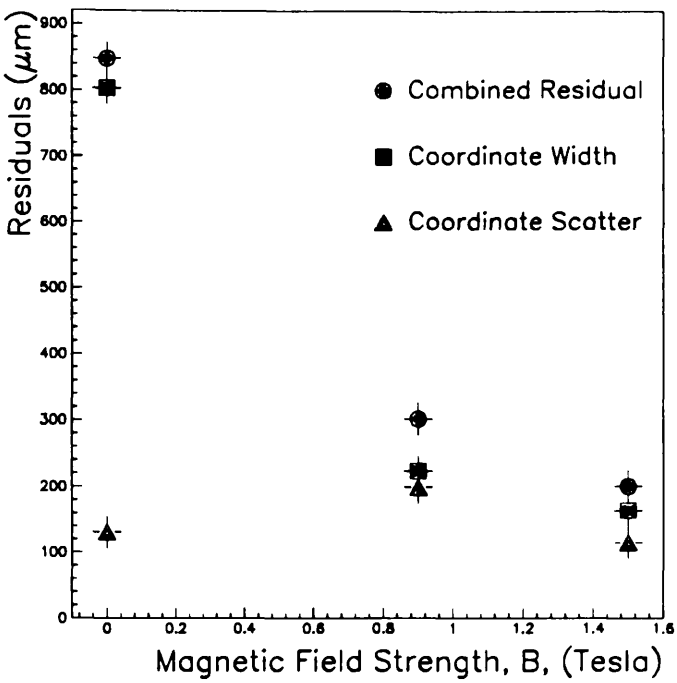

Measurements were carried out with superconducting coil currents of 0, 3000 and 5000 A corresponding to magnetic field strengths indicated. 200 laser shots were used for each point in sectors 2 and 10. The *combined residual* is due to the effects of the inherent *coordinate width*, ie. the spread of coordinates with each laser shot in conjunction with the *coordinate scatter* of points around the central track.

Figure 2.9: Observed decrease of coordinate residuals in the TPC as the strength of the magnetic field is increased.

dynamic pedestal does not significantly increase the spatial resolution while remaining sensitive to effects from electronic response and multiple pulses.

Pulses are grouped into clusters by checking adjacent pads for pulses which overlap by at least one time-sample. In this way a two-dimensional cluster (in pad number and time) is formed which can contain contributions from different tracks. An example of a cluster is shown in figure 2.10. Subsequent steps separate these pulses and clusters into *subpulses* and *subclusters* from evidence of multiple peaks, before trying to "recluster" these. Within a subcluster, each subpulse must be on a separate pad. Such distinctions are made using charge profiles of the pulses in conjunction with criteria to optimise the resolution and efficiency for overlapping tracks. If a valley is found between pads in a cluster, an attempt is made to separate them into two. If it fails, and subsequent checks on its maximum width and length indicate problems, it is flagged as being unusable.

Surviving charge information from subpulses and subclusters is used to provide a precise determination of the coordinate in time and ϕ using the following method :

(i) **The position in time** is determined from a weighted charge summation over mean arrival times of contributing subpulses. The arrival times are, in turn, calculated from the mid-time between rising and falling edges of the subpulse with reference

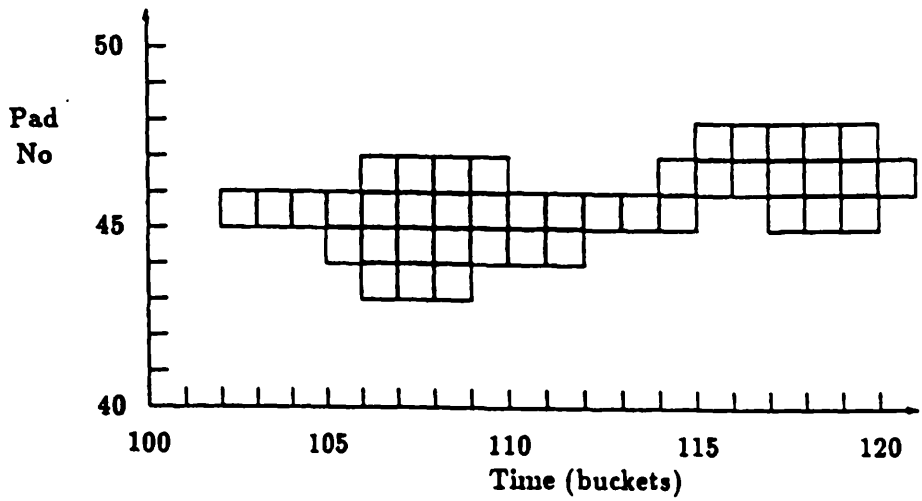

Figure 2.10: Padrow cluster formed from two nearby tracks.

to a constant fraction of the maximum sample value.

(ii) **The $r\phi$ position** is determined using several methods depending on the number of pads involved in the subcluster. For two and three pad clusters, a Gaussian *pad response function*, describing the response expected on the pads is used. This takes into account the charge collected on the sense wires and the coupling between the wires and pads for a track crossing at zero angle [18]. The width of the gaussian, σ_{prf}, is an important parameter since, in two pad clusters, the track position, x_{track} along the padrow is calculated from the ratio of the pad pulse heights[6] using relation 2.4.

$$x_{track} = \frac{\sigma_{\text{prf}}}{\delta} ln\left(\frac{P_1}{P_2}\right) \tag{2.4}$$

If more than three pads pads are involved, a weighted average of the charges is used.

With typical charged multiplicities of around 20, the assignment of coordinates to tracks represents a considerable pattern recognition exercise. In the (X,Y) or (r,ϕ) planes, a track appears as a circle while in the (S_{xy},Z) plane[7] it is a straight line. Fitted track parameters and conventions are shown in figure 2.11. Helix parameters are defined in table 2.5.

Coordinates are associated to helices using a three-stage algorithm based on the concept of adding small track segments, or *chains*, together. Final chains may be linked together if they appear to form repeated spirals from low momentum particles. Effects of multiple-scattering are included at each stage and increase coordinate errors as the distance from the origin grows. Fine-tuning algorithms are applied while searching for decay vertices and misassociated coordinates. Tracking is continued by extrapolating tracks into

[6] δ is the distance between adjacent pad centres.

[7] S_{xy} is defined as the arc length from the point of closest approach to the vertex.

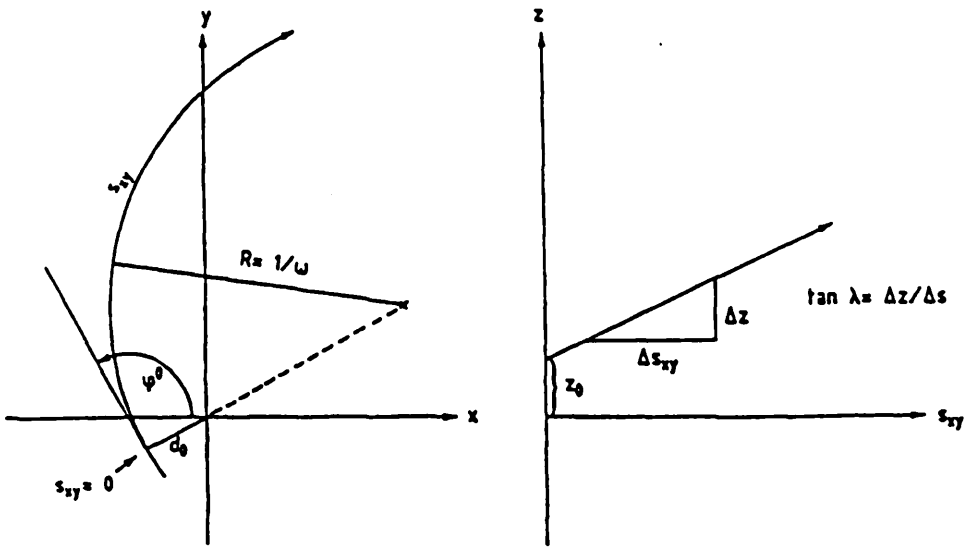

Figure 2.11: Helix parameters and notation for fitting TPC tracks.

Parameter	Definition
R	Inverse radius of curvature in (X, Y).
D0	Closest point of approach to the beam in (X, Y).
Z0	Z position at the point of closest approach.
ϕ_0	Initial angle of the track in the (X, Y) plane.
$tan\,\lambda$	Angle of the track in the (S_{xy}, Z) plane.

Table 2.5: Fitted helix parameters and their definitions.

the ITC where *hits* are associated to the fitted TPC track. The procedure starts with the outer two ITC layers and continues inward if at least one hit is found. A minimum of 3 associated hits out of a possible 8 is required before the track is refitted. TPC wire hits are used to provide $\frac{dE}{dx}$ information on the tracks to which they are associated. Association is performed using the track fit to calculate which wires are crossed by the track and searching for corresponding wire pulses in a given time window. A truncated mean of associated pulses is then calculated after normalising to the projected track length "seen" by the wire.

Tracking Systematics

The accuracy with which a track is measured depends upon the accuracy of contributing coordinates. There are several geometrical contributions which increase the inherent "width" of a coordinate which is detected. These are synonymous with an increase in $\sigma_{\rm prf}$, or the resolution in $r\phi$, and are summarised below :

- **Increasing Wire Crossing Angle** affects the projected track length for a given wire due to the direction of electron drift in the combined electric and magnetic fields.
- **Increasing Pad Crossing Angle** determines how widely the ionisation is spread along the padrow.
- **Increasing Drift Length** spreads the charge cloud from ionisation in proportion to the time of drift.

Further effects arise when the structure of the charge cloud is considered moving through the chamber. As the angle of the track relative to the beam *decreases*, pulses become longer in time which reduces the Z accuracy.

Additional complications arise at edges of sectors, where coupling between sense wires and pads becomes distorted due to unknown field components and difficulties in calibration. These result in coordinates being systematically shifted away from the sector edge as tracks cross the boundary. This is shown in figure 2.12 (a). Uncorrected tracks can

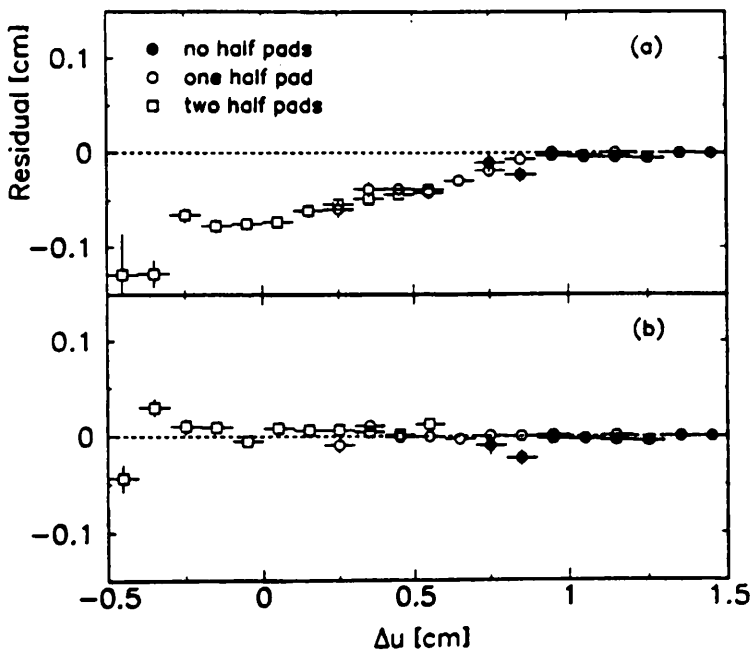

Figure 2.12: Coordinate residuals with respect to the outer sector edge before (a) and after (b) the correction of half-pad coordinates.

be both split or lost and the overall resolution degraded. Such effects were noted in early cosmic ray events before being fully understood and corrected using LEP events as shown in figure 2.12 (b) [18]. The overall resolution of coordinates containing half-pads remains approximately 30→40% lower than that of full pad coordinates.

2.7.3 Subdetector Performance

The nominal momentum resolution of the TPC is expected to be :

$$\frac{\Delta p}{p} = 0.0015\, p(GeV/c)^{-1} \tag{2.5}$$

for particles traversing the full 21 padrows. This corresponds to optimal coordinate resolutions of 160 μm in $r\phi$ and a Z resolution of 700 $\rightarrow$ 2300 μm depending on track angle. After corrections for magnetic field distortions derived from field maps, the laser calibration system, and geometrical alignment of the detector, average resolutions of 173 μm and 740 μm are measured, respectively[8].

The resulting momentum resolutions, including or excluding the ITC from the track fit, are [18] :

$$\frac{\Delta p}{p} = 0.0012\, p(\mathrm{GeV/c})^{-1} \text{ without the ITC,} \tag{2.6}$$

$$\frac{\Delta p}{p} = 0.0008\, p(\mathrm{GeV/c})^{-1} \text{ with the ITC.} \tag{2.7}$$

The collision vertex is determined with an accuracy of 140 μm while the separation of closely overlapping stiff tracks is possible if tracks have opening angles greater than 2.5° [18]. In all cases it is found that the Monte Carlo simulation of tracks in the TPC provides exceptionally close agreement with experimental data [18] [2].

2.8 Calorimeters and Muon Chambers

The ALEPH calorimeters and muon detectors consist of ECAL, HCAL and MUON. ECAL is situated inside the coil with HCAL and MUON immediately outside of it. The calorimeters feature *projective geometry* so that *towers* of sensitive pads point towards the vertex. This means that stiff tracks are measured uniformly and that the influence of cracks and insensitive regions is lessened. Considering the large size of these detectors, they possess a high degree of *granularity*, requiring fast readout and accurate calibration to ensure uniformity. Calorimeters are not used directly in the analysis presented here and are described only briefly because of their contribution to the ALEPH trigger scheme.

2.8.1 The Electromagnetic Calorimeter

ECAL is a lead plane/wire chamber sampling calorimeter presenting a total of 22 radiation lengths to particles. Sensitive cathode pads on wire planes are grouped into towers of area roughly 3 cm x 3 cm increasing slightly with distance from the vertex. The towers are read out in three separate *stacks* consisting of the first four, middle nine and last nine radiation lengths, providing information on the energy loss profile as particles interact

[8]These values are determined from $Z^o \rightarrow \mu^+\mu^-$ events where muons carrying the beam energy cross the pads with small angles and traverse *all* 21 padrows [18].

with the lead planes. The detector is largely hermetic, with cracks occupying only 2% of the barrel and 6% of endcap regions while the granularity of the detector allows the central position of particle showers to be located with an accuracy of 2—4 mm [12].

As a particle interacts within the material, EM showers are formed, producing ionisation in proportional wire chambers and inducing signals on wires and cathode pads. Readout of the $\sim 220,000$ channels is by zero-suppressed ADC modules through dedicated readout controllers (ROCs). Calibration and uniformity of the detector is achieved using techniques summarised in table 2.6. These techniques, together with online monitoring

Calibration Technique	Method Used
Absolute Calibration	(a) Electron and Pion Test Beam Measurements (b) Wide Angle Bhabhas
Relative Calibration	(a) Radioactive Krypton Gas Spectra (b) Cosmic Rays
Time Dependent Changes	Fe^{55} Test Cells

Table 2.6: Methods used for the absolute calibration and monitoring of the ECAL.

and updates of channel pedestals using random triggers, give good uniformity [13] and measured energy resolutions of :

$$\frac{\Delta E}{E} = 1.6\% + \frac{17\%}{\sqrt{E}} \text{ for the wires and} \tag{2.8}$$

$$\frac{\Delta E}{E} = 1.7\% + \frac{19\%}{\sqrt{E}} \text{ for the pads.} \tag{2.9}$$

The characteristic profiles of energy deposited in the three stacks allows various cluster shape estimators [19] to yield an electron identification efficiency of 95% while retaining pion contaminations of less than $\sim 0.1\%$ [13].

2.8.2 The Hadron Calorimeter And Muon Chambers

HCAL provides the main support for ALEPH subdetectors. It is made from self-supporting iron slabs (5 cm thick) interspersed with 23 layers of plastic streamer tubes. Two double layers[10] of streamer tubes outside HCAL form the muon chamber coverage. In HCAL, hits are detected using streamer tubes operating essentially as proportional counters, but in a higher voltage regime so that avalanches are independent of the number of primary electrons. Signals are induced on electrodes on both sides of the eight-cell unit surrounding the central wire. One side provides *analogue* signals (used to measure energy) while the other provides a *digital* readout, indicating which tubes have fired. The analogue

[10] During the 1989—1990 run period, only one layer of muon chambers was instrumented and read out by the DAQ.

readout measures energy by adding the total charge, which is effectively the total number of streamers produced in a shower, while the digital readout measures particle penetration and defines a track through the subdetector. The HCAL projective tower geometry preserves the general pattern of ECAL but the granularity is decreased so that one HCAL tower covers $\sim$ 14 ECAL towers.

The differing characteristics of pions, muons and electrons in HCAL are used for particle identification in conjunction with ECAL and $\frac{dE}{dx}$ from the TPC. The energy resolution from the analogue readout has been determined [13] to be $\frac{78\%}{\sqrt{E}}$ but is degraded at energies greater than 40 GeV, where it becomes non-linear by $\sim$ 4%, and at large angles where it becomes $\frac{82\%}{\sqrt{E}}$ in the overlap and endcap regions. At low energies, measuring the energy by counting the number of hits using the digital readout gives a better energy resolution than using analogue signals[11].

HCAL is used extensively as a fast-energy trigger due to the low rise time of the induced pulses ($\sim$ 50 ns) and the potential to distinguish muons by their characteristic behaviour in the material. These are selected by specifying a minimum number of fired planes in the *last* ten slabs of the detector. Muon chambers are used for position measurements only, since particles traversing HCAL are associated with their TPC tracks for a precise momentum measurement.

2.9 The Luminosity Monitors

Similar remarks apply here to those of section 2.8, where the ALEPH luminosity system is not used as part of the present analysis, and is mentioned here only for completeness.

The system consists of three components, LCAL, SATR and BCAL. LCAL and SATR are a combined calorimeter and tracking module placed approximately 2.7 m to the side of the interaction point. Measuring the absolute luminosity with a systematic uncertainty of $\sim$2% is essential so that lineshape and cross-section measurements are not limited by the luminosity error. This is achieved in LCAL using a lead-wire chamber sandwich[12] which measures the coincidence between Bhabha scattered electrons and positrons on each side of the vertex. At nominal LEP luminosities, the Bhabha rate is similar to that of Z^o decays in the detector. The LCAL-SATR combination provides position and energy measurements for identification and rejection of background. SATR is used to verify the position of the leptons passing through the sensitive area of LCAL. It is made from half-planes of drift tubes arranged in layers around the beam-pipe. The single hit spatial resolution of 320 μm [13] corresponds to a 0.25% error on the luminosity. The energy resolution of LCAL is given by :

$$\sigma_E = 0.14E + 0.20\sqrt{E} \tag{2.10}$$

so that for a 45 GeV e^+ or e^-, σ_E $\sim$8 GeV. Online calibration and uniformity of the

[11] When low-energy pion showers give 5.5 ± 0.8 hits per GeV.

[12] Similar in design to that of ECAL.

LCAL are achieved using selected e^+e^- data to maintain calibration factors and an Fe^{55} test cell to track gas-gain fluctuations.

BCAL is a separate subdetector used to provide immediate estimates of the luminosity in a period of minutes rather than the fill-by-fill measurements of LCAL. This is done using small sampling calorimeters on either side of the beam and vertex. The layers consist of tungsten converter sheets interspersed with plastic scintillator and silicon strips which are read out to give a Bhabha rate 20 times greater than LCAL.

2.10 Summary

The ALEPH detector provides detailed information about Z^o decays with a measured efficiency close to 100%. Together with the granularity of its subdetectors, a high-performance data-acquisition system allows large numbers of events to be collected and studied with precision. The tracking system, based around a large TPC, is seen to give high performance and close agreement with design expectations for the study of charged tracks.

Chapter 3

Fragmentation Models and Quark Charge Retention

Fermion pair production of leptons and quarks dominates e^+e^- interactions close to the Z^o resonance. They produce two characteristic types of event; (a) low multiplicity lepton events with high momentum tracks and (b) complex, high multiplicity hadronic events in the case of quark production. Differences are due to the coloured nature of individual quarks and gluons. These cannot exist as free objects and are forced to *fragment* into colourless hadrons. A typical hadronic event at LEP I consists of 20 or so charged particles with a similar number of neutrals forming *jet-like* structures first observed at lower energies [20]. Such structures are due in part to the boost given to outgoing partons. Fragmentation products are collimated into a conical shape when detected in the laboratory frame. Hard gluon radiation complicates this further by either broadening quark jets or giving rise to new ones. The physical process of this transformation from partons to particles is discussed in section 3.1 while two approaches to modelling it are described in sections 3.2 and 3.3.

Previous experiments [21] [22] [23] have noted that quark charge information is retained to some degree by the charges of jet particles with high momenta. *Charge retention* depends largely upon the **sign** of the quark charge, while the magnitude of the charge and its behaviour during fragmentation make the degree of retention flavour dependent. Some previous results are discussed briefly in sections 3.4 and 3.5. The dependence on fragmention makes it necessary to understand how it is modelled and to what degree results are dependent on the approach used. This is discussed in section 3.6.

The purpose of this chapter is to illustrate how fragmentation models are used to describe charge retention effects which are studied and used later in this analysis.

3.1 Fragmentation Schemes

Data from e^+e^- annihilation appear to show that production of hadronic final states can be described by two consecutive processes. The production of partons is predicted by electroweak and perturbative QCD calculations and is followed by their fragmentation into detectable particles. This is illustrated schematically in figure 3.1 After an e^+e^- interaction, initial partons can emit a series of quarks and gluons. Although QCD matrix

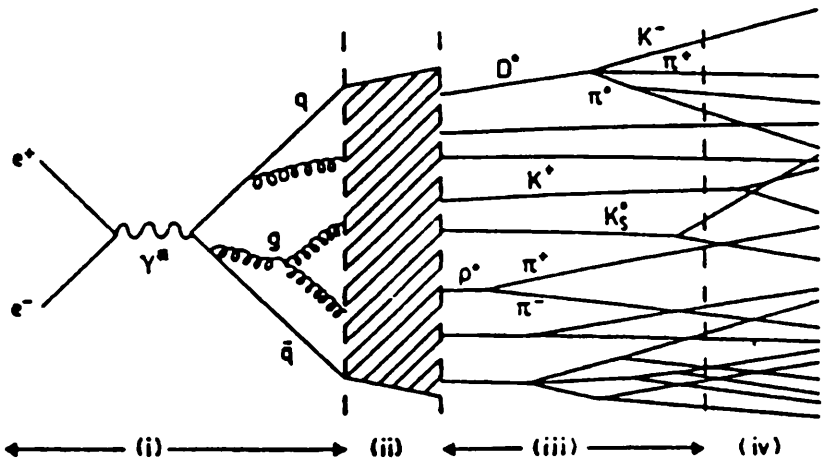

This shows (i) the perturbative phase, (ii) fragmentation, (iii) particle decays and experimental detection of decay products.

Figure 3.1: Schematic illustration of an e^+e^- annihilation event.

elements are known to second order, it is extremely difficult to make precise calculations for complex events. Higher order processes are predicted to become increasingly important at high energies so that discrepancies between data and second order calculations only are expected to increase as a result. These problems are approached using either :

- **Second order matrix elements** alone, where omission of all higher order processes allows only a three or four parton state.
- **Parton shower evolution**, where repeated splittings of the form $q \rightarrow qg$, $g \rightarrow gg$ and $g \rightarrow q\bar{q}$ are used with probabilities calculated from the leading log approximation (LLA) of QCD perturbation series. Evolution is continued until the parton energy falls below a cut-off usually defined so that α_s is small enough for perturbative calculations to remain valid.

In previous studies [33] it has been noted that the matrix element approach systematically underestimates the amount of gluon radiation required to agree with high energy e^+e^- annihilation data.

3.1.1 The Fragmentation Phase

The coloured quarks and gluons of QCD may be regarded as "free" during hard collisions. Subsequently, the colour forces between them organise them into colourless hadrons. This process of organisation is referred to as *fragmentation.* QCD is able to predict the results of hard scatters as large momentum transfers lead to a relatively small coupling strength. In this regime, perturbation theory is applicable. The transition from quarks and gluons into detectable hadrons is a *soft* process, involving strong couplings between partons, so

that perturbation theory is unable to yield convergent series. As a result, the problems of fragmentation and confinement of partons within hadrons are removed from the realm of calculable theory to that of phenomenological models.

Without precise calculations, several guidelines are used to model the fragmentation phase. The total colour of the final hadrons is zero (or colourless) so that the colour of an outgoing parton is balanced by that of the other, recoiling parton. Conservation of four-momentum and charge, together with general "characteristics" of QCD and confinement from experiment, are also used. Modelling is aided by the large amount of experimental data from different collisions and energy regimes which can be used for comparison.

A complete understanding of the fragmentation of a given event is currently unavailable and so this incomplete understanding must suffice. The reliance upon such incomplete knowledge may be minimised if all particles in an event are summed over. Thus, a study of partons using their jets as a whole can limit the dependence of measured quantities on fragmentation specifics.

3.1.2 Characteristics of Available Models

In the light of current uncertainties in the theory of fragmentation, available models employ various "philosophies" regarding each stage of the transition.

The model proposed by Field and Feynman [25], often referred to as *independent jet fragmentation*[1], has been shown to agree with data over a wide range of energies and types of collision [33]. The idea has been developed by several authors using different ways to distribute the original quark energy, momentum and quantum numbers between daughter particles which make up the jet. Different schemes share the basic ansatz of the Field-Feynman model. This presumes that quark jets can be "manufactured" on the basis of a recursive principle. The quarks create a strong colour field in which further $q\bar{q}$ pairs are created from the underlying "sea". As each pair arrives the original, most energetic quark couples together with one of the newly created pair, leaving the other "daughter" quark free to associate with further pairs. A hierarchical family structure composed of grandparents, parents and daughter partons etc. serves as a useful way to describe the layered structure of quarks and gluons.

As the process is carried out, new di-quarks receive smaller and smaller momenta before reaching an (arbitrary) cut-off. Quark pairs produced with the highest momentum are those immediately around the parent, or original, quark. Ordering the quark pairs in this way defines a *rank*, denoting how many splittings were required before a given quark was produced. Subsequent steps may be thought of as associating quark pairs with known mesons and decaying them using their branching fractions and decay properties.

Alternative approaches have been developed [26] based on multiple quark and gluon branchings into the non-perturbative region of QCD. After reaching a cut-off value, the

[1]Since the outgoing partons, and their jet evolution, are assumed to have negligible effect on each other after the hard scattering process.

particles are "clustered" into mesons and decayed according to phase space. Such models adhere to what information can be gleaned from the theory of QCD even when the perturbative limit is surpassed.

The most obvious problems with these models appear in their use of parameters. Analysis involving fragmentation models must take into account the dependence on these in order to separate the"physical" from the necessary conveniences of the model. Model parameters are fixed to some extent by the need for model predictions to resemble experimental distributions and the amount by which they may be varied without loss of consistency is often severely restricted. Two types of model are described here; the *string* and the *cluster* fragmentation models.

3.2 String Fragmentation

The string fragmentation model has been most successfully implemented in the context of the LUND Model used to hadronise partons created by the Lund Monte Carlo [27]. The model treats colour forces between separating partons in terms of a massless string, in analogy to coloured flux lines stretched between them. As partons move apart, these forces increase the energy in the string until it breaks with the creation of a $q\bar{q}$ pair at the endpoints. Often the break occurs after the string has executed oscillations as a result of the string tension.

Lorentz invariance is retained throughout, as each break is performed in the rest frame of the string before boosting to the new quark system. That invariance is preserved, is one of the "natural" strengths of the model. The Field-Feynman concept of rank ordering is also maintained by ordering the hadrons, allowing quarks to associate with antiquarks from adjacent string breakages. Two nearest neighbours in rank have one quark-antiquark pair in common.

Ordering in space and rank is directly maintained in string evolution. Gluons are treated by regarding them as "kinks" in the string spanning the space between quark and antiquark. These form polygons of string connections, attached to the quarks from which they were radiated. An example of such a $q\bar{q}g$ state is shown in figure 3.2. The gluon has two string connections relating to its doubled colour charge, as opposed to the single charge of a quark or antiquark. This method for producing quarks and gluons depends on the "string constant" and a cut-off at which string breaking terminates. The model has been shown to agree with a wide range of data, with particular support from the presence of the so-called *string effect* in e^+e^- multijet production. This describes the depletion of particles in the region between the two highest energy jets in three-jet events[2].

[2]Recently [28] this has been questioned. It is claimed that the independent jet model used by Field and Feynman, once corrected for anomalous soft particle emission at high P_T also displays this effect.

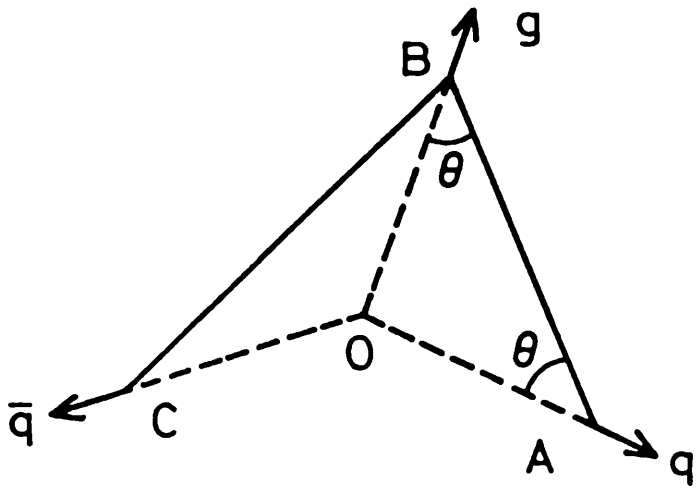

Colour neutral $q\bar{q}g$ system connected by the string ABC showing the difference in string "connections" between quarks and gluons in the string model.

Figure 3.2: Illustration of the string model.

3.2.1 Momentum Distribution and Meson Production

The distribution of transverse and longitudinal momenta of newly created quarks is considered by two separate techniques. For the case of transverse momenta, the string is assumed to have no transverse modes of oscillation until the break into a $q\bar{q}$ pair occurs. Newly produced quarks are created at the break with a probability of *tunnelling* into a region with a finite amount of transverse momentum. The probability depends on the distance from the break and on the transverse momentum given to the $q\bar{q}$ pair. As such, it is proportional to :

$$exp\left(\frac{-\pi m_T^2}{\not{k}}\right) = exp\left(\frac{-\pi m^2}{\not{k}}\right) exp\left(\frac{-\pi p_T^2}{\not{k}}\right) \tag{3.1}$$

where m_T is the "transverse" quark mass and k is the string constant. Separating the mass and transverse momentum in this manner gives a flavour independent Gaussian spectrum for the p_t of new $q\bar{q}$ pairs. This suppresses heavy quark production during fragmentation due to the quark mass in (3.1) and results in the proportions :

$$u : d : s : c : b = 1.0 : 1.0 : 0.3 : 10^{-11} : \sim 0 \tag{3.2}$$

where c and b flavoured secondary mesons are not expected as a result. Measurements of kaon and lambda multiplicities from different sources [23] are used to check such a suppression of strange meson states. These are are summarised in table 3.1. No significant variation with centre-of-mass energy is observed. Baryon production is similarly constrained by experimental data, however little or no theoretical guidance is available. This is due to the degree of uncertainty in diquark masses whereas estimates are at least available for individual quarks. Baryons are introduced by creating diquark pairs at string

Experiment	Measured Value
TASSO	0.35 (±0.03)
JADE	0.27 (±0.06)
TPC	0.37 (±0.17)
TPC	0.32 (±0.10)
HRS	0.34 (±0.03)
Average	0.33 (±0.02)

Values taken from [29] with statistical and systematic errors combined in quadrature.

Table 3.1: Values of the $\frac{s}{u}$ quark ratio from various experiments.

breakage points in the ratio :

$$q\bar{q} \ : \ q\bar{q}q\bar{q} \ = \ 1.0 \ : \ 0.09 \tag{3.3}$$

where the value is fixed by experiment. Similarly the ratio of vector to pseudoscalar mesons must be decided. It can be expected from considerations of spin to be :

$$\text{pseudoscalar} \ : \ \text{vector} \ = \ 1 \ : \ 3 \tag{3.4}$$

The formation of a meson at this stage is mass dependent as quark pair energies are close to threshold. Thus the spectroscopy of meson states is also important. This modifies the ratio (3.4). Flavour dependence becomes important as the ratio of masses is closer to unity for heavier quarks. Three flavour dependent ratios are used for the cases of (u,d), (s) and (c,b) flavoured mesons as a result.

The longitudinal distribution of momentum amongst newly created quarks is carried out using *fragmentation functions*. These are probability distributions, $f(z)$, where z is defined as :

$$z \ = \ \frac{(E+p_z)_{\text{new string}}}{(E+p_z)_{\text{parent string}}} \tag{3.5}$$

and is chosen to preserve Lorentz covariance as successive string breaks occur. Several formulations have been suggested for these functions, indicating the limited physical guidelines which are available. What indications there are come from calculations of transition probabilities and experimental spectra [30]. The original Field-Feynman parameterisation has the form :

$$f(z) = 1 - a + 3a(1-z)^2 \quad \text{for } a \ = \ 0.77 \tag{3.6}$$

As the energies of available data have increased, with the production of c and b quarks, new functions have been proposed :

$$f(z) \ = \ \frac{1}{z}(1-z)^a \, e^{\frac{-bm_T^2}{z}} \quad \text{the LUND } \textit{symmetric} \text{ form} \tag{3.7}$$

$$f(z) \ = \ \frac{1}{z(1-\frac{1}{z}-\frac{\epsilon}{1-\epsilon})^2} \quad \text{the SLAC or } \textit{Peterson} \text{ form} \tag{3.8}$$

The fragmentation of heavy quarks is generally *harder* than that of light quarks. This can be argued in terms of inertia; the heavier the quark, the less energy it will lose when transferring momentum to lighter vacuum $q\bar{q}$ pairs. Heavy pairs are not generally produced for reasons explained previously. Fragmentation of heavy quarks is peaked at higher values of z, forming c and b hadrons with higher momentum fractions of the initial quark energy than lighter hadrons from u, d or s production. This is visible experimentally in the momentum of leptons from semi-leptonic decays of heavy quarks.

3.2.2 Summary

The string model provides a plausible explanation of hadron production from partons. In addition, the concept allows elegant use of the ideas of colour and rank to guide the flavour composition of final-state particles. Support for such a concept is given by particle flow distributions in $e^+e^- \rightarrow f\bar{f}$ annihilation data. Use of parameterisation dependent variables to determine the longitudinal momentum flow through the jet, and the number of parameters which must be either measured or estimated from loose physical constraints, means that substantial uncertainties remain.

3.3 Cluster Fragmentation

Cluster fragmentation [31] differs from string fragmentation at the point where the parton shower stops. This statement is an oversimplification, as the shower is terminated in the string model while the cluster[3] scheme lets it continue in a modified way. The cluster model prefers to continue branching to a cut-off which lies *below* the point at which perturbative calculations remain exact. The mass-scale of clusters at the cut-off is set so that clusters have masses of a few GeV or less. These are decayed according to phase space calculations into known resonances. The various stages are shown in figure 3.3. The strengths of this model are its relative scarcity of free parameters and functions describing the transition of partons at the end of the perturbative phase to final-state hadrons. For the purposes of the current discussion, important considerations are the processes guiding flavour composition and distribution of transverse and longitudinal momentum. These are outlined below, highlighting differences between this and the string model.

3.3.1 Non-Perturbative Shower Development

Continuing the perturbative phase of the parton shower into the non-perturbative region is achieved by lowering the cut-off at which parton branching is terminated. This results in more partons being produced, tailing off to lower energies, than otherwise would be the case. For this process, all available partons are assigned a mass. The gluon "mass" is

[3]The "cluster" refers to the method of associating the final quarks with *clusters* synonymous with baryon and meson states

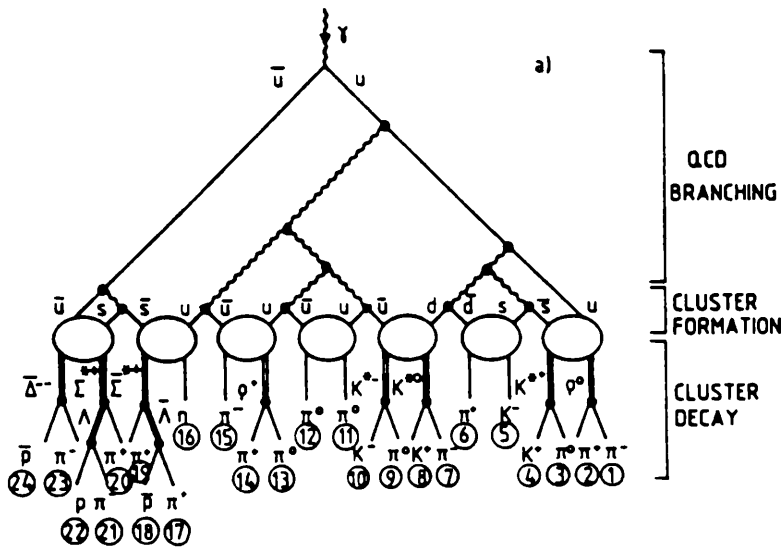

Figure 3.3: Time development of an event using cluster fragmentation.

equivalent to the cut-off, Q_0 with remaining masses defined as in table 3.2. Setting the

Particle Type	gluon	u quark	d quark	s quark	c quark	b quark
Assigned Mass	Q_0	$\frac{1}{2}Q_0$	$\frac{1}{2}Q_0$	0.5 GeV	1.5 GeV	5.0 GeV

Table 3.2: Cluster model parton mass values.

cut-off to a gluon mass greater than or equal to twice the light quark masses means that all gluons will eventually decay into $q\bar{q}$ pairs. Care must be taken in these definitions of quark masses, as they are more analogous to their mean constituent masses than those of "free" quarks[4]. Here again, quark masses are used to suppress production of heavy quark pairs from the vacuum. This is done according to the, now-approximate, matrix elements instead of the tunnelling mechanism used by the string model. Generally speaking, the relative fractions of $q \rightarrow qg$, $g \rightarrow gg$ and $g \rightarrow q\bar{q}$ branching proceed in agreement with perturbative expectations until close to the light quark threshold where gluons all suddenly decay as $g \rightarrow q\bar{q}$.

After branching has terminated, the masses of clusters are set to the values at which the cut-off took effect. Their momenta are calculated from the energies and angles used in the shower production. The shower is developed in terms of angles and energies so that Lorentz invariance is *not* specifically maintained at each branching and is satisfied only after the shower has terminated. This invariance is approximate and is largely independent of the shower energy and initial opening angle of the jet [31]. So for a given

[4]This refers to their mean mass, calculated when the quark is a constituent of a meson or baryon, weighted by the estimated production probability.

parent quark mass, the characteristics of a jet are invariant with regard to the development of the shower. This statement is made only if the *complete* state is considered. Showers cannot be combined as if they were independent otherwise the invariance is lost.

3.3.2 Cluster Formation and Decay

When showering has terminated, remaining partons form colour-singlet clusters with a mass spectrum peaked at low values, just above the cut-off and a long tail extending towards masses of $1 \rightarrow 30$ GeV. The model treats these clusters as "primordial" resonances made from a superposition of lower lying states. Clusters are then decayed isotropically according to the following scheme :

1. If the cluster has a mass *below* a certain cut-off, (denoted by m_C) then it is decayed by choosing a random $q\bar{q}$ or $q\bar{q}q\bar{q}$ pair from the vacuum to form meson or baryon states. These are selected from a table of resonances with appropriate flavours. Phase space and production rates are used, with a random number as a test, to select the combination or to repeat until a successor is found. Mesons and baryons are then decayed via known channels into lower lying states.

2. If the cluster has a mass *above* the cut-off then the cluster is broken into two smaller clusters using "symmetrical string breaking"[5]. This continues until all clusters fall below the m_C cut-off where the preceding decay scheme is used.

This mass dependent scheme is necessary as for massive clusters an isotropic decay can no longer be assumed. It is important to note that the flavour composition of mesons and baryons is *not* fixed by random selection of quark-diquark pairs chosen from the vacuum. This is done with equal probability. In contrast to the LUND model, it is the weighting contributions from available phase space and spin states which are the determinant factors.

This elegant picture is modified somewhat for the case of clusters containing heavy quarks, as knowledge of heavy flavour resonances is incomplete. A heavy flavour cluster is forced to decay into lower mass clusters via a cascade involving semileptonic decay or direct decay into two smaller clusters.

3.3.3 Summary

The cluster model, as implemented in the HERWIG Monte Carlo, uses second order matrix element calculations as an approximation to extend parton showers into the confined region of QCD. As such, it benefits from being relatively free of input parameters apart from the QCD scale, Λ_{QCD}, and the gluon "mass" to limit extension of the method to progressively lower masses. Similarly, the formation and decay of clusters is carried out using the availability of states as far as possible. This in turn involves one further input parameter, the threshold at which massive clusters are forcibly broken into smaller ones.

[5]It is assumed that this choice of scheme is not crucial, as only about 10% of clusters are involved.

The aesthetically pleasing lack of tunable parameters is partly a result of using algorithms to avoid massive clusters and details of heavy flavour fragmentation [31].

3.4 Quark Jet Charges in Antineutrino Interactions

In the type of reaction most commonly studied, an antineutrino beam impinges on a nucleon target [32]. Due to contamination of the beam however, typically 15% of analysed events are due to neutrino reactions. Neutrino and antineutrino reactions produce u and d-type quark jets respectively via the channels :

$$\nu_\mu d \rightarrow \mu^- u \tag{3.9}$$

$$\overline{\nu}_\mu u \rightarrow \mu^+ d \tag{3.10}$$

where the charge of the muon at high transverse momentum with respect to remaining hadrons is used to determine the parent quark responsible for the jet [22]. This method of separating u and d quark contributions unambiguously is a result of the neutrino coupling only to the negative muon and vice versa for the antineutrino. A weighted charge summation over constituent particles of hadronic jets is calculated using their fractional energy, z, as in equation (3.11) :

$$Q_w = \sum_i (z_i)^r q_i \tag{3.11}$$

where q_i is the integer charge of the i^{th} hadron in the jet. The resultant charge distributions for u and d quarks are shown in figure 3.4 for r values of 0.5. The mean deviations from zero of these charge distributions are given in table 3.3. A clear differentiation is apparent, both in the magnitude and sign of the weighted jet-charges, in accordance with the different quark charges. The observed distributions are consistent with the Field-Feynman prediction that quark quantum numbers are retained after fragmentation. Distinguishing between quark flavours in this way yields important information concerning the momentum spectra of hadrons in u or d quark jets. This has been used to test and develop the fragmentation models described previously.

3.5 Charge Properties of Quark Jets in Low Energy e^+e^- Data

In e^+e^- collisions at PETRA, the properties of quark jets were studied in the centre-of-mass energy range from 27 → 32 GeV [21].

In this regime, a high thrust ($T > 0.8$) cut is used to select events with expected $e^+e^- \rightarrow q\bar{q}$ topologies. Using the thrust axis to define the resulting two jets and taking

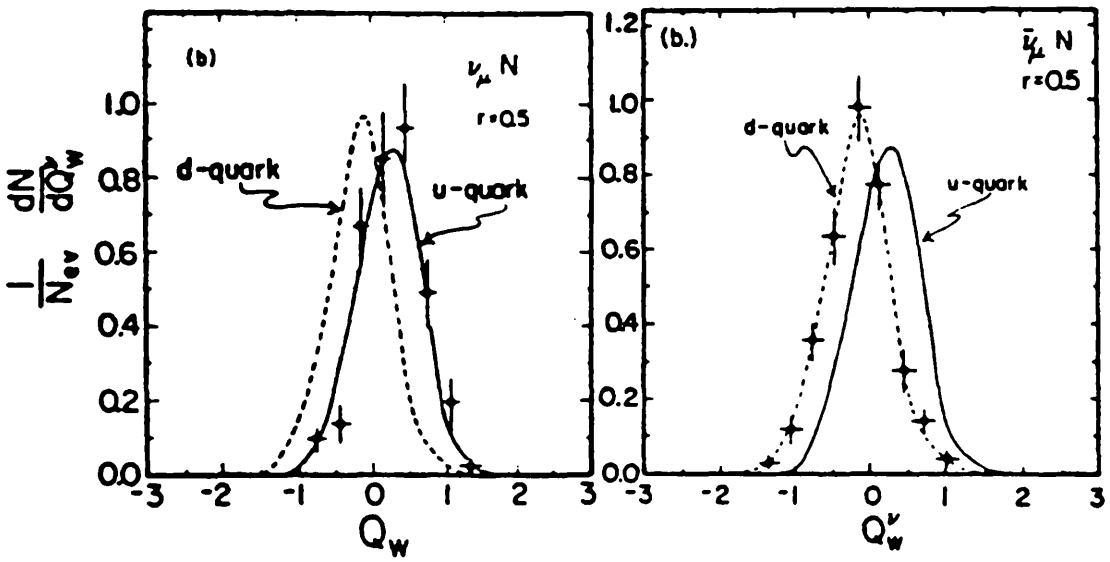

Weighted charge distributions for neutrino and antineutrino produced hadron jets respectively. The solid curve represents Field and Feynman predictions arising from the fragmentation of a u or d – type quark with 10 GeV incident momentum. Separation between flavours is clearly visible [22].

Figure 3.4: Weighted charge distributions for antineutrino and neutrino events.

Reaction	Mean Unweighted Charge (r = 0.0)	Mean Weighted Charge (r = 0.2)	Mean Weighted Charge (r = 0.5)
$\nu_\mu d \rightarrow \mu^- u$			
(Measured)	$-0.44(\pm 0.09)$	$-0.24(\pm 0.03)$	$-0.14(\pm 0.02)$
(Predicted)	-0.39	-0.25	-0.15
$\bar{\nu}_\mu u \rightarrow \mu^+ d$			
(Measured)	$+0.54(\pm 0.12)$	$+0.42(\pm 0.04)$	$+0.27(\pm 0.03)$
(Predicted)	$+0.60$	$+0.39$	$+0.26$

Mean jet charges for r values of 0.0, 0.2 and 0.5. The corresponding values from the Field and Feynman model are shown as predictions [22].

Table 3.3: Mean jet charges for antineutrino and neutrino reactions.

the lower multiplicity jet[6], the mean jet charge is estimated using equation (3.11) with $r = 0$. The observed distribution of charges in the data is compared with randomised and Field-Feynman expectations in figure 3.5. Mean values for data and corresponding

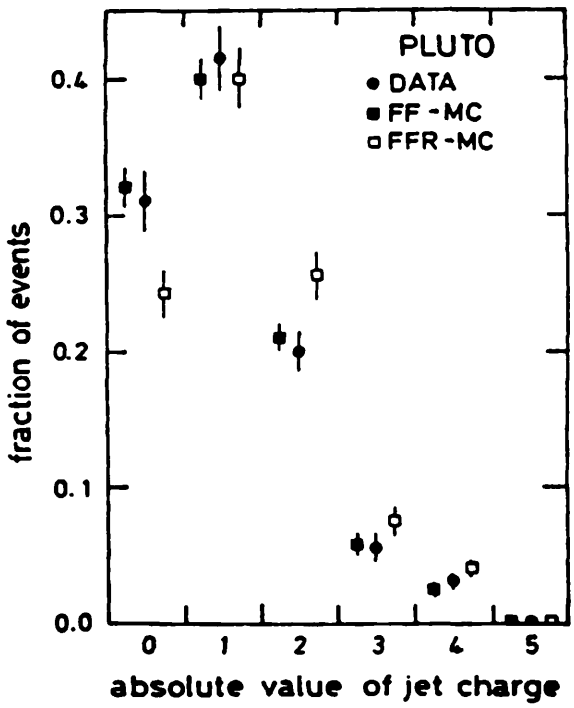

Distribution of the absolute value of the net charge for data and two types of Field-Feynman Monte Carlo using different kinds of charge ordering during fragmentation [21]. The models used are given in table 3.4.

Figure 3.5: The charge distribution of jets in e^+e^- events as measured by the PLUTO collaboration.

numbers from different models are shown in table 3.4. The observed mean jet charge in the Field-Feynman model is found to be consistent with data while ruling out models employing a more randomised ordering of charges as the jet is formed. The mean jet charge in data (1.04 ± 0.03) is interpolated using the Field-Feynman model to yield a jet charge of 0.55 (± 0.25) after unfolding detector effects and meson decays. This uses the model dependent assumption that a maximum of one quark passes across the boundary between two jets.

The small value of the unfolded jet charge implies that charge leakage from the jet is small and leads to the assumption that jet and quark charges are strongly correlated.

Further studies of correlations between particles (a) adjacent in rapidity and (b) possessing the highest momentum in each jet, indicate the presence of local charge compensation and long-range correlations between leading charges of particles in jets of the same event.

[6]To minimise the effect of particle losses.

	Key	Fragmentation Model	Mean Jet Charge
(i)		Real Data with Randomised Charges	1.31 (±0.02)
(ii)	FFR	Randomised Field-Feynman Model	1.24 (±0.04)
(iii)		Field-Feynman with $Q_{jet} = \pm 1$	1.14 (±0.03)
(iv)		Field-Feynman with $Q_{jet} = 0$	0.93 (±0.03)
(v)	FF	Standard Field-Feynman Model	1.04 (±0.02)
(vi)		Real Data with Measured Charges	1.04 (±0.03)

Values for the mean jet charges in data and different Monte Carlo event samples. The various models are : (i) real data but with charges in each jet randomised to provide an estimation of the value expected from statistical considerations only, (ii) the Field-Feynman expectation, also with randomised charges (iii) the Field-Feynman expectation for the case where a single quark passes across the boundary between the two jets, (iv) the Field-Feynman expectation for the case where no quark passes across the boundary and (v) the standard Field-Feynman model [21].

Table 3.4: The net charge of jets in e^+e^- events as measured by the PLUTO collaboration.

3.6 Model Dependence

Using phenomenological schemes to measure physical quantities leads to a systematic dependence upon the physics and parameters employed by the models. Two methods are used to estimate the extent of this dependence :

(I) Varying the "unknown" parameters of a single model.

(II) Using alternative models which employ different philosophies to emulate the same process.

These embody two complementary concepts; the former that models are correct in principle and it is the determination of the parameters which is necessary, and in the latter case, that the parameters are accurate and the physics which is unknown. Ideally it should be possible to alter or change a model with little effect on measured results. However, this is rarely the case.

There are significant problems to be considered with either of the approaches mentioned both because of correlations between model parameters and the limited number of models available. Event characteristics can typically be altered by several parameters simultaneously[7] so it is possible for a change in one parameter to compensate for a change in another. This can produce unpredictable effects in measured quantities. With a large number of variables, two main procedures are used to study this effect :

(a) Using a set of measured values or distributions, the model parameters are floated simultaneously in a fit to data until overall agreement is found. If local minima are

[7] In some models the number of sensitive parameters can be the order of between 10 and 20, while for others it can be as low as 3.

to be avoided, then iterating the procedure helps and allows errors to be reliably determined.

(b) Studying the dependence on each parameter in turn, allows its effect to be observed in isolation, but ignores correlations between variables. The overall spread of measurements results in an estimate of the model dependence.

Systematic errors from the two techniques should be compatible. As decribed in preceding sections, several models are available, although only two have been found to retain agreement with data over a wide range of energies. Procedure (a) is used in this analysis to tune both models to ALEPH data distributions [33] while procedure (b) is used here to perturb the model and study the effects of individual parameters.

3.7 Summary

The LUND and HERWIG models employ substantially different philosophies for fragmentation of e^+e^- to hadrons. Both contain uncertainties in the type and rates with which particles are produced, although both give rise to charge retention effects which are observed in data. These indicate that charges of quarks and their jets are related. The model dependence of measurements can be estimated by comparing the two models and the effect of uncertainties in their parameters.

Chapter 4

Jets and Quark Charge Determination

As a prerequisite to measuring quark asymmetries, it is necessary to determine quark charges from jets of particles in the detector. An asymmetry measurement depends on knowledge of how this information is extracted. The purpose of this chapter is to introduce the charge determination method used later.

The quark charge is distributed throughout a jet and can be studied using the charge and momentum distributions of detected particles. As discussed in chapter 3 it is high-rank particles with large momenta close to the centre of jets which are most likely to be closely related to the parent quark. Previous methods of using these particles have been developed using *charge summations* [10] [34] or *weighting schemes* [6]. In these methods, jets are defined and particle separation criteria applied, to emphasise contributions from high-rank particles.

Separating an event into jets or hemispheres is discussed in section 4.2 while weighting schemes and isolation parameters are given in 4.3. Properties of the *jet charges* are examined in section 4.4 with the efficiency for reconstructing quarks charges correctly discussed briefly in section 4.5. Finally, the effects of $B^0 - \overline{B^0}$ mixing are outlined in section 4.6.

4.1 Definitions and Terminology

Methods of charge determination have a certain probability of assigning the sign of a parent quark charge correctly to a given jet of particles. This is defined as the *charge finding efficiency* :

$$E_C = \frac{\text{Number of Correctly Assigned Jet Charges}}{\text{Total Jet Charge Assignments}} \tag{4.1}$$

For the purposes of this chapter, reconstructed data and Monte Carlo events are used to compare observed jet phenomena with predictions from models described earlier in chapter 3. Unless otherwise stated, the reconstructed Monte Carlo sample consists of events generated by the DYMU[1] program, fragmented using LUND string fragmentation

[1]Original version (DYMU2) from J.E. Campagne, LPNHE Paris. Code transmitted in November 1988 and interfaced in June 1989 to the ALEPH offline software.

with parton shower evolution and the HVFL[2] parameters and heavy flavour decays. Fragmentation model parameters have been tuned previously using ALEPH data and give close agreement [33]. Monte Carlo events are passed through the ALEPH detector simulation (GALEPH) before both data and Monte Carlo are reconstructed by the JULIA package.

Tracks are chosen by demanding a minimum of 4 TPC coordinates, D0 and Z0 cuts of 2 and 10 cm respectively for tracks with transverse momenta greater than 200 MeV/c within an angular acceptance of $18.2^\circ < \theta < 171.8^\circ$ relative to the beam. Events are accepted as having at least 5 such tracks totalling a greater charged energy than 10% of the centre-of-mass energy.

To separate fragmentation and detector contributions, the analysis makes use of Monte Carlo events at four levels :

1. The **Parent Quark Level** of final-state quarks, gluons and photons.
2. The **Parton Level** where parton shower evolution is completed, leaving multiple quarks, gluons and photons prior to hadronisation.
3. The **Generator Level** where all particles after fragmentation are available. This represents the full event prior to long-lived particle decays and detection.
4. The **Reconstructed Level** of reconstructed particle tracks in the detector.

The above terminology is used throughout. Charged particles only are considered at each level.

4.2 Jet Finding and Hemisphere Determination

Jet structures arise when the quark energy is significantly larger than that involved in hadronisation. At high energies around the Z° peak, collimated jets of charged and neutral particles are well defined and can be distinguished over much of the detector acceptance. An example of a *multijet*[3] event is shown in figure 4.1 indicating the presence of hard gluon radiation. This can lead to further quark-antiquark pairs being produced. The cross-section for such radiation increases dramatically if gluon energies are small so there is an abundance of soft gluons almost collinear with the quark. The distinction between parent quarks and hard gluons at the reconstructed level depends upon the "resolution" with which a jet is defined.

Associating final-state particles to a jet is referred to as the *jet finding* process. To a certain approximation, a jet is assumed to be synonymous with a parton, so that jet finding is analogous to "undoing" fragmentation effects. An alternative is also discussed here; namely separating an event into two hemispheres around a given axis.

[2] A set of ALEPH standard modifications to LUND incorporating modified branching ratios, decay modes and fragmentation functions for heavy quarks.

[3] ie. an event containing $\geq$ 2 jets.

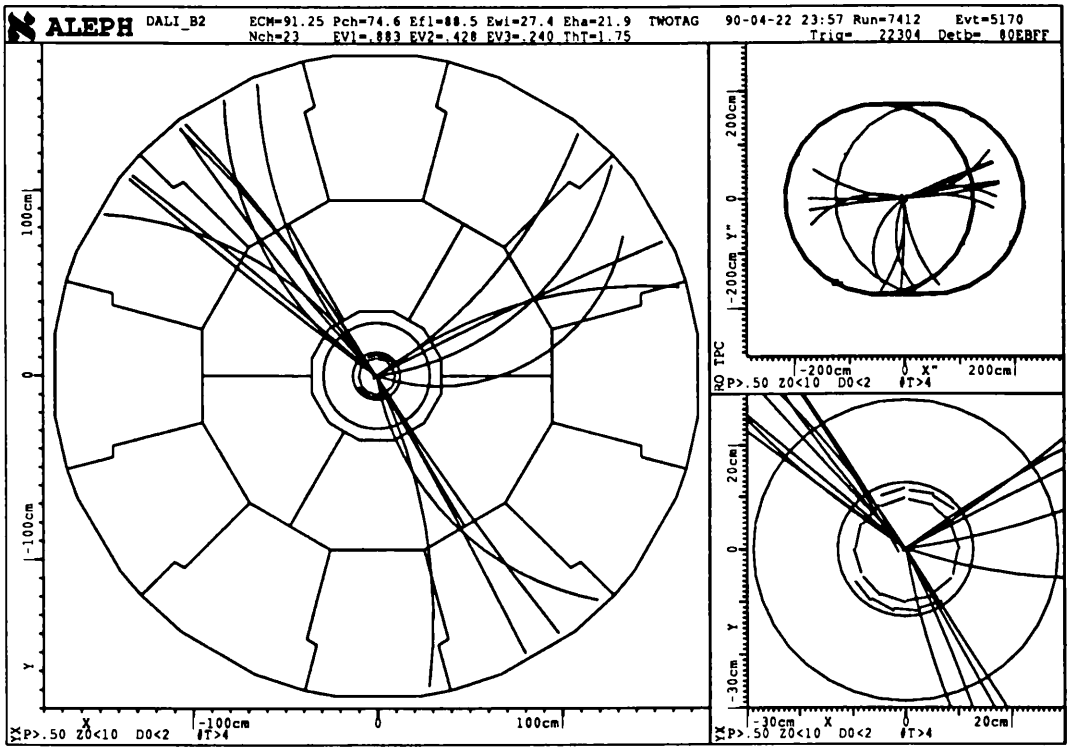

Figure 4.1: An example of a multijet hadronic event in the ALEPH tracking detectors.

The important issue, for the purpose of charge determination, is how accurately these methods reproduce the direction of the parent quark. The two techniques are compared in section 4.2.3.

4.2.1 Jet Finding Algorithms

Jet finding is an iterative process; taking a relatively large number of particles from the measured event and combining them to form a smaller number of "clusters". Several jet finding algorithms are widely used [16] [36] [35], although they have many similarities. In some schemes, final-state particles are sorted in order of decreasing energy, with high energy particles selected as "initiators" around which cluster formation commences. The effective mass of remaining particles is calculated with the initiator. If the mass is found to be below a cut-off, the two are combined, their momenta added to form a "pseudo-particle", and the process repeated until no further merging can be performed.

The cut-off is analogous to the resolution determining the separation above which two clusters may not be merged. Lowering this parameter infers use of a greater power when looking at particle formation closer to the parent parton direction. The process has

been modified by several authors[4], attempting to improve agreement between parton and generator levels [1].

4.2.2 Definition of an Event Axis

For the present study, quantities of interest are at the level of the fermions produced by the interaction. Higher order $q\bar{q}g$ and $q\bar{q}gg$ states disguise these somewhat and lead to jet algorithms finding three or four-jet configurations. If instead, all events are treated as "two-jet", then they can be handled equally without using cut-off dependent algorithms. Neutral jets from gluon fragmentation are incorporated into either jet or hemisphere and by this method.

One way of achieving this is to divide events into hemispheres around an axis close to the direction of the $q\bar{q}$ pair, ie. an *event axis.* Particles are associated to a quark depending on the hemisphere in which they lie. Several methods of determining an event axis are available :

1. The **thrust** axis, $\hat{n}$, is defined to maximise the quantity :

$$T = \frac{\sum_i \mid p_i \cdot \hat{n} \mid}{\sum_i \mid p_i \mid} \tag{4.2}$$

   and is pulled towards the high momentum tracks at the expense of the lower ones.

2. The **sphericity** axis is similarly defined by minimising the quantity :

$$S = \frac{\sum_j (p_j)^2_{\text{transverse}}}{\sum_j (p_j)^2} \tag{4.3}$$

   Sphericity and thrust axes are highly correlated .

3. The **long-arm** axis is defined using the jet axes found by a jet finding algorithm. It is calculated as shown in figure 4.2.

Two jet vectors may be defined for *all* events by using a sufficiently large cut-off in the jet finding algorithm to lower the resolution.

4.2.3 Reproduction of the Parent Quark Direction

Accurate determination of the parent quark direction is essential for a jet charge measurement. The angular difference between the parent quark direction and that found using the above algorithms is studied using Monte Carlo events. By taking the mean of the distribution, the *angular resolution* of an algorithm is defined.

For the case of jet finding algorithms, the angular resolution depends on the cut-off used. This is shown[5] in figure 4.3 where it is clear that the resolution rises significantly as the cut-off is increased. Using a jet finding algorithm introduces an arbitrary cut-off

[4]These include, for example, the JADE minimum mass algorithm [16], the PTCLUS [35] perpendicular merging algorithm and the LUND LUCLUS [36] algorithm.

[5]eg. for the JADE minimum mass algorithm [16].

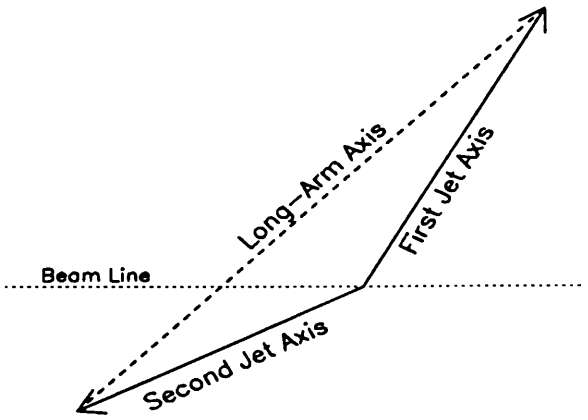

Figure 4.2: Definition of the long-arm event axis.

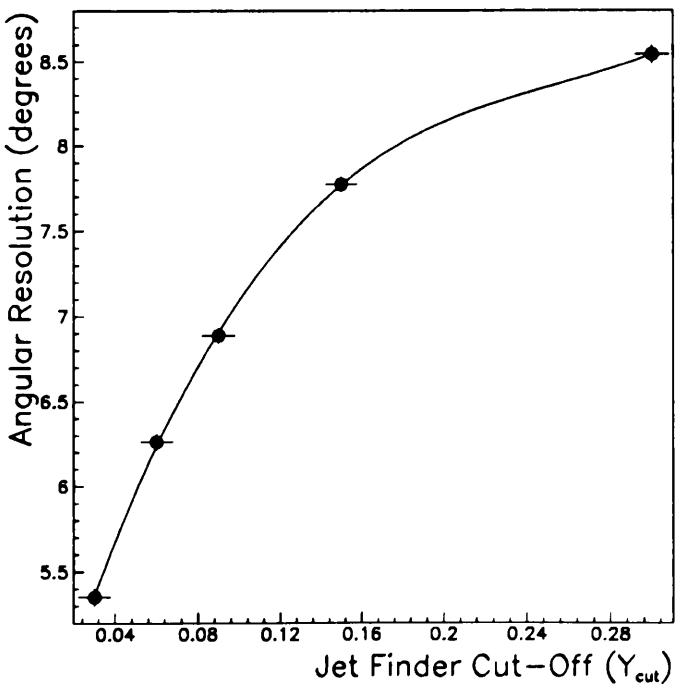

The angular resolution is calculated using two-jet events only, to avoid the complications of separating quark and gluon jets.

Figure 4.3: Dependence of the angular resolution on the jet finder resolution parameter.

into the charge finding process. When compared with event axis algorithms, the results are shown in table 4.1. It is clear that event axis measurements are more accurate while

Method	Angular Resolution
Jet Finding	$4.63\,(\pm 0.03)^{o}$
Thrust Axis	$2.06\,(\pm 0.02)^{o}$
Sphericity Axis	$2.29\,(\pm 0.02)^{o}$
Long-Arm Axis	$2.06\,(\pm 0.02)^{o}$

The jetfinder value is measured using a low Y_{cut} value of 0.03 (see figure 4.3).

Table 4.1: Comparison of jet finding and methods of event axis determination.

the particular choice of algorithm is not crucial. The thrust axis is preferred here for practical reasons[6].

The effect on a charge summation of a 5 degree shift of axes can be illustrated by considering that the longitudinal momentum of a particle relative to such an axis will change by less than 0.4% when lying along the axis, growing to less than 4% when lying up to 20^{o} from the axis.

Detector effects are seen to be small in the case of ALEPH. This is shown[7] in figure 4.4 where it is apparent that the distribution of angular differences is dominated by fragmentation rather than detector considerations. In ALEPH, detector effects are most important at low angles where particle losses distort the axes. This is indicated by a decrease in angular resolution for jet finder and event axes close to the beam, as shown in figure 4.5. At low angles, particles are lost by exiting the detector, or by having insufficient transverse momentum to provide well-defined tracks in the TPC. These contribute to the overall decrease in the multiplicity of particles in jets at low angles shown in figure 4.6. To avoid this region, an angular cut is invoked later to select events whose axes lie within a limited range of $|\cos\theta| \leq 0.9$. These are marked in figure 4.5. The track selection places a cut on tracks at angles below 18.2^{o}, which also contributes to the small decrease in multiplicity which is observed.

In conclusion, reproduction of the parent quark direction is apparently feasible to within $\sim \pm 5^{o}$. Use of an event axis, such as thrust, gives a slightly better accuracy while avoiding dependence on arbitrary parameters. Fragmentation effects dominate those of the detector. The latter can be minimised by loose cuts on the angle of tracks and axes around the beam.

[6]The definition of (4.3) introduces a quadratic dependence on the particles transverse momentum and is more susceptible to non-isotropic decays [1]. The long-arm axis requires a jet finding algorithm and use of the arbitrary cut-off.

[7]For the case of the JADE algorithm.

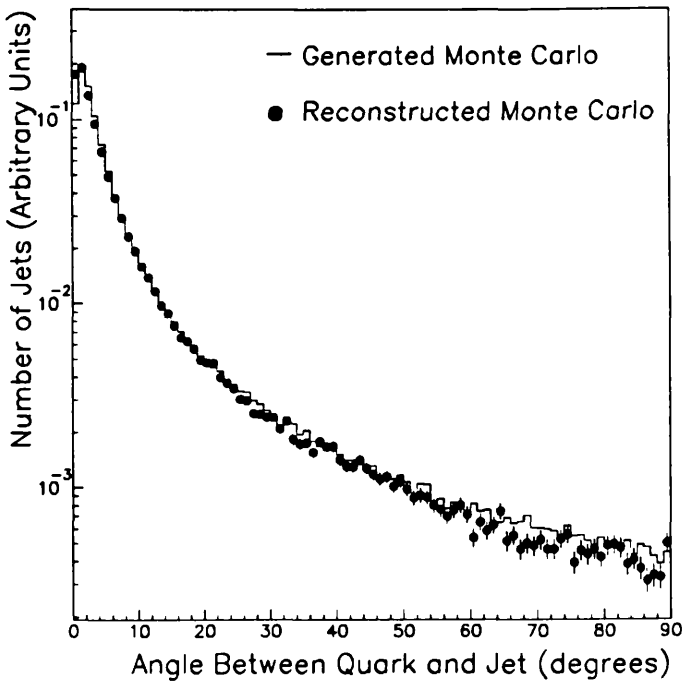

The x-axis denotes the angle between the original quark direction and the reconstructed jet axis using charged particles only.

Figure 4.4: Jet finder angular resolutions.

4.3 Charge Weighting Schemes

Various charge summations have been used by previous experiments :

1. The MAC Collaboration [37] uses the summation :

$$q_{jet} = \sum_{i=1}^{n} q_i \tag{4.4}$$

where $i = 1 \ldots n$ runs over the constituent particles of the jet.

2. The MAC Collaboration [10] also uses the rapidity weighted summation :

$$q_{jet} = \frac{\sum_{i=1}^{n} q_i \, y_i^{\kappa}}{\sum_{i=1}^{n} y_i^{\kappa}} \quad \text{where} \quad y_i = \frac{1}{2} ln \left[\frac{E_i + (p_L)_i}{E_i - (p_L)_i} \right] \tag{4.5}$$

Longitudinal momentum is calculated relative to the thrust axis of the event and κ fixed at 0.2. AMY [34] uses the same form, with $\kappa = 1.0$.

3. The JADE collaboration [6] uses a statistical weight function involving the z of the three fastest particles in each jet where z is defined as :

$$z_i = \frac{q_i \, (p_L)_i}{E_{\text{beam}}} \tag{4.6}$$

Here, longitudinal momentum is calculated relative to the sphericity axis.

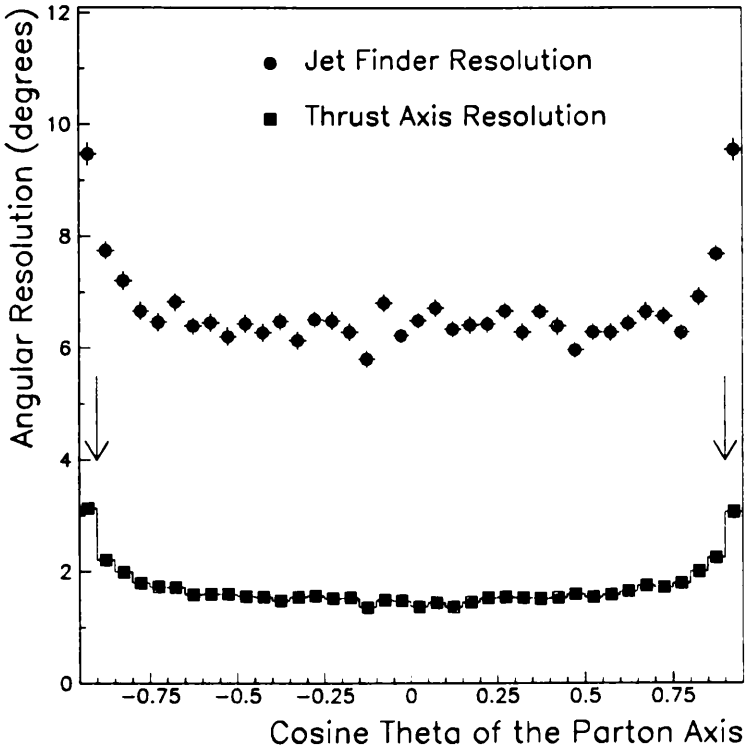

The jet finder measurement is carried out with a Y_{cut} of 0.15 using the JADE minimum mass algorithm. Vertical arrows denote the acceptance cuts on axes used later in the analysis at $|\cos\theta| = 0.9$.

Figure 4.5: Resolution of jet finder and thrust axes as a function of angle around the beam.

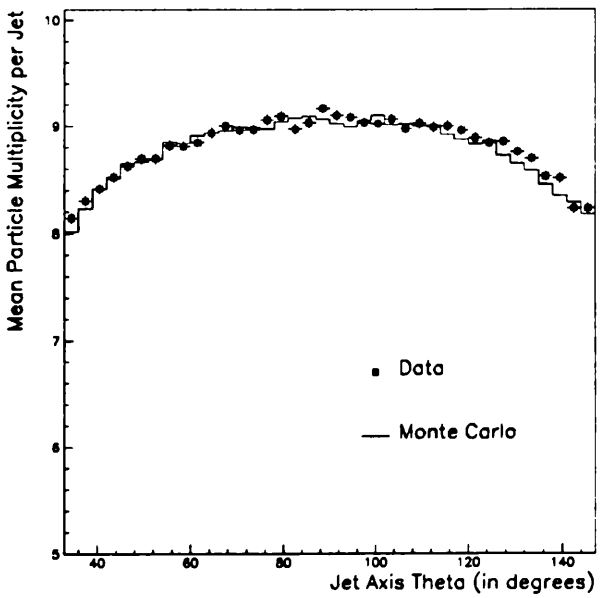

Note the suppressed zero.

Figure 4.6: Mean charged multiplicity in jets as a function of the angle of the jet axis.

4. The JADE Collaboration [38] also uses the summation :

$$q_{jet} = \frac{\sum_{i=1}^{n} q_i \ (p_L^i)^\kappa}{\sum_{i=1}^{n} (p_L)_i^\kappa} \tag{4.7}$$

with $\kappa = 0.5$.

In equation (4.5), the idea of a *weighting power*, κ, is introduced to control the emphasis given to leading tracks. Its value can be varied to enhance the sensitivity of a method, or to minimise systematic effects.

Several weighting schemes[8] were studied using ALEPH data and found to give similar results [39]. Combining two isolation criteria within a single summation was similarly found to produce a negligible increase in charge finding efficiency. In the subsequent analysis, only summations (4.5) and (4.7) are used.

4.4 Jets and their Charges

With the above techniques of reconstructing the charge of a quark jet, it is important to examine the characteristics of charges which are produced. A test of the fragmentation and detector simulation is the extent to which trends agree between data and Monte Carlo. This section is devoted to the study of *general* charge characteristics, ie. using all flavours, and so does not exclude cancelling effects between different quark types.

The charge summation gives each particle a positive or negative weight according to the sign of its charge. The distribution of weights has the form shown in figure 4.7 when using summation (4.5) with a κ of 0.4. Agreement between data and Monte Carlo is good while indicating that, although high momentum tracks carry large weights, low momentum tracks make a significant contribution by virtue of their number. Cancellation of charges amongst lower momentum tracks results in the jet acquiring the charge of leading particles. The distribution of jet charges in data and Monte Carlo is shown in figure 4.8 which similarly exhibits close agreement. Normalisation of jet charges ensures that they lie between -1 and $+1$.

Figure 4.8 is split into two cases; (a) where the jets in each event are found to be of *opposite* sign and (b) when they are of *like* sign. The assumption that hadronic events arise from $q\bar{q}$ production suggests that the latter case, (b), arises more from mistaken charge assignment than (a). This is shown in figure 4.9, for Monte Carlo, where charges are instead separated into correct and incorrect assignments. Here, the distribution of incorrect assignments is narrowed in a similar way to that of the like-sign charges in figure 4.8. The close agreement with figure 4.8 (a) *and* (b) gives confidence that charge retention effects in data are reproduced by Monte Carlo.

[8] Those tested included using rapidity, pseudorapidity, momentum, angle and transverse momentum weighting schemes with variable powers, κ.

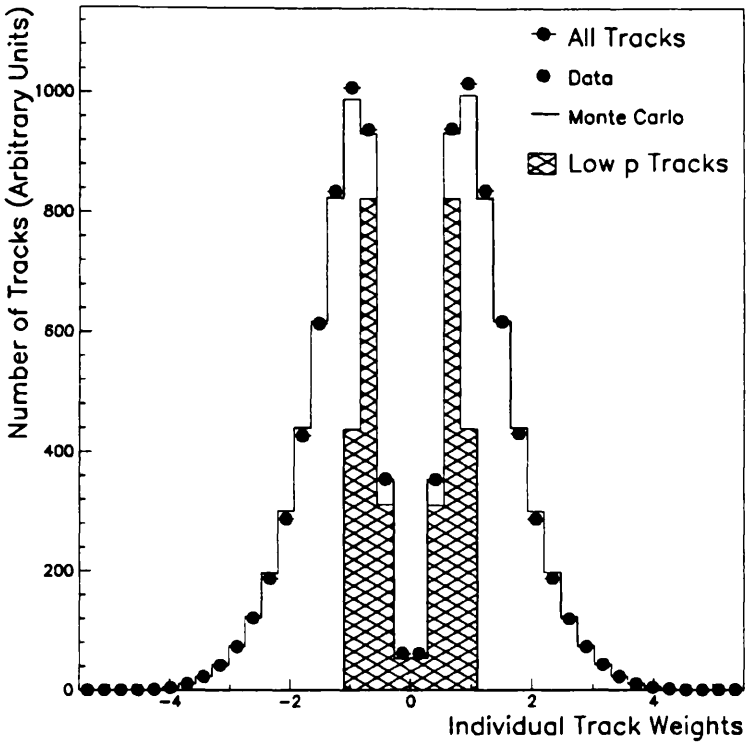

Particle weight distribution in reconstructed two-jet events using a pseudorapidity summation. The shaded region indicates track weights of particles with momenta below 1.0 GeV.

Figure 4.7: Particle weight spectra for data and Monte Carlo.

4.4.1 Opposite Sign Events and Jet Correlations

In a $q\bar{q}$ event with two jets or hemispheres and a probability (E_C) of correctly retaining the sign of quark charge, the fraction of events with oppositely signed jets is :

$$F_{\pm} = E_C^2 + (1 - E_C)^2 + C_{JJ} \tag{4.8}$$

where $F_{\pm}$ represents cases where both jets are identified correctly *or* both incorrectly. Other possibilities lead to like-sign combinations. $F_{\pm}$ is referred to as the *opposite sign fraction* and, as shown in figure 4.10, depends strongly on E_C. As E_C approaches 0.5, $F_{\pm}$ tends to the same value and similarly for the case when $E_C \rightarrow 1.0$. The situations correspond to random guessing and absolute certainty respectively. It is important to note that $F_{\pm}$ is measurable for data and Monte Carlo and represents a valuable test of charge retention. Equation (4.8) is verified using Monte Carlo where both $F_{\pm}$ and E_C are known. As shown in figure 4.10, it is necessary to introduce the correction term, C_{JJ}, the *jet-jet correlation.* This is due to the interdependency of charge determination in each jet and arises from charge conservation at the $q\bar{q}$ level.

C_{JJ} is found to be slightly larger when using event axes as compared to separate jet axes. It is typically of the order of a few percent at low κ and decreases rapidly thereafter. Jet-jet correlations, for hemispheres defined by the thrust axis and charges determined

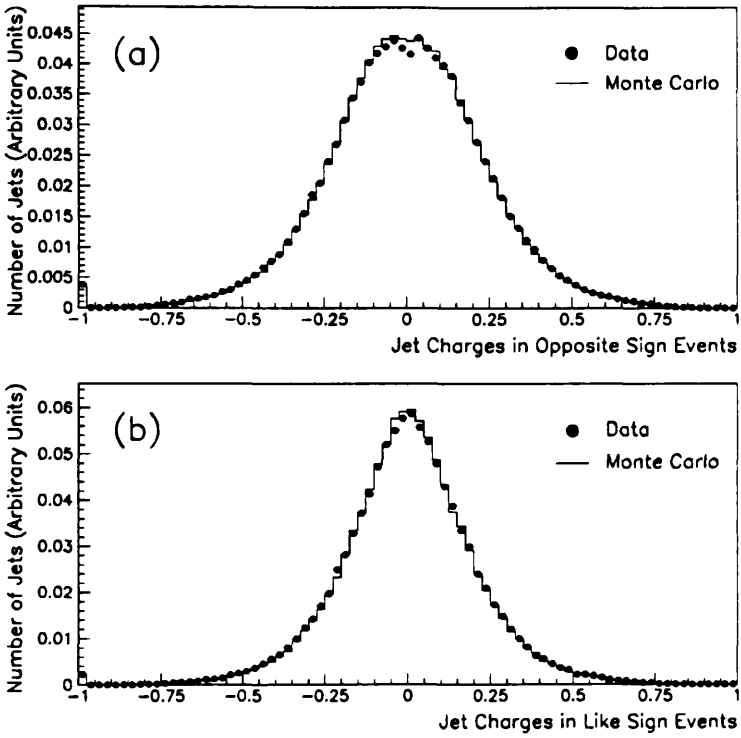

Comparision of jet charges between data and Monte Carlo using the longitudinal momentum charge summation with $\kappa = 0.4$ for like and oppositely signed jet charges in two jet events only.

Figure 4.8: Jet charge distributions for data and Monte Carlo.

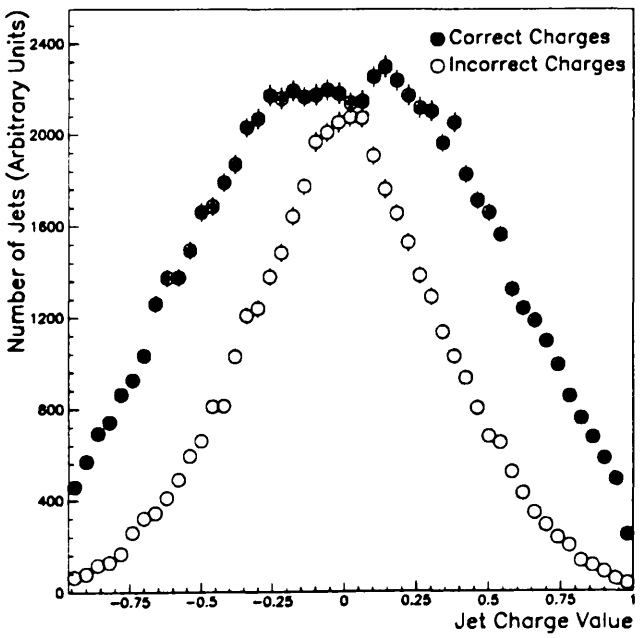

Figure 4.9: Monte Carlo jet charge distributions for correct and incorrectly determined charges.

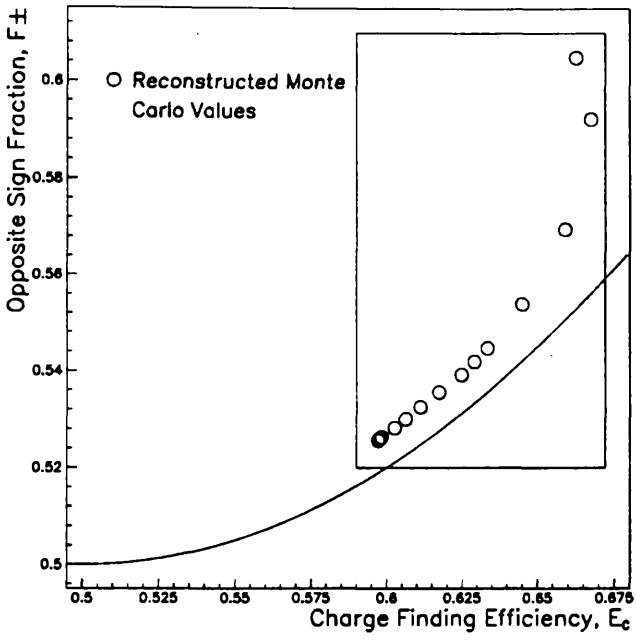

The solid line represents expectations from relation (4.8) with $C_{JJ} = 0$. The points inside the box indicate values found in reconstructed Monte Carlo events. Jet-jet correlations are clearly visible and increase at higher values of E_C due to smaller values of κ.

Figure 4.10: Dependence of $F_\pm$ as a function of E_C.

using relation (4.7), are given in table 4.2. As C_{JJ} requires knowledge of $F_\pm$ *and* E_C,

κ	0.2	0.3	0.5	0.7	0.9	1.0	1.1	1.4
C_{JJ} (%)	5.2	3.6	1.9	1.2	0.9	0.9	0.8	0.8
κ	1.8	2.3	3.0	6.0	9.0	14.0	20.0	∞
C_{JJ} (%)	0.8	0.7	0.7	0.7	0.7	0.7	0.7	0.7

Correlations are calculated using relation (4.8) with $F_\pm$ and E_C derived from reconstructed Monte Carlo events using the thrust event axis and longitudinal momentum weighting scheme. The statistical uncertainty on each correlation is $\pm 0.3\%$.

Table 4.2: Jet-jet correlations as a function of κ.

it represents the limit of accuracy with which data and Monte Carlo can be compared unambiguously.

4.4.2 Properties of Jet Charges

Charge finding involves the weighting parameter κ. Its effect on the jet charge distributions of figure 4.8 is shown in figure 4.11. As κ is increased, the distribution changes from a central peak to a flatter shape, peaked at charges of ± 1, corresponding to the central,

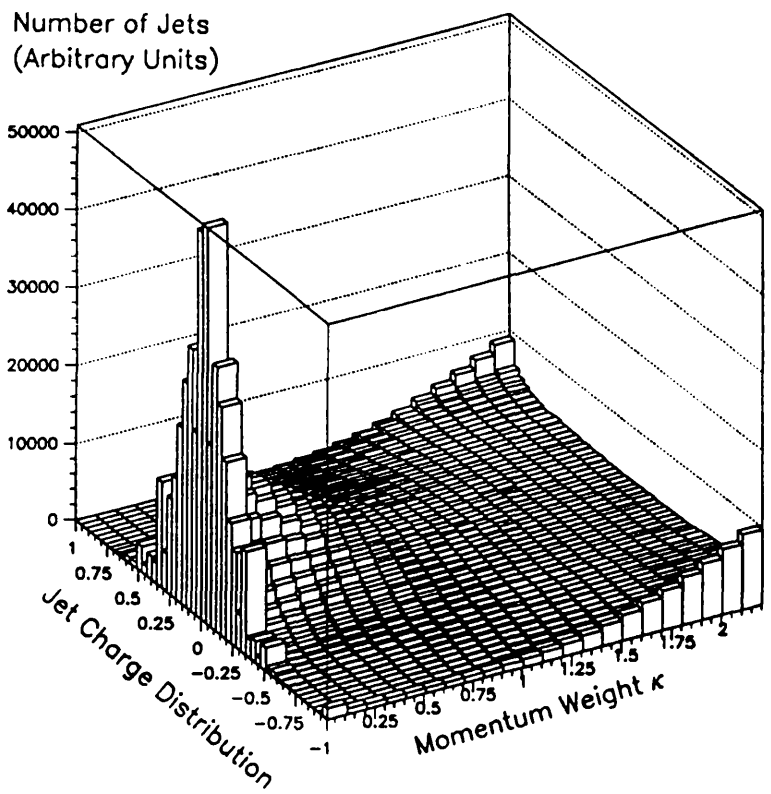

Change in the weighted charge distribution as a function of the tuning parameter κ using the QJMMCL jetfinder with a resolution cut-off of 0.30 and a longitudinal momentum charge summation. The value of κ is optimal for all flavours at 0.4.

Figure 4.11: Charge distribution versus κ.

fastest track in each jet. The charges become more evenly distributed, implying a loss of sensitivity as κ increases.

The method depends on details of the jet itself; its energy, track properties and position in the detector. The opposite sign fraction allows changes to E_C to be monitored indirectly in data and Monte Carlo. The charged energy fraction of events fluctuates depending on the fragmentation. Consequently, the charged momentum of jets has the large width shown in figure 4.12 (a). In events where the charged momentum is large, more information from the quark fragmentation is available and an increase in the charge finding efficiency is observed. This effect appears equally in data and Monte Carlo as seen by the rise in opposite sign fraction as jet momentum increases (see figure 4.12 (b)) and also affects the variation of $F_{\pm}$ with the charged multiplicity in jets shown in figure 4.13 (a). The decrease in $F_{\pm}$ is due to the combined effects of ; increased dissemination of the charge information, and the smaller probability of track loss[9] at jet boundaries. The twin effects of increased charged information and how "broadly" it is spread throughout the

[9]This is observed by the PLUTO collaboration [21] which uses the lower multiplicity jet in an event for the latter reason.

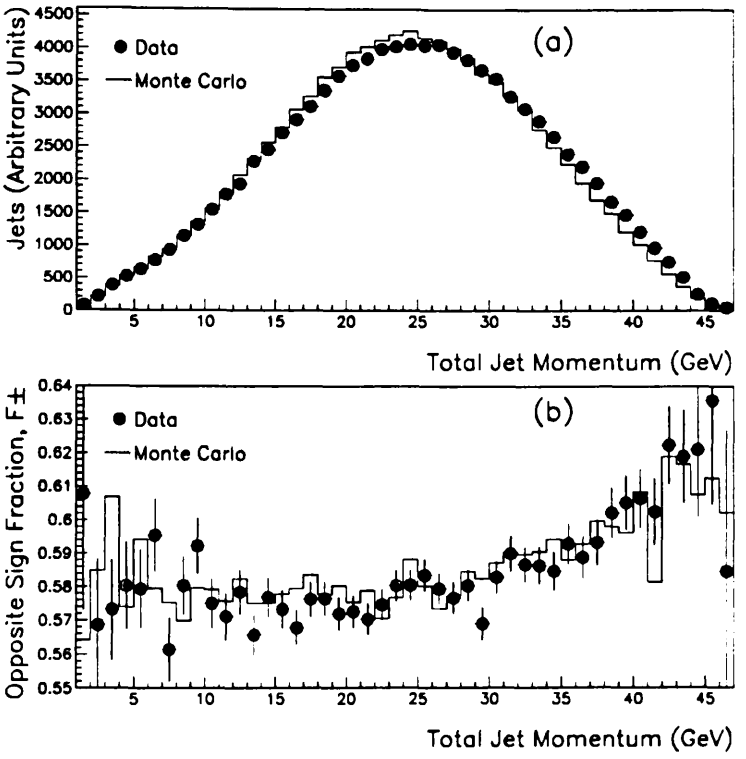

(a) Distribution of total jet momenta and (b) opposite sign fraction as a function of jet momentum.

Figure 4.12: Jet momentum and resulting opposite sign fraction.

jet may be distinguished by observing how the *average* momentum of jet particles affects $F_{\pm}$. This separates the increased charge information from the "hardness" of fragmentation and is shown in figure 4.13 (b) where $F_{\pm}$ is seen to increase with mean particle momentum.

Track losses affect the method at low angles. The charge finding efficiency as a function of azimuthal angle is shown in figure 4.14 indicating the decrease in this region. This may be avoided by limiting the acceptance to the region shown. Within the remainder, the efficiency is flat within the current statistical uncertainty.

From these trends, it is clear that a low multiplicity jet possessing a large charged energy fraction in the centre of the detector has a high charge finding efficiency. This is consistent with concepts of charge retention where Monte Carlo expectations are seen to agree closely with ALEPH data.

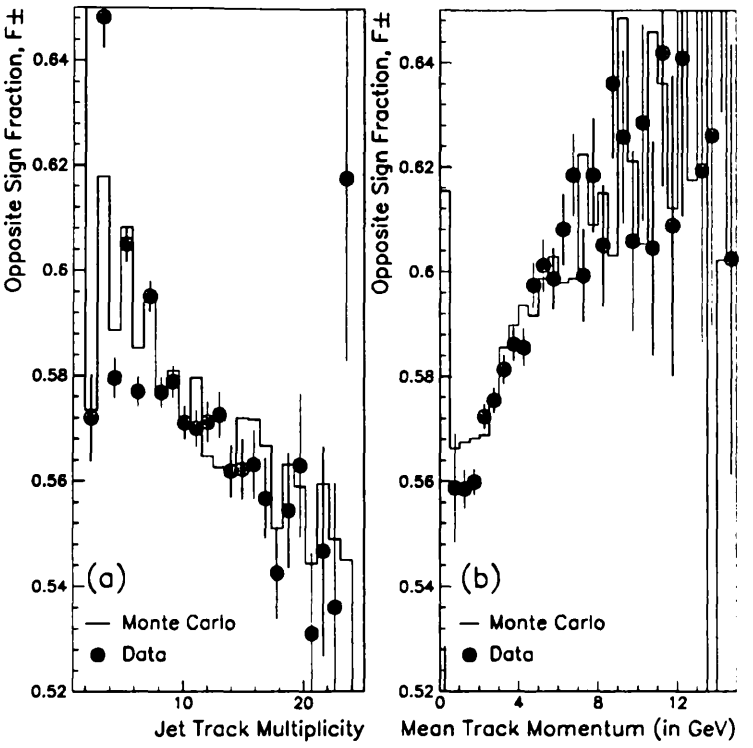

(a) Variation in $F_{\pm}$ as a function of the charged track multiplicity in a jet and (b) as a function of average momentum of particles in the jet.

Figure 4.13: Opposite sign dependence on multiplicity and leading particle momentum.

4.5 Charge Finding Efficiencies

The charge finding efficiency of a *combined* quark sample[10] contains flavour dependent efficiencies weighted by relative branching fractions ($\mathcal{F}$) for each quark type :

$$E_C \equiv (E_C)_{combined} = \sum_{f=u...}^{b} (E_C)_f \, \mathcal{F}_f \tag{4.9}$$

Considerable variation exists between individual efficiencies $(E_C)_f$. The weighting schemes of section 4.3 are tuned by varying κ to select a point of maximum efficiency for all flavours. An example of a tuning curve[11] is shown in figure 4.15 with that of the opposite sign fraction. Similar curves are found for other weighting schemes tested [39]. There is no clear optimum in the opposite sign fraction as the drop in E_C at low κ is compensated for by the jet-jet correlation (as shown in section 4.4.1). This prevents tuning of weighting schemes[12] from data alone. Using a jet finder to select two-jet events for charge determination depends on the cut-off used in the jet finding algorithm. For example, with the

[10] ie. for all flavours.

[11] For the longitudinal-momentum weighting scheme.

[12] This contrasts with the method used by the MAC collaboration [10].

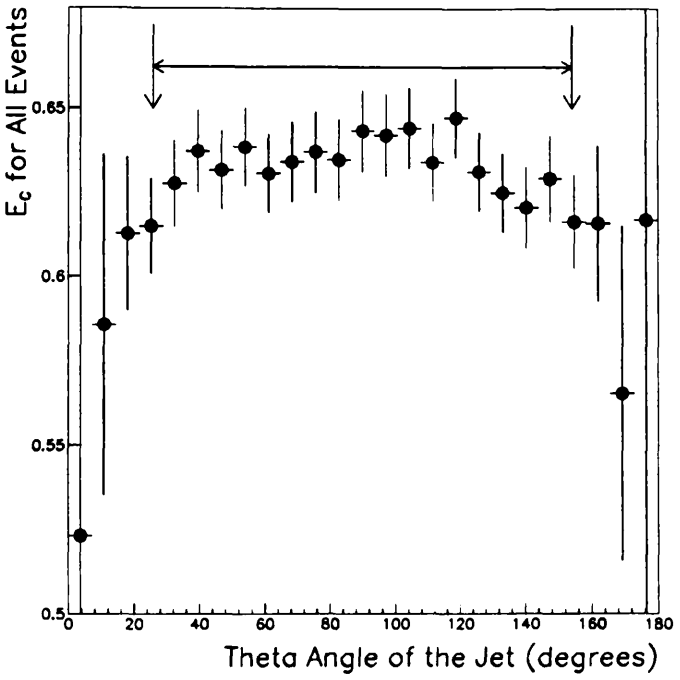

Points represent the Monte Carlo *single arm charge finding efficiency* for getting the sign of the charge correct without imposing a selection on oppositely signed events. The arrows indicate the included region and cut positions at $|\cos\theta| \leq 0.9$.

Figure 4.14: Variation in E_C as a function of jet angle for all events.

JADE minimum mass algorithm, the variation of E_C and two-jet fraction with different cut-off values are shown in table 4.3. It appears that there is only a weak dependence of

Y_{cut} Value	Two Jet Rate (±0.2%)	Opposite Sign Fraction $F_\pm$ (±0.3%)	Charge Finding Efficiency E_C (±0.3%)
0.03	56.7%	52.2%	71.3%
0.06	74.1%	52.3%	71.3%
0.09	83.1%	52.3%	71.1%
0.15	91.9%	52.4%	70.9%
0.30	96.9%	52.3%	70.6%

Results obtained using the longitudinal momentum weighting scheme with a κ value of 0.3.

Table 4.3: Dependence of E_C on the cut-off used in the JADE jet finding algortihm.

E_C upon the cut-off value. Relaxing the cut-off, so that two-jets are found in *all* hadronic events, has little effect on E_C while avoiding the flavour dependence of a two-jet event selection at lower cut-offs.

The jet charge distributions of figure 4.9 shows that the majority of jets have charges close to zero. This implies that the difference between a positive or negative charge assign-

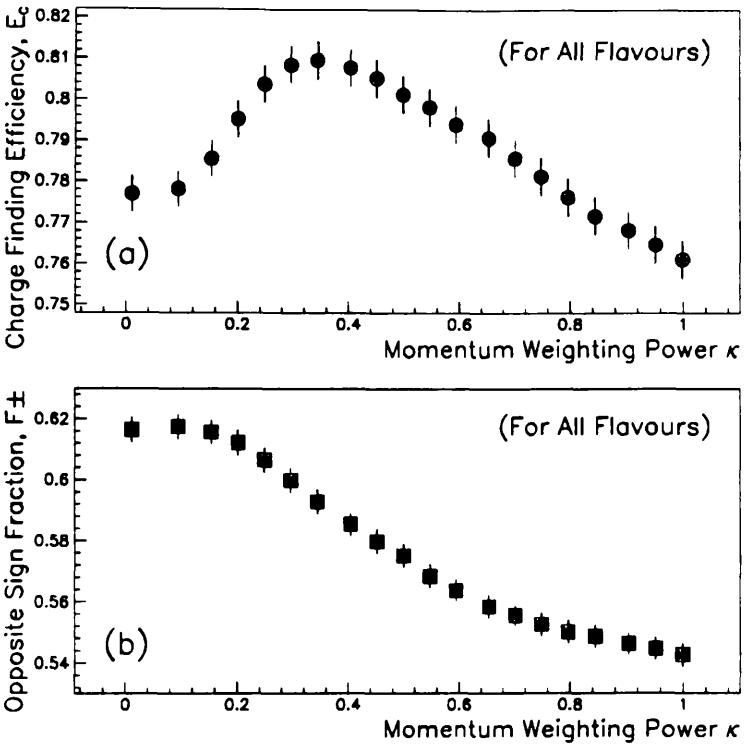

(a) Variation of charge finding efficiency in oppositely signed events as a function of κ and (b) the corresponding change in the fraction of oppositely signed events.

Figure 4.15: Charge finding efficiency as a function of κ for the longitudinal momentum weighting scheme.

ment depends on the correct association and weight of a few jet particles and introduces the possibility of increasing E_C by only selecting charges with large absolute value, or reassigning charges where there is a large imbalance between jets [39] [9].

Reassignment of low charge jets involves like-sign events. In cases where one jet has a large charge value, the other jet is re-assigned the opposite charge. In this way, it is possible to increase the opposite sign fraction at the cost of slightly lowering the overall efficiency, E_C. An alternative method is to apply a cut on the absolute charge difference between jets.

The flavour dependence of these techniques is important, as it is unlikely that the systematics of such a selection could be accurately verified in data and Monte Carlo. Flavour tagging methods could be used for example, but generally suffer from low efficiencies and further systematic contributions. In the current study charge reassignment methods are not used and are mentioned here for reference only.

4.5.1 Dependence on Quark Flavour

The charge and fragmentation of different flavours lead to significant differences in their charge finding efficiencies. Each flavour has a unique tuning curve of the form shown in figure 4.16. The combined efficiency is the weighted average of the constituent curves. The influence of quark charges ($\frac{1}{3}$ and $\frac{2}{3}$) and fragmentation effects are apparent. For

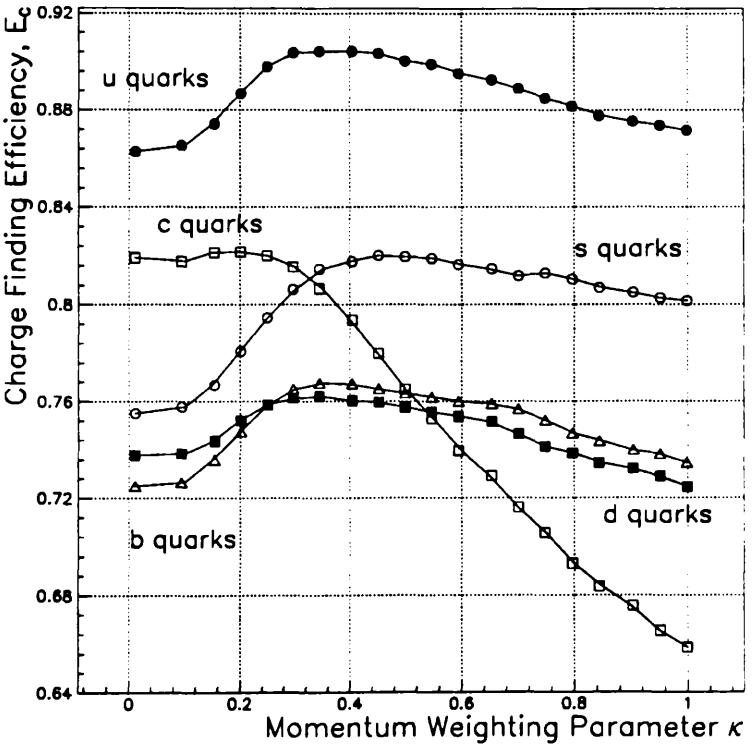

Tuning is carried out using the longitudinal momentum weighting scheme. Correlated statistical errors on each point are $\sim \pm 1.1\%$ and are suppressed for clarity.

Figure 4.16: Charge finding efficiency curves for individual flavours using the longitudinal momentum weighting scheme.

example, the u quark efficiency is greater than the d whereas the fragmentation is known to be similar. The same can be said for c and s quarks with the qualification that the c quark efficiency, although higher at low κ, falls rapidly below that of the s. This is related to the decay of D^* mesons in c quark jets which act to significantly reduce the observable charge retention in this channel [9]. The combined efficiency can be selected using κ to emphasise contributions from one flavour at the expense of another. Variation in the opposite sign fraction of individual flavours is shown in figure 4.17 where jet-jet correlations exist at low κ and are observed to be flavour dependent. As an *preliminary* investigation of the importance of fragmentation models, three were used[13] to estimate

[13]These were; the independent fragmentation model of LUND and the string and cluster models described previously.

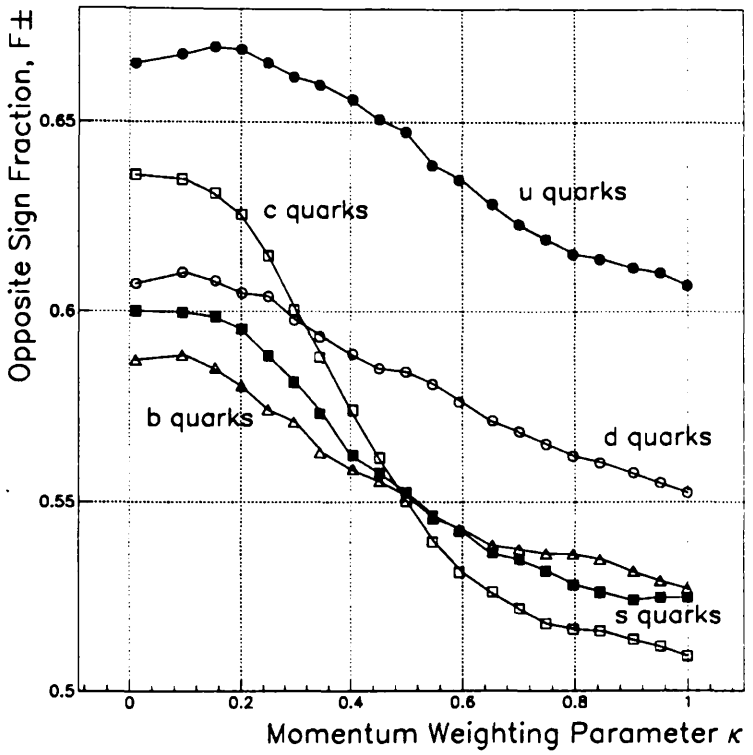

Tuning is carried out using the longitudinal momentum weighting scheme. Correlated statistical errors on each point are $\sim \pm 1.0\%$ and are suppressed for clarity. The curves represent fitted polynomials.

Figure 4.17: The opposite sign fraction as a function of κ for individual flavours.

changes to the tuning curves of figure 4.15. Small event samples were simulated and reconstructed for this purpose. The resulting behaviour indicated [39] that model changes give rise to shifts in the magnitude of E_C of $\sim 5\,(\pm 3)\%$ for all values of κ. More accurate and detailed studies are described in chapter 8.

4.5.2 Detector Effects

The properties of jets and charges discussed so far arise almost completely from fragmentation while detector effects remain small except at low angles. Detector contributions to the opposite sign fraction are summarised in figure 4.18. It is seen that the difference between generator and reconstructed levels manifests itself as an overall drop of a few percent across the range of κ tested. The overall shape is followed closely by the generator level.

Differences between jet finder and event axes based methods are found to be small at this level, both in their combined and flavour dependent efficiencies. Methods differ slightly in the κ value which gives maximum efficiency and in the behaviour of jet-jet correlations at low κ.

Detector considerations are involved in the track selection. This is studied by varying

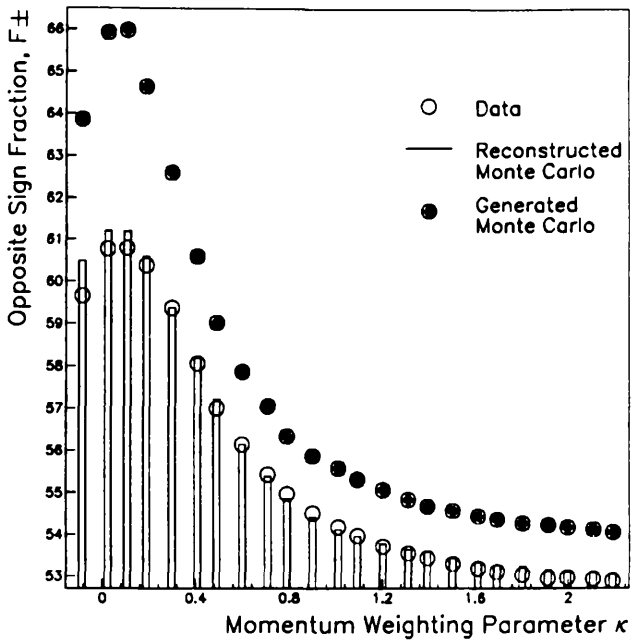

Statistical errors are of the same order as point sizes for data and Monte Carlo.

Figure 4.18: Variation of opposite sign fraction with κ for data and Monte Carlo at the generator and reconstructed levels.

each cut in turn about its chosen value and monitoring changes to E_C via the opposite sign fraction. These are shown in figures 4.19 and figure 4.20. Some differences between generator and reconstructed events arise from differences between the impact parameters (D0 and Z0), and are limited by using the fitted vertex from ALEPH, calculated for each run. D0 and Z0 are derived relative to this fitted position rather than the nominal centre of the detector which is used as the interaction point for the generator level. The track cuts are seen to lie in a stable region as the opposite sign fraction is insensitive to small changes in their value.

4.6 Effects of $B^0 - \overline{B^0}$ Mixing

In a previous quark charge study by JADE [6], corrections for $B^0 - \overline{B^0}$ mixing are applied to take into account the effect on jet charges of b quarks. An understanding of how this affects the current measurement is required at the greater energies of LEP with numerical results presented later in section 8.5.2.

The effect of $B^0 - \overline{B^0}$ mixing upon the charge of a b jet may be interpreted in terms of how the process of $b \rightarrow$ hadrons proceeds with time. During the decay of a B^0 meson, the charge information of the parent b quark is distributed throughout its daughter particles. If the B^0 undergoes mixing then its component of parent charge information is *reversed.* The remainder of the jet is unaffected, so that the degree to which the jet charge is affected

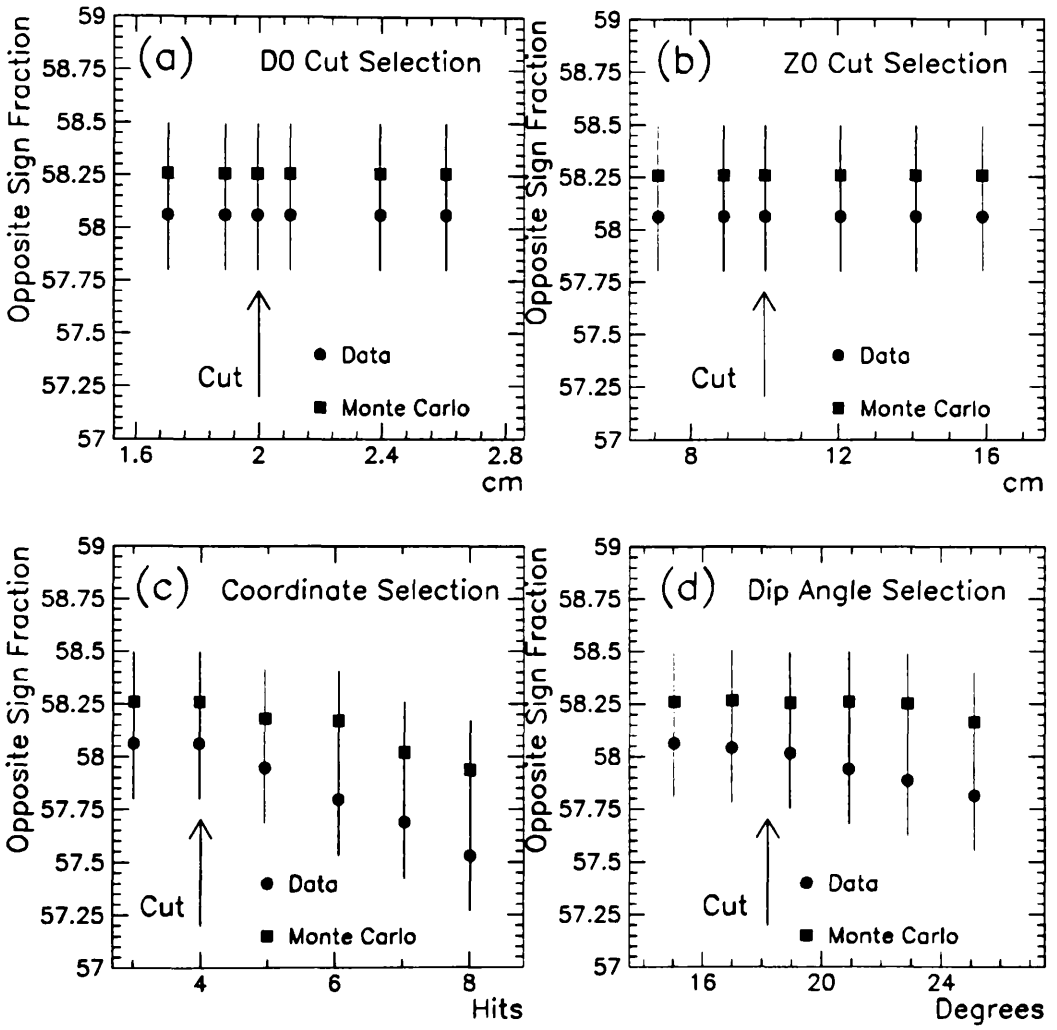

Figure 4.19: Variation in opposite sign fraction as track selection cuts are varied.

depends on the charge content of the jet as a whole and not only upon the meson that has mixed.[14].

The purpose of this section is to understand the way in which a weighted charge summation is altered by mixing and how the current uncertainty on mixing parameters can influence jet charge measurements.

4.6.1 Jet Charges From b Quarks

As a b quark moves out from the interaction vertex, it rapidly fragments and can form a neutral meson state with a partner from a $d\bar{d}$ or $s\bar{s}$ pair. At this point, the B^0 meson and remaining jet particles may be thought of as two "components" of the jet charge. If

[14]This is in contrast to the JADE correction.

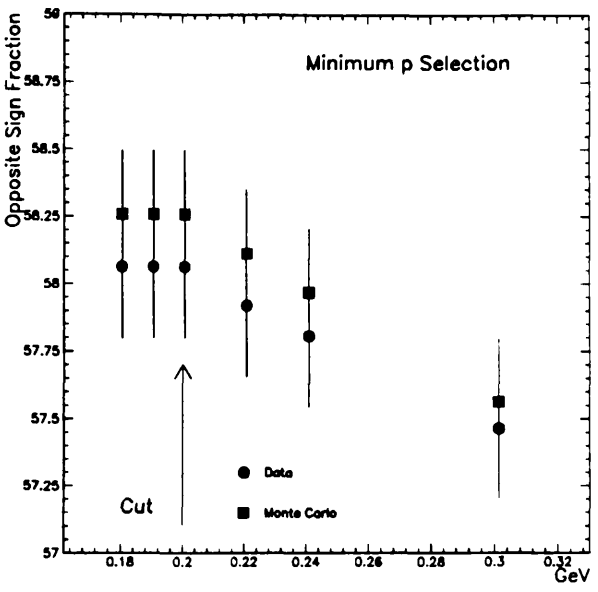

Figure 4.20: Variation in opposite sign fraction as a function of minimum track momentum cut.

the B^0 undergoes mixing then its decay products will carry opposite charge information to that originally. Cancellation between mixed B^0 charge information and "spectator" particles in the jet serves to *reduce* charge retention effects in jets which are detected.

The amount of cancellation depends upon decay characteristics of neutral B mesons. Typically, daughter products of neutral B mesons carry $\sim$ 68% of the charge weight[15] in b jets although this clearly depends upon κ and the type of meson (B_d^0 or B_s^0) which is involved. In the example of semileptonic decays, daughters of the B^0 consist of a lepton with the *same* sign as the quark in the decaying meson, produced with a large momentum. Other decay particles from the meson tend to have opposite charge to that of the heavy quark while the remaining jet particles will generally have the same sign as the parent quark from the Z^o decay. It is expected therefore that decays of B^0 and $\overline{B^0}$ mesons are noticeably different when studied using a weighted charge summation sensitive to the momenta and direction of the entire jet's particles.

4.6.2 Monte Carlo Simulation of B^0 Jet Charges

In neutral B decays, particles with large momentum carry the same charge as the primary quark. The amount of weight they receive in a charge summation depends on their longitudinal components. Track weights given to detected daughter particles of neutral B mesons in the Monte Carlo are shown in figure 4.21. For mesons containing a negatively charged b quark, the weight distribution displays an abundance of particles at high weights

[15]This is using rapidity weighting with $\kappa = 0.4$.

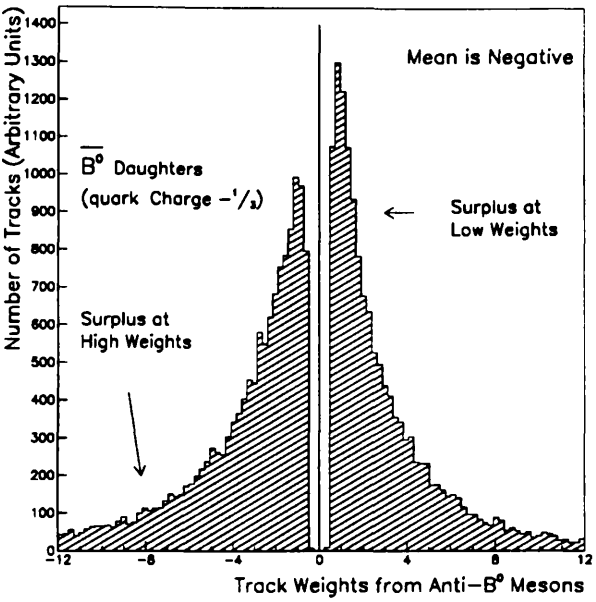

Figure 4.21: Weight distribution of daughter particles of $\overline{B^0}$ mesons.

of the *same sign* while possessing a corresponding increase of particles with low weights but of *opposite sign* to the parent quark. This indicates that decay products of the B, with the same sign as the parent quark, have a larger weight than opposite sign contributions. If the charge of the b was irrelevant to the decay of the *neutral* B mesons then the distributions of figure 4.21 would be symmetric around zero. This is clearly seen not to be the case.

The effect of reversing the jet charge component of a neutral B is observed by comparing jet charges containing B^0's which have mixed with those which have not. These are shown in figure 4.22. It is clear that mixing lowers the degree of charge retention in b jets and as a result *reduces* the shift of the jet charge distribution from zero.

The distributions of figure 4.22 are examples of zero and maximal mixing. The uncertainty of current mixing measurements represents a fraction of the shift between the two distributions. When combined with the rate of neutral B production, the branching fraction of $Z^o \rightarrow b\bar{b}$ and the uncertainty of mixing measurements, this leads to an expectation that mixing uncertainties in a *combined* quark asymmetry are small.

4.7 Summary

Using either jets or hemispheres in conjunction with a weighted charge summation allows charge retention effects to be seen in ALEPH data via the fraction of oppositely charged jets. Observations are dominated by fragmentation effects while detector contributions remain small. By suitable choices of jet definition, charge summation and loose angular cuts, a high charge finding efficiency ($\sim$ 70%) can be obtained with close agreement

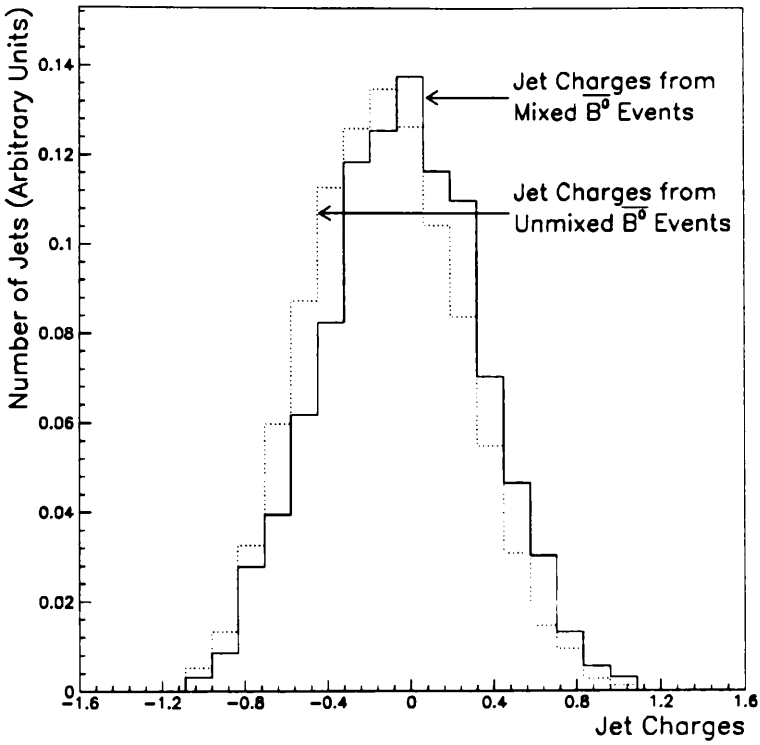

Charges of jets from b quarks fully mixed and from b quarks where no mixing has occurred with longitudinal momentum weighting and $\kappa = 0.4$.

Figure 4.22: Effects of zero and maximal mixing on charge distributions of b quark jets.

between data and Monte Carlo expectations. $B^0 - \overline{B^0}$ mixing effects are expected to be present but small in a combined sample of quark flavours.

Chapter 5

Method of Measuring the Combined Quark Asymmetry

Combined quark forward-backward asymmetries have been measured at the lower energies of PEP [10] and PETRA [6]. The analysis presented here represents the first such measurement around the Z^o peak. Measured asymmetries remain small because of large cancellations between flavours. These arise since it is only possible to differentiate between positive jet charges (mainly from u, $\bar{d}$, $\bar{s}$, c and $\bar{b}$ quarks) and negative jet charges (mainly from $\bar{u}$, d, s, $\bar{u}$ and b quarks) rather than between fermions and antifermions.

The asymmetry is discernible from a surplus of negatively charged jets in the forward[1] hemisphere of the detector with angular distribution :

$$\frac{d\sigma}{d\cos\theta} = \left[\frac{3}{8}\left(1+\cos^2\theta\right) + A_{FB}\cos\theta \right] \sigma_{hadron} \tag{5.1}$$

where σ_{hadron} is the total hadronic cross-section . A_{FB} is defined as :

$$A_{FB} = \frac{\sigma_F - \sigma_B}{\sigma_F + \sigma_B} \tag{5.2}$$

where σ_F and σ_B are the integrated forward and backward cross-sections respectively for positive quarks. A_{FB} is expected to be small and negative for combined flavours at the peak (see figure 1.4). In order to measure A_{FB} the direction and charge of hadronic jets are determined while the probability of charge misidentification must be taken into account as it dilutes the asymmetry.

The purpose of this chapter is to outline the method and notation for the current measurement and the criteria used to select tracks and events. The method of *charge flow* is introduced in section 5.1 with details of track and event selection in section 5.2.

In previous studies [10] [6] [34], various methods have been used to incorporate the probability of charge misidentification when extracting an asymmetry from jet charge measurements. Preliminary investigations of these methods were carried out [9] [39] before using the current method. These methods provide complementary information, some results of which are given later in section 6.5.

[1] Corresponding to the +Z detector hemisphere in the direction of electron travel.

5.1 The Method of Charge Flow

Previous methods [10] [34] have used the charge information of single jets or hemispheres to identify the direction of the positive quark in hadronic events. The method presented here represents an original[2] attempt to utilise the charge information through the *charge flow* between quark and antiquark hemispheres.

The method is inspired by the observed differences between weighted charge distributions of u and d quarks in deep inelastic neutrino-nucleon scattering experiments 3.4 [22]. Charge flow is defined as the net difference between jet charges of event hemispheres, so that both "sides" of an event are used. The charges are reconstructed by dividing events into hemispheres around an axis and using a weighted charge summation in each. For the ideal case of perfect charge reconstruction in both hemispheres, the charge flow is equal to twice the parent quark charge; eg. for a $d\bar{d}$ pair, the charge flow would have magnitude : $\frac{1}{3} - \left(-\frac{1}{3}\right) = \frac{2}{3}$.

The calculation is ordered as in (5.3) so that charges are subtracted according to which half of the detector the jet lies in :

$$Charge\ Flow = \underbrace{Forward\ Jet\ Charge}_{\cos\theta>0} - \underbrace{Backward\ Jet\ Charge}_{\cos\theta<0} \tag{5.3}$$

The asymmetry appears as an overall shift from zero of the charge flow distribution due to a surplus of *forward-negative* events. Component asymmetries for each flavour contribute additively to the combined shift depending on the charge finding efficiency for each flavour. Additional detector or fragmentation contributions can be quantified by extra shifts and distortions of the charge distributions.

This section provides definitions and derivations of important quantities used later in the measurement.

5.1.1 Measured Quantities

In a given hadronic event, the thrust axis is defined using charged track information. A weighted charge summation is carried out in each hemisphere, using the longitudinal momentum weighting scheme with weighting power κ and the sign conventions in figure 5.1. The two summations :

$$\begin{aligned} Q_{\mathrm{F}} &= \frac{\sum_{i=1}^{N_F} \mid p_i \cdot \hat{e}_{\mathrm{T}} \mid q_i}{\sum_{i=1}^{N_F} \mid p_i \cdot \hat{e}_{\mathrm{T}} \mid} \quad \text{for particles with } p_i \cdot \hat{e}_{\mathrm{T}} > 0 \\ Q_{\mathrm{B}} &= \frac{\sum_{i=1}^{N_B} \mid p_i \cdot \hat{e}_{\mathrm{T}} \mid q_i}{\sum_{i=1}^{N_B} \mid p_i \cdot \hat{e}_{\mathrm{T}} \mid} \quad \text{for particles with } p_i \cdot \hat{e}_{\mathrm{T}} < 0 \end{aligned} \tag{5.4}$$

are performed relative to the thrust unit vector, $\hat{e}_{\mathrm{T}}$, the third (Z) component of which is defined to point in the forward direction. The convention determines the overall sign of

[2] First conceived by Alain Blondel, $q\bar{q}$ Analysis Group-ALEPH, CERN, Spring 1990.

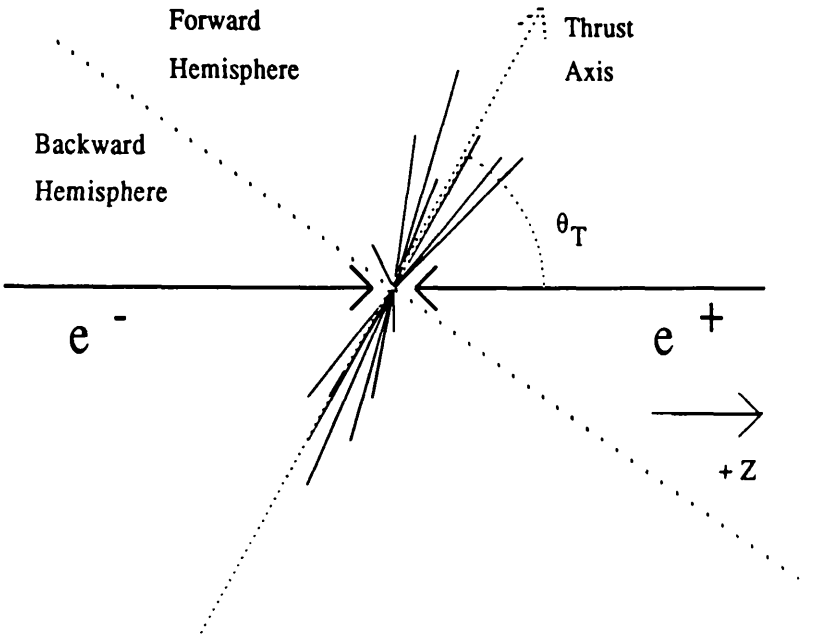

Figure 5.1: Sign conventions for the charge flow method.

asymmetry with respect to the colliding beams. Using jet charges, the following quantities are defined for each event :

$$\begin{aligned} \text{The } \textit{Charge Flow} &= Q_{FB} = Q_F - Q_B \\ \text{The } \textit{Total Charge} &= Q \quad = Q_F + Q_B \end{aligned} \tag{5.5}$$

In a sample of events, the charge flow distribution is shifted from zero by an amount proportional to the asymmetry while the total charge distribution should remain centred on zero from charge conservation. The characteristic parameters of the charge distributions are :

$\overline{Q_{FB}}$ = The mean of the charge flow distribution,
σ_{FB} = The RMS width of the charge flow distribution,
$\overline{Q}$ = The mean of the total charge distribution,
σ_Q = The RMS width of the total charge distribution.

These quantities are calculable in data and Monte Carlo. The method may best be understood by considering the case of a single quark flavour. With a sample of $u\bar{u}$ events, the charge flow distributions when a u quark is either moving forward or backward are shown in figure 5.2. The *separation* of the $\overline{Q_{FB}}$ distribution mean from zero, indicated in each case, is a measure of the separation power between quark and antiquark jet charges and is denoted by q_f. The subscript refers to the flavour involved. The charge symmetry between fragmentation of quarks and antiquarks means that :

$$\overline{Q^f_{FB}} \equiv q_f \equiv -q_{\bar{f}} \equiv -\overline{Q^{\bar{f}}_{FB}} \tag{5.6}$$

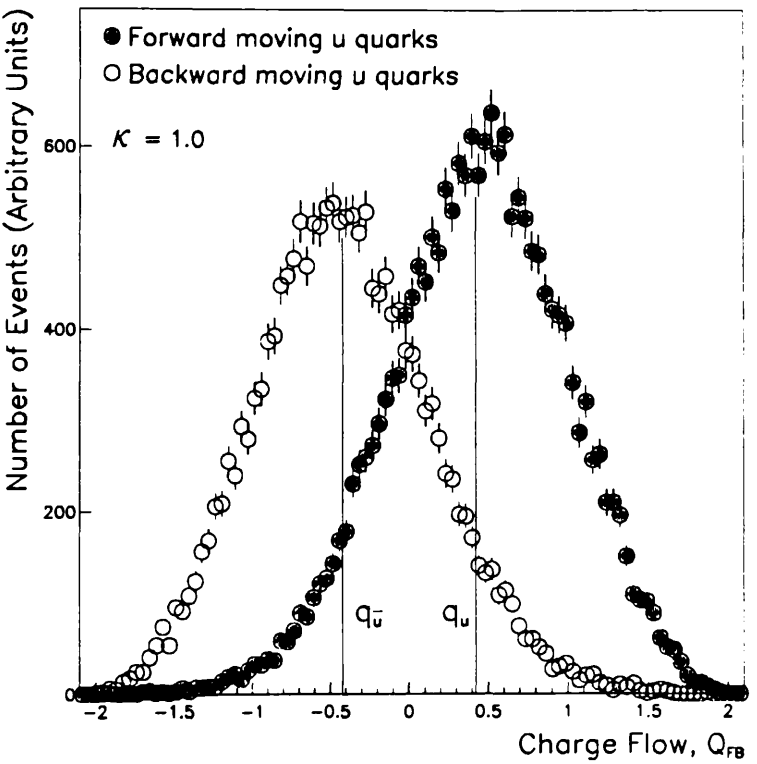

Example of charge flow distributions for u quarks with a κ of 1.0. Vertical lines denote values of q_u and $q_{\bar{u}}$, synonymous with $\overline{Q^u_{FB}}$ and $\overline{Q^{\bar{u}}_{FB}}$, with positive and negative charge separations respectively.

Figure 5.2: Charge flow distributions for u quarks depending on their direction of motion in the detector.

Cancellation between opposite sign charges of up and down-type flavours decreases the the mean shift from zero ($\overline{Q_{FB}}$) of the observed data distribution containing all flavours.

5.1.2 Extraction of the Asymmetry from $\overline{Q_{FB}}$

The differential cross-section for a given quark flavour, f, is given by :

$$\begin{aligned} \frac{d\sigma^f}{d\cos\theta} &= \left[\frac{3}{8}\left(1 + \cos^2\theta\right) + A^f_{FB}\cos\theta\right] \sigma_{had}\frac{\Gamma_f}{\Gamma_{had}} \\ \frac{d\sigma^{\bar{f}}}{d\cos\theta} &= \left[\frac{3}{8}\left(1 + \cos^2\theta\right) - A^f_{FB}\cos\theta\right] \sigma_{had}\frac{\Gamma_f}{\Gamma_{had}} \end{aligned} \tag{5.7}$$

If the limited angular acceptance of the detector, $0 < \cos\theta < \cos\theta_c$, is taken into account, then equation (5.2) may be written as :

$$A_{FB}(\cos\theta_c) = \frac{\sigma^f - \sigma^{\bar{f}}}{\sigma^f + \sigma^{\bar{f}}} \tag{5.8}$$

σ^f and $\sigma^{\bar{f}}$ are the integrated cross-sections for quarks and antiquarks in the *forward* region :

$$\sigma^f = \int_0^{\cos\theta_c} \frac{d\sigma^f}{d\cos\theta}\, d\cos\theta \qquad \sigma^{\bar{f}} = \int_0^{\cos\theta_c} \frac{d\sigma^{\bar{f}}}{d\cos\theta}\, d\cos\theta \tag{5.9}$$

Integrating top and bottom of (5.8) yields :

$$\begin{aligned} \int_0^{\cos\theta_c} \left(\sigma^f + \sigma^{\bar{f}}\right) d\cos\theta &= \frac{3}{4}\left[\cos\theta_c + \frac{\cos^3\theta_c}{3}\right] \sigma_{had}\, \frac{\Gamma_f}{\Gamma_{had}} \\ \int_0^{\cos\theta_c} \left(\sigma^f - \sigma^{\bar{f}}\right) d\cos\theta &= A_{FB}^f \cos^2\theta_c\, \sigma_{had}\, \frac{\Gamma_f}{\Gamma_{had}} \end{aligned} \tag{5.10}$$

so that equation (5.8) becomes :

$$A_{FB}^f(\cos\theta_c) = \int_0^{\cos\theta_c} A_{FB}^f\, d\cos\theta = \frac{4}{3}\, \frac{\cos\theta_c}{1 + \frac{\cos^2\theta_c}{3}}\, A_{FB}^f \tag{5.11}$$

It is then possible to relate this integrated asymmetry to the mean charge flow in a given $\cos\theta$ range of the detector. Defining $P(Q_{FB})^f$ and $P(Q_{FB})^{\bar{f}}$ to be probability density functions for a given quark type to give rise to a charge flow, Q_{FB}, allows the mean charge flow to be written as the weighted average :

$$\overline{Q_{FB}^{f\bar{f}}} = \frac{\int_{-\infty}^{\infty} Q_{FB}\left[\sigma^f P^f(Q_{FB}) + \sigma^{\bar{f}} P^{\bar{f}}(Q_{FB})\right] dQ_{FB}}{\int_{-\infty}^{\infty}\left[\sigma^f P^f(Q_{FB}) + \sigma^{\bar{f}} P^{\bar{f}}(Q_{FB})\right] dQ_{FB}} \tag{5.12}$$

$$= \frac{\overline{Q_{FB}^f}\,\sigma^f + \overline{Q_{FB}^{\bar{f}}}\,\sigma^{\bar{f}}}{\sigma^f + \sigma^{\bar{f}}} \tag{5.13}$$

This is related to the mean charge flow in an angular range by the integration :

$$\begin{aligned} \int_0^{\cos\theta_c} \frac{d\overline{Q_{FB}^{f\bar{f}}}}{d\cos\theta}\, d\cos\theta &= \frac{\int_0^{\cos\theta_c}\left[\frac{3}{8}(1+\cos^2\theta)\left(\overline{Q_{FB}^f} + \overline{Q_{FB}^{\bar{f}}}\right)\right] d\cos\theta}{\frac{3}{4}\left(\cos\theta_c + \frac{\cos^2\theta_c}{3}\right)} \\ &+ \frac{\int_0^{\cos\theta_c}\left[A_{FB}^f \cos\theta\left(\overline{Q_{FB}^f} - \overline{Q_{FB}^{\bar{f}}}\right)\right] d\cos\theta}{\frac{3}{4}\left(\cos\theta_c + \frac{\cos^2\theta_c}{3}\right)} \end{aligned} \tag{5.14}$$

$\overline{Q_{FB}^f}$ and $\overline{Q_{FB}^{\bar{f}}}$ are independent of the integration. Simplifying (5.14) yields :

$$\int_0^{\cos\theta_c} \frac{d\overline{Q_{FB}^{f\bar{f}}}}{d\cos\theta}\, d\cos\theta = \frac{\overline{Q_{FB}^f} + \overline{Q_{FB}^{\bar{f}}}}{2} + \frac{4}{3} A_{FB}^f\, \frac{1}{2}\, \frac{\cos\theta_c}{1 + \frac{\cos^2\theta_c}{3}} \left(\overline{Q_{FB}^f} - \overline{Q_{FB}^{\bar{f}}}\right) \tag{5.15}$$

Assuming that flavour separations are equal for quark and antiquark (ie. relation (5.6)) means that the first term of (5.15) disappears, and the second simplifies to leave :

$$\int_0^{\cos\theta_c} \frac{d\overline{Q_{FB}^{f\ or\ \bar{f}}}}{d\cos\theta}\, d\cos\theta = \frac{4}{3}\, \frac{\cos\theta_c}{1 + \frac{\cos^2\theta_c}{3}}\, q_f\, A_{FB}^f \tag{5.16}$$

This relates an underlying asymmetry to the integrated measurement of $\overline{Q_{FB}}$ using Monte Carlo determined separations, q_f. The generalisation of equation (5.16) to combined flavours is given by the summation :

$$\int_0^{\cos\theta_c} \frac{d\overline{Q_{FB}}}{d\cos\theta}\, d\cos\theta \;=\; \frac{\cos\theta_c}{1+\frac{\cos^2\theta_c}{3}}\,\frac{\mathcal{A}_e}{\Gamma_{had}}\sum_{f=u\ldots}^{b} q_f\,\mathcal{A}_f\,\Gamma_f \tag{5.17}$$

where $A_{FB}^f = \frac{3}{4}\mathcal{A}_e\mathcal{A}_f$ as given in chapter 1.

5.1.3 Relation Between Charge Distribution Widths

Quark and antiquark charge distributions are conjugates of each other. Their means (equation (5.6)) and widths are equivalent :

$$\sigma_{FB}^f \;=\; \sigma_{FB}^{\bar{f}} \tag{5.18}$$

For $q\bar{q}$ events of a specific flavour, the width of the charge flow distribution is related to that of the total charge by :

$$\left(\sigma_{FB}^{f\bar{f}}\right)^2 \;=\; \overline{\left(Q_{FB}^{f\bar{f}}\right)^2} \;-\; \left(\overline{Q_{FB}^{f\bar{f}}}\right)^2 \tag{5.19}$$

The second term of (5.19) is the square of the mean charge flow ($\propto$ the asymmetry) for flavour f, and remains small when compared to the first term. Assuming that this contribution is negligible for the moment leaves :

$$\left(\sigma_{FB}^{f\bar{f}}\right)^2 \;\approx\; \overline{\left(Q_{FB}^{f\bar{f}}\right)^2} \tag{5.20}$$

Charge flow distributions of quarks and antiquarks are identical but opposite in sign so that :

$$\overline{\left(Q_{FB}^{f\bar{f}}\right)^2} \;=\; \overline{\left(Q_{FB}^{f}\right)^2} \;=\; \overline{\left(Q_{FB}^{\bar{f}}\right)^2} \tag{5.21}$$

Considering the charge flow distribution of quarks only and using (5.21) gives :

$$\overline{\left(Q_{FB}^{f\bar{f}}\right)^2} \;=\; \left(\sigma_{FB}^{f}\right)^2 + \left(\overline{Q_{FB}^{f}}\right)^2 \tag{5.22}$$

$$\;=\; \left(\sigma_{FB}^{f}\right)^2 + q_f^2 \tag{5.23}$$

again using assumption (5.6). From (5.20) and (5.23), it is clear that :

$$\left(\sigma_{FB}^{f\bar{f}}\right)^2 \;\approx\; \left(\sigma_{FB}^{f}\right)^2 + q_f^2 \tag{5.24}$$

The approximation is due to the assumption that the asymmetry squared is small compared to the separation of a given flavour. This is valid as the ignored term is typically small ($\sim 10^{-4}$) compared to the separations ($\sim 10^{-2}$) and becomes increasingly so with κ as the separations increase in magnitude.

The measurable quantity, $\bar{q}$, is defined as the difference between the charge distribution widths :

$$\bar{q} = \sqrt{\sigma_{FB}^2 - \sigma_Q^2} \tag{5.25}$$

and is expected to be approximately equivalent to :

$$\bar{q} \approx \sqrt{\left[\sum_{f=u...}^{b} q_f^2 \frac{\Gamma_f}{\Gamma_{had}}\right]} \tag{5.26}$$

$\bar{q}$ is non-zero because charge retention effects in Q_{FB} broaden its distribution when compared with the distribution of total charges, Q. The importance of $\bar{q}$ lies in its use for comparison between data and Monte Carlo and it represents a *sensitive* test of the shape of charge distributions.

5.1.4 Standard Model Calculations

This section outlines the method of calculating an expected value of $\overline{Q_{FB}}$, from the relations of section 5.1.3 and chapter 1.

Relation (5.17), with a limited angular acceptance of $-0.9 < \cos\theta < +0.9$, gives :

$$\overline{Q_{FB}}(\cos\theta_c) = \mathcal{A}_e \times 0.71 \times \sum_{f=u...}^{b} q_f \times \mathcal{A}_f \times \frac{\Gamma_f}{\Gamma_{had}} \tag{5.27}$$

which can be simplified using the lowest order cross-section for $e^+e^- \rightarrow q\bar{q}$ on the Z^o peak to yield :

$$\begin{aligned} \Gamma_f^o &\propto \left(a_f^2 + v_f^2\right) \\ \Gamma_{had}^o &\propto \sum_{f=u...}^{b} \left(a_f^2 + v_f^2\right) \text{ with } \mathcal{A}_f = \frac{2a_f v_f}{\left(a_f^2 + v_f^2\right)} \end{aligned} \tag{5.28}$$

In the ratio $\frac{\Gamma_f^o}{\Gamma_{had}^o}$, there is a cancellation of all flavour independent terms, transforming equation (5.27) into :

$$\overline{Q_{FB}}(\cos\theta_c) = \mathcal{A}_e \times 0.71 \times \frac{2\sum_{f=u...}^{b} q_f\, a_f\, v_f}{\sum_{f=u...}^{b}\left(a_f^2 + v_f^2\right)} \tag{5.29}$$

Using values for a_f and v_f from table 1.2 reduces (5.29) to :

$$\begin{aligned} \overline{Q_{FB}^{ref}}(\cos\theta_c) &= 0.16 \times 0.71 \times \frac{2\sum_{f=u...}^{b} q_f\, a_f\, v_f}{6.74} \\ &= 0.033 \times \sum_{f=u...}^{b} q_f\, a_f\, v_f \end{aligned} \tag{5.30}$$

This relation for the *expected* charge flow, $\overline{Q_{FB}^{ref}}$, is used to relate the separations, q_f, to the mean charge flow independently of statistical uncertainties in measured values of $\mathcal{A}_e$ and $\mathcal{A}_f$.

It is important to note that the definition of $\overline{Q_{FB}^{ref}}$ assumes the Standard Model form of the electroweak couplings for quarks and leptons, with quark universality. These are calculated assuming a $sin^2\theta_w$ of 0.230. The purpose of $\overline{Q_{FB}^{ref}}$ is to show how changes in quark separations affect an expected asymmetry on the peak. It does not contain the statistical fluctuations of the quantities $\frac{\Gamma_f}{\Gamma_{had}}$ or the asymmetries $\mathcal{A}_e$ and $\mathcal{A}_f$ and so avoids the need for essentially infinite Monte Carlo statistics. $\overline{Q_{FB}^{ref}}$ is useful for studying systematic changes to the expected value of $\overline{Q_{FB}}$ as a result of fragmentation, decays and detector effects.

5.1.5 Angular Dependence of $\overline{Q_{FB}}$

The angular dependence of $\overline{Q_{FB}}$ arises from the difference between the angular distributions of fermions in the forward and backward hemispheres. From the differential cross-section, it is possible to write equation (5.13) as follows :

$$\frac{d\overline{Q_{FB}^{f}}}{dcos\,\theta} = \frac{\overline{Q_{FB}^{f}}\frac{d\sigma^{f}}{dcos\,\theta} + \overline{Q_{FB}^{\bar{f}}}\frac{d\sigma^{\bar{f}}}{dcos\,\theta}}{\frac{d\sigma^{f}}{dcos\,\theta} + \frac{d\sigma^{\bar{f}}}{dcos\,\theta}} \tag{5.31}$$

which, after substitution using (5.7), becomes :

$$\frac{d\overline{Q_{FB}^{f}}}{dcos\,\theta} = q_f \times \frac{8}{3} \times \frac{cos\,\theta}{1+cos^2\theta} \times A_{FB}^{f} \tag{5.32}$$

Equation (5.31) is obtained by taking the angular derivative of $\overline{Q_{FB}}$ and treating $\overline{Q_{FB}^{f}}$ and $\overline{Q_{FB}^{\bar{f}}}$ as constants. There is an implicit assumption that the detector is symmetric in $cos\,\theta$ and so all possible non-zero values of $\overline{Q_{FB}}$ result from the difference between $\sigma^{f}(cos\,\theta)$ and $\sigma^{\bar{f}}(cos\,\theta)$ only. The differential form of (5.32) contains the quantity $\frac{8}{3}\,q_f\,A_{FB}$ and so is directly related to the asymmetry itself.

5.2 Track and Event Selection

Hadronic events are selected for the asymmetry analysis using the ALEPH electroweak hadronic event selection based upon charged tracks. This has a measured efficiency of 97.5(±0.6)% with negligible two-photon (3.0×10^{-3}) and $\tau^+\tau^-$ (2.0×10^{-3}) background [2].

Events with at least 5 charged tracks are required to have a total energy greater than 10% of the centre-of-mass energy. Tracks are selected to have a angle of greater than 18.2° relative to the beam, at least 4 TPC coordinates and to lie within 2 cm and 10 cm of the vertex in D0 and Z0 respectively. The thrust axis of the event is calculated using these tracks.

The quark asymmetry analysis places further restrictions on the selection of tracks and events which are discussed here with their rejection rates and efficiencies.

It is important that event and track selections give good agreement between data and Monte Carlo while remaining free of any flavour dependent bias. The hadronic event selection described above is found to be independent of event flavour. This is verified to first order by applying identical event selections to reconstructed Monte Carlo events. The observed branching fractions found in this sample (using the hadronic event selection) are compared with theoretical expectations in table 5.1 which indicates that this selection introduces no significant bias.

Flavour	Reconstructed Monte Carlo Fraction	Theoretical Branching Fraction
u	0.171 ($\pm$0.001)	0.171 ($\pm$0.001)
d	0.218 ($\pm$0.001)	0.220 ($\pm$0.001)
s	0.218 ($\pm$0.001)	0.220 ($\pm$0.001)
c	0.172 ($\pm$0.001)	0.171 ($\pm$0.001)
b	0.221 ($\pm$0.001)	0.219 ($\pm$0.001)

Theoretical branching fractions are calculated using the DYMU generator and compared with reconstructed Monte Carlo events after the ALEPH hadronic event selection based on charged tracks.

Table 5.1: Comparision of measured and expected branching fractions using the ALEPH hadronic event selection.

5.2.1 Track Selection

Track criteria for selecting hadronic events and determination of jet charges in this analysis are largely the same. The latter introduces an additional[3] loose (200 MeV) selection on the minimum transverse momentum of tracks which cuts away badly reconstructed and "looping" tracks. The TPC cannot track below this limit and so no *valid* tracks are rejected. This is apparent from the plateau in the opposite sign fraction as the cut is varied in figure 4.20.

The distributions of track parameters used in the selection are shown in figure 5.3, prior to any selection. These show small disparities between data and Monte Carlo tracks with large impact parameters which are largely cut away by the selection. The effects of track selection are shown in table 5.2 using the rejection rate of each cut in turn. These indicate that slightly more tracks are rejected in data than Monte Carlo as expected from figure 5.2. This is especially noticeable in the relative rejection rates of the low angle cut in table 5.2. A large fraction of the rejected tracks are candidates with ITC hits only or low momentum tracks which loop repeatedly and are broken by the pattern recognition.

As shown later, the track selection gives good agreement between data and Monte Carlo in event shape [2] and charge flow distributions. The mean charged multiplicities

[3] Additional to the track cuts described in the preceding section.

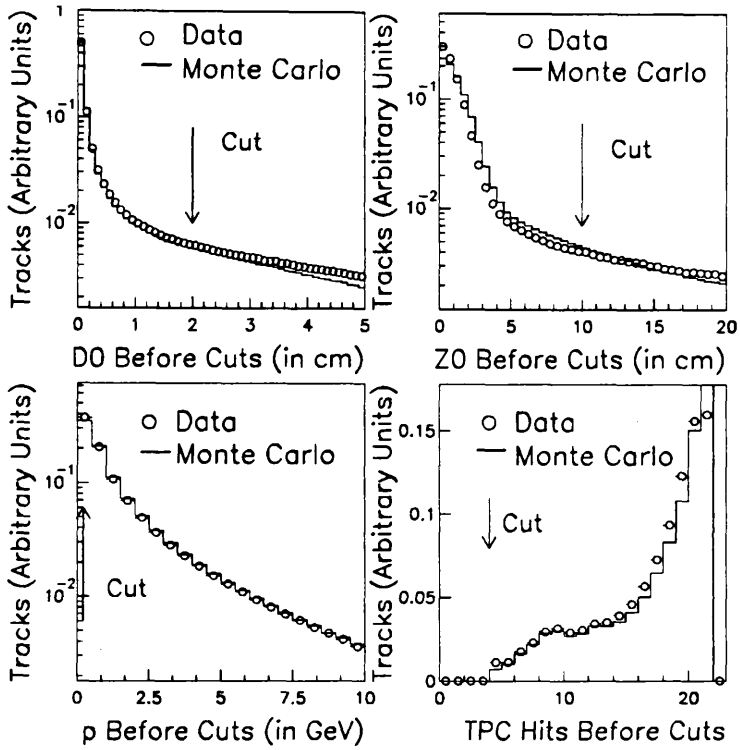

Logarithmic vertical scales are used except for the number of TPC hits on tracks.

Figure 5.3: Normalised track parameter distributions used to select tracks for analysis prior to track selection.

		Data	Monte Carlo
Cut Type	Value	Track Rejection Rate	Track Rejection Rate
Track Hits	4 hits	21.53 (± 0.01)%	18.61 (± 0.01)%
Vertex D0	2.0 cm	32.33 (± 0.01)%	26.22 (± 0.01)%
Vertex Z0	10.0 cm	31.58 (± 0.01)%	22.50 (± 0.01)%
Momentum	0.2 GeV	23.07 (± 0.01)%	19.17 (± 0.01)%
Track Angle, θ	18.2°	8.55 (± 0.01)%	4.29 (± 0.01)%
Combined		45.05 (± 0.01)%	39.91 (± 0.01)%

Table 5.2: Track rejection rates for individual selection criteria.

are shown in table 5.3, taken from the distributions of figure 5.5. The small difference

Event Sample	Selected Charged Multiplicity
Data	17.72 (±0.01)
Reconstructed Level Monte Carlo	17.63 (±0.01)
Generator Level Monte Carlo	16.53 (±0.01)

The quoted errors are statistical only.

Table 5.3: Selected Charged Multiplicities

of 0.09 (± 0.01(*stat.*)) between data and Monte Carlo does not take into account the systematic error from detector simulation and fragmentation effects which is of the order of ~ 1.2% [40].

5.2.2 Thrust Angle Acceptance

As mentioned in chapter 4, it is necessary to restrict jet charge calculations to the central region of the detector. This avoids substantial track losses which can distort jet charge determination. A compromise must be made between track losses and discarding events in the low angle region where an asymmetry is largest.

In the low angle region of the detector, tracks with small transverse momenta create few coordinates in the TPC. The 18.2° track selection cut represents the minimum angle which may be used to define the thrust acceptance. The degree with which tracking is accurately simulated in this region is shown in figure 5.4 and by the rate of rejected events from the $cos\,\theta_c$ cut on the thrust axis angle ($cos\,\theta_T$) in data and Monte Carlo. These are given in table 5.4 where the rates of events rejected in data and Monte Carlo agree to better than 10^{-3} in the region $0.80 \leq cos\,\theta_c \leq 0.95$. To minimise track loss and any

	Data	Monte Carlo
$cos\,\theta_c$	Event Rejection Rate	Event Rejection Rate
0.80	22.54 (±0.02)%	22.54 (±0.02)%
0.85	15.72 (±0.01)%	15.56 (±0.01)%
0.90	8.15 (±0.01)%	8.05 (±0.01)%
0.95	1.61 (±0.01)%	1.58 (±0.01)%

Table 5.4: Event rejection rates as a function of the thrust acceptance cut.

lowering of charge finding efficiency, the thrust acceptance cut is fixed at :

$$cos\,\theta_c = 0.9 \tag{5.33}$$

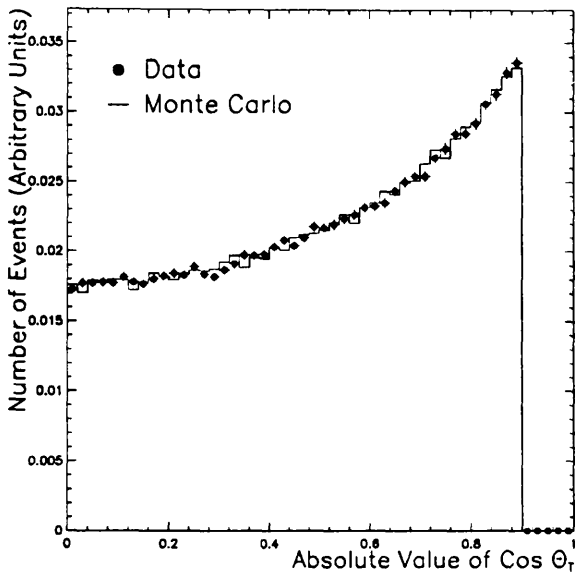

Figure 5.4: Absolute value, $\mid cos\,\theta_T \mid$, of the thrust axis angle in data and Monte Carlo.

where it rejects 8.1% of hadronic events. As a check, the behaviour of the measurable asymmetry in this region is studied using the variation of $\overline{Q_{FB}}$ as a function of $cos\,\theta_c$, described in section 6.3.

5.2.3 Selection of Hemispheres with $\geq$ 1 Track

The sample of events passing the hadronic event selection, and the additional cut on tracks below 200 MeV, includes a few events where all selected tracks lie within *one* hemisphere. The effect on $\overline{Q_{FB}}$ and its interpretation are minimal as such events are rare and arise in both data and Monte Carlo. Any changes in charge finding efficiency are incorporated into the separation factors from the Monte Carlo.

Charged multiplicity distributions of data and Monte Carlo are compared in figure 5.5 and show excellent agreement. The charge calculations in both hemispheres require that there is at least one selected charged track per hemisphere. This requirement excludes very few events in data ($1.8\,(\pm 0.1)\,\%$) and Monte Carlo ($1.6\,(\pm 0.1)\,\%$) indicating that the source of such events is understood.

Table 5.5 shows that any flavour dependence of the cuts on the thrust axis and minimum number of tracks per hemisphere is below the level of 10^{-3} and may be assumed negligible. Event rejection rates and selected event fractions for all flavours in data and Monte Carlo are summarised in table 5.6.

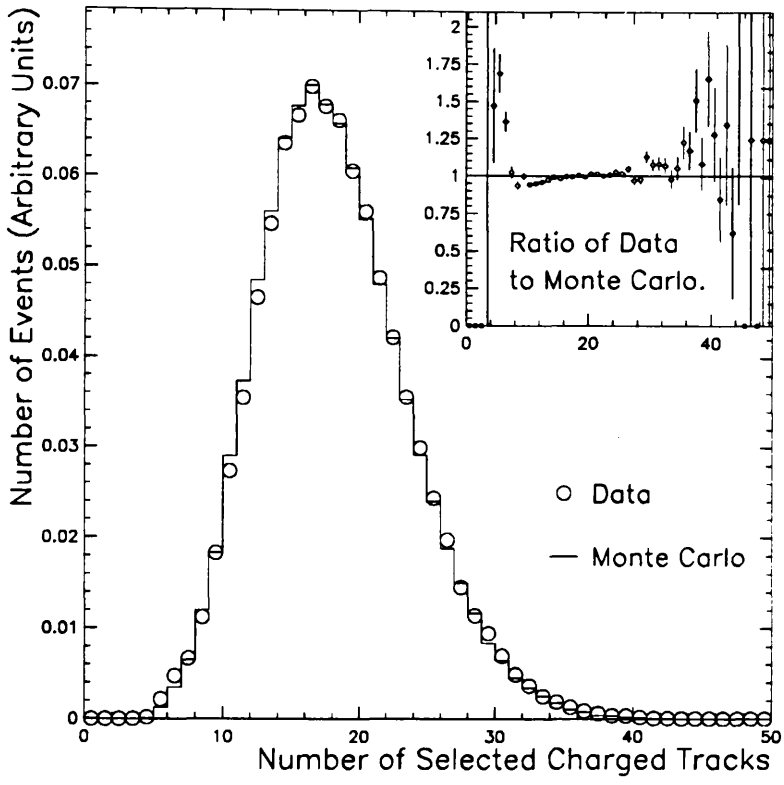

Selected charged multiplicities in data and Monte Carlo. The insert shows the ratio of data to Monte Carlo.

Figure 5.5: Charged multiplicity distributions for data and Monte Carlo after track selection.

Flavour	Thrust Axis Cut Rejection Rate	Minimum Track Cut Rejection Rate
u	$8.1\,(\pm 0.1)\%$	$0.17\,(\pm 0.02)\%$
d	$7.9\,(\pm 0.1)\%$	$0.19\,(\pm 0.02)\%$
s	$8.1\,(\pm 0.1)\%$	$0.23\,(\pm 0.02)\%$
c	$7.9\,(\pm 0.1)\%$	$0.15\,(\pm 0.02)\%$
b	$8.2\,(\pm 0.1)\%$	$0.04\,(\pm 0.01)\%$

Table 5.5: Event rejection statistics for the cuts on thrust angle and minimum number of tracks per hemisphere.

Event Statistics	Data	Monte Carlo
Thrust selection rejection rate	8.15 %	8.05 %
≥ 1 track per hemisphere rejection rate	0.13 %	0.14 %
Fraction of selected events	91.85 %	91.95 %

Table 5.6: Fractions of rejected and selected events used in the asymmetry analysis for data and Monte Carlo.

5.3 Summary

The method of charge flow allows the asymmetry of a combined quark sample to be measured from the shift of $\overline{Q_{FB}}$ from zero. This can be interpreted in terms of Standard Model couplings by use of Monte Carlo separation factors related to the degree of charge retention in each flavour channel. The combined separations are monitored in data and Monte Carlo using the difference in width of the Q and Q_{FB} distributions which serves as a sensitive test of the method.

The ALEPH hadronic event selection, based on charged tracks, is used to give a high efficiency and purity without introducing any flavour-dependent bias to the sample. Track and event selections are seen to agree closely between data and Monte Carlo.

Chapter 6

Charge Distributions and Separations

Q and Q_{FB} charge distributions are used to measure and interpret a forward-backward asymmetry. As interpretation of its magnitude relies upon Monte Carlo separations, comprehensive agreement with data is necessary. In addition, the observed behaviour of the asymmetry with angle and energy should follow that expected from quark pair production. The charge flow method includes the variable κ to govern the degree of emphasis given to to leading jet particles. Since its effect also depends on the fragmentation of individual flavours, κ may be used to optimise the accuracy of measured quantities and to reduce systematic contributions.

The purpose of this chapter is to present the results, taken from the charge distributions, which demonstrate the excellent agreement between data and Monte Carlo. These are given, with the methods sensitivity to an asymmetry, in section 6.1. The choice of longitudinal momentum weight (κ) is discussed in section 6.2 and the angular and energy dependence of $\overline{Q_{FB}}$ in sections 6.3 and 6.4. The asymmetry, measured using the complementary *"Classical" Method* of a fit to the angular distribution of positively charged jets, is described in section 6.5.

6.1 Charge Flow and Total Charge Distributions

As charge distributions vary with κ, comparing data and Monte Carlo over a wide range of values represents a valuable test. Important considerations for the study of systematic discrepancies between the two are : (a) how well charge distributions agree and (b) the values of $\bar{q}$ which are related to the quark separations for each flavour. The cancellation between jet charges of each hemisphere is visible in the mean Q of data and Monte Carlo and acts as a general check of the detector simulation.

As far as an asymmetry is concerned, it is the value of $\overline{Q_{FB}}$ which is of importance. The results from charge distributions of data and Monte Carlo are given in table 6.1 for a wide range of κ values. The value of $\overline{Q_{\mathrm{FB}}}$ in data is shown in figure 6.1 as a function of κ. This shows that a significant, non-zero charge flow, ($\overline{Q_{\mathrm{FB}}}$), is observed in data over the entire range of κ. The change in charge distributions as κ increases, is due to greater emphasis being placed on the track with highest longitudinal momentum in each hemisphere. A κ value of ∞ means that *only* the leading particles are used to determine the forward and backward charges. Thus, the charge flow tends to values around 0 and ± 2

Data						
κ	$\overline{Q_{FB}}$	$\Delta\overline{Q_{FB}}$ and $\Delta\sigma_{FB}$	σ_{FB}	$\overline{Q}$	$\Delta\bar{Q}$ and $\Delta\sigma_Q$	σ_Q
0.2	-0.0022	0.0008	0.335	0.00282	0.0006	0.264
0.3	-0.0029	0.0008	0.352	0.00262	0.0007	0.282
0.5	-0.0045	0.0010	0.410	0.00221	0.0008	0.342
0.7	-0.0061	0.0012	0.487	0.00183	0.0010	0.418
0.9	-0.0076	0.0014	0.568	0.00152	0.0012	0.496
1.0	-0.0084	0.0014	0.608	0.00140	0.0013	0.535
1.1	-0.0091	0.0015	0.646	0.00129	0.0014	0.572
1.4	-0.0109	0.0018	0.750	0.00108	0.0016	0.673
1.8	-0.0129	0.0021	0.861	0.00094	0.0019	0.783
2.3	-0.0146	0.0023	0.966	0.00088	0.0021	0.887
3.0	-0.0161	0.0026	1.066	0.00085	0.0024	0.988
6.0	-0.0181	0.0030	1.252	0.00077	0.0028	1.178
9.0	-0.0186	0.0032	1.318	0.00082	0.0030	1.246
14.0	-0.0190	0.0033	1.364	0.00106	0.0031	1.294
20.0	-0.0190	0.0033	1.388	0.00119	0.0032	1.320
∞	-0.0188	0.0035	1.446	0.00128	0.0033	1.381
Monte Carlo						
κ	$\overline{Q_{FB}}$	$\Delta\overline{Q_{FB}}$ and $\Delta\sigma_{FB}$	σ_{FB}	$\overline{Q}$	$\Delta\bar{Q}$ and $\Delta\sigma_Q$	σ_Q
0.2	-0.0049	0.0007	0.326	0.00573	0.0006	0.255
0.3	-0.0057	0.0007	0.343	0.00543	0.0006	0.275
0.5	-0.0074	0.0009	0.404	0.00478	0.0007	0.337
0.7	-0.0091	0.0010	0.484	0.00412	0.0009	0.414
0.9	-0.0106	0.0012	0.567	0.00354	0.0011	0.494
1.0	-0.0112	0.0013	0.608	0.00329	0.0011	0.533
1.1	-0.0119	0.0014	0.647	0.00307	0.0012	0.571
1.4	-0.0134	0.0016	0.752	0.00256	0.0014	0.673
1.8	-0.0148	0.0019	0.866	0.00216	0.0017	0.783
2.3	-0.0159	0.0021	0.970	0.00191	0.0019	0.887
3.0	-0.0167	0.0023	1.071	0.00169	0.0021	0.988
6.0	-0.0175	0.0027	1.257	0.00109	0.0025	1.177
9.0	-0.0176	0.0028	1.322	0.00072	0.0027	1.244
14.0	-0.0176	0.0029	1.368	0.00046	0.0028	1.292
20.0	-0.0177	0.0030	1.392	0.00045	0.0028	1.318
∞	-0.0180	0.0031	1.450	-0.00036	0.0030	1.377

Errors are statistical only, and measurements at different values of κ are highly correlated.

Table 6.1: Charge distribution parameters as a function of κ for data and Monte Carlo.

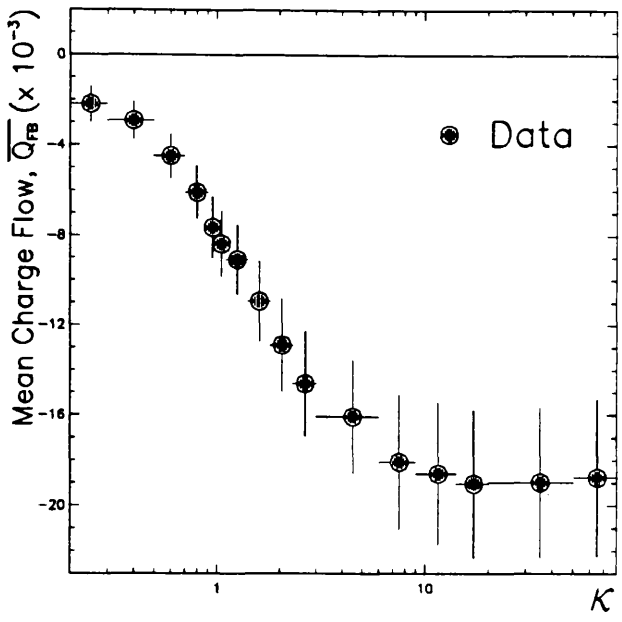

Figure 6.1: $\overline{Q_{\rm FB}}$ in data as a function of κ.

and the approximately Gaussian distribution at low κ takes on a more peaked appearance.

6.1.1 Comparison of Data and Monte Carlo

Examples of charge distributions are shown in figures 6.2 and 6.3. Studying the shape of these in more detail, the widths of Q and Q_{FB} distributions are shown as a function of κ in figure 6.4. Agreement between data and Monte Carlo is seen to be very close over a wide range of κ. Comparisons across the full range of κ values act as a severe test of the method and highlight any systematic discrepancy between data and Monte Carlo. Such discrepancies are seen to remain at a low level. They may be distinguished by the κ variation of sensitive quantities, such as $\bar{q}$, derived from relation (5.25) and calculated using charge distribution widths. The values of $\bar{q}(\kappa)$ for data and Monte Carlo are given in table 6.2 and plotted in figure 6.5. As shown, $\bar{q}$ displays a smooth variation with κ in data and Monte Carlo, rising steeply in the region $\kappa \approx 0.5 \rightarrow 9.0$ as the charge distributions change in shape. Data and Monte Carlo may be usefully compared using the quantity :

$$\alpha = \frac{\bar{q}_{data}}{\bar{q}_{mc}} \tag{6.1}$$

The observed values of α are also given in table 6.2 and plotted in figure 6.6 showing that the difference from unity varies smoothly between $+2.1\,(\pm 1.0)\%$ and $-6.0(\pm 4.4)\%$, depending on κ. Close to the value of $\kappa = 1$, agreement between data and Monte Carlo is better than $0.8\ (\pm 1.8)\,\%$. The variation of α with κ is significantly affected by correlated statistical errors between widths measured at each κ value.

The mean of the total charge distribution, $\bar{Q}$, is indicative of cancellation between

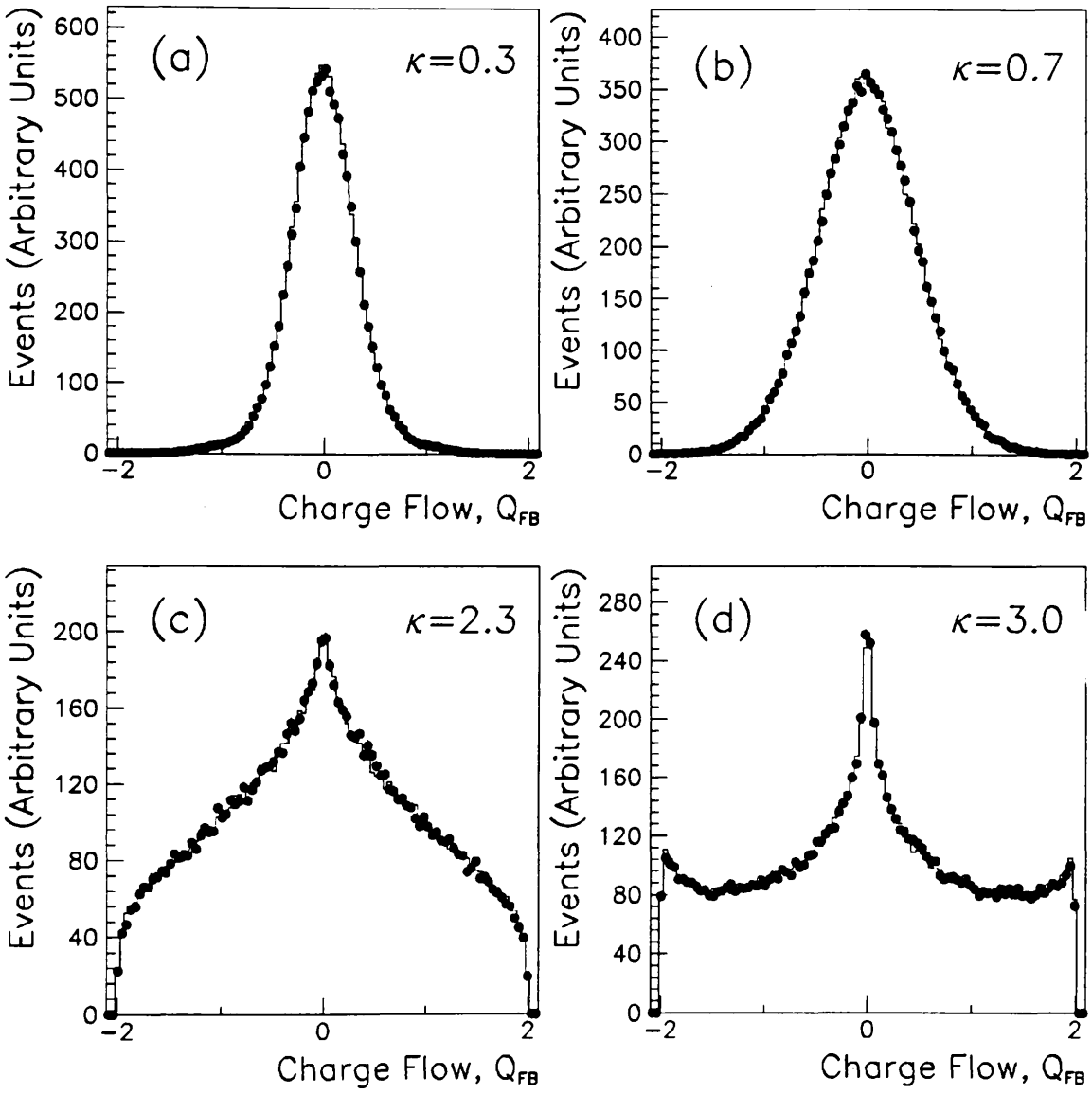

Data are represented by points with Monte Carlo as histograms. Figures (*a*) → (*d*) correspond to increasing κ values.

Figure 6.2: Q_{FB} distributions for different κ values in data and Monte Carlo.

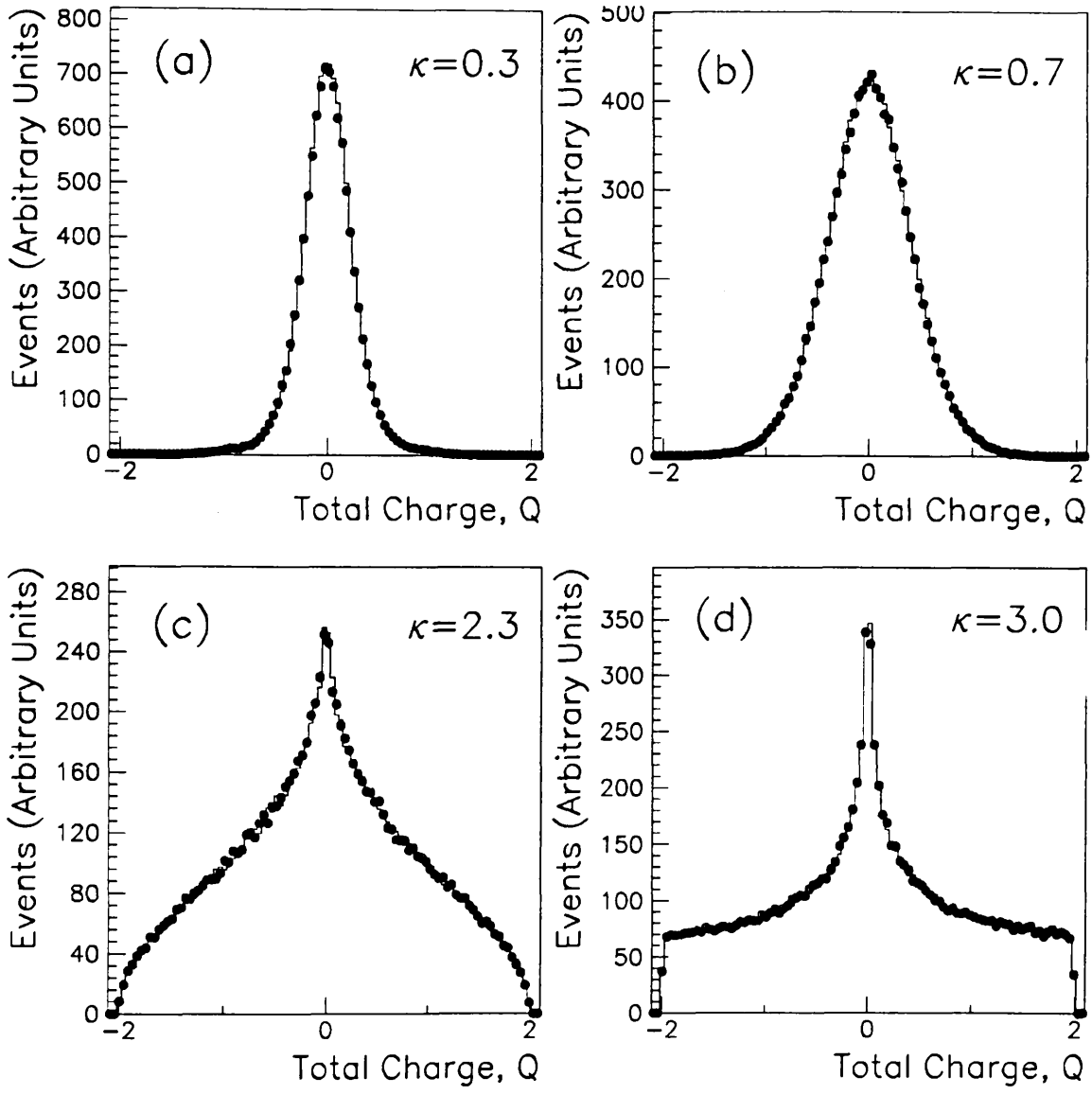

Data are represented by points with Monte Carlo as histograms. Figures (*a*) → (*d*) correspond to increasing κ values.

Figure 6.3: Q distributions for different κ values in data and Monte Carlo.

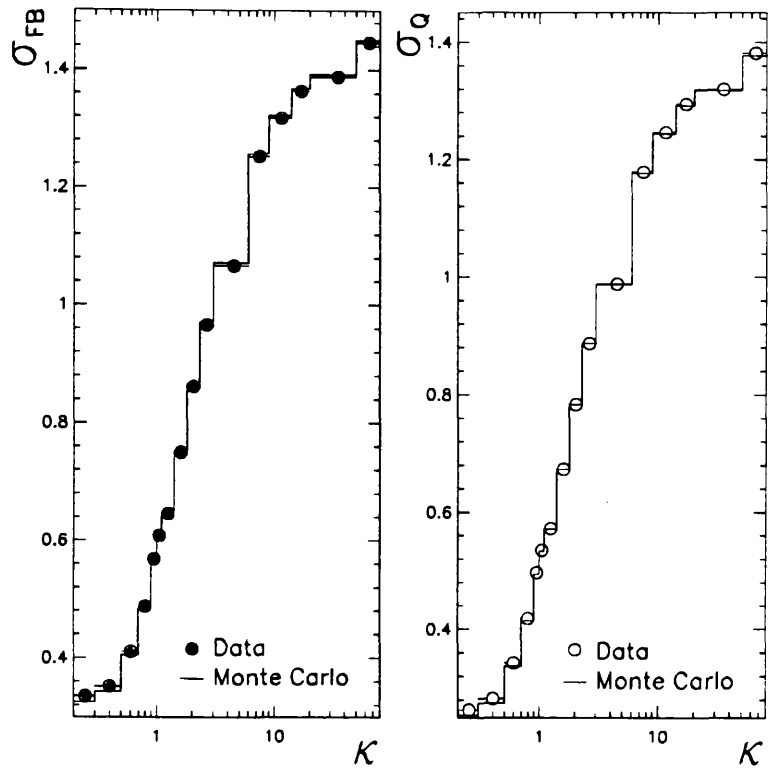

Charge distribution widths compared in data and Monte Carlo as a function of κ. Monte Carlo errors are approximately equivalent to data and remain smaller than the point size shown.

Figure 6.4: Individual charge distribution widths in data and Monte Carlo as a function of κ.

forward and backward regions of the detector. The variation of $\bar{Q}$ with κ shows the *degree* of cancellation in different momentum regions of jets and is shown in figure 6.7. The values of $\bar{Q}$ decrease in data and Monte Carlo at low κ where there are contributions from lower momentum particles. It becomes compatible with zero close to $\kappa = 1.0$. At low κ, $\bar{Q}$ in the data remains significantly smaller than in the Monte Carlo sample where a $> 1\,\sigma$ shift is observed in the region $\kappa \approx 0.2 \rightarrow 2.3$.

6.1.2 Quark Charge Separations

The charge flow method relies upon flavour dependent separations, q_f, to interpret the observed mean charge flow in terms of electroweak parameters. Separations are affected by the absolute value of the parent quark charge, characteristics of its fragmentation and dilution caused by the detector. For these reasons, it is necessary to extract them from a reconstructed Monte Carlo sample of events. As a result, the separations are subject to statistical[1] and systematic uncertainties.

The separations are determined from distinct charge flow distributions in the cases

[1]The sample used here consists of $(u, d, s, c, b) = (37169, 47491, 47488, 37501, 48006) = 217655$ events.

κ	$\bar{q}$ in Data	$\bar{q}$ in Monte Carlo	α
0.2	0.207 ($\pm$0.002)	0.203 ($\pm$0.002)	1.02 ($\pm$0.01)
0.3	0.210 ($\pm$0.002)	0.206 ($\pm$0.002)	1.02 ($\pm$0.01)
0.5	0.226 ($\pm$0.002)	0.223 ($\pm$0.002)	1.01 ($\pm$0.01)
0.7	0.250 ($\pm$0.003)	0.250 ($\pm$0.003)	1.00 ($\pm$0.02)
0.9	0.276 ($\pm$0.004)	0.278 ($\pm$0.003)	1.00 ($\pm$0.02)
1.0	0.289 ($\pm$0.004)	0.291 ($\pm$0.004)	0.99 ($\pm$0.02)
1.1	0.300 ($\pm$0.004)	0.304 ($\pm$0.004)	0.99 ($\pm$0.02)
1.4	0.330 ($\pm$0.005)	0.336 ($\pm$0.005)	0.98 ($\pm$0.02)
1.8	0.359 ($\pm$0.006)	0.394 ($\pm$0.006)	0.98 ($\pm$0.02)
2.3	0.382 ($\pm$0.008)	0.415 ($\pm$0.007)	0.97 ($\pm$0.03)
3.0	0.401 ($\pm$0.009)	0.417 ($\pm$0.008)	0.97 ($\pm$0.03)
6.0	0.424 ($\pm$0.012)	0.441 ($\pm$0.010)	0.96 ($\pm$0.04)
9.0	0.428 ($\pm$0.013)	0.447 ($\pm$0.011)	0.96 ($\pm$0.04)
14.0	0.429 ($\pm$0.014)	0.449 ($\pm$0.012)	0.96 ($\pm$0.04)
20.0	0.429 ($\pm$0.014)	0.449 ($\pm$0.012)	0.96 ($\pm$0.04)
∞	0.428 ($\pm$0.016)	0.455 ($\pm$0.013)	0.94 ($\pm$0.04)

Table 6.2: Values for $\bar{q}$ and α as a function of κ.

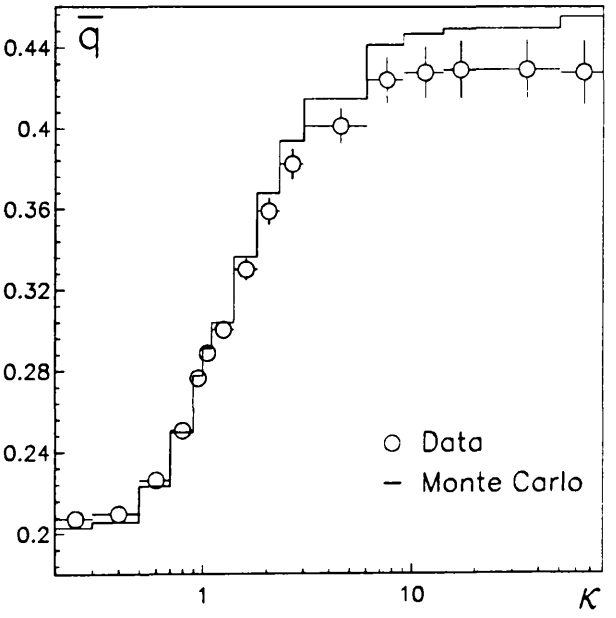

Dependence of $\bar{q}$ on κ for data and Monte Carlo. Statistical errors of data and Monte Carlo are approximately equivalent.

Figure 6.5: Variation of $\bar{q}$ with κ in data and Monte Carlo.

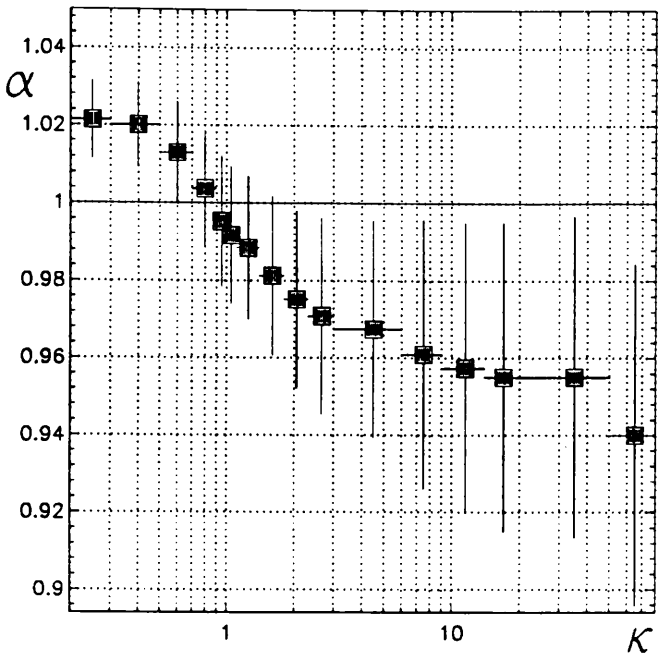

Figure 6.6: Variation of α with κ.

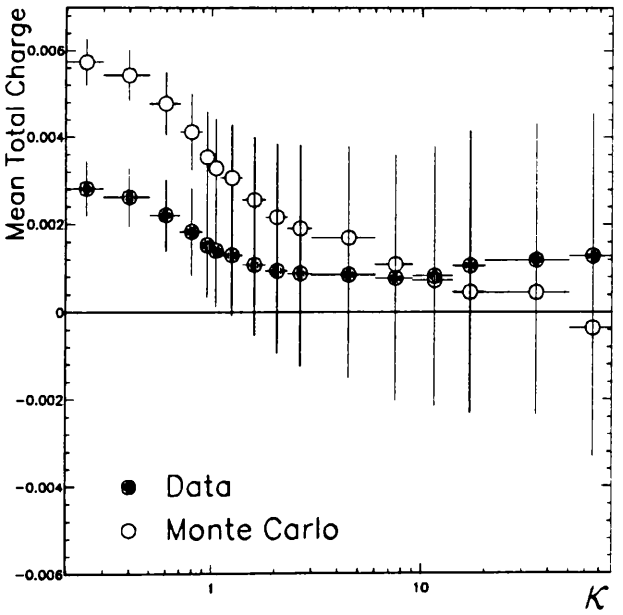

Figure 6.7: Variation of the mean total charge, $\bar{Q}$, in data and Monte Carlo.

where *either* the parent quark travels forward *or* backwards. Examples of these are shown previously for $u\bar{u}$ events in figure 5.2. As the magnitudes of separations from quarks and antiquarks are degenerate[2] it is possible to take the mean value of q_f and $q_{\bar{f}}$ as *the* separation for a given flavour.

The magnitudes of separations are κ dependent, leading to the observed rise in $|\overline{Q_{\rm FB}}|$ as κ increases. Separations for all flavours are shown in table 6.3. Individual separations

	Quark Flavour									
Kappa	u	Err.	d	Err.	s	Err.	c	Err.	b	Err.
0.20	0.210	0.002	0.120	0.002	0.129	0.002	0.162	0.002	0.103	0.001
0.30	0.238	0.002	0.133	0.002	0.149	0.002	0.166	0.002	0.118	0.001
0.50	0.295	0.002	0.157	0.002	0.190	0.003	0.171	0.002	0.148	0.002
0.70	0.350	0.002	0.180	0.002	0.230	0.003	0.173	0.002	0.178	0.002
0.90	0.399	0.003	0.199	0.002	0.267	0.004	0.172	0.003	0.204	0.002
1.00	0.422	0.003	0.208	0.003	0.283	0.004	0.171	0.003	0.217	0.002
1.10	0.442	0.003	0.216	0.003	0.299	0.004	0.170	0.003	0.228	0.003
1.40	0.492	0.004	0.235	0.003	0.337	0.005	0.165	0.004	0.257	0.003
1.80	0.540	0.004	0.253	0.004	0.374	0.006	0.160	0.004	0.284	0.004
2.30	0.578	0.005	0.266	0.004	0.403	0.006	0.154	0.005	0.306	0.004
3.00	0.609	0.005	0.277	0.005	0.427	0.008	0.151	0.005	0.323	0.005
6.00	0.650	0.006	0.291	0.006	0.456	0.008	0.148	0.006	0.343	0.006
9.00	0.659	0.006	0.295	0.006	0.459	0.008	0.149	0.007	0.347	0.006
14.00	0.664	0.007	0.297	0.006	0.460	0.008	0.149	0.007	0.349	0.006
20.00	0.666	0.007	0.299	0.006	0.460	0.008	0.149	0.007	0.350	0.006
∞	0.669	0.007	0.302	0.006	0.465	0.008	0.148	0.007	0.352	0.006

Table 6.3: Individual flavour separation factors as a function of κ.

are plotted in figure 6.8 showing the asymptotic behaviour as κ increases. Statistical errors lead to a combined statistical contribution of less than 2% on the expected value of $\overline{Q_{\rm FB}}$ from the Monte Carlo separations alone.

Using the separations of table 6.3, it is possible to check the extent to which relation (5.26) is valid in the Monte Carlo. $\bar{q}$ is approximated by the sum of separations squared, weighted by quark branching fractions, while the asymmetry is proportional to $\overline{Q_{FB}}$ which may be written in terms of a linear summation ($\propto \sum_{f=u\ldots}^{b} q_f a_f v_f$) Hence, it is of interest to study the relation between $\bar{q}$ and $\sum_{f=u\ldots}^{b} q_f a_f v_f$ as it is only $\bar{q}$ which is determined in both data and Monte Carlo. The observed value of $\bar{q}$ is compared with that expected in table 6.4. It is found that $\bar{q}$ is $\sim 8\%$ larger than the relation (5.26) would predict although changes in both $\sum_{f=u\ldots}^{b} q_f a_f v_f$ and $\sqrt{\sum_f q_f^2 \frac{\Gamma_f}{\Gamma_{had}}}$ are followed by corre-

[2]This has been verified in the Monte Carlo for all flavours and all κ.

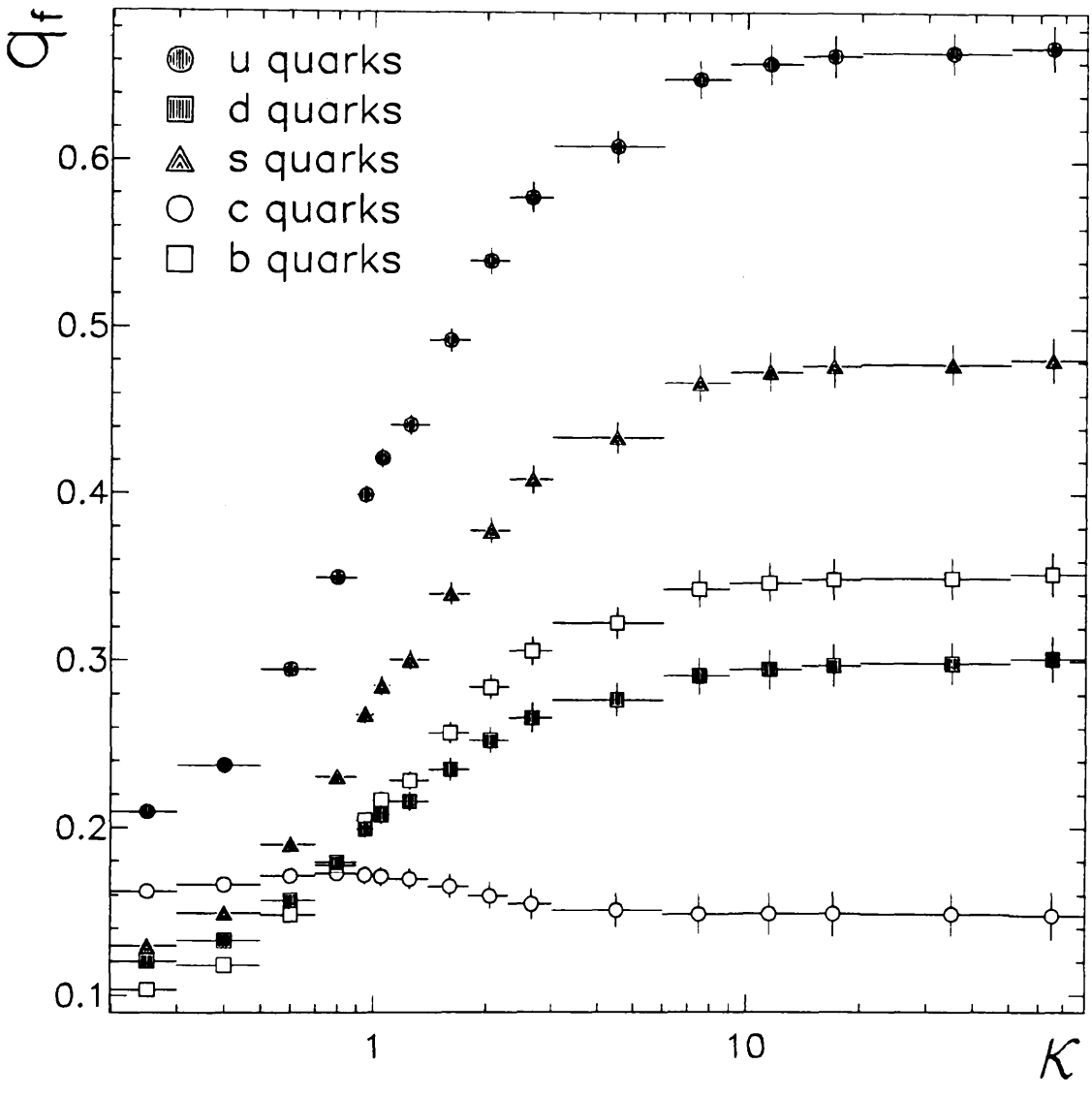

Quark separations for a range of κ values in the Monte Carlo, calculated using the mean of q_f and $q_{\bar{f}}$ separations.

Figure 6.8: Quark separations as a function of κ.

κ	$\bar{q}$	$\Delta\bar{q}$	$\sum_f q_f a_f v_f$	$\frac{\bar{q}}{\sum_f q_f a_f v_f}$	$\sqrt{\sum_f q_f^2 \frac{\Gamma_f}{\Gamma_{had}}}$	$\frac{\bar{q}}{\sqrt{\sum_f q_f^2 \frac{\Gamma_f}{\Gamma_{had}}}}$
0.2	0.203	0.001	0.112	1.81 ($\pm$0.01)	0.146	1.39 ($\pm$0.01)
0.3	0.206	0.002	0.135	1.52 ($\pm$0.01)	0.162	1.27 ($\pm$0.01)
0.5	0.223	0.002	0.184	1.21 ($\pm$0.01)	0.195	1.14 ($\pm$0.01)
0.7	0.250	0.002	0.234	1.07 ($\pm$0.01)	0.227	1.10 ($\pm$0.01)
0.9	0.278	0.003	0.280	0.99 ($\pm$0.01)	0.257	1.08 ($\pm$0.01)
1.0	0.291	0.003	0.302	0.97 ($\pm$0.01)	0.270	1.08 ($\pm$0.01)
1.1	0.304	0.004	0.321	0.94 ($\pm$0.01)	0.282	1.08 ($\pm$0.01)
1.4	0.336	0.005	0.372	0.90 ($\pm$0.01)	0.313	1.08 ($\pm$0.02)
1.8	0.368	0.006	0.421	0.87 ($\pm$0.01)	0.342	1.08 ($\pm$0.02)
2.3	0.394	0.007	0.460	0.86 ($\pm$0.01)	0.366	1.08 ($\pm$0.02)
3.0	0.415	0.008	0.491	0.84 ($\pm$0.02)	0.385	1.08 ($\pm$0.02)
6.0	0.441	0.010	0.528	0.84 ($\pm$0.02)	0.410	1.08 ($\pm$0.03)
9.0	0.447	0.011	0.536	0.83 ($\pm$0.02)	0.415	1.08 ($\pm$0.03)
14.0	0.449	0.012	0.540	0.83 ($\pm$0.02)	0.418	1.07 ($\pm$0.03)
20.0	0.449	0.012	0.542	0.83 ($\pm$0.02)	0.420	1.07 ($\pm$0.03)
∞	0.455	0.013	0.548	0.83 ($\pm$0.02)	0.422	1.08 ($\pm$0.03)

Table 6.4: Comparison of simulated values of $\bar{q}$ and those expected from the relation (5.26).

sponding shifts in $\bar{q}$. Above $\kappa \sim 0.9$, the ratios of $\bar{q}$ to $\sum_{f=u,\ldots}^{b} q_f a_f v_f$ and $\sqrt{\sum_f q_f^2 \frac{\Gamma_f}{\Gamma_{had}}}$ stabilise even though their values almost double in the region $\kappa \approx 0.9 \rightarrow \infty$. Thus, $\bar{q}$ is a sensitive check of the combined magnitude of separations in data and Monte Carlo.

6.1.3 Sensitivity of the Method

The sensitivity of the charge flow method is expressed by comparing the expected value of $\overline{Q_{\rm FB}^{ref}}$ with the inherent measurement error, proportional to $\sigma_{\rm FB}$. The quantity is proportional to the number of statistical standard deviations with which an asymmetry is measured and is κ dependent. The *sensitivity* is defined by the ratio :

$$\mathcal{S} \equiv \text{Sensitivity} = \frac{\overline{Q_{\rm FB}^{ref}}}{0.033 \times \sigma_{\rm FB}} \tag{6.2}$$

where $\overline{Q_{\rm FB}^{ref}}$ is the expected mean charge flow determined using theoretical branching fractions, asymmetries and Monte Carlo separations. The sensitivities in generated and reconstructed Monte Carlo samples are given in table 6.5 and shown in figure 6.9 as functions of κ. The curves of figure 6.9 show a well defined position of optimum sensitivity

κ	Generator Level Sensitivity		Reconstructed Level Sensitivity	
0.2	0.370	($\pm$0.004)	0.344	($\pm$0.001)
0.3	0.422	($\pm$0.004)	0.393	($\pm$0.001)
0.5	0.484	($\pm$0.004)	0.455	($\pm$0.001)
0.7	0.512	($\pm$0.004)	0.483	($\pm$0.002)
0.9	0.523	($\pm$0.004)	0.494	($\pm$0.002)
1.0	0.525	($\pm$0.004)	0.496	($\pm$0.002)
1.1	0.526	($\pm$0.004)	0.497	($\pm$0.002)
1.4	0.524	($\pm$0.004)	0.495	($\pm$0.002)
1.8	0.516	($\pm$0.004)	0.486	($\pm$0.003)
2.3	0.504	($\pm$0.004)	0.474	($\pm$0.003)
3.0	0.488	($\pm$0.004)	0.458	($\pm$0.003)
6.0	0.449	($\pm$0.004)	0.420	($\pm$0.003)
9.0	0.432	($\pm$0.004)	0.405	($\pm$0.003)
14.0	0.420	($\pm$0.004)	0.395	($\pm$0.003)
20.0	0.413	($\pm$0.004)	0.389	($\pm$0.003)
∞	0.398	($\pm$0.004)	0.378	($\pm$0.003)

Table 6.5: Sensitivities of the charge flow method as a function of κ.

around a κ value of 1.0. The small difference between σ_{FB} values at low κ in data and Monte Carlo from table 6.1 does not affect the optimum position. Dramatic changes in sensitivity as a function of κ are due to charge and fragmentation characteristics of different jet flavours. Each flavour behaves differently so that figure 6.9 reflects a compromise where, *on average*, a measurement is most accurate.

Sensitivities of individual flavours are shown in figure 6.10. This shows that all flavours, with the exception of c quarks, have extreme sensitivities around $\kappa \sim 0.5 \rightarrow 0.7$ while the c quark sensitivity decreases monotonically in absolute value.

The existence of a position of optimal sensitivity indicates that there is a specific degree of resolution, for each flavour, where the charge information of jet fragments is most clearly defined on average. If higher or lower κ values are used then the relative accuracy with which that information can be extracted is reduced. The flavour sensitivities of figure 6.10 suggest that the optimal sensitivity for all flavours at $\kappa = 1.0$ is largely due to *cancellation* between quark types.

6.2 Method Dependence on κ

The charge flow method can use one, or more, κ values. The choice between the two alternatives depends largely on method systematics since a statistically significant asym-

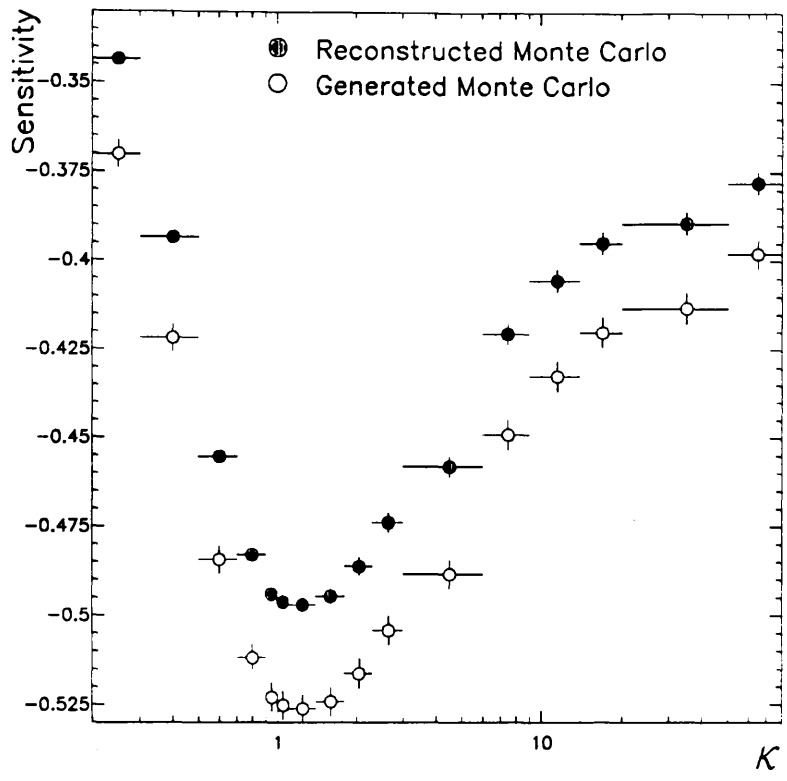

Figure 6.9: Method sensitivity as a function of κ for Monte Carlo at generator and reconstructed levels.

metry is observed for all κ. If a range of values is used, then the considerable correlations between measurements must be taken into account when evaluating the statistical error of results. Systematic errors are harder to quantify over a range of values. This is because the characteristics of measurements vary greatly between high and low κ. This section outlines the quantitative and qualitative argument for preferring a particular κ value.

6.2.1 Optimal Choice of κ

Extracting results from a single κ value of $\overline{Q_{FB}}$ benefits from allowing systematic effects to be studied and minimised at one point. Further considerations for selecting a particular κ value are :

(a) The absolute sensitivity of the method increases rapidly in the κ range $0.2 \rightarrow 1.0$ and decreases thereafter. The increase in relative accuracy of a charge flow measurement at $\kappa = 1.0$, relative to values close to 0 and ∞, is of the order of 40%.

(b) Qualitatively, it is preferable to avoid low values of κ where charge retention depends to a greater degree on lower momentum tracks. In this region jet-jet correlations increase (see table 4.2) and contributions from particle creation in detector material are likely to be more significant.

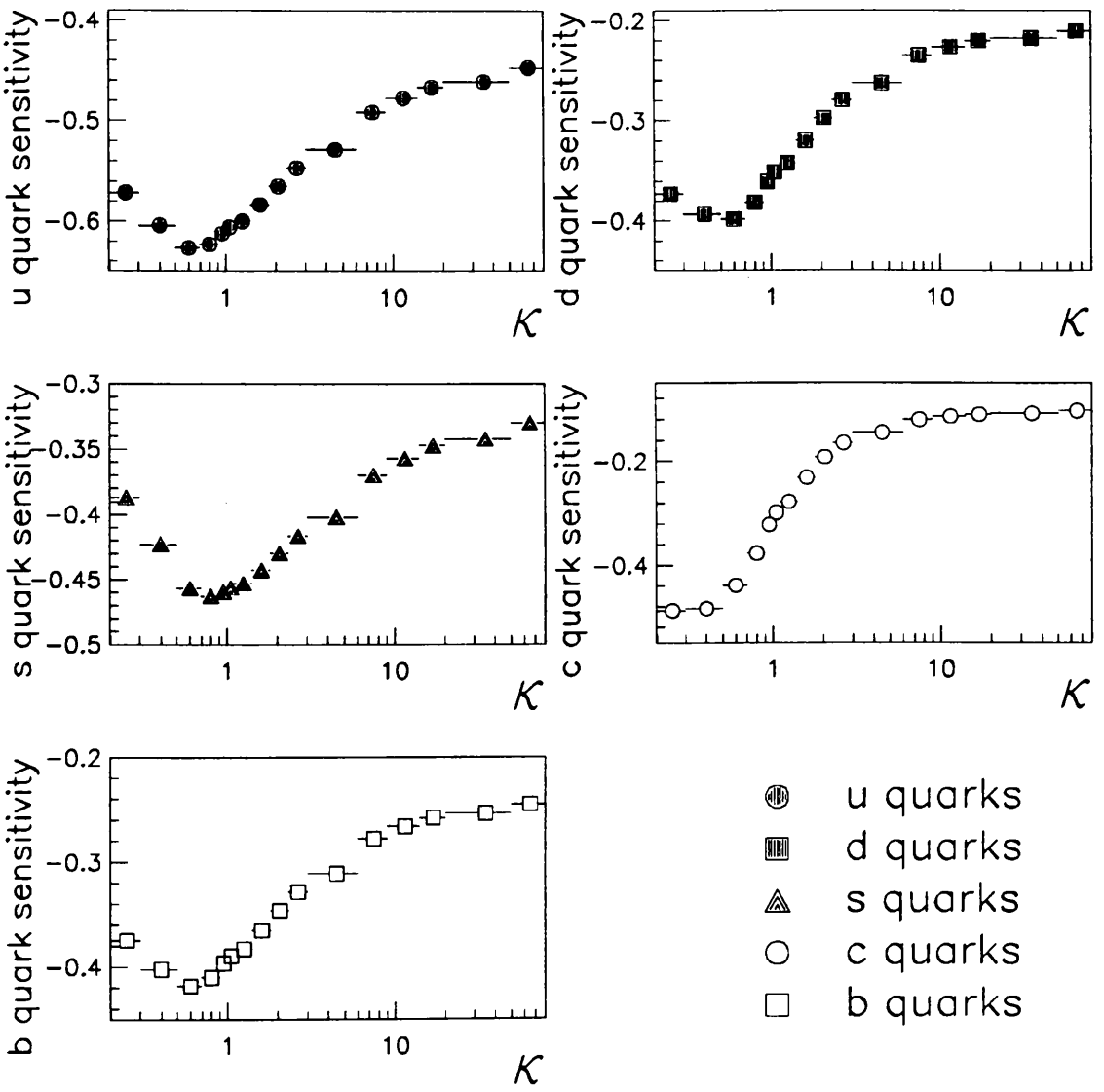

Different vertical scales are used throughout to emphasise the behaviour of individual flavours.

Figure 6.10: Sensitivities of individual flavours as functions of κ.

A κ value of 1.0 is selected here, largely as the point of optimum sensitivity of $\overline{Q_{FB}}$ for all flavours. In ALEPH, detector systematics are seen to be small so that (a) above is more important than (b) as it reduces the dominant (statistical) uncertainty by a large fraction.

At this position, the measured value of $\overline{Q_{FB}}$ in data is :

$$\overline{Q_{FB}} = -0.0084 \underbrace{(\pm 0.0014)}_{stat.} \tag{6.3}$$

6.2.2 Correlations Between Measurements

The correlation between two different $\overline{Q_{\mathrm{FB}}}$ measurements, at separate κ values, is estimated from their distribution formed in the $[Q_{\mathrm{FB}}(\kappa_1), Q_{\mathrm{FB}}(\kappa_2)]$ plane. For example, figure 6.11 shows correlations between measurements at κ values of 1.8 and 2.3. This

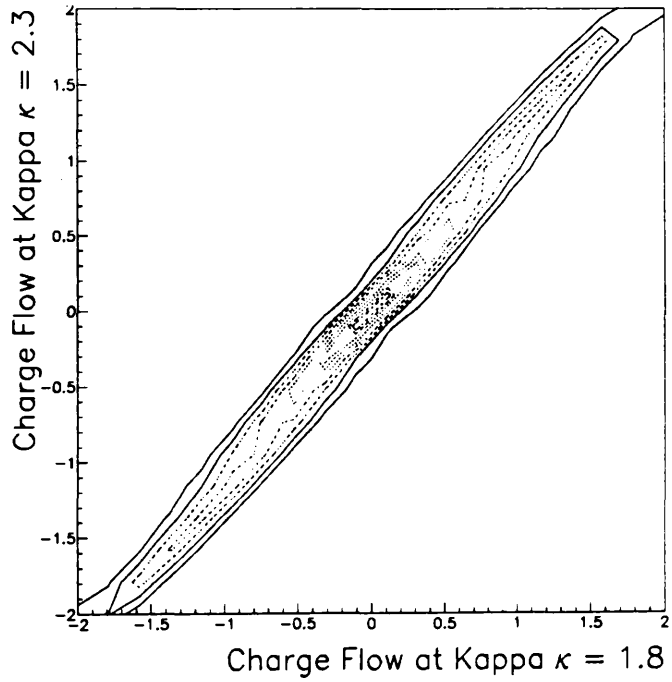

Figure 6.11: Correlation between charge flow measurements at different κ values.

shows that the correlation coefficient is close to unity. The correlation coefficient, ρ, is calculated for measurements using :

$$\rho\left[\overline{Q_{\mathrm{FB}}}(\kappa_1), \overline{Q_{\mathrm{FB}}}(\kappa_2)\right] = \frac{cov\left[Q_{\mathrm{FB}}(\kappa_1), Q_{\mathrm{FB}}(\kappa_2)\right]}{var\left[Q_{\mathrm{FB}}(\kappa_1), Q_{\mathrm{FB}}(\kappa_2)\right]} \tag{6.4}$$

with the resulting correlation matrices shown in table 6.6 for data and in table 6.7 for Monte Carlo. These matrices could be used in the calculation of physical parameters with a range of κ, as many correlation terms are large and lead to significant modifications to statistical errors at a single κ.

κ	0.30	0.70	1.00	1.40	2.30	6.00	14.0	∞
0.30	1.00	0.91	0.82	0.75	0.66	0.55	0.51	0.49
0.70	0.91	1.00	0.98	0.95	0.88	0.77	0.72	0.68
1.00	0.82	0.98	1.00	0.99	0.94	0.84	0.79	0.75
1.40	0.75	0.95	0.99	1.00	0.98	0.90	0.86	0.81
2.30	0.66	0.88	0.94	0.98	1.00	0.96	0.92	0.87
6.00	0.55	0.77	0.84	0.90	0.96	1.00	0.99	0.94
14.00	0.51	0.72	0.79	0.86	0.92	0.99	1.00	0.96
∞	0.49	0.68	0.75	0.81	0.87	0.94	0.96	1.00

Table 6.6: Correlation matrix for data at different κ values.

κ	0.30	0.70	1.00	1.40	2.30	6.00	14.0	∞
0.30	1.00	0.90	0.83	0.75	0.66	0.56	0.51	0.49
0.70	0.90	1.00	0.99	0.95	0.87	0.77	0.72	0.69
1.00	0.83	0.99	1.00	0.99	0.94	0.85	0.80	0.76
1.40	0.75	0.95	0.99	1.00	0.98	0.90	0.86	0.82
2.30	0.66	0.87	0.94	0.98	1.00	0.96	0.92	0.88
6.00	0.56	0.77	0.85	0.90	0.96	1.00	0.99	0.94
14.00	0.51	0.72	0.80	0.86	0.92	0.99	1.00	0.96
∞	0.49	0.69	0.76	0.82	0.88	0.94	0.96	1.00

Table 6.7: Correlation matrix for Monte Carlo at different κ values.

6.3 Angular Dependence of $\overline{Q_{FB}}$

The angular dependence of $\overline{Q_{FB}}$ is the difference between differential cross-sections in forward and backward regions given in section 5.1.5. It is possible to detect an electroweak asymmetry using a fit to the angular distribution of $\overline{Q_{FB}}$ which should be compatible with the integrated values of table 6.1. The fit is carried out in the $cos\,\theta$ range of $0 \rightarrow cos\,\theta_c$ using the function :

$$\begin{aligned} \frac{d\overline{Q_{FB}}}{dcos\,\theta} &= 2\,\frac{cos\,\theta}{1+cos^2\theta}\,\frac{\mathcal{A}_e}{\Gamma_{had}}\sum_{f=u\ldots}^{b} q_f \mathcal{A}_f \Gamma_f \\ &= \left[\frac{8}{3}\sum_{f=u\ldots}^{b} q_f\, A_{FB}^f\right]\frac{cos\,\theta}{1+cos^2\theta} \end{aligned} \tag{6.5}$$

where the fitted coefficient ($\frac{8}{3}\sum_{f=u\ldots}^{b} q_f A_{FB}^f$) is related to the integrated charge flow ($\overline{Q_{FB}}$) after it has been corrected for acceptance. The measured angular distribution of $\overline{Q_{FB}}$ is shown in figure 6.12 with the prediction from (6.5) and a κ of 1.0. This shows that

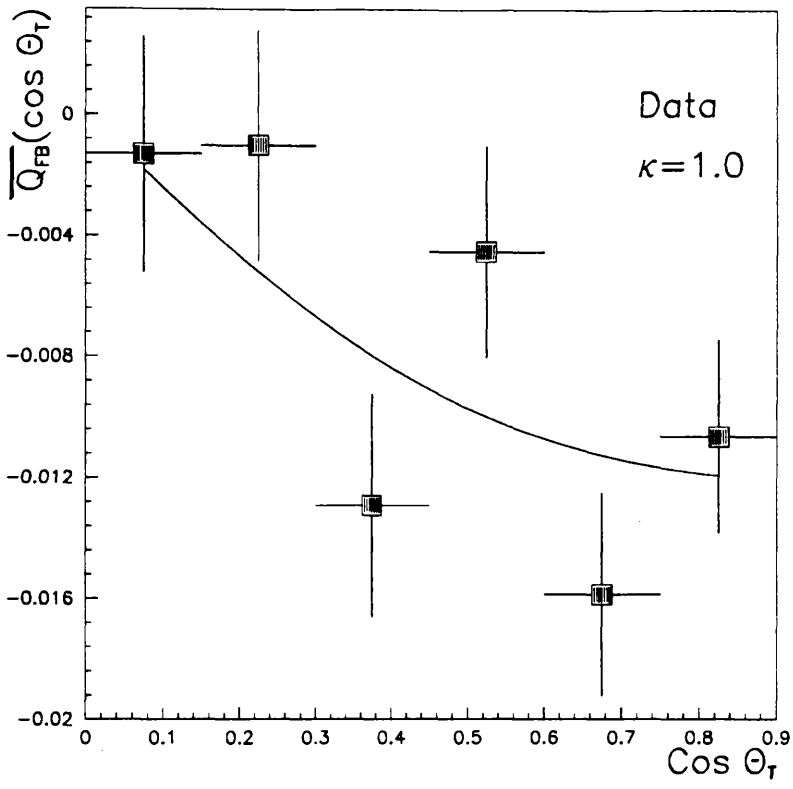

Figure 6.12: Angular dependence of $\overline{Q_{FB}}$ in data for a κ value of 1.0.

the data display the expected behaviour as $\overline{Q_{FB}}$ increases with thrust angle, $cos\,\theta_T$, and yields a full-acceptance charge flow of $-0.0158\,(\pm 0.0026)$ comparable to the acceptance corrected value of $-0.0162\,(\pm 0.0028)$ from integrated measurements.

The definition of maximum thrust angle at which an event is accepted is crucial for an asymmetry measurement as the cut is in a region where an asymmetry is greatest. Conversely, it is the region where losses and degradation of track resolution are most likely. These affect the charge flow method in different ways depending on which method of extracting $\overline{Q_{FB}}$ is used.

(i) In an *integrated* measurement, systematic changes to the direction of the thrust axis at low angles have little effect on extracted parameters since the behaviour is modelled accurately in Monte Carlo and included in the charge separations.

(ii) In a *fit* to the angular distribution, separations are assumed *independent* of angle. This is true within the current statistical accuracy, but may introduce small systematic losses of charge retention close to the beam (see figure 4.14) where an asymmetry in concentrated.

The two techniques are investigated in this region by varying the cut, $cos\,\theta_c$, and comparing results. These are shown in table 6.8. Taking into account the increase in the number of selected events with $cos\,\theta_c$, the two methods remain consistent. This gives confidence

$cos\,\theta_c$	Fitted $\overline{Q_{FB}}\,\vert^{1.0}$	Integrated $\overline{Q_{FB}}\,\vert^{1.0}$
0.80	$-0.0164\,(\pm 0.0031)$	$-0.0160\,(\pm 0.0032)$
0.85	$-0.0164\,(\pm 0.0029)$	$-0.0161\,(\pm 0.0029)$
0.90	$-0.0162\,(\pm 0.0028)$	$-0.0158\,(\pm 0.0026)$
0.95	$-0.0170\,(\pm 0.0027)$	$-0.0170\,(\pm 0.0026)$
1.00	$-0.0164\,(\pm 0.0026)$	$-0.0161\,(\pm 0.0026)$

Table 6.8: Variation of fitted and integrated $\overline{Q_{FB}}$ measurements at $\kappa = 1.0$ for different values of the maximum thrust angle cut $cos\,\theta_c$. Integrated values are corrected for acceptance.

that changes to the thrust direction within the angular binning of figure 6.12 are small and that separations do not vary significantly in this region.

6.4 Energy Dependence of $\overline{Q_{FB}}$

In the period Autumn 1989 → Autumn 1990 a total of 190,656 hadronic Z^o decays were collected by ALEPH and selected for analysis using the criteria of section 5.2. The distribution of events over the eleven individual energy points scanned by LEP is shown in figure 6.13. The $\frac{1}{\sqrt{N}}$ behaviour of the statistical error on a charge flow measurement makes it impractical to determine $\overline{Q_{FB}}$ for each LEP energy due to the size of error at some energies. Monte Carlo events are generated largely at the peak energy. The dependence of Monte Carlo separations on energy has been investigated and found to be entirely negligible[3].

The combined electroweak asymmetry is expected to decrease in absolute magnitude from below the peak to energies above it. Events from different energies are combined with the average energy calculated from the weighted average :

$$E_{combined} = \frac{\sum_{i=1\ldots}^{N_p} N_i^{events} E_i}{\sum_{i=1\ldots}^{N_p} N_i^{events}} \text{ for energy points } i = 1 \ldots N_p \qquad (6.6)$$

This is permissible, as A_{FB} varies almost linearly over the relatively small range of energies studied, and is carried out for the ALEPH 1989 → 1990 data sample where events are combined into three separate energy points. These are *"below"*, *"on"* and *"above"* the LEP peak running position, shown in table 6.9 with their mean energies. The resulting charge distribution parameters for the three points are given in table 6.10 with $\overline{Q_{FB}}$ values shown in figure 6.14. Figure 6.14 shows that the asymmetry increases with energy for all κ. Higher κ values give rise to larger values of $\overline{Q_{FB}}$, but with larger statistical uncertainties due to the increasing width of the Q_{FB} distribution.

[3]This is checked at the generator level and any dependence is found to be below the statistical uncertainty on $\sum_{f=u\ldots}^{b} q_f a_f v_f$ of 8×10^{-3}.

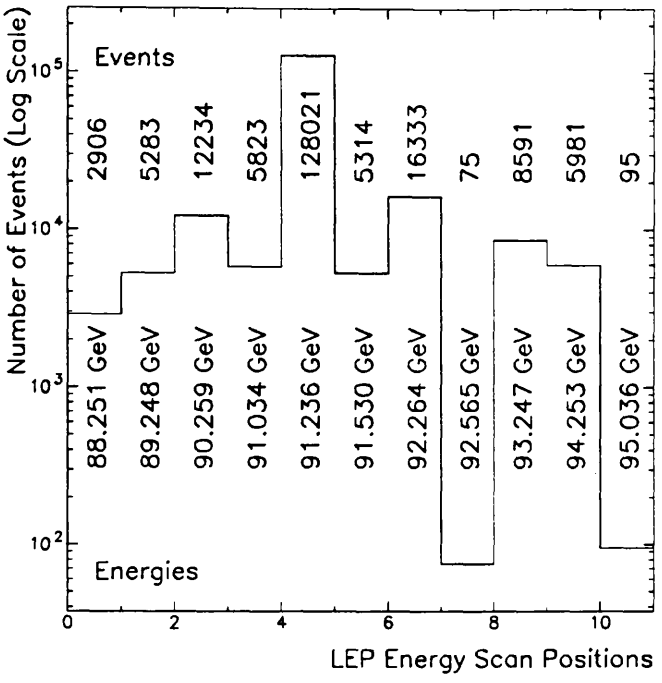

Figure 6.13: Distribution of data events with LEP running energy.

Mean Energy	Number of Hadronic Events	Selected Events
89.76 GeV	20423	18672
91.30 GeV	139158	127775
92.97 GeV	31075	28416

Selected events represent hadronic events which subsequently passed both the cut on the angle of the thrust axis and the requirement of having a minimum of one track per hemisphere.

Table 6.9: Event and energy statistics for three combined energy points.

Energy	$\overline{Q_{FB}}$	σ_{FB}	$\overline{Q}$	σ_Q	$\bar{q}$
89.76 GeV	$-0.0178(\pm 0.0044)$	0.607	$-0.0053(\pm 0.0039)$	0.532	$0.293(\pm 0.012)$
91.30 GeV	$-0.0086(\pm 0.0017)$	0.608	$+0.0024(\pm 0.0015)$	0.536	$0.287(\pm 0.005)$
92.97 GeV	$-0.0013(\pm 0.0036)$	0.608	$+0.0015(\pm 0.0032)$	0.533	$0.291(\pm 0.010)$

All numbers are for a κ value of 1.0.

Table 6.10: Charge distribution parameters for three combined energy points.

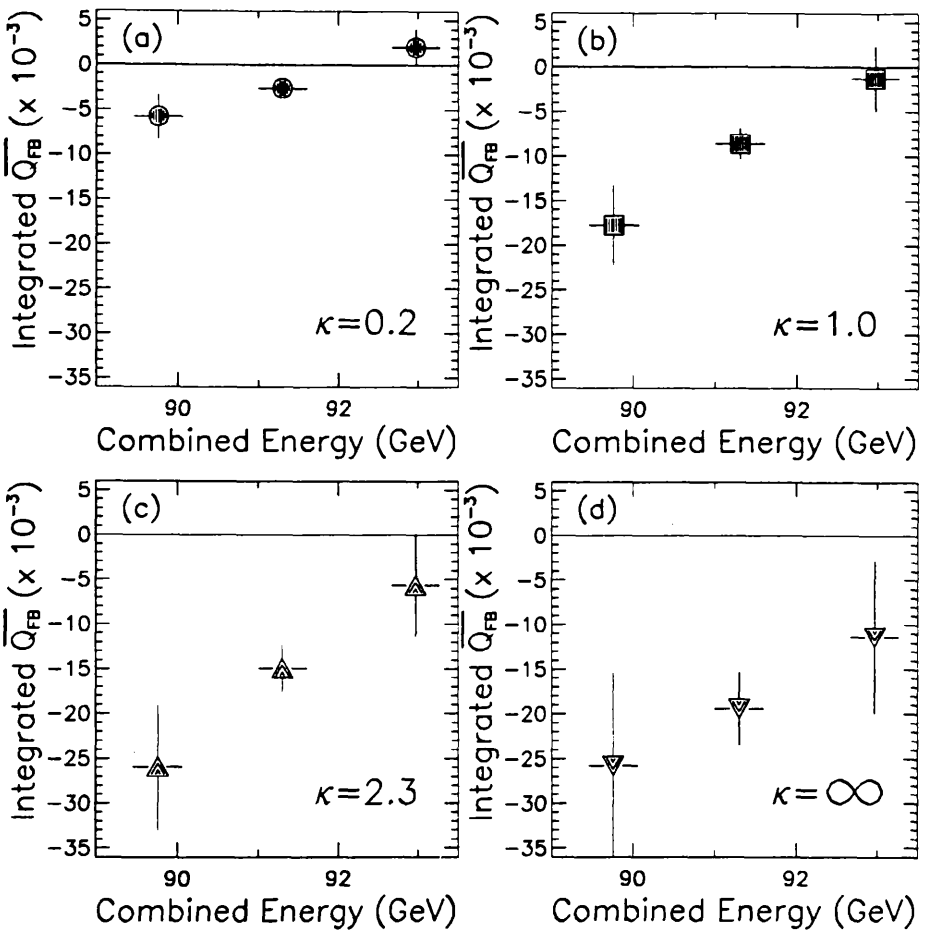

Figure 6.14: Measured variation of $\overline{Q_{FB}}$ with energy using data at three combined energy points and different κ values.

6.5 The Classical Method

The "Classical Method" of calculating forward backward asymmetries refers to the previously used technique [10] [34] of using single jet or hemisphere charges. An asymmetry is extracted by either counting the numbers of positive and negative jets moving forward and backward or performing a fit to the angular distribution of positively charged jets. The presence of substantial charge misidentification is taken into account using *dilution factors* for each flavour. The purpose of this section is both to demonstrate the applicability of the method to ALEPH data and to complement the results of the charge flow technique. The method is implemented with the same selection of tracks and events and the identical weighted charge summation based around the thrust axis.

6.5.1 Opposite Sign Events and Charge Efficiencies

The probability for correctly determining the sign of a parent quark charge is embodied in the charge finding efficiency[4]. This quantity, E_C, depends on the event flavour, κ and whether events with like or oppositely signed jets are selected. The combined charge finding efficiency ie. for all flavours, is found to be optimal around $\kappa \approx 0.3 \rightarrow 0.5$. This differs from the charge flow method as only single hemispheres are considered and the charge finding is optimised, rather than the sensitivity to $\overline{Q_{FB}}$ used previously. The fraction of asymmetry which remains after charge misidentification is calculated using dilution factors, D_f, for each flavour to be :

$$\begin{aligned} (A_{FB})_{observed} &= \sum_{f=u...}^{b} D_f \, A_{FB}^f \\ &= \sum_{f=u...}^{b} \left(2E_C^f - 1\right) A_{FB}^f \end{aligned} \tag{6.7}$$

The combined charge finding efficiency for all events is generally $\sim 67\%$ which gives an approximate dilution of ~ 0.34. This is increased to approximately $\sim 79\%$ and ~ 0.58 respectively by selecting oppositely signed events only with a corresponding drop in event statistics of around $\sim 40\%$. The charge finding efficiencies for all events are denoted by E_C^{all} while those in oppositely signed events only are denoted using E_C^{opp}. With current statistics, the expected number of standard deviations with which an asymmetry can be measured[5] is of order ~ 5 while selecting opposite sign events increases this to ~ 7. This is due to the slow decrease in the $\frac{1}{\sqrt{N}}$ asymmetry error at high statistics compared to the large increase in $E_C^{all} \rightarrow E_C^{opp}$ when such events are selected. Small changes are seen when flavour dependent efficiencies are considered but the increased significance of the signal remains. Combined opposite sign fractions and efficiencies are shown in figure 6.15. The flavour dependent efficiencies, used to calculate the contribution from each flavour, are shown in table 6.11. An additional complication arises from the flavour dependence of an opposite sign event selection. As efficiencies are different for each flavour, so too are the event rejection rates when the selection is applied. The rejection rates for each flavour are shown in table 6.12 for a κ of 0.3. As a result, quark branching fractions must be modified, in an asymmetry calculation, by these factors after opposite sign selection. The presence of such a flavour dependent event selection is unique to the classical method in this case. The values of table 6.12 can only be determined by resort to Monte Carlo and cannot be directly verified in data. Some confidence may be taken that the *combined* opposite sign fractions agree, however this does not exclude cancellation between flavours.

[4] Analogous to the quark separations of the charge flow method

[5] Assuming an underlying combined asymmetry of 4%.

	Quark Flavour									
κ	E_C^u	ΔE_C^u	E_C^d	ΔE_C^d	E_C^s	ΔE_C^s	E_C^c	ΔE_C^c	E_C^b	ΔE_C^b
0.2	85.36	0.23	73.54	0.26	74.66	0.26	79.70	0.26	73.47	0.26
0.3	87.05	0.22	74.73	0.26	77.01	0.25	79.49	0.27	74.87	0.26
0.5	87.61	0.21	73.93	0.27	78.46	0.25	75.53	0.30	75.01	0.27
0.7	86.41	0.23	71.87	0.28	77.99	0.25	71.13	0.32	73.76	0.27
0.9	85.43	0.24	70.13	0.29	77.05	0.26	67.45	0.34	72.57	0.28
1.0	84.87	0.24	69.36	0.29	76.60	0.26	66.00	0.34	72.06	0.28
1.1	84.42	0.24	68.84	0.30	76.20	0.26	64.74	0.34	71.46	0.28
1.4	83.27	0.25	67.63	0.30	75.27	0.27	62.39	0.35	70.45	0.29
1.8	82.21	0.26	66.74	0.30	74.58	0.27	60.49	0.35	69.45	0.29
2.3	81.41	0.27	66.15	0.30	73.90	0.28	59.23	0.36	68.67	0.29
3.0	80.89	0.27	65.56	0.30	73.43	0.28	58.35	0.36	68.06	0.30
6.0	80.04	0.28	65.03	0.31	72.84	0.28	57.56	0.36	67.24	0.30
9.0	79.94	0.28	64.88	0.31	72.67	0.28	57.38	0.36	67.13	0.30
14.0	79.89	0.28	64.78	0.31	72.71	0.28	57.31	0.36	67.03	0.30
20.0	79.87	0.28	64.74	0.31	72.67	0.28	57.30	0.36	67.00	0.30
∞	79.87	0.28	64.71	0.31	72.61	0.28	57.22	0.36	67.03	0.30

Table 6.11: Flavour dependent charge finding efficiencies (in %) as a function of κ in oppositely signed events.

Flavour	Opposite Sign Fraction
u	$65.2\,(\pm 0.2)\%$
d	$57.3\,(\pm 0.2)\%$
s	$58.4\,(\pm 0.2)\%$
c	$59.7\,(\pm 0.2)\%$
b	$56.9\,(\pm 0.2)\%$

Table 6.12: Opposite sign selection rates for $\kappa = 0.3$.

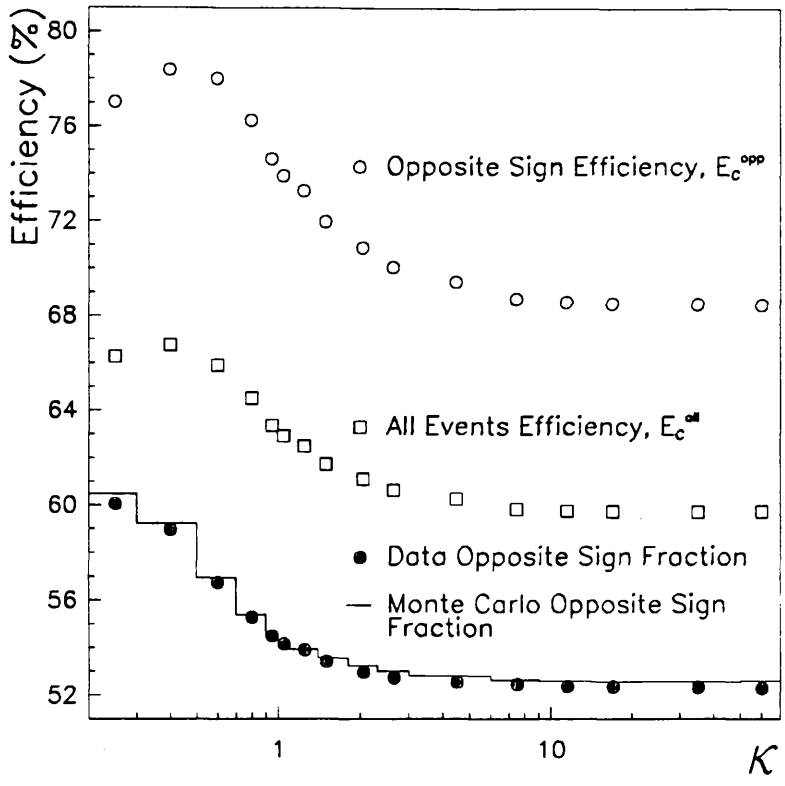

Figure 6.15: Variation in the combined charge finding efficiencies and opposite sign fractions for data and Monte Carlo. Statistical errors are equal to the point size.

6.5.2 Measured Asymmetries

As in the method of charge flow, the asymmetry is extracted by either of two methods; using the integrated or fitted values from equation (5.1). The integrated values are shown in figure 6.16 as a function of κ. A fit to the asymmetric term in the angular distribution of positively charged jets for opposite sign events yields values which are compatible with integrated measurements after corrections for acceptance. These are compared in table 6.13 with angular distributions shown in figure 6.17.

The two sets of results are seen to be compatible. The fitted angular distributions give good agreement with that expected, especially at large $cos\,\theta_T$ where an asymmetry is most pronounced.

6.6 Summary

The charge flow method demonstrates the presence of a statistically significant charge asymmetry which is most significant in the high $cos\,\theta_T$ region of the detector. The Monte Carlo gives an excellent description of data throughout while indicating a position of optimal sensitivity around $\kappa = 1.0$. Here, $\overline{Q_{FB}}$ is 6 standard deviations from zero and has a value of $-0.0084\,(\pm 0.0014)$(stat.). The asymmetry is seen to increase with energy

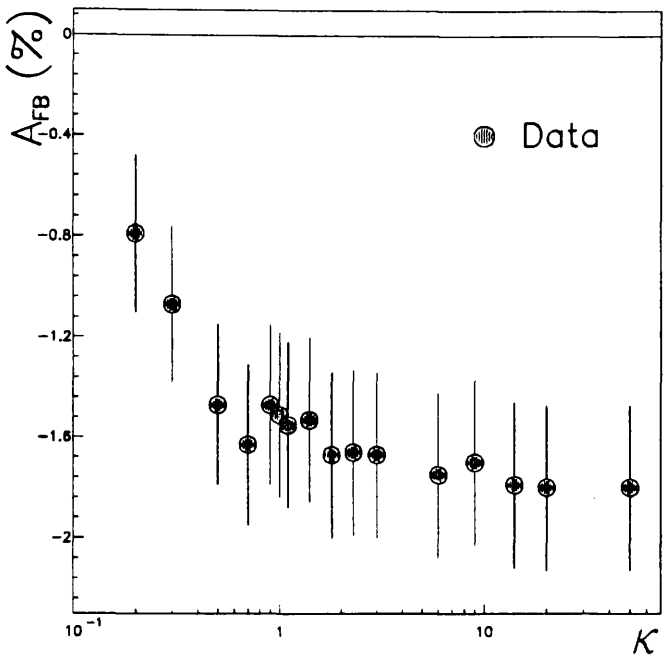

Figure 6.16: Variation of integrated classical method values of A_{FB} with κ.

κ	Integrated Method	Angular Fit Method
	$A_{FB}\|^{1.0}$ (in %)	$A_{FB}\|^{1.0}$ (in %)
0.2	$-0.84\,(\pm 0.33)$	$-1.21\,(\pm 0.38)$
0.3	$-1.13\,(\pm 0.33)$	$-1.51\,(\pm 0.38)$
0.5	$-1.56\,(\pm 0.34)$	$-1.72\,(\pm 0.40)$
0.7	$-1.73\,(\pm 0.34)$	$-1.66\,(\pm 0.41)$
0.9	$-1.56\,(\pm 0.34)$	$-1.70\,(\pm 0.40)$
1.0	$-1.60\,(\pm 0.33)$	$-1.72\,(\pm 0.40)$
1.1	$-1.64\,(\pm 0.33)$	$-1.78\,(\pm 0.40)$
1.4	$-1.62\,(\pm 0.33)$	$-1.52\,(\pm 0.40)$
1.8	$-1.77\,(\pm 0.33)$	$-1.64\,(\pm 0.40)$
2.3	$-1.76\,(\pm 0.33)$	$-1.55\,(\pm 0.40)$
3.0	$-1.77\,(\pm 0.33)$	$-1.56\,(\pm 0.41)$
6.0	$-1.85\,(\pm 0.33)$	$-1.58\,(\pm 0.41)$
9.0	$-1.80\,(\pm 0.33)$	$-1.52\,(\pm 0.41)$
14.0	$-1.89\,(\pm 0.33)$	$-1.63\,(\pm 0.41)$
20.0	$-1.90\,(\pm 0.33)$	$-1.68\,(\pm 0.41)$
∞	$-1.90\,(\pm 0.33)$	$-1.66\,(\pm 0.41)$

Integrated asymmetries are corrected for limited angular acceptance.

Table 6.13: Summary of integrated and fitted classical asymmetries.

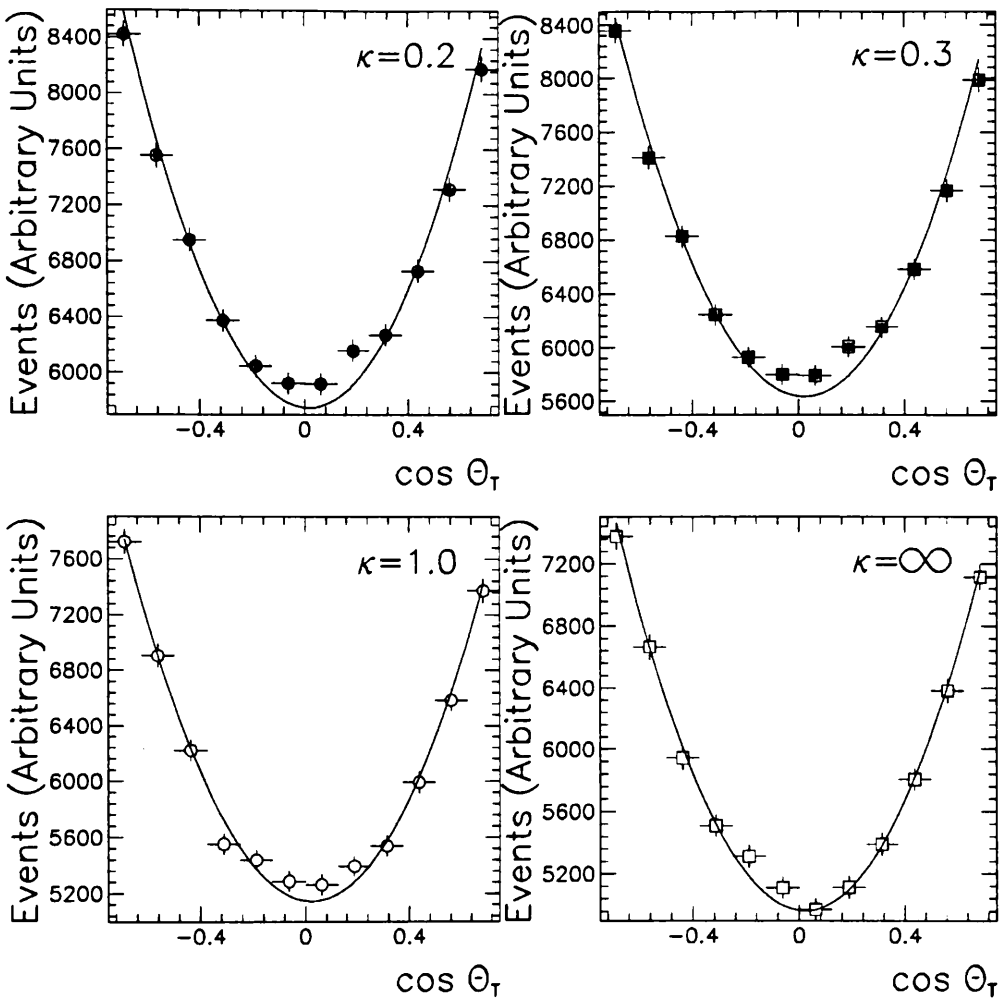

Figure 6.17: Angular distribution of positive jets in data for oppositely signed events.

as predicted.

In addition, the complementary classical method displays an asymmetry of positive jets in opposite sign events with $A_{FB} = -1.72\,(\pm 0.40)\%$ from a fit to their angular distribution at $\kappa = 0.5$.

Chapter 7

Detector Systematic Effects

Systematic detector contributions to an asymmetry measurement arise from asymmetric detector response and deviations from the ideal in our knowledge of the detector. Fortunately, for such effects to seriously affect an asymmetry, they have to be *both* forward-backward *and* charge asymmetric. Many effects possess one of these qualities but few share both. Any significant effect represents a "false" asymmetry in addition to the electroweak imbalance which is measured. The small physical asymmetry means that small systematic contributions can have a large relative effect. Alignment of the detector relative to the beam, its performance and geometrical acceptance for positive and negative tracks can induce such an additional asymmetry.

The purpose of this chapter is to quantify detector contributions to $\overline{Q_{FB}}$ where possible, and to ascribe an appropriate systematic error.

7.1 Measurement Systematics

The measurement of an asymmetry relies on accurate and unbiased tracking within a well-defined geometrical acceptance. Discrepancies between the treatment of an ionised track from charged particles in forward or backward regions will distort the measurement. Geometrical effects such as a general tilt of the detector relative to the beam, or a general deformation of the sensitive volume give negligible effects. The effects of such misalignment on an integrated $\overline{Q_{FB}}$ measurement are small since the thrust axis is usually only crucial close to the central membrane where an asymmetry is also small. Such problems are highly constrained by survey measurements of detector components and analyses of particle balance within detector hemispheres.

The charge flow method incorporates several quantities useful for identifying symmetric and asymmetric detector effects. The total charge and charge flow are sensitive to forward-backward charge symmetric and asymmetric differences respectively. Thus, many detector differences appear as non-zero components of $\overline{Q}$ which are then used to place conservative limits of their effect on $\overline{Q_{FB}}$.

In general, detector systematics are very small in ALEPH so much of the detector systematic comes from uncertainties rather than significant deviations from expectations.

7.2 Tracking Momentum Bias

Detection and measurement of particle momenta is carried out in the TPC using a superposition of parallel electric and magnetic fields. The detection of particle ionisation is performed using endplates segmented into 18 separate sectors with independently sensitive areas and electronics. Uniformity and alignment of these components are essential for the system to remain unbiased in its treatment of positive and negative tracks. Magnetic field distortions give rise to radial components which produce effects depending on whether a track spirals one way or the other in the field. The distortions depend on the dimensions of the detector solenoid and the material which surrounds it and so are position dependent. The combined effect of this is to produce charge asymmetric distortions of tracking in the TPC. During the construction phase of ALEPH, field maps and sector-subdetector alignment surveys were taken with the intention of correcting for these effects in the offline reconstruction software. This is done using parameterised corrections for known distortions and misalignments in terms of track direction and momentum. Using a combination of detector information, with corrections and measurements from existing data, most dangerous effects are removed. Further checks are made with laser or cosmic ray data leaving only small discrepancies due largely to uncertainties in the original field measurements and uniformity of the electric drift field created by the TPC resistor chain. These are combined with the limited accuracy of the detector survey measurements[1].

7.2.1 Muon Measurements

A forward-backward disparity in the mean momentum of tracks is observed in the ALEPH 1990 muon-pair data [41]. Using $e^+e^- \rightarrow \mu^+\mu^-$ events, and demanding limited acollinearity from initial and final-state radiation, yields a relatively pure sample of monoenergetic tracks. Such events display noticeable differences between the average beam energy and differently charged muons in the forward and backward regions of the detector[2]. This is shown in table 7.1. The effect appears as an additional contribution to the true sagitta

Energy of	Forward (GeV)	Backward (GeV)
Positive Muons	45.46 ($\pm$0.05)	45.83 ($\pm$0.05)
Negative Muons	45.83 ($\pm$0.05)	45.51 ($\pm$0.05)

Table 7.1: Difference between mean muon energies of positive and negative charge averaged over forward and backward regions. The mean beam energy for all the μ – pair events is 45.61 GeV.

and is largely due to residual field distortions. As a result of the angular dependence

[1] These were carried out as the detector was assembled with quoted accuracies in translation of 300μ when in place, although sector positions in the laboratory were measured with an accuracy of 50μ.

[2] Analysis carried out by the ALEPH tracking and μ-pair analysis groups.

of distortions, the difference between measured and expected muon momenta also varies with angle. The ratio of expected to measured momentum is shown in figure 7.1 as a function of azimuthal angle for both positive and negative tracks. The characteristically

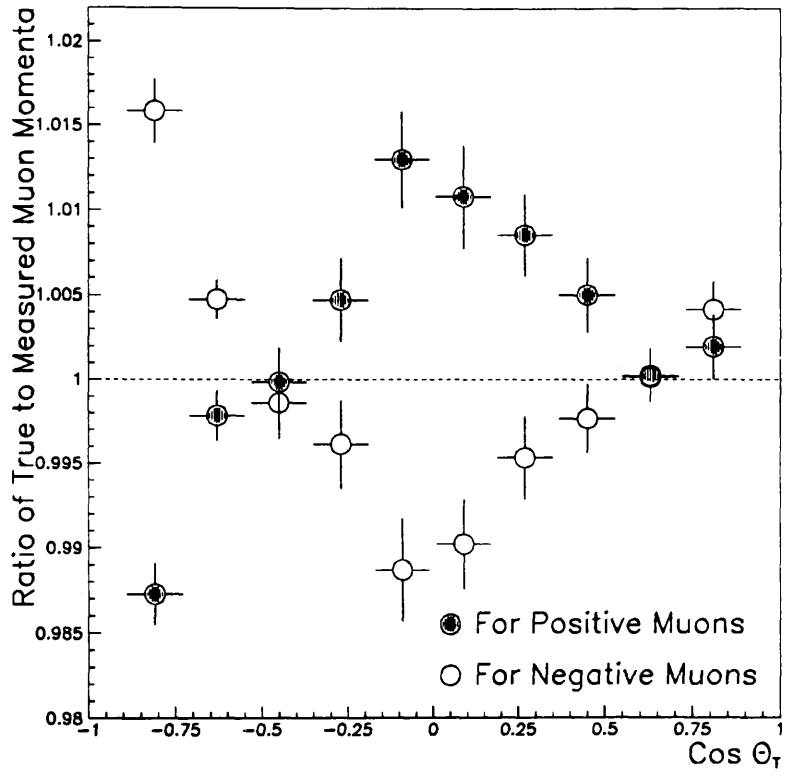

Figure 7.1: Ratio between expected and measured muon momenta as a function of polar angle in the TPC.

smooth variation with angle is opposite in direction for different track charges, although it is clear that the absolute magnitude of such an effect is small. The variation in the central region of the detector is less than $\pm 2\%$. Measurements at either extreme of the range, $0.9 < |\cos\theta| < 1.0$, suffer from poor statistics and are partially excluded by the track selection. Field corrections in this region are complicated by the presence of laser mirrors etc. close to the inner field cage.

7.2.2 Extrapolation to Lower Momenta and κ Dependence

The observed shift in muon momenta at ~ 45 GeV is present as an additional component to the measurement of all tracks. The effect represents an additional contribution to the true sagitta of tracks bending in the magnetic field. As it is only possible to measure the effect using monoenergetic lepton pairs, it is necessary to extrapolate the effect to lower momenta. This is performed using the following equation for muons and hence all particles :

$$p_{measured} = p_{true} + dp_{true} \tag{7.1}$$

where dp_{true} is the result of a fixed shift in the sagitta, S. The latter is proportional to $\frac{1}{p_{true}}$ while a constant sagitta shift dS is proportional to $\frac{-1}{p_{true}^2} dp_{true}$. The correction is parameterised as a function of track momentum and depends on the particle charge :

$$\begin{aligned}(p_+)_{corrected} &= (p_+)_{measured} + \epsilon_+ (cos\theta)(p_+)^2_{measured} \\ (p_-)_{corrected} &= (p_-)_{measured} + \epsilon_- (cos\theta)(p_-)^2_{measured}\end{aligned} \tag{7.2}$$

where correction terms, ϵ, for positive and negative tracks are given in table 7.2 from the momentum ratios of figure 7.1. The correction factors are calculated using relation (7.3).

$cos\,\theta$	Momentum Ratio of Positive Tracks	Momentum ratio of Negative Tracks	Correction, ϵ_+ (Positive Tracks)	Correction, ϵ_- (Negative Tracks)
-0.81	0.987 (±0.002)	1.016 (±0.002)	-0.00028	+0.00034
-0.63	0.998 (±0.001)	1.005 (±0.001)	-0.00005	+0.00010
-0.45	1.000 (±0.002)	0.999 (±0.002)	+0.00000	-0.00003
-0.27	1.005 (±0.002)	0.996 (±0.002)	+0.00010	-0.00008
-0.09	1.013 (±0.003)	0.989 (±0.003)	+0.00028	-0.00025
+0.09	1.010 (±0.003)	0.990 (±0.003)	+0.00023	-0.00022
+0.27	1.009 (±0.002)	0.995 (±0.002)	+0.00019	-0.00010
+0.45	1.005 (±0.002)	0.998 (±0.002)	+0.00011	-0.00005
+0.63	1.000 (±0.002)	1.000 (±0.001)	+0.00001	+0.00000
+0.81	1.002 (±0.002)	1.004 (±0.002)	+0.00004	+0.00009

The muon momentum difference ratio is calculated from the quantity $\frac{E_{beam}}{p_\mu}$ while correction terms are calculated using equation (7.3).

Table 7.2: Muon momentum difference ratios and correction factors as a function of angle.

$$\epsilon = \frac{\left(\frac{p_{measured}}{p_{true}}\right) - 1}{p_{true}} \tag{7.3}$$

The *true* momentum is the mean beam energy for selected events and is known with great precision compared to the the measured muon momenta. The total effect is summarised for forward and backward regions using the integrated differences in expected and measured momenta from table 7.1, showing the marked difference between hemispheres.

$$\begin{aligned}(p)^{cos\,\theta>0}_{measured} &= (p)^{cos\,\theta>0}_{true} - 0.00009\,q\left[(p)^{cos\,\theta>0}_{measured}\right]^2 \\ (p)^{cos\,\theta<0}_{measured} &= (p)^{cos\theta<0}_{true} + 0.00008\,q\left[(p)^{cos\,\theta<0}_{measured}\right]^2\end{aligned} \tag{7.4}$$

Effect on $\overline{Q_{FB}}$

The effect of a sagitta shift on $\overline{Q_{FB}}$ can be examined by studying the weighted charge summation in the forward region for the case when $\kappa = 1.0$. p_L is the *true* longitudinal momentum of a given track, hence :

$$(Q_F)_{measured} = \frac{\sum_i q_i (p_L)_i^{measured}}{\sum_i (p_L)_i^{measured}} \text{ for all forward tracks : i } = 1 \ldots \text{N} \tag{7.5}$$

Employing the parameterised correction $p_L^{measured} = p_L (1 - \epsilon q p_L)$ separates this into :

$$(Q_F)_{measured} = \frac{\sum_i q_i (p_L)_i - \epsilon \sum_i q_i^2 (p_L)_i^2}{\sum_i (p_L)_i - \epsilon \sum_i q_i (p_L)_i^2} \tag{7.6}$$

After dividing all terms by $\sum_i (p_L)_i$ and multiplying top and bottom by $\left[1 + \epsilon \frac{\sum_i q_i (p_L)_i^2}{\sum_i (p_L)_i}\right]$ it is possible to obtain the following relation by ignoring higher order terms in ϵ :

$$\begin{aligned} (Q_F)_{measured} &= (Q_F)_{true} - \epsilon \frac{\sum_i (p_L)_i^2}{\sum_i (p_L)_i} + \epsilon \frac{\sum_i q_i (p_L)_i}{\sum_i (p_L)_i} \frac{\sum_i q_i (p_L)_i^2}{\sum_i (p_L)_i} \\ &\approx (Q_F)_{true} - \epsilon \frac{\sum_i (p_L)_i^2}{\sum_i (p_L)_i} \left[1 - \frac{\sum_i q_i (p_L)_i^2 \sum_i q_i (p_L)_i}{\sum_i (p_L)_i \sum_i (p_L)_i^2}\right] + \ldots \end{aligned} \tag{7.7}$$

It is seen that, for positive corrections ϵ, $(Q_F)_{measured}$ decreases. If a similar change occurs in the backward region, but to a greater or lesser degree, then the effect on $\overline{Q_{FB}}$ is a net increase or decrease, respectively. The discrepancy noted in equation (7.4) means that equation (7.7) predicts that distortions will *increase* the observed asymmetry from its ideally measured value. Thus, the application of an appropriate sagitta correction *reduces* the measured charge flow somewhat. This is indeed found to be the case.

Dependence on κ

It is expected that such a momentum dependent correction is also κ dependent. Using a similar derivation to above, but for the general case where κ is not necessarily unity, allows the correction formula to be approximated as :

$$\begin{aligned} \left(p_L^{measured}\right)^\kappa &= p_L^\kappa (1 - \epsilon q p_L)^\kappa \\ &\approx p_L^\kappa (1 - \kappa \epsilon q p_L) \end{aligned} \tag{7.8}$$

This takes into account only the first term of the binomial expansion in κ for the correction and yields :

$$[Q_F(\kappa)]_{measured} \approx [Q_F(\kappa)]_{true} - \kappa \epsilon \frac{\sum_i (p_L)_i^{1+\kappa}}{\sum_i (p_L)_i^\kappa} [1 - Q_F(\kappa)\, Q_F(1+\kappa)] \tag{7.9}$$

where the forward charge is now κ dependent, ie. $Q_F(\kappa)$. The derivation ignores the effect of all higher order terms in ϵ. This is reasonable because of the small size of the quantity $\epsilon^2 \sim 10^{-7}$. The approximation indicates that the effect of the correction increases with κ while its relative size stabilises as differences between measured quantities at κ and $1 + \kappa$ become progressively less.

Observed Shift in $\overline{Q_{FB}}$

The results of $\overline{Q_{FB}}$ before and after applying the sagitta correction, with corresponding fractional differences are shown in table 7.3.

κ	0.2	0.3	0.5	0.7	0.9	1.0	1.1	1.4
$\overline{Q_{FB}}$ Shift ($\times 10^{-4}$)	1	1	2	3	4	4	5	5
Percentage Shift	2.7 %	3.8 %	4.5 %	4.8 %	5.0 %	4.9 %	5.0 %	5.0%
κ	1.8	2.3	3.0	6.0	9.0	14.0	20.0	∞
$\overline{Q_{FB}}$ Shift ($\times 10^{-4}$)	6	7	8	9	9	9	9	13
Percentage Shift	5.0%	5.0 %	5.0 %	5.0 %	4.9 %	4.9 %	4.9%	6.8%

Differences are calculated using : $Difference = (\overline{Q_{FB}})_{uncorrected} - (\overline{Q_{FB}})_{corrected}$ where *corrected* refers to data where a sagitta correction has been applied to the momenta of all tracks.

Table 7.3: Result of using the sagitta correction.

7.2.3 Estimated Error on the Correction

The systematic error due to the effects of using a sagitta correction remains small due to the accuracy of the μ – pair measurements. The error on a typical $cos\,\theta$ correction term is 0.2% and includes statistical and systematic contributions to the momentum resolution of muons at that energy. The uncertainties of applying this kind of sagitta correction come from several sources :

(a) The errors on the correction terms, ϵ, from the statistics and systematics of the muon measurements.

(b) The uncertainty of corrections in the region $0.90 <| cos\,\theta_T |< 0.95$ where muon measurements are relatively inaccurate.

It is found that varying correction terms in the centre of the detector (to maximally distort $\overline{Q_{FB}}$) leads to smaller changes than current uncertainties on the outer bin corrections; ie. varying the corrections in the region $-0.90 < cos\,\theta_T < +0.90$ to give the greatest shift in $\overline{Q_{FB}}$ and results in changes of 0.2 % at $\kappa = 1.0$ while uncertainty in the outer bins gives contributions of 1.7 %.

A conservative estimate of the uncertainty of the sagitta correction is taken to be the maximal shift from uncertainties in outer bin corrections which gives results shown in table 7.4. At $\kappa = 1.0$, the sagitta correction reduces the measured value of $\overline{Q_{FB}}$ in data by $0.00041\,(\pm 0.00014) \equiv 4.7\,(\pm 1.6)\,\%$. The systematic error is seen to rise with κ although the percentage change with $\overline{Q_{FB}}$ varies only slightly over the full range.

κ	Shift in $\overline{Q_{FB}}$ from ϵ in $-0.9 < cos\,\theta_T < +0.9$	Shift in $\overline{Q_{FB}}$ from ϵ in $0.9 <\mid cos\,\theta_T \mid < 0.95$	Systematic Error (%)
0.2	0.00001	0.00003	1.3%
0.3	0.00001	0.00004	1.3%
0.5	0.00001	0.00007	1.5%
0.7	0.00002	0.00010	1.6%
0.9	0.00001	0.00013	1.6%
1.0	0.00002	0.00014	1.6%
1.1	0.00002	0.00016	1.7%
1.4	0.00002	0.00019	1.7%
1.8	0.00003	0.00022	1.6%
2.3	0.00003	0.00024	1.6%
3.0	0.00003	0.00027	1.6%
6.0	0.00004	0.00030	1.5%
9.0	0.00004	0.00030	1.6%
14.0	0.00004	0.00031	1.6%
20.0	0.00004	0.00031	1.6%
∞	0.00013	0.00042	2.1%

The error on the sagitta correction is taken to be the maximum shift of $\overline{Q_{FB}}$ as a result of applying and distorting the extreme $cos\,\theta_T$ corrections for positive and negative tracks.

Table 7.4: Estimated error on the sagitta correction.

7.3 Track Losses

The agreement between charged multiplicities in data and Monte Carlo implies that particle creation and losses are well modelled by the detector simulation. Such effects remain small as generator and reconstructed Monte Carlo mean charged multiplicities are 16.60 and 17.63 respectively, a change of only $\sim 6\%$, which does not include the effects of implementing track selection cuts at the generator level or the decay of long-lived particles. The selection of tracks with transverse momenta greater than 200 MeV, and reliance of the charge flow method on high momentum tracks, means that $\overline{Q_{FB}}$ is largely immune to small differences. Additional particle creation comes from secondary interactions in the detector material and the software reconstruction.

Track losses are highly unlikely to be charge asymmetric. Losses occur for a variety of reasons, but are most likely due to confusion or inefficiencies in pattern recognition and cluster finding of hits in the TPC during reconstruction of track helices. The case where two tracks lie sufficiently close so as to overlap and share hits also enters in this regard. As the same reconstruction program is used for data and Monte Carlo, the only way to identify problems is by visual scanning.

A scan of a large number of tracks was undertaken[3] using a sample of hadronic events in the TPC [42]. Tracks which failed reconstruction were sought by studying event projections in the $\theta - \phi$ plane. The results of the scan are given in table 7.5. The momentum

Track Type	Number
Number of tracks fully reconstructed.	2250
Tracks not reconstructed and pointing close to the vertex.	2
Tracks not reconstructed and not pointing towards the vertex.	5

Table 7.5: Results of the visual track scan of run 7575.

of "lost" tracks is found to be very low, typically less than 500 MeV, with *no* evidence of any forward-backward or charge asymmetry. The effect of losing so few tracks, with low momenta and no observable asymmetry is very small while the tracking efficiency is conservatively estimated as :

$$\text{Tracking Efficiency} = 1 - \frac{\text{Number of Lost Tracks}}{\text{Total Number of Tracks}} = 1 - \frac{7}{2250} = 99.7\% \quad (7.10)$$

For the purposes of charge flow measurement, the tight vertex cuts of the track selection mean that the inefficiency for tracks pointing close to the vertex is 0.1%. A subsequent scan of 3600 tracks[4] revealed no further evidence of track loss which is not also apparent in Monte Carlo. Studies of the addition of tracks near to the edge of selection criteria also supports the conclusion that any artificial asymmetry (in terms of $\overline{Q_{FB}}$) is less than 0.0003 [43]. The conclusion is based upon the 2 unreconstructed tracks of table 7.5 which are found to point close to the vertex, and assumes the worst case that they both lie close to the centre of the jet and are maximally asymmetric, contrary to those actually found in this sample.

7.4 High Momentum Tracks

The beam energy of LEP represents the maximum energy of a single particle in the TPC. However, a small sample of tracks are found with larger energies than this physical limit. The event and track statistics are given in table 7.6 for data and Monte Carlo. Passing such tracks through a visual scan shows that they generally appear as a result of two-track confusion or from the pattern recognition when dealing with large hit densities of multiple low-momentum tracks spiralling in the TPC. These occur in a very small fraction

[3]Scan carried out by Chris Grab for the ALEPH $q\bar{q}$ analysis group.

[4]Carried out subsequently by Rick St Denis for the ALEPH $q\bar{q}$ analysis group.

	Forward		Backward	
Charge	Data	Monte Carlo	Data	Monte Carlo
Positive	0.0025(3)%	0.0030(3)%	0.0028(3)%	0.0034(3)%
Negative	0.0025(3)%	0.0030(3)%	0.0029(3)%	0.0029(3)%

Percentages represent the fraction of total selected tracks which have unphysically large momenta. Monte Carlo statistics are normalised to data.

Table 7.6: Fraction of tracks with abnormally high momenta in data and Monte Carlo.

of events, and appear with similar frequency in the Monte Carlo sample, which implies that they are artefacts of the common reconstruction program.

The forward and backward distributions of *charged* momentum for such tracks are shown in figure 7.2. There is no detectable charge *or* forward-backward asymmetry in

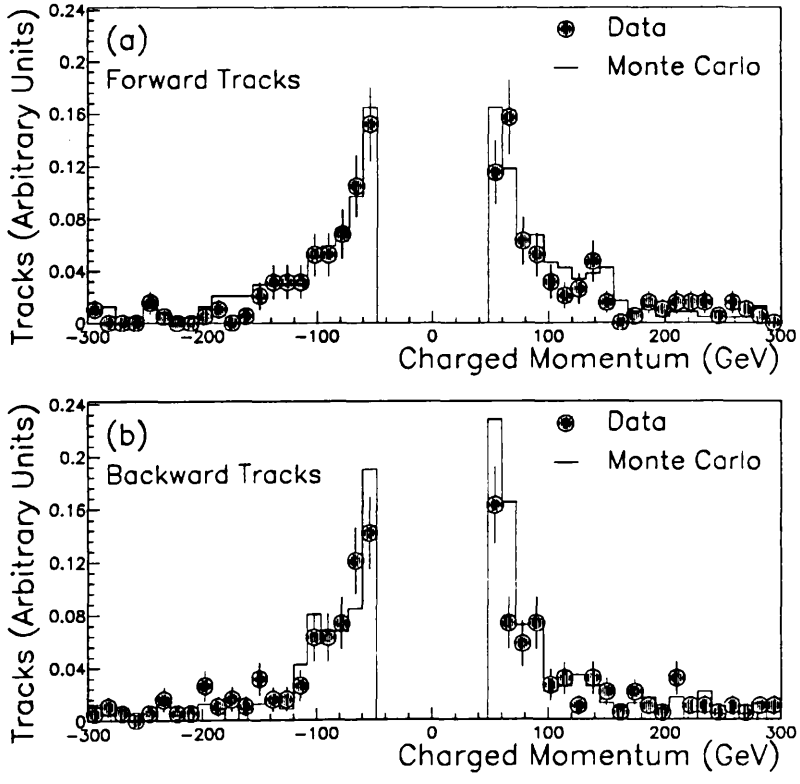

The number of cases are normalised between data and Monte Carlo.

Figure 7.2: Charged momentum distribution in the forward (a) and backward (b) regions for tracks with unphysically large momenta.

this sample, which is consistent with the hypothesis of confusion during reconstruction. The close agreement of the distribution shape in data and Monte Carlo also supports this view. The effect on the measured value of $\overline{Q_{FB}}$ remains small due to their low statistical

significance and is seen in the results of integrated $\overline{Q_{FB}}$ in data shown in table 7.7. This indicates that the effect of either excluding the tracks, or the events containing the tracks, has a negligible impact on the mean charge flow. The systematic error assigned to

κ	Excluding the Tracks		Excluding the Events		Maximal
	Difference	Percentage	Difference	Percentage	Difference (%)
0.2	0.00001	-0.5	0.00001	-0.5	0.5
0.3	0.00002	-0.7	0.00001	-0.3	0.7
0.5	0.00002	-0.4	0.00000	0.0	0.4
0.7	0.00003	-0.5	-0.00001	0.2	0.5
0.9	0.00005	-0.6	0.00000	0.0	0.6
1.0	0.00005	-0.6	0.00000	0.0	0.6
1.1	0.00005	-0.6	0.00000	0.0	0.6
1.4	0.00007	-0.6	0.00001	-0.1	0.6
1.8	0.00006	-0.5	0.00000	0.0	0.5
2.3	0.00006	-0.4	0.00000	0.0	0.4
3.0	0.00005	-0.3	-0.00001	0.0	0.3
6.0	0.00003	-0.2	-0.00003	0.2	0.2
9.0	0.00002	-0.1	-0.00005	0.3	0.3
14.0	0.00003	-0.2	-0.00006	0.3	0.3
20.0	0.00002	-0.1	-0.00006	0.3	0.3
∞	0.00007	-0.4	-0.00002	0.1	0.4

Table 7.7: Effect on $\overline{Q_{FB}}$ of including or excluding tracks (or events) with unphysically high momenta.

$\overline{Q_{FB}}$ is conservatively estimated to be the maximum difference in $\overline{Q_{FB}}$ from including or excluding the tracks *or* the events. From table 7.7 it is clear that the maximal difference is 0.00005 at $\kappa = 1.0$ and never exceeds 0.00007 for all κ.

7.5 Effects of Detector Material

An asymmetry measurement is affected by excess production of positive or negative particles, in one region of the detector, which is not due to the electroweak asymmetry. This can arise from an imbalance of detector material between forward and backward hemispheres, which can create a charged track imbalance due to different nuclear absorption cross-sections for particles such as pions, kaons and protons etc. [44]. Differences in cross-sections have been measured by a variety of fixed-target experiments using various particles incident on protons. These arise from the number of isospin channels open for each process and, in the case of antiprotons, from the greater available energy following

$\bar{p}p$ annihilation. Differences are greatest at low particle energies. As mesons are more likely to be produced during fragmentation than baryons, it is particles such as pions and kaons which are most significant in this regard.

A material asymmetry is of importance in the region immediately surrounding the vertex. The VDET material was altered between the autumn 1989 and spring-summer 1990 run periods as additional sections were added. Several remain incomplete while the support material, cabling and cooling equipment etc, contribute to an overall material imbalance. Analysis of the materialisation length of photons [45] is consistent with the fact that only $\frac{2}{3}$ of the outer 15 sections in ϕ are installed, while analysis of pair conversions in this material [46] yields the following material asymmetry between the forward and backward regions :

$$A_m = -2.01\ (\pm 1.15)\% \tag{7.11}$$

Note that, although this is consistent with zero, the error on A_m is useful in determining a systematic error on $\overline{Q_{FB}}$. In the analysis of photon conversion data it is apparent that the amount of material is not *precisely* reproduced in the 1990 detector geometry for the Monte Carlo, although it is seen be be θ symmetric [47].

7.5.1 Relation Between A_m and $\overline{Q_{FB}}$

The contribution from differences in nuclear cross-sections cannot be quantified as the relative fluxes of particles and their energies are not known. However, the charge flow method is used to place limits on the influence of such an effect.

In an ideally symmetric detector (with no material imbalance) the cross-section difference will affect Q_F and Q_B equally. This would lead to a non-zero value of the total charge $\overline{Q}$ while cancelling out in $\overline{Q_{FB}}$. Thus, as a first approximation, the consistently small value of $\overline{Q}$ for all values of κ indicates that even without the "second-order" effect of a material asymmetry, the effect on $\overline{Q_{FB}}$ is likely to be very small. This is to be expected, considering the dependence of the charge flow on high momentum tracks coming from close to the vertex.

The effect on $\overline{Q_{FB}}$ from the nuclear cross-section imbalance can be estimated using the product of the symmetric component from the difference in cross-sections and the asymmetric component from the measured material asymmetry. The value of $\overline{Q}$ never exceeds 0.003 in data. Since $\overline{Q}$ contains *all* charge asymmetric contributions from any momentum bias or track inefficiencies etc, taking this as the asymmetric component is a highly conservative estimate, especially considering its large error. This results in the following contribution to $\overline{Q_{FB}}$ using the maximum value of $\bar{Q}$ for all values of κ and taking a 1σ variation on all quantities :

$$\begin{aligned} \Delta\overline{Q_{FB}} &\approx \overline{Q} \times A_m \\ &= 0.0028\ (\pm 0.0006) \times 0.02010\ (\pm 0.01150) \\ &= 0.00006\ \left(^{+0.00005}_{-0.00004}\right) \end{aligned} \tag{7.12}$$

The systematic error on $\overline{Q_{FB}}$ from this source is the taken to be :

$$\underbrace{0.00006}_{\Delta\overline{Q_{FB}}} + \underbrace{0.00005}_{\Delta(\Delta\overline{Q_{FB}})} = 0.00011 \tag{7.13}$$

It is noted that there is a discrepancy between values of $\overline{Q}$ in data and Monte Carlo at low κ, where the latter exhibits a excess mean total charge. This is unrelated to a possible asymmetry in VDET material as it appears also in the 1989 and 1990 versions of the detector simulation which employ radically different geometries in this region. As shown in figure 7.3, the agreement between the two samples indicates that the data-Monte Carlo discrepancy is likely to be due to a more general difference in the material of the simulated and actual detectors.

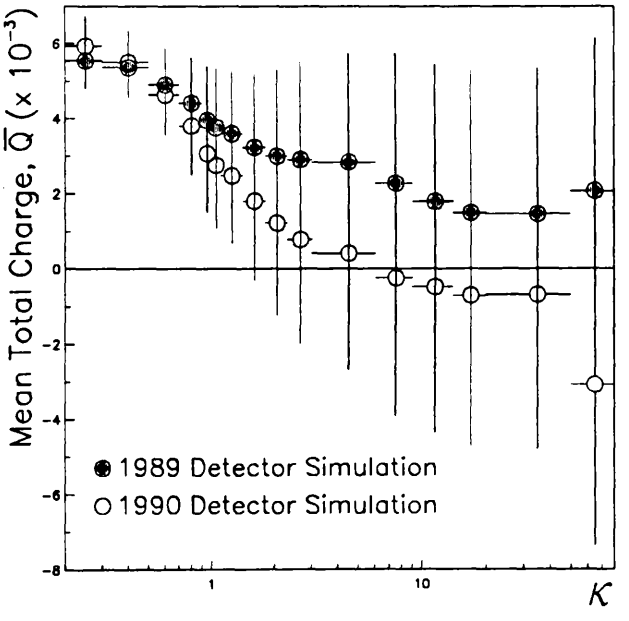

Mean values for $\overline{Q}$ for different Monte Carlo data sets simulated separately using the 1989 and 1990 VDET geometries.

Figure 7.3: Mean total charge in the 1989 and 1990 detector simulations.

7.5.2 Symmetric Effects

There are additional symmetric contributions to $\overline{Q_{FB}}$ from the detector and event reconstruction which dilute the measurement of an asymmetry. The detector and reconstruction algorithms introduce small losses and particle measurement errors which are included in the simulation and reconstruction of Monte Carlo events. Their contribution is quantified by comparing the expected asymmetry at the generator and reconstructed levels. This includes additional contributions from long-lived particles in the generator

which are subsequently decayed during simulation of the detector. Their combined effect reduces the method sensitivity by $\sim 6\%$ at $\kappa = 1.0$.

For a given flavour, the effects reduce the charge separation between forward moving quarks and antiquarks. This is monitored by $\bar{q}$, which acts as a generalised flavour summation for data and Monte Carlo. At $\kappa = 1.0$ this is summarised in table 7.8 and indicates that the detector and decays produce an $\sim 12\%$ overall reduction in the $\bar{q}$ sum of the quark separations. The charge flow measurement has a different dependence on the

Event Sample	$\bar{q}$	$\overline{Q_{FB}^{ref}}$
Generated Monte Carlo	0.330 ($\pm$0.002)	-0.0108($\pm$0.0001)
Reconstucted Monte Carlo	0.291 ($\pm$0.003)	-0.0085($\pm$0.0001)
Data	0.289 ($\pm$0.004)	

Table 7.8: Summary of $\bar{q}$ and $\overline{Q_{FB}^{ref}}$ at $\kappa = 1.0$

separations to $\bar{q}$, as it relies on the cancellation between flavours in a linear sum. $\overline{Q_{FB}^{ref}}$ is used to interpret the outcome of the changes in the separations caused by the presence of the detector and particle decays. The changes observed in Monte Carlo are shown in figure 7.4 and summarised in table 7.8. It is necessary to verify that such a decrease in measurable asymmetry is present in data to an equivalent extent. These are the roles of $\bar{q}$ and α. The accuracy with which symmetric effects can be said to be correctly implemented in the detector simulation corresponds to the degree of agreement between $\bar{q}$ in data and Monte Carlo. As shown by $\alpha = \frac{\bar{q}_{data}}{\bar{q}_{mc}}$ in table 7.8, this is found to be 0.99 with an error of ± 0.02. Thus, a conservative estimate of any misrepresentation of symmetric effects in detector material is taken to be :

$$\begin{aligned} \left(\Delta\overline{Q_{FB}}\right)_{symmetric} &= 0.02 \times (\overline{Q_{FB}})_{data} \\ &= 0.0002 \end{aligned} \tag{7.14}$$

This does not take into account the fact that the detector and decays are only responsible for $\sim 12\%$ of changes to $\bar{q}$ since this cannot be verified with data. Thus $\left(\Delta\overline{Q_{FB}}\right)_{symmetric}$ represents a highly conservative estimate of this systematic error.

7.6 Summary

The systematic errors introduced by the detector from all sources discussed are summarised as a function of κ in table 7.9. This shows that at $\kappa = 1.0$ the asymmetry measured in data is :

$$\overline{Q_{FB}} = -0.0084 \quad \underbrace{\pm\ 0.0014}_{\text{(statistical)}} \quad \underbrace{\pm\ 0.0004}_{\text{(detector syst.)}} \tag{7.15}$$

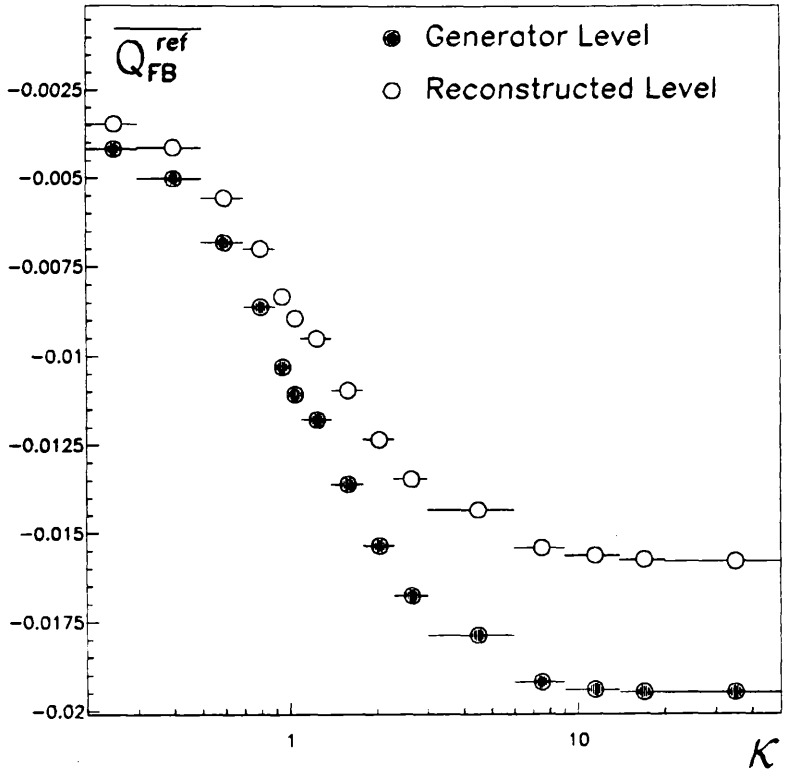

Figure 7.4: $\overline{Q_{FB}^{ref}}$ in generated and reconstructed Monte Carlo event samples.

The combined systematic error from detector effects is seen to increase with κ although the relative error falls slowly.

	All values are $\Delta\overline{Q_{FB}} \times 10^{-4}$						
κ	Sagitta Correction	Track Losses	High p Tracks	Material Asymmetry	Detector Dilution	Total Error	Relative Error
0.2	0.3	3.0	0.1	1.1	0.2	3.2	14.7%
0.3	0.4	3.0	0.2	1.0	0.3	3.2	11.1%
0.5	0.7	3.0	0.2	1.0	0.4	3.3	7.3%
0.7	1.0	3.0	0.3	0.9	1.2	3.5	5.8%
0.9	1.3	3.0	0.5	0.9	1.5	3.7	4.9%
1.0	1.4	3.0	0.5	0.8	1.7	3.8	4.6%
1.1	1.6	3.0	0.5	0.8	1.8	4.0	4.4%
1.4	1.9	3.0	0.7	0.9	2.2	4.3	3.9%
1.8	2.2	3.0	0.6	0.9	2.6	4.7	3.6%
2.3	2.4	3.0	0.6	1.0	4.4	5.9	4.1%
3.0	2.7	3.0	0.5	1.0	4.8	6.4	4.0%
6.0	3.0	3.0	0.3	1.1	7.2	8.5	4.7%
9.0	3.0	3.0	0.5	1.2	7.4	8.7	4.7%
14.0	3.1	3.0	0.6	1.3	7.6	8.9	4.7%
20.0	3.1	3.0	0.6	1.4	7.6	8.9	4.7%
∞	4.2	3.0	0.0	1.5	7.5	9.2	4.9%

Table 7.9: Summary of κ dependent systematic errors of a detector measurement of $\overline{Q_{FB}}$.

Chapter 8

Fragmentation and Mixing Systematics

The main source of systematic error in an interpretation of $\overline{Q_{FB}}$ in terms of electroweak parameters arises from uncertainties inherent in the use of fragmentation models. These enter equation (8.1) through use of the Monte Carlo separations.

$$\underbrace{\int_0^{\cos\theta_c} \frac{d\overline{Q_{FB}}}{d\cos\theta} d\cos\theta}_{\text{Measured in Data}} = \frac{4}{3} \frac{\cos\theta_c}{1+\frac{\cos^2\theta_c}{3}} \underbrace{\sum_{f=u\ldots}^{b} q_f \quad A_{FB}^f \frac{\Gamma_f}{\Gamma_{had}}}_{\text{From Monte Carlo}} \tag{8.1}$$

Cancellation between asymmetries in the flavour summation depends critically on the separations and is highly sensitive to anti-correlated effects between up and down-type quarks. This mixture of electroweak and fragmentation dependent quantities is unique to combined quark measurements and is the distinction between lepton studies and the current analysis.

Many degrees of freedom exist when considering uncertainties of fragmentation models. As discussed in chapter 3, and in more detail in section 3.6, such uncertainties are characterised as arising from either limited knowledge of parameters within a model, or limited knowledge of the physics being modelled. Either case involves a calculation of the dependence of measured quantities on sets of parameters. Practical difficulties arise when trying to compare the effects of model parameters. The size and complexity of ALEPH tracking subdetectors means that the sheer quantity of computer time to simulate complex events is very large. This places limitations on the size and number of Monte Carlo samples which are simulated. However, as the fragmentation process is the dominant source of uncertainty, the problem becomes one of establishing sensitive tests at the generator level which can be related to $\overline{Q_{FB}}$, and which are relatively unaffected by the detector.

In parallel studies of ALEPH events [33], two fragmentation models are found to give agreement with detector-corrected distributions. These are the LUND string and HERWIG cluster models, both of which employ parton shower evolution from the final quark-gluon state. Some parameters of the LUND and HERWIG models have been studied by ALEPH QCD analyses [48] while others remain largely undetermined at LEP energies or are embedded in the models themselves. The models are used here to test the interpretation of $\overline{Q_{FB}}$ for dependence on parameters of a particular model and upon a change to an alternative one.

The purpose of this chapter is to demonstrate how uncertainties in the use of fragmentation models affect the charge flow method. In addition, the effects on individual flavours and observables are studied in an attempt to understand how such systematics come about and how they may be identified.

8.1 Measurement Techniques

The problems of detecting changes to the expected value of $\overline{Q_{FB}}$ at the generator level, and relating them to an uncertainty after reconstruction, may be studied separately. This wou ld allow the fragmentation dependence of $\overline{Q_{FB}}$ to be studied at the generator level while the corresponding change to the reconstructed value may be derived from a single, large Monte Carlo sample of reconstructed events. The expected charge flow is calculated in the context of the Standard Model, using a relation outlined in section 5.1.4, namely :

$$\overline{Q_{FB}^{ref}} = \frac{\mathcal{A}_e}{\sum_{f=u}^{b} a_f^2 + v_f^2} \frac{\cos\theta_c}{1 + \frac{\cos^2\theta_c}{3}} \times \sum_{f=u...}^{b} q_f\, a_f\, v_f = 0.033 \times \sum_{f=u...}^{b} q_f\, a_f\, v_f \qquad (8.2)$$

where a_f and v_f are the axial and vector couplings for flavour f, assuming the standard form of quark couplings and a $sin^2\theta_W$ (M_Z^2) value of 0.230. This reduces to :

$$\overline{Q_{FB}^{ref}} = 0.033 \times [0.39\, q_u - 0.69\, q_d - 0.69\, q_s + 0.39\, q_c - 0.69\, q_b] \qquad (8.3)$$

Any change in separation, q_f, is related directly to a shift, $\Delta\overline{Q_{FB}^{ref}}$, in the expected mean charge flow. This expected value of $\overline{Q_{FB}}$, between generator and reconstructed levels, drops by $\sim$ 21% at κ = 1.0 due to a general decrease in quark separations. Individual flavour changes are shown in table 8.1 at κ = 1.0. Separations decrease due to the effects

Flavour	Separation at the Generator Level	Separation at the Reconstructed Level	Percentage Difference
u	0.446 (±0.004)	0.422 (±0.003)	−5.4 %
d	0.233 (±0.004)	0.208 (±0.003)	−10.7 %
s	0.348 (±0.004)	0.283 (±0.004)	−18.7 %
c	0.184 (±0.004)	0.171 (±0.003)	−7.1 %
b	0.241 (±0.004)	0.217 (±0.002)	−10.0 %

Table 8.1: Difference between quark separations at the full event and detector levels.

of (a) detector resolution with particle creation and losses in the material, (b) dilution caused by decays of long-lived particles with lifetimes of the order of nonoseconds. The latter contributes $\sim$ 6% out of the total change between the expected generator and reconstructed level asymmetries, $\overline{Q_{FB}}$ at κ = 1.0.

Data measurements are less direct due to the combined flavours present in the hadronic sample, hence it would be useful to have a "scale-factor" in data and Monte Carlo to translate shifts in the expected $\overline{Q_{FB}}$ at the generator level to one after reconstruction. This is partially fulfilled by $\bar{q}$, which remains largely constant during fragmentation changes and may be determined at generator and reconstructed levels.

The relationship between $\bar{q}$ and $\sum_f q_f a_f v_f$ seen in figure 8.1 and given in table 8.2 shows that they are strongly correlated under large changes in quark separations. Much of the scatter in figure 8.1 is due to fragmentation changes with the values for reconstructed Monte Carlo also indicated. Figure 8.2 shows the behaviour of the ratio $\frac{\sum_f q_f a_f v_f}{\bar{q}}$ with

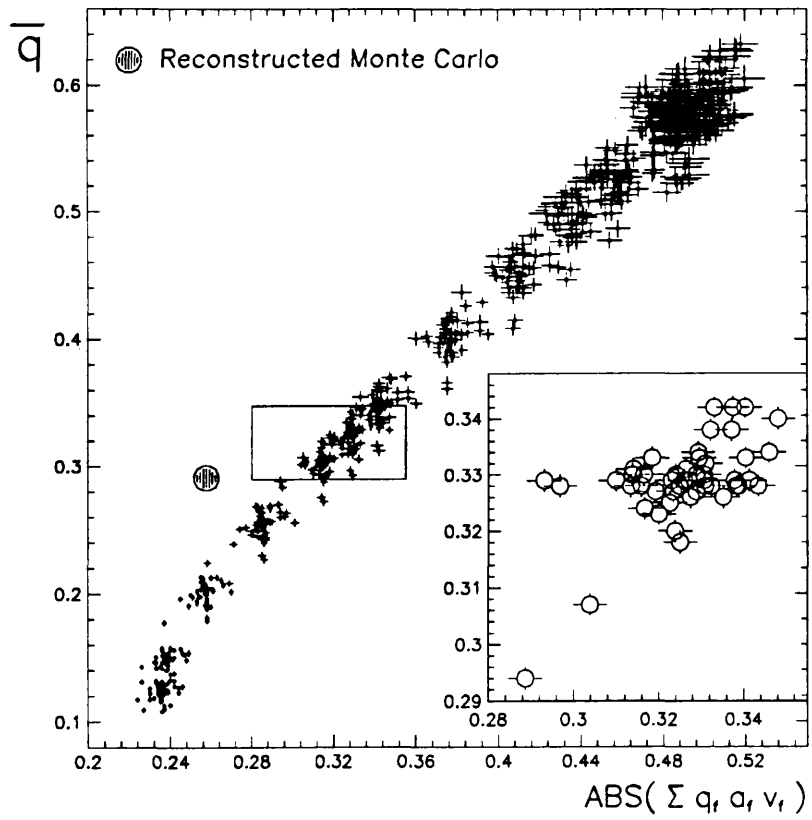

Correlation plot between $\sum_f q_f a_f v_f$ and $\bar{q}$ for all values of κ and different sets of fragmentation parameters. The insert indicates the region indicated by the box and contains points for $\kappa = 1.0$ only. The solid point represents the values of $\sum_f q_f a_f v_f$ and $\bar{q}$ found in reconstructed Monte Carlo.

Figure 8.1: Plot of $\sum_f q_f a_f v_f$ versus $\bar{q}$ under the effects of changes in fragmentation.

κ at the generator and reconstructed levels. These make it clear that the ratio $\frac{\overline{Q_{FB}^{ref}}}{\bar{q}}$ is relatively stable under large changes in the separations, such as from a change of κ, and shows that the detector, and long-lived particle decays, change the value of $\sum_f q_f q_f v_f$ and $\bar{q}$ by a relatively small amount when compared to the scatter from fragmentation effects. Hence, it is unlikely that using $\bar{q}$, to translate from generator to reconstructed levels, will reduce a systematic error on $\overline{Q_{FB}}$ due to fragmentation.

	Full-Event Level		Detector Level	
Kappa	$\frac{\sum_f q_f a_f v_f}{\bar{q}}$ Ratio	Error	$\frac{\sum_f q_f a_f v_f}{\bar{q}}$ Ratio	Error
0.2	0.524	(±0.006)	0.487	(±0.011)
0.3	0.623	(±0.006)	0.576	(±0.011)
0.5	0.782	(±0.007)	0.715	(±0.014)
0.7	0.891	(±0.008)	0.806	(±0.014)
0.9	0.965	(±0.009)	0.864	(±0.016)
1.0	0.992	(±0.009)	0.885	(±0.017)
1.1	1.016	(±0.009)	0.902	(±0.017)
1.4	1.067	(±0.010)	0.939	(±0.019)
1.8	1.108	(±0.011)	0.966	(±0.021)
2.3	1.135	(±0.012)	0.983	(±0.023)
3.0	1.154	(±0.013)	0.993	(±0.025)
6.0	1.168	(±0.016)	0.998	(±0.030)
9.0	1.169	(±0.017)	0.996	(±0.032)
14.0	1.168	(±0.019)	0.994	(±0.033)
20.0	1.166	(±0.020)	0.995	(±0.034)

Table 8.2: Relation of $\frac{\sum_f q_f a_f v_f}{\bar{q}}$ between generator and reconstructed Monte Carlo levels.

8.2 Observables in Data and Monte Carlo

The close agreement between data and Monte Carlo shown in previous chapters is degraded by substantial changes to the fragmentation models. Charge distributions are sensitive to such changes while quantities like $F_{\pm}$ and $\bar{q}$ are even more so. It is possible to use these observables as a guide to the magnitude of changes which are induced when varying the parameters of a given model. Use of observables is limited by correlations and the statistical accuracy with which they can be measured, relative to fragmentation changes which are induced. Again, the problem of relating changes in quantities between generator and reconstructed levels arises. For the purpose of observing parameter dependent effects, percentage shifts in observables are used to translate between the two levels. A summary of available observables at $\kappa = 1.0$ is shown in table 8.3 for data and reconstructed Monte Carlo with corresponding ranges at the generator level calculated in proportion. Correlations between model parameters prevent observables being used to "constrain" the allowed amount of variation. They do however, provide an indication of how severely the agreement with data is affected.

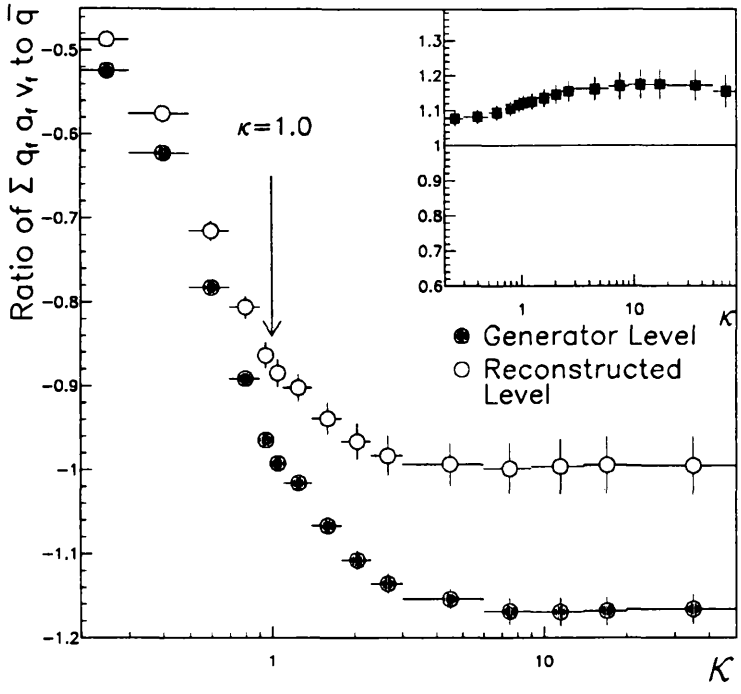

The insert compares reconstructed and generator levels as a function of κ by the fraction : $\left[\frac{\sum_f q_f a_f v_f}{\bar{q}}\right]_R \left[\frac{\bar{q}}{\sum_f q_f a_f v_f}\right]_G$ where the subscripts R and G denote reconstructed and generated Monte Carlo samples respectively.

Figure 8.2: Variation of the ratio $\frac{\sum_f q_f a_f v_f}{\bar{q}}$ as a function of κ at the generator and reconstructed Monte Carlo levels.

Observable	Data	Reconstructed Monte Carlo	Generator Level	Generator Level Range
$\bar{q}$	0.289 (±0.004)	0.291 (±0.003)	0.330 (±0.002)	0.008
σ_{FB}	0.608 (±0.001)	0.608 (±0.001)	0.624 (±0.001)	0.002
σ_Q	0.535 (±0.001)	0.533 (±0.001)	0.529 (±0.001)	0.002
$F_\pm$	0.541 (±0.001)	0.542 (±0.001)	0.554 (±0.001)	0.002
Multiplicity	17.72 (±0.01)	17.63 (±0.01)	16.60 (±0.01)	0.10

The Generator Level Ranges are calculated by combining the difference between data and reconstructed Monte Carlo in quadrature with the observables measurement error. This is translated to the generator level in proportion.

Table 8.3: Summary of observables in data and Monte Carlo.

8.3 Analysis Method

The purpose of studies at the generator level is to quantify the effects of fragmentation separate from detector contributions. The default model parameters which are employed for this study, using the LUND and HERWIG fragmentation models, are described in detail in Appendix A. The need for an accurate Monte Carlo representation of data is fulfilled by the large reconstructed sample used previously.

At the generator level, event and track selections are made so that those which are likely to be visible in the detector are accepted. The degree to which this is achieved is limited by difficulties in applying detector-style cuts to tracks which have not been subjected to simulation and reconstruction. The generator information, with a selection of charged tracks and analogous cuts to that used in data need only provide an adequate description of events prior to long-lived particle decays and detection.

8.3.1 Track Selection

Tracks are selected at the generator level according to the criteria :

(1) The particle is stable and charged.

(2) It lies within an angular acceptance defined by $18.2^{o} \leq \theta \leq 171.8^{o}$.

(3) The particles primary vertex lies within 2 cm and 10 cm of the Z^0 vertex in XY and Z respectively.

(4) It possesses a transverse momentum of greater than 200 MeV.

The vertex is smeared into a beam spot, due to the size of colliding bunches, using a Gaussian beam profile. This is done independently in each dimension using values of 0.035 cm for the width in X, 0.0012 cm in Y and 1.28 cm in Z.

It is important to note that the cut on the position of the particles vertex is not directly analogous to detected impact parameters (D0 and Z0) and is used here only as an approximation[1] . The momentum spectra of tracks at this level agree well with data as shown in figure 8.3. The mean charged multiplicity of generator particles surviving this selection are compared with data and reconstructed Monte Carlo in table 8.4. The agreement between charged multiplicities (g) and (h) of table 8.4 is limited by different track selections used in the multi-parameter fits and the current analysis. However, as agreement is at the level of $\sim$ 0.3%, it is within the $\sim$ 1.2% systematic error on the detector-corrected mean multiplicity [40].

8.3.2 Event Selection

Event selection at the generator level is analogous to that used in data with the following selection procedure :

[1]This could be considerably improved by attempting to extrapolate particle trajectories in a similar way to that used for reconstructed tracks.

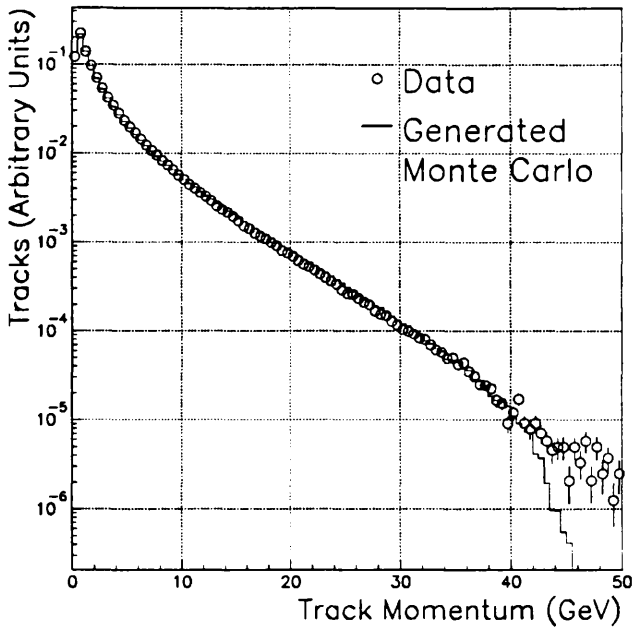

Figure 8.3: Comparison of momenta spectra, after track selection, between data and generated Monte Carlo.

	Level	Mean Multiplicity	Stat. Error
(a)	Reconstructed Data	17.72	0.01
(b)	Reconstructed Monte Carlo	17.63	0.01
(c)	Matched Monte Carlo Tracks	17.35	0.02
(d)	Tracks Created During Simulation	0.33	0.01
(e)	Underlying Generated Multiplicity	16.54	0.02
(f)	Fragmentation Reference Multiplicity	16.60	0.02
(g)	Generator level (LUND)	16.18	0.01
(h)	Generator level (HERWIG)	16.14	0.01

Mean charged multiplicities in data and Monte Carlo events. Quantities are ; (a) the measured data value, (b) the measured value in reconstructed Monte Carlo, (c) the multiplicity of tracks found in reconstructed Monte Carlo which are associated to a "true" track from either the generator or detector simulation, (d) the multiplicity of tracks created during simulation from secondary interactions and long-lived particle decays, (e) the generated multiplicity in reconstructed Monte Carlo, (f) the generator multiplicity using fragmentation parameters from the reconstructed event sample, (g) the LUND generator multiplicity and (h) the HERWIG generator multiplicity. The last two multiplicities refer those measured in the generators where the fragmentation parameters are slightly different from those of the reconstructed Monte Carlo set for the reasons of consistency explained in Appendix A.

Table 8.4: Comparision of generated and reconstructed charged multiplicities.

(i) The thrust axis is calculated using selected charged tracks and constrained to lie within an angular acceptance of $|\ cos\theta_T\ | < 0.9$.

(ii) Events with less than 2 tracks, after track selection, are rejected.

This ensures that important quantities of the charge flow method are consistently described at the generator level.

Samples of 200,000 $e^+e^- \rightarrow q\bar{q}$ events are generated and analysed for each change of model parameters[2]. The effect on $\overline{Q_{FB}^{ref}}$ and observables are measured at extrema of parameter ranges. In addition, intermediate values are used later to understand the effect on individual separations. The latter method remains applicable in the light of future measurements which may restrict current ranges further.

8.4 Parameter Variation Within the LUND Model

As discussed previously in chapter 3, the LUND model relies upon a set of constrained parameters corresponding to theoretical and experimental uncertainties in jet formation. These include the QCD parameters of the previous section and others related to jet development following the parton shower. The total number of parameters is large (~ 20), however many are restricted by theoretical expectations or by measurement. A subset of parameters is relevant to the current measurement. These are determined from tests of the method sensitivity in their regard and are *loosely* classified as follows :

(a) Parameters which affect *jet development*, such as the QCD tuned parameters.

(b) *Fragmentation function* parameters which control the longitudinal momentum development of the jet.

(c) Parameters affecting the *characteristics of mesons* during the *SF* phase of the model by dictating their flavour content and spin.

The charge flow method sensitivity to these parameters is studied by varying each parameter in turn throughout a well defined range. As parameters are often (highly) correlated with each other, the charge flow variation represents a *conservative* estimate of model dependence since it excludes compensation between parameters.

The effect of changes to the three general categories of parameters are discussed with their results in subsequent sections using measurements at $\kappa = 1.0$ throughout for comparison.

8.4.1 Jet Development Parameters

In a model with many interrelated parameters, it is difficult to define those which alone affect jet development. Parameters discussed here are loosely defined as those which directly alter particle momenta and the charged multiplicity without specific relation to

[2]Roughly corresponding to the size of the data sample.

a particular quark flavour. These are shown, with their ranges of variation, in table 8.5. The choice of parameters includes the parton shower (*PS*) evolution quantities, Λ_{QCD} and

Parameter	Range		
Λ_{QCD}	0.26	$\rightarrow$	0.40 GeV
M_{min}	1.0	$\rightarrow$	2.00 GeV
σ	0.34	$\rightarrow$	0.40 GeV

Table 8.5: Jet development parameters and ranges of variation.

M_{min}, while the width of the transverse momentum distribution, σ, is used during the string fragmentation (*SF*) phase. Λ_{QCD} enters via the strong coupling constant, α_s, in a logarithmic term and governs the radiation of gluons and production of further quark pairs in the parton shower. From previous e^+e^- experiments [49] [50] [51] its value is expected to lie in the range 0.26 $\rightarrow$ 0.40 GeV. The minimum parton mass (M_{min}) at which parton showers are terminated is determined by previous experiments to lie in the region around 1.0 GeV whereas the ALEPH QCD tuning prefers a value of 1.50. Due to this variation, a relatively large range of 1.0 $\rightarrow$ 2.0 GeV is used. The parameter, σ, controls the distribution of *transverse* momenta of particles at string breakages in the *SF* phase. The range 0.34 $\rightarrow$ 0.40 GeV is the spread in values at LEP [52] [53] and lower energies [49] [50].

The parameter ranges are substantially larger than the statistical errors of table A.1 and reflect their model dependence while ensuring a conservative estimate of the systematic error. The effect of variation within these ranges is summarised in table 8.6 which shows that such parameters have little effect on the expected mean charge flow, proportional to $\sum_f q_f a_f v_f$. The maximum change incurred is due to a Λ_{QCD} of 0.26 which

Extremity	$\sum_f q_f a_f v_f$ ($\pm$0.004)	$\bar{q}$ ($\pm$0.002)	σ_{FB} ($\pm$0.002)	σ_Q ($\pm$0.001)	$F_\pm$ ($\pm$0.1)	Multiplicity ($\pm$0.01)
$\Lambda_{QCD} = 0.260$	0.340	0.342	0.639	0.540	55.6	16.06
$\Lambda_{QCD} = 0.400$	0.320	0.323	0.616	0.524	55.2	16.89
$M_{min} = 1.0$	0.324	0.320	0.614	0.524	55.3	16.82
$M_{min} = 2.0$	0.333	0.342	0.636	0.537	55.5	16.35
$\sigma = 0.33$	0.326	0.329	0.623	0.529	55.4	16.63
$\sigma = 0.40$	0.332	0.338	0.634	0.536	55.4	16.14
Default	0.328	0.330	0.624	0.529	55.4	16.60

Table 8.6: Summary of effects of varying jet development fragmentation parameters.

leads to a shift of less than 4% in the value of $\sum_f q_f a_f v_f$. In all other cases, changes to individual quark separations are within 1.5 standard deviations of default settings for

all κ. The effect on individual separations for these Λ_{QCD} values are shown in figure 8.4 with those for M_{min}. These indicate that it is the u and s separations which are affected

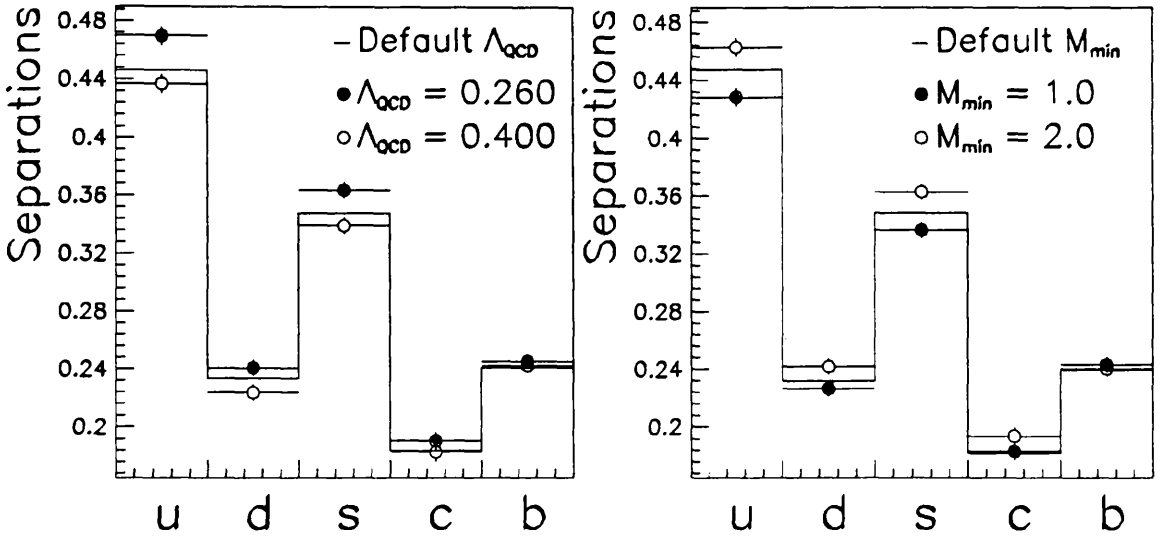

Quark separation values at κ = 1.0. Equivalent errors are involved in the calculation of the "Default" histogram as are included on plotted points.

Figure 8.4: Variation of quark separations at extreme values of Λ_{QCD} and M_{min}

most, with smaller changes in d and c channels while the b separations remain almost unaffected. The observed shifts in $\sum_f q_f a_f v_f$ arise from the combination of changes to several flavours at once. As the shifts of u and s separations are in the same direction, much of their effect is cancelled in the combined asymmetry. Shifts in separations from changes to σ are shown in figure 8.5. This shows again that the effect on $\sum_f q_f a_f v_f$ is due to smaller effects in all flavours, the exception here being the b channel.

8.4.2 Fragmentation Functions

The fragmentation functions which distribute longitudinal momenta of partons to daughter particles during *SF* differ for light (u, d and s) and heavy (c and b) quarks. For light quarks, the symmetric form of equation (3.7) is used. As the functions directly influence the rank-order, they are of great consequence to the charge flow method. The symmetric form introduces two parameters, a and b, which share a high degree of correlation. The fragmentation of heavy quarks uses the Peterson form of equation (3.8) which requires two quantities, ϵ_c and ϵ_b, for c and b quarks respectively. Default parameters and ranges are given in table 8.7. Previous experiments have used the high degree of correlation between a and b to fix one and fit for the other. This reduces the parameter space somewhat during multi-parameter fits but causes fitted values to be method dependent. Two approaches are used to give values of $a \sim 0.5$, $b \sim 0.9$ [52] [50] [51] and $a \sim 0.18$,

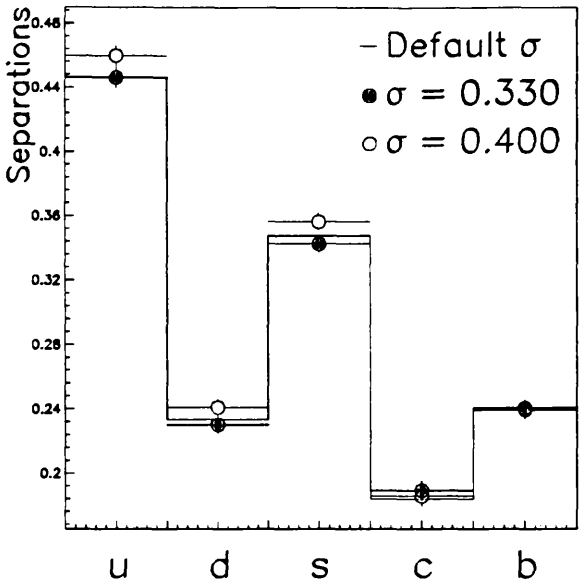

Quark separation values at $\kappa = 1.0$. Equivalent errors are involved in the calculation of the "Default" histogram as are included on plotted points.

Figure 8.5: Variation of individual quark separations with extreme values of σ.

Parameter	Range		
a fixed at 0.50, b varied	0.85	→	0.93
b fixed at 0.34, a varied	0.13	→	0.30
ϵ_c	0.002	→	0.071
ϵ_b	0.003	→	0.010

Table 8.7: Fragmentation function parameters and their ranges of variaton.

$b \sim 0.34$ [53] [49]. Due to their method dependence, using the latter values where b is held constant results in significant disagreement with ALEPH observables. The most fundamental of these is the increase in mean charged multiplicity of roughly one track per event. Further discrepancies from using such parameters are discussed in Section 8.4.5. ALEPH QCD parameters, fitted using the option of fixing a and fitting for b, results in a range of $0.85 \rightarrow 0.93$, taking into account results of similar studies [50] [51].

Ranges of ϵ_c and ϵ_b are chosen from values and errors in the ALEPH analysis of heavy flavour events [54] using the semi-leptonic decay tagging scheme. The errors contain both statistical and systematic contributions. The effects of the extreme values are shown in table 8.8. It is clear from the variation of $\sum_f q_f a_f v_f$, that keeping b fixed and varying a results in very large effects. Disagreement between data and Monte Carlo observables implies that such parameters should not be used here. For remaining changes, the effects are small, with the maximum shift to $\sum_f q_f a_f v_f$ remaining below 5% for the ϵ parameters and below 4% from varying b. This implies that, even with the dependence of the charge

Extremity	$\sum_f q_f a_f v_f$ (±0.004)	$\bar{q}$ (±0.002)	σ_{FB} (±0.002)	σ_Q (±0.001)	$F_\pm$ (±0.1)	Multiplicity (±0.01)
$a = 0.5, b = 0.85$	0.317	0.324	0.618	0.527	55.4	16.90
$a = 0.5, b = 0.93$	0.319	0.327	0.621	0.528	55.6	16.73
$a = 0.13, b = 0.34$	0.304	0.307	0.616	0.534	54.7	17.29
$a = 0.30, b = 0.34$	0.289	0.294	0.603	0.527	54.4	17.87
$\epsilon_c = 0.002$	0.314	0.330	0.630	0.537	55.4	16.45
$\epsilon_c = 0.071$	0.338	0.329	0.619	0.525	55.4	16.72
$\epsilon_b = 0.003$	0.340	0.333	0.629	0.534	55.4	16.48
$\epsilon_b = 0.010$	0.324	0.330	0.624	0.529	55.5	16.62
Default	0.328	0.330	0.624	0.529	55.4	16.60

Table 8.8: Summary of effects of variation in fragmentation function parameters.

flow on longitudinal momenta, the model is sufficiently constrained so as to have little effect.

Effects on individual separations are shown in figure 8.6 for the a, b and ϵ parameters. This shows that adjustments of a and b away from their defaults ($a = 0.5$ and $b = 1.0$) lead to a decrease in all light quark separations. Cases where a is fixed and b is varied lead to a substantially smaller degree of change. If b is varied then the decrease in q_u is partially compensated by a corresponding decrease in q_s while other separations remain stable. This leads to a small change in $\sum_f q_f a_f v_f$.

The extremities of variation in the ϵ parameters lead to a larger difference in q_c than in q_b. However, as the b quark is responsible for a larger fraction of the total asymmetry[3], the percentage change to $\sum_f q_f a_f v_f$ is larger.

8.4.3 Characteristics of Meson Production

Meson production in the LUND model is the dominant source of particles and occurs after breakage of colour strings in the *SF* phase of the model. The type of mesons produced, their spin and flavour characteristics, are governed by two types of parameters. Their values are constrained by theoretical considerations and more tightly by experimental observations from e^+e^- collisions [29]. Parameters and ranges are given in table 8.9. When a new $q\bar{q}$ pair is created at a point of string breakage, with a higher rank quark Q, the spin of the resulting $Q\bar{q}$ state can be 0 or 1. The proportions of available states leads to a simple prediction of the ratio of pseudoscalar to vector mesons of 1:3.

This difference in production rates is modified by contributions from the differing

[3]Due to its stronger couplings and lack of cancellation with the prospective top quark.

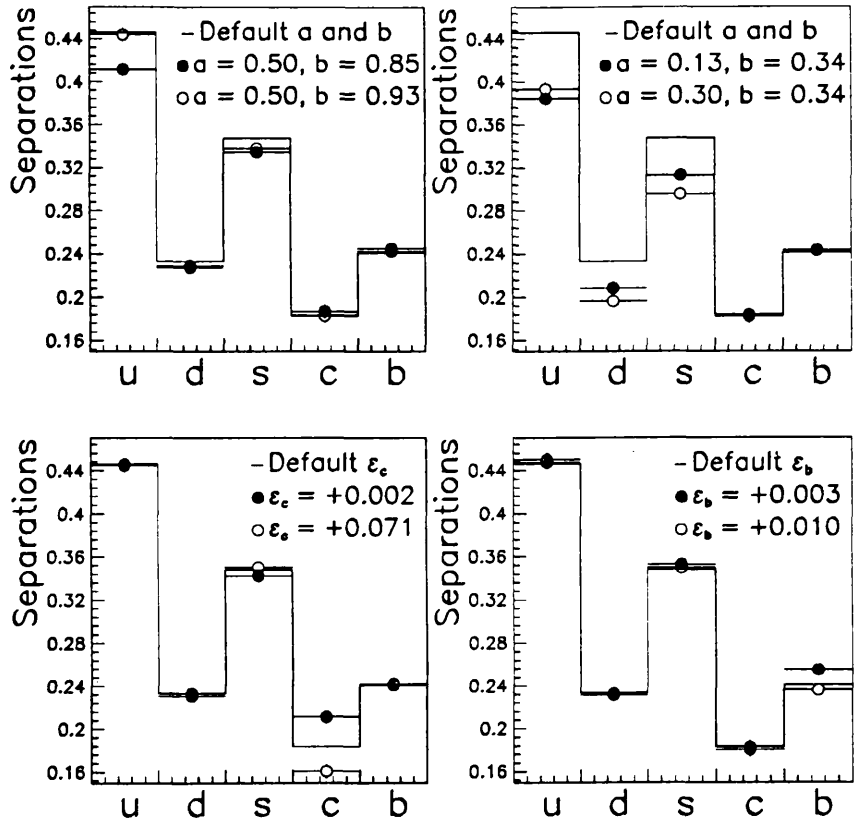

Quark separation values at $\kappa = 1.0$. Equivalent errors are involved in the calculation of the "Default" histogram as are included on plotted points.

Figure 8.6: Variation of the individual quark separations with the extreme values of the a, b, ϵ_c and ϵ_b parameter combinations.

Parameter	Range		
$\frac{V}{V+PS_{u,d}}$	0.30	→	0.75
$\frac{V}{V+PS_{s}}$	0.50	→	0.75
$\frac{V}{V+PS_{c,b}}$	0.65	→	0.80
$\frac{s}{u}$	0.27	→	0.40

Table 8.9: Meson characteristic paremeters and their ranges of variation.

masses of respective states. This has been parameterised [29] using the formulation :

$$\frac{\text{Pseudoscalar}}{\text{Vector}} = \frac{PS}{V} = \frac{1}{3}\left(\frac{M_V}{M_P}\right)^{\alpha} \text{ where } \alpha = 0.55\ (\pm 0.12) \tag{8.4}$$

for a range of meson states[4]. Mass effects have the tendency to increase the ratio $\frac{V}{V+PS}$, as masses of the two meson states become larger. Experimental measurements of $\frac{M_{\rho^0}}{M_{\pi^0}}$, $\frac{M_{K^{*0}}}{M_{K^0}}$ and $\frac{M_{D^{*0}}}{M_{D^0}}$ lead to $\frac{V}{V+PS}$ values of 0.53, 0.68 and 0.74 respectively according to relation (8.4). Theoretical limitations constrain the upper value for $\frac{V}{V+PS}$ to 0.75 from simple spin considerations and define the range of variation for light quark mesons. In the case of heavy quark mesons, $\frac{V}{V+PS}$ can rise as far as 0.80. Default parameters for the (u,d), (s) and (c,b) ratios are 0.5, 0.6 and 0.75 respectively with their ranges defined symmetrically around these defaults.

The flavour composition of mesons in LUND is determined by quantum tunnelling arguments which suppress heavier quark production due to the larger mass. As quark masses are poorly known, this leads to an uncertainty in the degree of suppression. With (u,d), (s), (c) and (b) masses of 0.325, 0.5, 1.6 and 5.0 GeV respectively (as assumed by LUND) the suppressions as are given previously in equation (3.2). In the LUND model, uncertainties on u, d and s masses are embodied in a single parameter, the $\frac{s}{u}$ ratio, to determine meson flavours. The default value of 0.30 agrees with the average measured value from lower energy experiments, 0.33 ($\pm$0.02) [29]. The range used here includes measurements from PEP and PETRA experiments, implying uncertainties of $\frac{s}{u}$ in the range $\sim$ 0.26 $\rightarrow$ 0.37 [29], while including values up to 0.40 allows for any possible increase in s production at LEP.

The effects of changes to the fragmentation in these ranges are shown in table 8.10. Changes to the $\frac{V}{V+PS}$ ratios are dominated by the effects of the $\frac{s}{u}$ ratio. The variation of $\sum_f q_f a_f v_f$ from changing the $\frac{s}{u}$ ratio from the world average 0.33 to 0.40 is $\sim$ 8%, more than double that of contributions from any other source. Effects of various spin ratios are significant only for the (u,d) and (c,b) cases.

Shifts in individual separations for $\frac{V}{V+PS}$ and $\frac{s}{u}$ changes are shown in figure 8.7 and again demonstrate that changes to $\sum_f q_f a_f v_f$ arise from small changes in several flavours. Changes from $\frac{V}{V+PS}$ ratios for (u,d), (s) and (c,b) flavoured mesons are not limited to their particular flavour. In the case of the $\frac{V}{V+PS}_{u,d}$ and $\frac{V}{V+PS}_{c,b}$ ratios, many of the changes are in the appropriate flavour separation, however in the case of the $\frac{V}{V+PS}_{s}$ ratio, the dominant change is in the c separation while the s channel remains unaffected. This is indicative of the importance of strange meson production to c charge retention and differences between decays of the spin states.

The $\frac{s}{u}$ ratio effect on individual separations explains its large shift of $\sum_f q_f a_f v_f$. The "up-type" (u and c) flavour separations rise with increasing $\frac{s}{u}$, while the "down-type" flavours behave oppositely. In the flavour summation, the relatively small changes per

[4]Note that $\frac{V}{V+PS} \equiv \left(1+\frac{PS}{V}\right)^{-1}$ for comparison.

Extremity	$\sum_f q_f a_f v_f$ (± 0.004)	$\bar{q}$ (± 0.002)	σ_{FB} (± 0.002)	σ_Q (± 0.001)	$F_\pm$ (± 0.1)	Multiplicity (± 0.01)
$\frac{V}{V+PS}_{u,d} = 0.30$	0.338	0.342	0.636	0.537	55.6	16.05
$\frac{V}{V+PS}_{u,d} = 0.75$	0.325	0.318	0.611	0.522	55.2	17.22
$\frac{V}{V+PS}_{s} = 0.50$	0.329	0.334	0.629	0.533	55.4	16.49
$\frac{V}{V+PS}_{s} = 0.75$	0.325	0.328	0.618	0.524	55.4	16.80
$\frac{V}{V+PS}_{c,b} = 0.65$	0.318	0.333	0.625	0.529	55.6	16.61
$\frac{V}{V+PS}_{c,b} = 0.80$	0.335	0.326	0.623	0.530	55.4	16.61
$\frac{s}{u} = 0.27$	0.344	0.328	0.622	0.528	55.5	16.77
$\frac{s}{u} = 0.40$	0.293	0.329	0.625	0.532	55.3	16.33
Default	0.328	0.330	0.624	0.529	55.4	16.60

Table 8.10: Effects of changing meson-characteristic parameters.

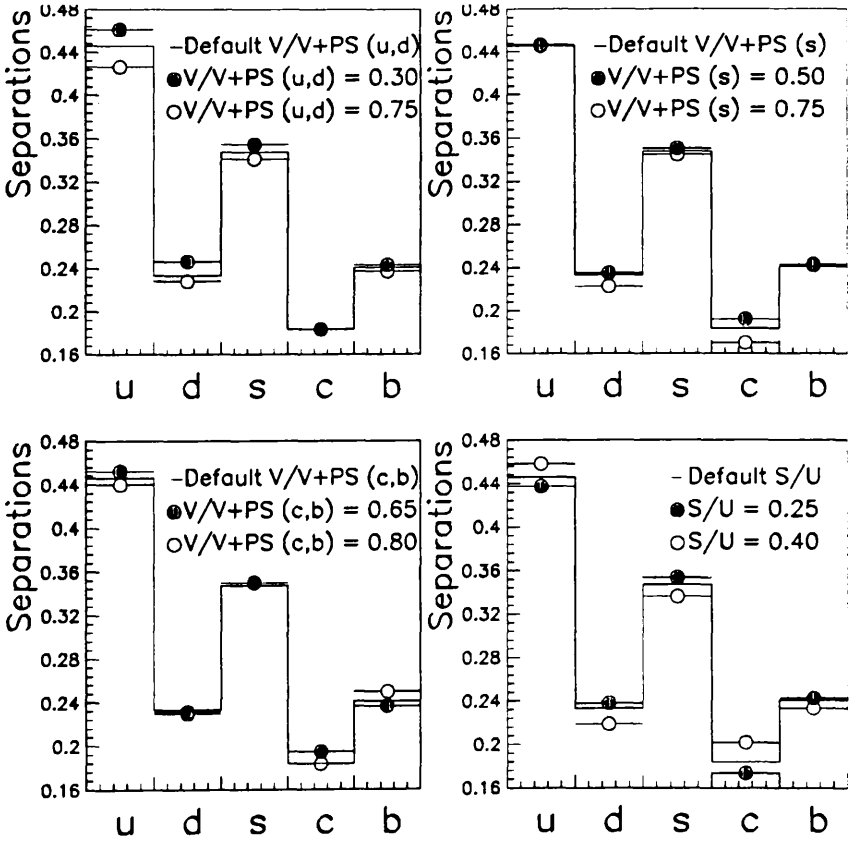

Quark separation values at $\kappa = 1.0$. Equivalent errors are involved in the calculation of the "Default" histogram as are included on plotted points.

Figure 8.7: Variation of the individual quark separations with the extreme values of the $\frac{V}{V+PS}$ ratios and the fraction of strange quarks from the sea ($\frac{s}{u}$).

flavour are combined, and enhance the total difference. The flavour summation of $\bar{q}$ is insensitive to this because the direction of change is not important.

8.4.4 Effect on Observables

The degree to which fragmentation changes may be visible in reconstructed events depends upon the choice of observables. Those selected in table 8.3 are chosen because of :

(a) The accuracy with which they can be measured.

(b) Their sensitivity to the quark separations.

(c) Their insensitivity to detector effects.

The total effect of the detector and particle decays on quantities such as σ_{FB}, σ_Q and $F_\pm$ is less than 3% while remaining accurate to $\pm 0.4\%$. Both $\bar{q}$ and the mean charged multiplicity change by the order of $\sim 10\%$ with measurement accuracies of 1% and 0.05% respectively.

The uncertainty on observables at the generator level is extrapolated from the reconstructed level by taking the difference between data and reconstructed Monte Carlo as a percentage. Errors in data and reconstructed Monte Carlo are then combined with this in quadrature. This defines a range of tolerance around observables at the generator level which is intended to show the sensitivity of the quantities while indicating how severely the fragmentation is being distorted. The effects of fragmentation on observables $\bar{q}$, $F_\pm$, σ_{FB} and σ_Q, shown in figures 8.8 and 8.9, show that both $\bar{q}$ and $F_\pm$ are insensitive to fragmentation changes of this magnitude. This is with the exception of varying a while keeping b fixed in the context of a different method of multi-parameter fit to that used by ALEPH.

The widths, σ_{FB} and σ_Q, are more sensitive to fragmentation changes due to their greater measurement accuracy. Several parameter variations exceed the 2σ range marked. The mean charged multiplicity suffers from a significant discrepancy of ~ 0.09 tracks per event between data and reconstructed Monte Carlo while being measurable with an accuracy of ~ 0.01. The values under various changes in fragmentation , shown in figure 8.10, demonstrate that the multiplicity is both sensitive and accurate. However, it cannot be related directly to $\sum_f q_f a_f v_f$.

To summarise; the effect on observables is sufficient to demonstrate that significant distortions are made when varying fragmentation parameters in the ranges studied. However, the close interdependence of parameters, and their effect on several flavours at once, limits their usefulness. The large disagreement induced by variation of the a parameter is an exception, where the fact that the central value of the parameter lies far from the default range indicates that this is clearly unrepresentative of data and reconstructed Monte Carlo.

Percentage changes to $\sum_f q_f a_f v_f$ from extremities of fragmentation parameters are summarised in table 8.11. They are determined by the maximum shift to $\sum_f q_f a_f v_f$ due

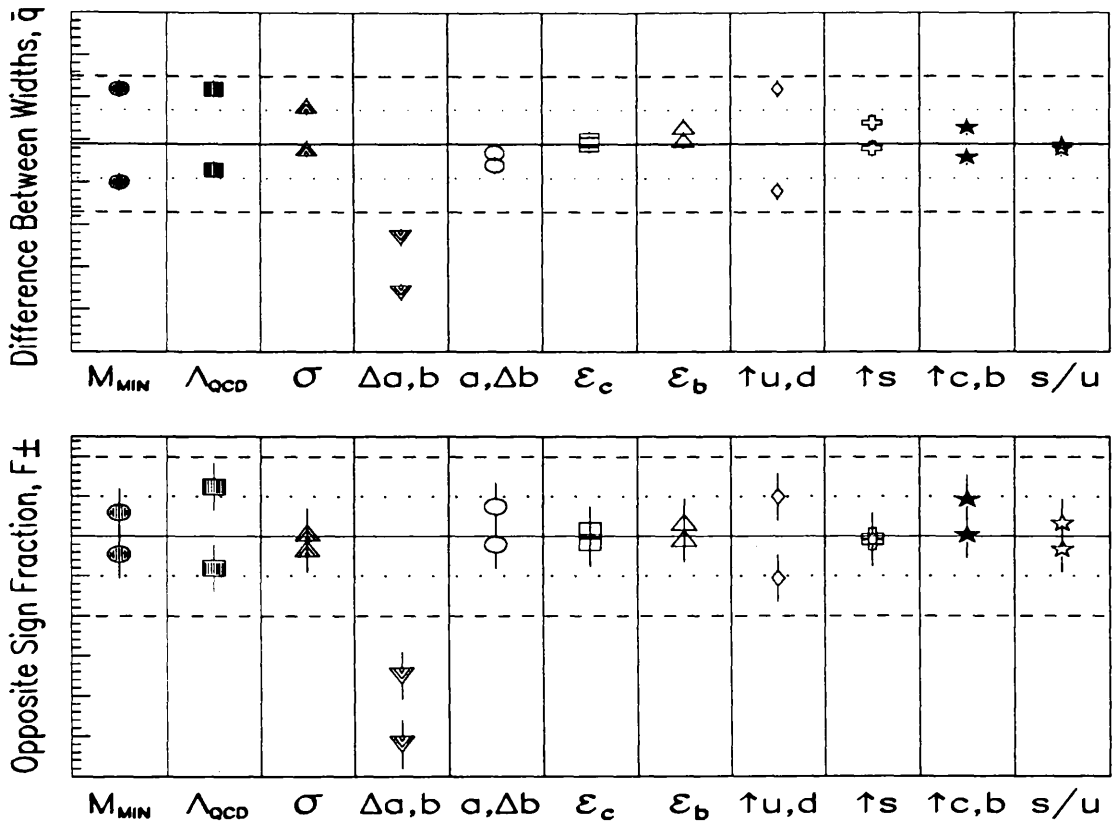

The x-axis represents the various types of fragmentation parameter varied as discussed in previous sections. These are in order of appearance; (a) M_{min}, (b) Λ_{QCD}, (c) σ, (d) varying a while keeping b fixed, (e) varying b while keeping a fixed, (f) ϵ_c, (g) ϵ_b, (h) $\frac{V}{V+PS}_{u,d}$, (i) $\frac{V}{V+PS}_{s}$, (j) $\frac{V}{V+PS}_{c,b}$ and (k) the $\frac{s}{u}$ ratio. Horizontal lines indicate the 1 and 2σ values from data and the reconstructed Monte Carlo.

Figure 8.8: Effects of modified fragmentation schemes on $\bar{q}$ and $F_{\pm}$.

to a given parameter change, and are defined symmetrically for reasons of simplicity and conservatism.

The $\frac{s}{u}$ value of $\frac{\Delta\overline{Q^{ref}_{FB}}}{Q^{ref}_{FB}}$ is taken as the maximum variation of $\sum_f q_f a_f v_f$ relative to $\frac{s}{u} = 0.33$, as this is the world average[5].

8.4.5 Behaviour of Separations and $\sum_f q_f a_f v_f$

The manner in which some LUND parameters change the quark separations is of interest when using the charge flow method. The distinctive behaviour of sensitivities for each flavour, and the wish to minimise the fragmentation systematic uncertainty, are two reasons for this interest.

[5]The reconstructed Monte Carlo sample was fragmented using a value of 0.30 and is used as the generator default as a result. This calculation assumes a linear dependence of $\sum_f q_f a_f v_f$ on the $\frac{s}{u}$ ratio and is verified in section 8.4.5.

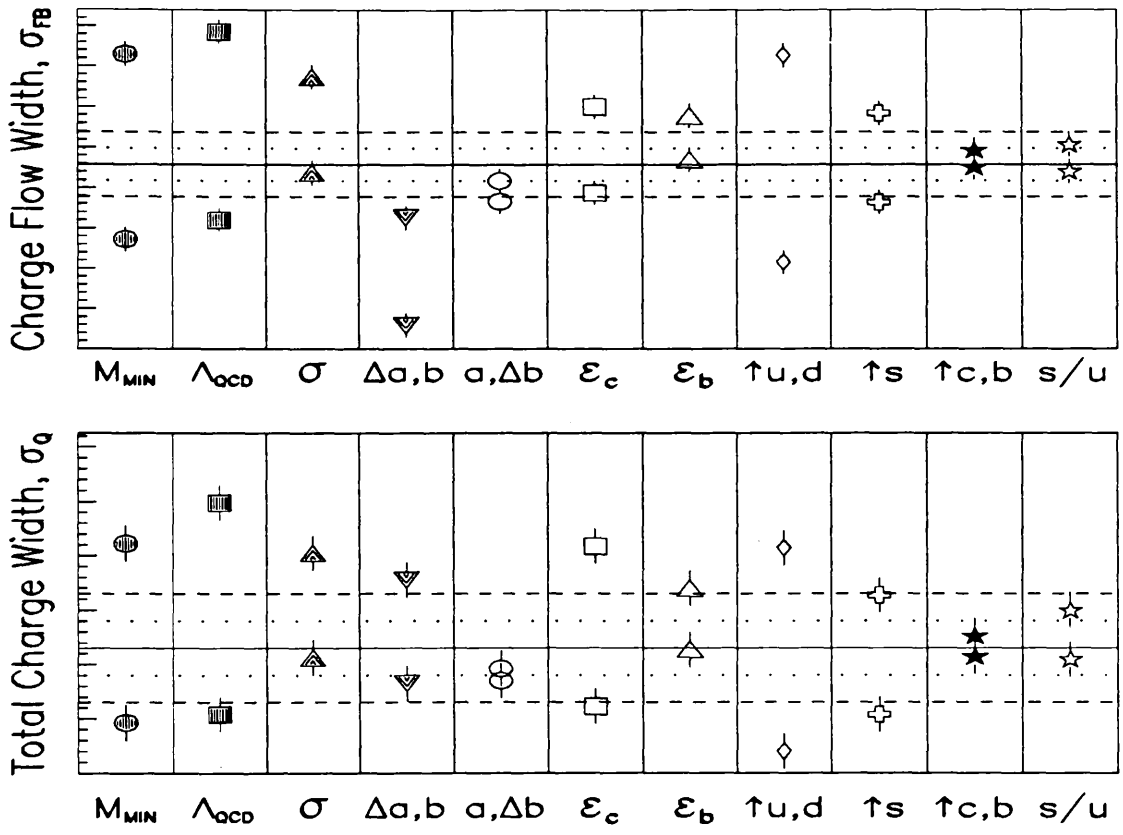

The x-axis represents the various types of fragmentation parameter varied as discussed in previous sections. These are in order of appearance; (a) M_{min}, (b) Λ_{QCD}, (c) σ, (d) varying a while keeping b fixed, (e) varying b while keeping a fixed, (f) ϵ_c, (g) ϵ_b, (h) $\frac{V}{V+PS}_{u,d}$, (i) $\frac{V}{V+PS}_{s}$, (j) $\frac{V}{V+PS}_{c,b}$ and (k) the $\frac{s}{u}$ ratio. Horizontal lines indicate the 1 and 2σ values from data and the reconstructed Monte Carlo.

Figure 8.9: Effects of modified fragmentation schemes on charge distribution widths, σ_{FB} and σ_Q.

Fragmentation uncertainties are κ dependent, as shown in figure 8.11, which represents the mean shift of $\sum_f q_f a_f v_f$ with κ as the LUND fragmentation is distorted. As shown, the mean shift drops rapidly with κ in the region $\sim 0.2 - 1.8$ before it stabilises. By avoiding $0.2 \leq \kappa \leq 1.0$, a reduction of $\sim 23\%$ in the mean ΔQ_{FB}^{ref} is realised.

It is clear from the preceding section that large contributions to the fragmentation systematic error arise from uncertainties in parameters Λ_{QCD}, ϵ_c, ϵ_b, $\frac{V}{V+PS}_{u,d}$, $\frac{V}{V+PS}_{c,b}$ and are dominated by that from the $\frac{s}{u}$ ratio. General characteristics of changes to the individual separations are studied by varying a single parameter and studying its effect on individual flavour separations.

The purpose of this section is to understand how $\sum_f q_f a_f v_f$ varies with important fragmentation parameters and to indicate how the systematic error might be reduced.

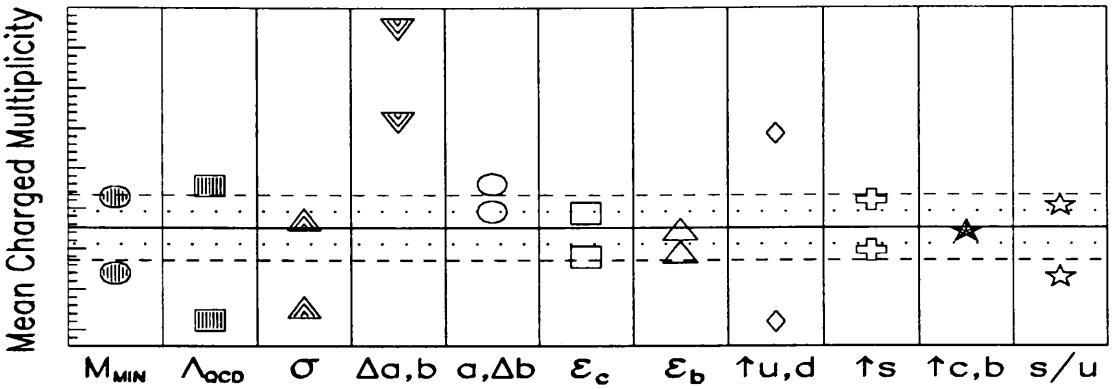

The x-axis represents the various types of fragmentation parameter varied as discussed in previous sections. These are in order of appearance; (a) M_{min}, (b) Λ_{QCD}, (c) σ, (d) varying a while keeping b fixed, (e) varying b while keeping a fixed, (f) ϵ_c, (g) ϵ_b, (h) $\frac{V}{V+PS}_{u,d}$, (i) $\frac{V}{V+PS}_{s}$, (j) $\frac{V}{V+PS}_{c,b}$ and (k) the $\frac{s}{u}$ ratio. Horizontal lines indicate the 1 and 2σ values from data and the reconstructed Monte Carlo.

Figure 8.10: Effects of modified fragmentation schemes on the mean charged multiplicity at the generator level.

Parameter	Range	$\frac{\Delta\overline{Q_{FB}^{ref}}}{\overline{Q_{FB}^{ref}}}$ (%)
Λ_{QCD}	0.26 - 0.40 GeV	2.3
M_{min}	1.0 - 2.0 GeV	1.6
σ	0.34 - 0.40	1.4
b	0.85 - 0.93	3.4
ϵ_c	0.002 - 0.071	4.2
ϵ_b	0.003 - 0.10	3.9
$\frac{V}{V+PS}_{u,d}$	0.3 - 0.75	3.0
$\frac{V}{V+PS}_{s}$	0.5 - 0.75	0.9
$\frac{V}{V+PS}_{c,b}$	0.65 - 0.8	2.8
$\frac{s}{u}$	0.25 - 0.40	7.7

Table 8.11: Variation in the expected value of $\overline{Q_{FB}^{ref}}$ due to extreme changes in fragmentation parameters. The statistical error on uncertainties is $\pm 1.2\%$.

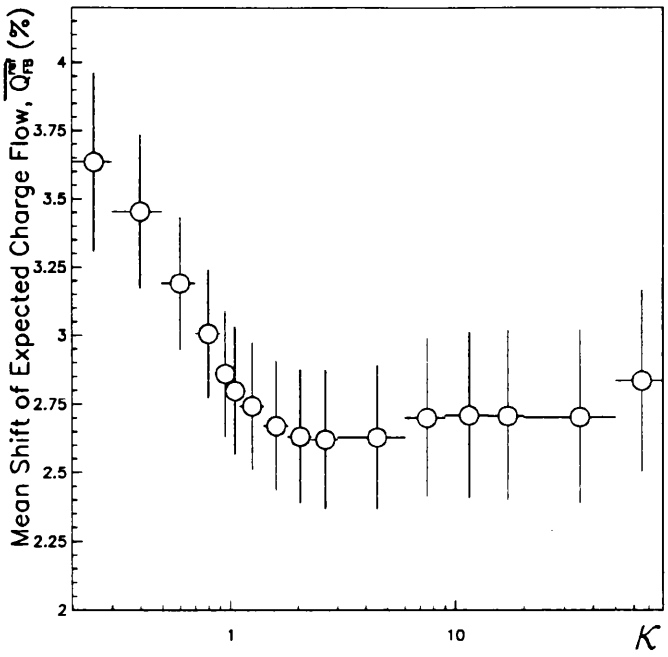

The mean percentage shift in the value of $\overline{Q_{FB}^{ref}}$ is calculated using information from 50 independent samples of events with modified fragmentation parameters within ranges given in table 8.11.

Figure 8.11: Mean percentage shift to $\sum_f q_f a_f v_f$ as a function of κ from modified LUND fragmentations.

Λ_{QCD} Variation

Separations of light quarks are most dependent on Λ_{QCD}, although it affects all flavours to some extent. This is shown in figure 8.12 where a clear reduction in light quark separations is apparent with increasing Λ_{QCD}. This may be understood as increasing the value of α_s, which increases the number of gluons and quarks produced during parton shower development. This *reduces* the information retained concerning the charge of the parent quark and is consistent with the reduction in size of the effect as quark masses increase. It is expected that, the heavier the quark, the more likely it is to retain parent quark information as it is influenced less by lighter daughters which are produced.

Changes to $\sum_f q_f a_f v_f$ with Λ_{QCD} in figure 8.12, show that the maximal difference does not occur at either extremity of the range, but close to $\Lambda_{QCD} = 0.295$ and so increases $\frac{\Delta\overline{Q_{FB}^{ref}}}{Q_{FB}^{ref}}$ for this parameter. The small rise in $\sum_f q_f a_f v_f$ at this value of Λ_{QCD} is largely due to statistical scatter in the variation of the d quark separation.

ϵ Variation

Fragmentation functions of heavy quarks govern the amount of momentum given to particles during string fragmentation. The charge flow method depends on how this momentum splitting is carried out, as it directly affects the momentum ordering of jet fragments. If

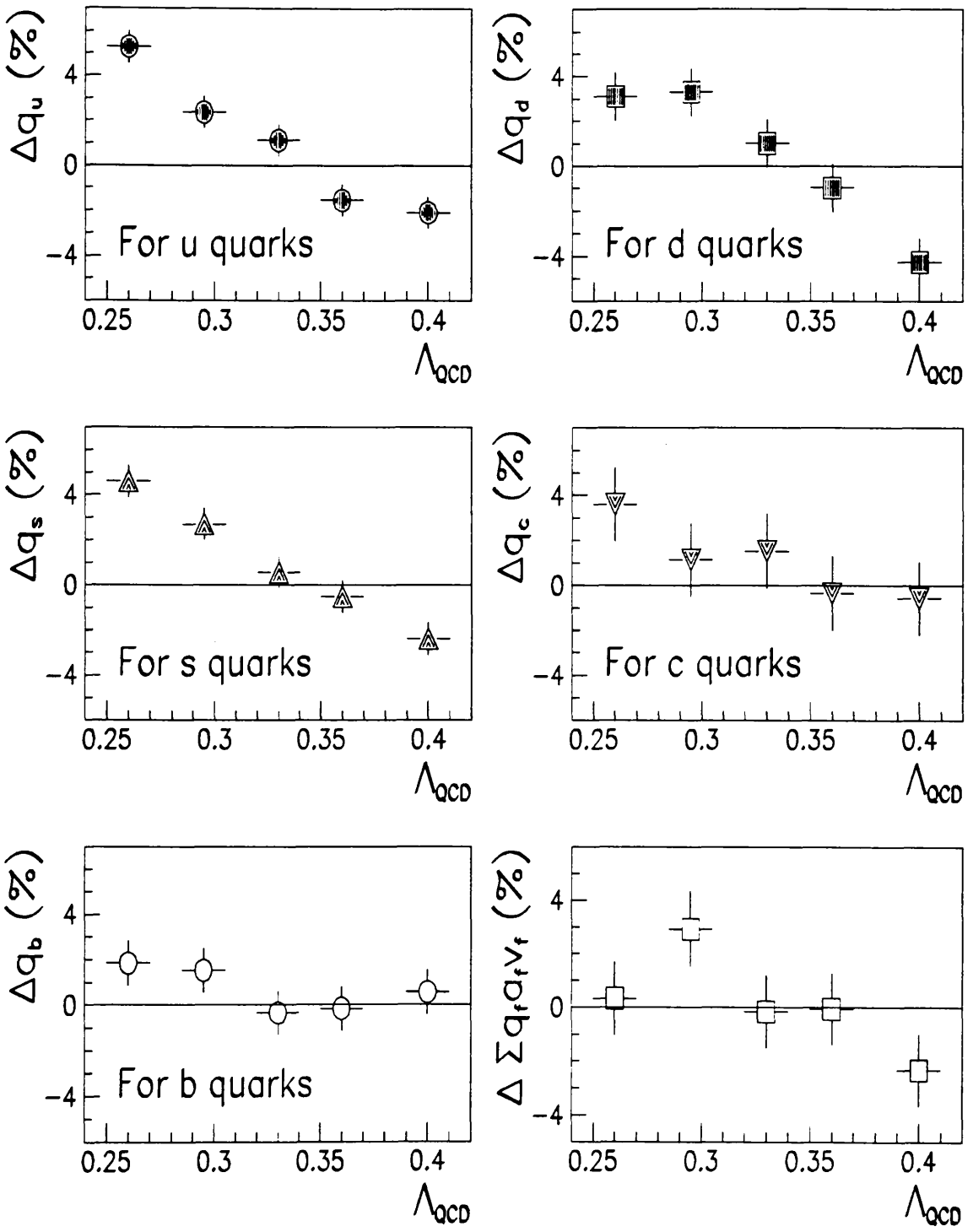

Separation changes are calculated as the percentage shift from default values at $\kappa = 1.0$ and are plotted with same scales throughout.

Figure 8.12: Relative shifts in individual quark separations and expected charge flow $\propto \sum_f q_f a_f v_f$ as a result of varying Λ_{QCD} .

a higher momentum is given to primary particles, ie. the *harder* the fragmentation, the greater the probability of retaining parent quark charges in leading jet particles. The Peterson fragmentation function contains the parameter, ϵ, which determines the hardness of fragmentation for c and b quarks. Varying the two parameters within ranges described previously results in variation of q_c and q_b as shown in figure 8.13. These indicate that as ϵ

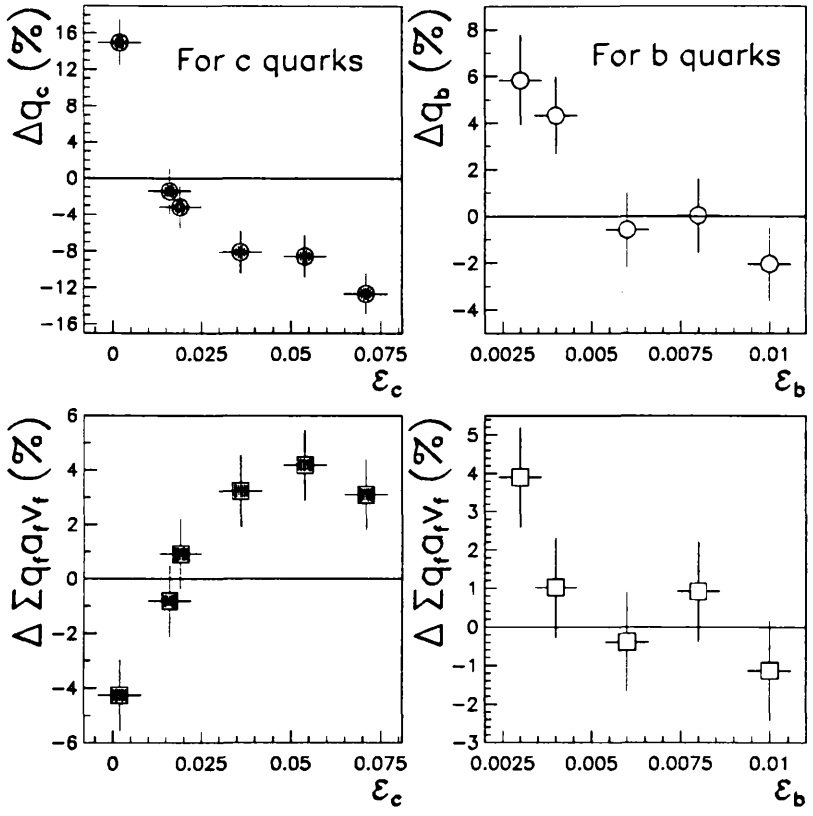

Separation changes are calculated as the percentage shift from default values at $\kappa = 1.0$.

Figure 8.13: Relative shifts in individual quark separations and expected charge flow $\propto \sum_f q_f a_f v_f$ as a result of varying ϵ_c and ϵ_b.

increases, the separations decrease as expected. This is due to softening of fragmentation as ϵ increases. The effects of such changes to $\sum_f q_f a_f v_f$ are also shown in figure 8.13, where the difference in the sign of gradients with ϵ_c and ϵ_b is due to the sign of the two flavours in the summation.

Within the ranges of ϵ_c and ϵ_b, the c quark separation exhibits the largest relative degree of variation, although absolute changes are similar and Δq_c is amplified by the smaller value of q_c generally. The maximal change to $\sum_f q_f a_f v_f$ as a result of ϵ_c is at the extreme values, although a slight enhancement is seen at $\epsilon_c \sim 0.055$ due to statistical fluctuations in other flavours.

$\frac{V}{V+PS}$ Variation

The method of controlling spin characteristics of mesons by using 3 independent parameters for light, strange and heavy mesons has several consequences for the charge flow method. Increasing the value of $\frac{V}{V+PS}$ generally enhances production of heavier mesons. This reduces the remaining energy of the jet system where there are two competing effects :

(a) Less particles are produced so that charge reconstruction is easier (see figure 4.13).

(b) Heavy meson decays are more isotropic and so daughter charge weights are reduced making charge reconstruction more difficult.

These effects act in opposing directions so that the behaviour of separations with increasing $\frac{V}{V+PS}$ represents the interplay between them.

Since heavy meson production is thought to be entirely as a result of the parent quark, then changing $\frac{V}{V+PS}_{c,b}$ is expected to affect c and b separations only. The effects of $\frac{V}{V+PS}_{u,d}$ are likely to be more widespread due to lighter mesons produced during fragmentation of all flavours. The observed effects on separations and $\sum_f q_f a_f v_f$ are shown in figures 8.14 and 8.15. From these it is apparent that in most cases an increase in vector meson production leads to a decrease in quark separations. The combined effect on $\sum_f q_f a_f v_f$ is confined to the relative difference between rates of decrease of cancelling flavours. For the $\frac{V}{V+PS}_{u,d}$ ratio, the value of $\sum_f q_f a_f v_f$ is seen to fall, while in the case of $\frac{V}{V+PS}_{c,b}$, the opposite occurs.

$\frac{s}{u}$ Variation

From table 8.11 and figure 8.7, it is clear that the $\frac{s}{u}$ ratio represents the largest uncertainty on $\sum_f q_f a_f v_f$ whereas its effect on observables remains largely invisible due to cancellation between flavours. The range of variation is large and is mainly due to a lack of strong theoretical constraints and experimental measurements of strange particle production at LEP energies.

Changes to component separations and $\sum_f q_f a_f v_f$ as a function of $\frac{s}{u}$ are shown in figure 8.16 and indicate the opposite behaviour of up and down-type quarks. This confirms the effects observed at extremities of the range. The behaviour of (u,c) and (d,s,b) flavours maximally distorts the value of $\sum_f q_f a_f v_f$ because of their opposite behaviour. The relative shift in the value of q_c is the largest of all flavours, however the absolute change remains roughly constant for all flavours. The variation of $\sum_f q_f a_f v_f$ with $\frac{s}{u}$ is linear with the world average ($0.33\ (\pm 0.02)$) marked as the vertical line inside the dotted 1σ band. The variation of $\sum_f q_f a_f v_f$, using a straight line parameterisation,in this 1σ region is $\pm 2\%$ whereas the total variation within $0.26 \rightarrow 0.40$ is $^{+5}_{-11}\%$.

Although individual separations suffer dramatic effects, observables are almost entirely unaffected. The mean charged multiplicity is the only observable used which displays any corresponding variation. This varies smoothly between 16.33 and 16.77 as $\frac{s}{u}$ increases.

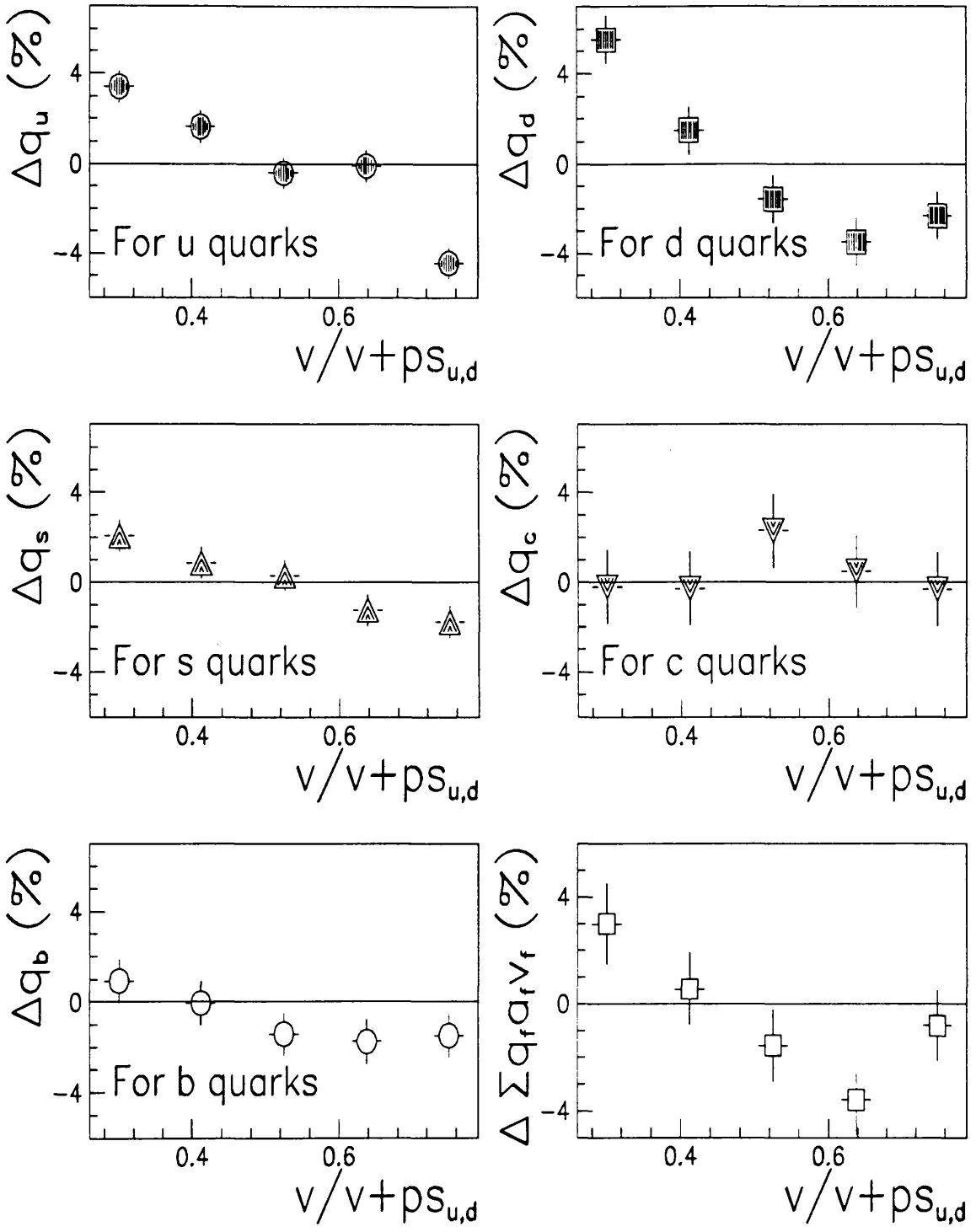

Separation changes are calculated as the percentage shift from default values at $\kappa = 1.0$ and are plotted with same scales throughout.

Figure 8.14: Relative shifts in individual quark separations and expected charge flow $\propto \sum_f q_f a_f v_f$ as a result of varying $\frac{V}{V+PS_{u,d}}$.

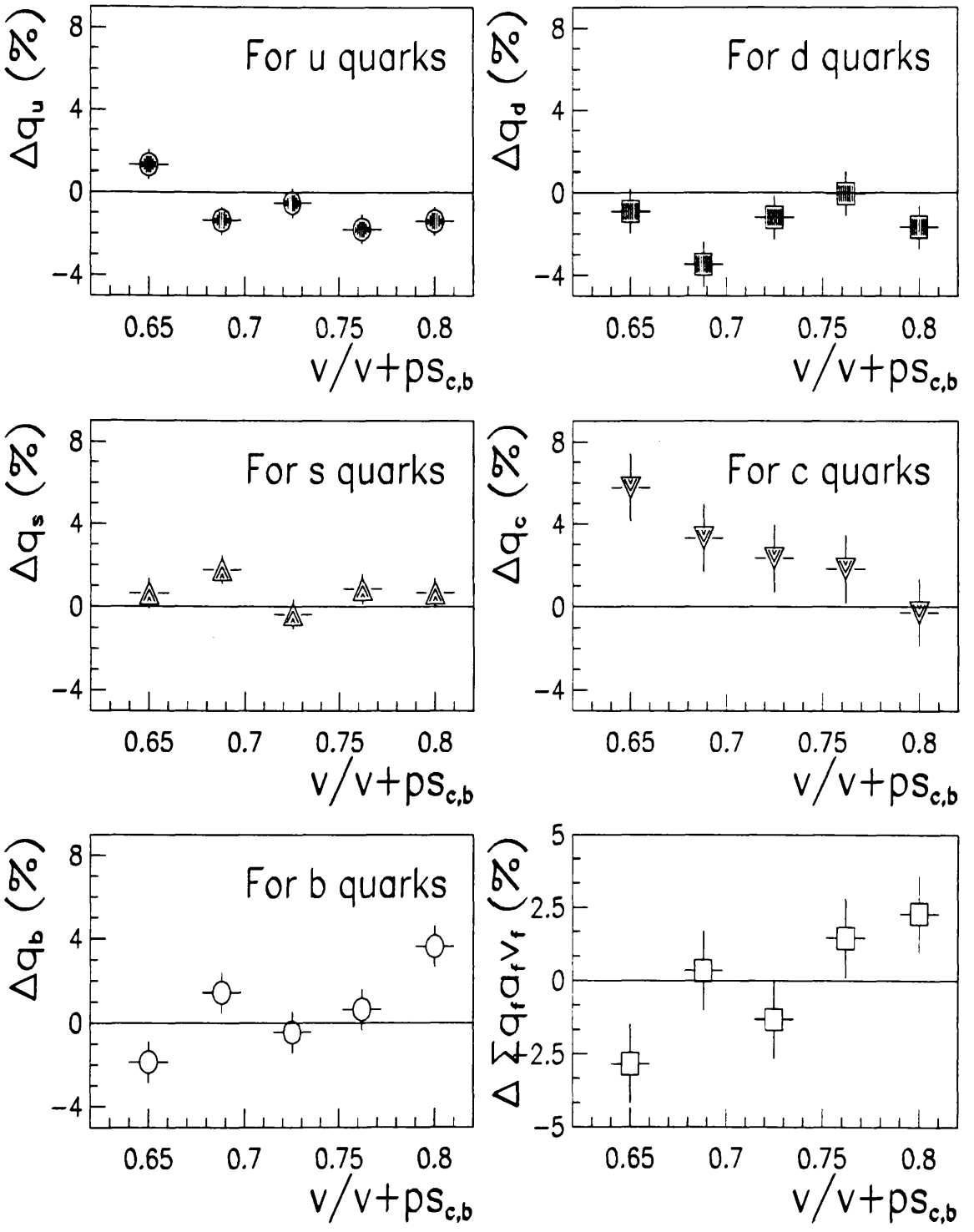

Separation changes are calculated as the percentage shift from default values at $\kappa = 1.0$ and are plotted with same scales throughout.

Figure 8.15: Relative shifts in individual quark separations and expected charge flow $\propto \sum_f q_f a_f v_f$ as a result of varying $\frac{V}{V+PS}_{c,b}$.

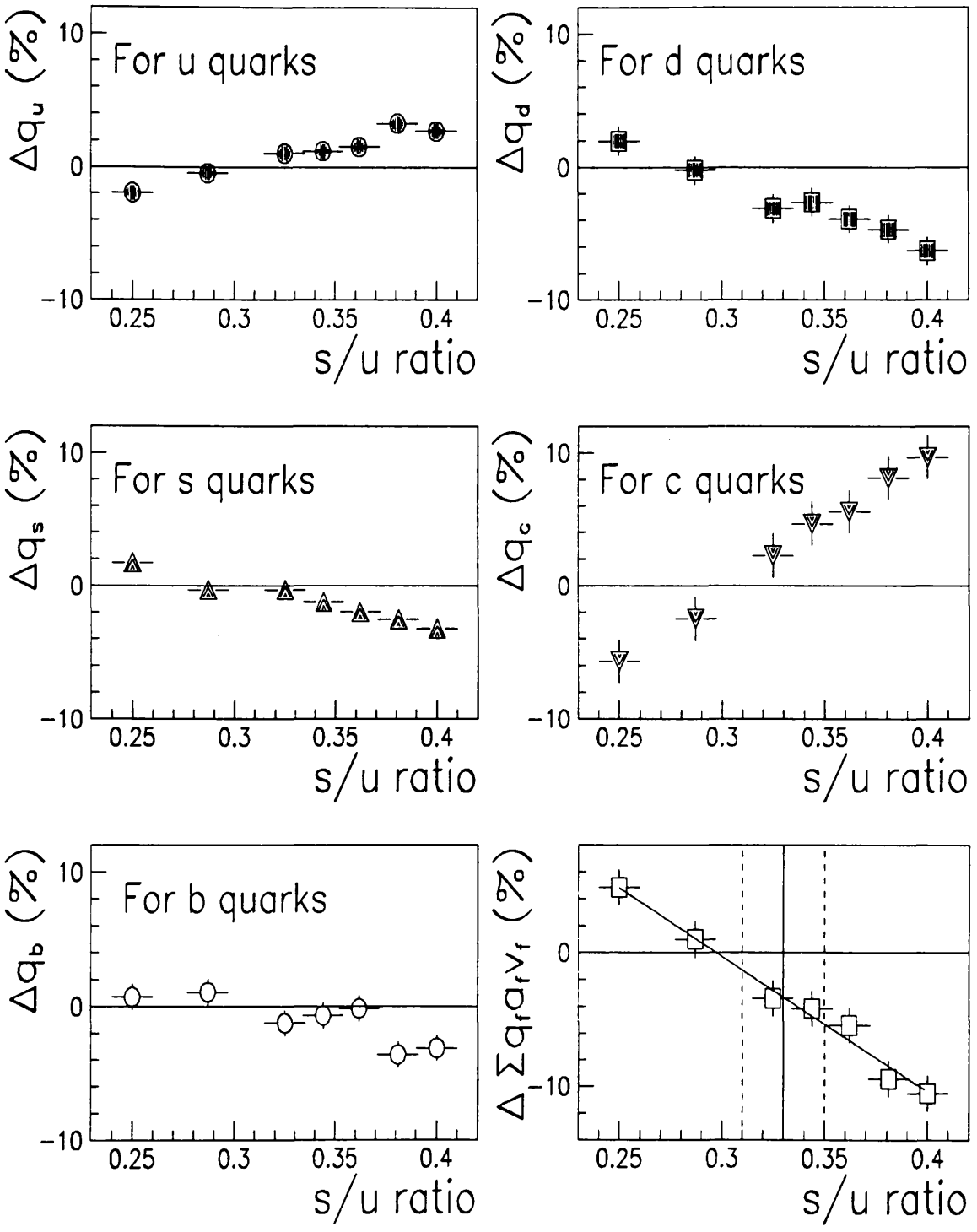

Separation changes are calculated as the percentage shift from default values at $\kappa = 1.0$ and are plotted with same scales throughout.

Figure 8.16: Relative shifts in individual quark separations and expected charge flow $\propto \sum_f q_f a_f v_f$ as a result of varying the $\frac{s}{u}$ ratio.

The number of strange mesons produced also increases and is reflected by the mean kaon rate[6] shown in figure 8.17. The determination of $\frac{s}{u}$ is often carried out using the mean

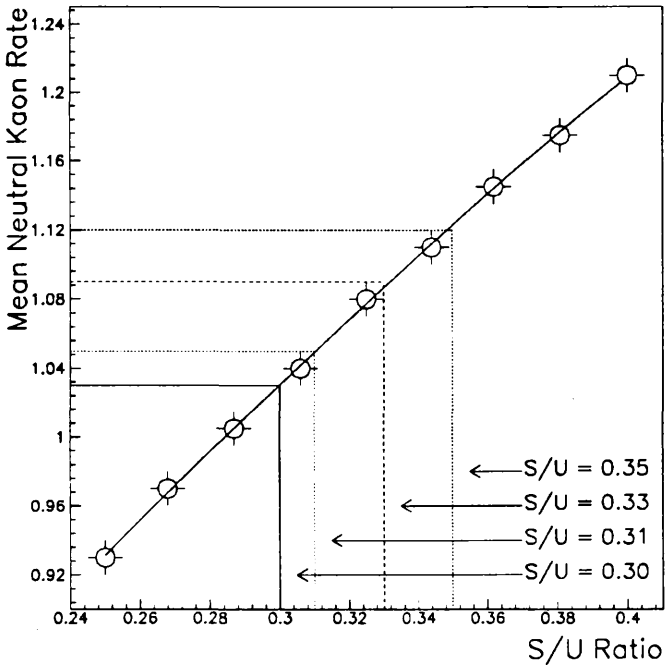

Neutral kaons are counted at the generator level with no selection criterion applied using Monte Carlo "truth" only. The fitted curve represents a quadratic polynomial and is used to indicate default and world average values of $\frac{s}{u}$ with their 1σ bands.

Figure 8.17: Generated neutral kaon rate as a function of $\frac{s}{u}$ ratio.

$\frac{K}{\pi}$ rates, or the mean kaon rate itself, when compared to expected LUND production. Figure 8.17 indicates that measured values within an error of $\sim \pm 15\%$ would serve to reduce the large range of $\frac{s}{u}$ values used here.

8.5 Effects of $B^0 - \overline{B^0}$ Mixing

As introduced briefly in section 4.6, the effects of B^0 mixing on a combined quark asymmetry are expected to be small. The effects are interpreted here as additional contributions to the systematic error from limited knowledge of the degree of mixing in the B_d^0 and B_s^0 systems. The purpose of this section is to examine quantitatively how mixing affects the b quark separation and the magnitude of uncertainties on $\overline{Q_{FB}^{ref}}$ which result.

8.5.1 Mixing Parameters and Previous Results

There are several sources of information concerning mixing of B^0 mesons [55]. Results come either from e^+e^- colliders operating around the $\Upsilon(4S)$ resonance or from high-

[6] Calculated as the mean number of neutral kaons produced per event at the generator level.

energy $p\bar{p}$ or e^+e^- experiments. An essential difference between the two types of results concerns their production of different meson flavours. High-energy experiments such as UA1 [56] produce both B_d^0 and B_s^0 mesons while at the $\Upsilon(4S)$ the $B_s^0 - \overline{B_s^0}$ decay mode is kinematically forbidden. Several parameters are used to define and measure the degree of mixing, the most common being χ defined in (8.5).

$$\chi = \frac{\Gamma\left(B^0 \to \overline{B^0}\right) + \Gamma\left(\overline{B^0} \to B^0\right)}{\Gamma\left(b \to \text{all}\right)} \tag{8.5}$$

χ may be split into its component parts due to different flavoured mesons, namely :

$$\chi = R_d \chi_d + R_s \chi_s \tag{8.6}$$

where R_d and R_s are the relative rates of producing d and s quarks from the sea as the b quark fragments. This is estimated from tunnelling mechanisms within the framework of the string model, or from experimental measurements [29], both of which give consistent results. Thus equation (8.5) becomes :

$$\chi = \frac{\chi_d + 0.3\chi_s}{2.3} \tag{8.7}$$

ARGUS [57] and CLEO [58] measurements give values of :

$$\chi_d = 0.16\,(\pm 0.05) \qquad \text{(ARGUS)} \tag{8.8}$$

$$\chi_d = 0.16\,\left(^{+0.05}_{-0.06}\right) \qquad \text{(CLEO)} \tag{8.9}$$

respectively, resulting in a combined value of $0.16\,(\pm 0.04)$ from [55]. The average $B^0 - \overline{B^0}$ mixing parameter χ is measured by UA1 [56] and ALEPH [48] to be :

$$\chi = 0.16\,(\pm 0.06) \qquad \text{(UA1)} \tag{8.10}$$

$$\chi = 0.13\,(\pm 0.03) \qquad \text{(ALEPH)} \tag{8.11}$$

respectively. These measurements unfortunately provide a poor measurement of χ_s, giving $\chi_s = 0.46\,(\pm 0.27)$.

8.5.2 Mixing Dependence of q_b and $\sum_f q_f a_f v_f$

As discussed above, it is the combined uncertainty of parameters χ_d and χ_s which is important. The range of uncertainty associated with these parameters and their effects on $\sum_f q_f a_f v_f$ and observables are given in table 8.12. These show that mixing effects are small, as expected, with changes to $\sum_f q_f a_f v_f$ of 4% at extremes of χ_d and 1.2% for χ_s. This is expected for three reasons (a) only one flavour being affected, (b) only a fraction of those events mixing and (c) mixing having a relatively small effect on jet charges anyway. This is shown for $\kappa = 1.0$ in figure 8.18. For the purpose of parameterising the effect of mixing parameters, it is interesting to study the effect on $\sum_f q_f a_f v_f$ as a

Extremity	$\sum_f q_f a_f v_f$ (± 0.004)	$\bar{q}$ (± 0.002)	σ_{FB} (± 0.002)	σ_Q (± 0.001)	$F_\pm$ (± 0.1)	Multiplicity (± 0.01)
$\chi_d = 0.10$	0.341	0.333	0.625	0.528	55.6	16.61
$\chi_d = 0.22$	0.323	0.333	0.625	0.529	55.5	16.59
$\chi_s = 0.10$	0.331	0.335	0.626	0.528	55.7	16.61
$\chi_s = 0.50$	0.332	0.334	0.625	0.528	55.5	16.61
Default	0.328	0.330	0.624	0.529	55.4	16.60

Table 8.12: Summary of effects of varying mixing parameters, χ_d and χ_s.

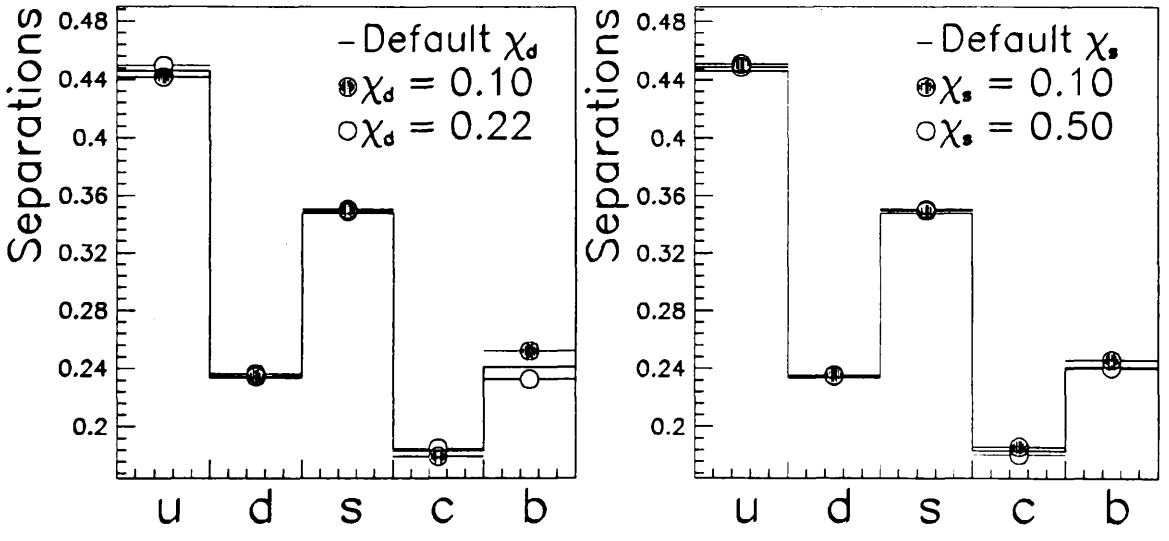

Figure 8.18: Variation of separations at $\kappa = 1.0$ for extreme values of mixing parameters, χ_d and χ_s.

function of χ_d and χ_s. This allows future mixing measurements to limit the range used here, and highlights the possibility of using the charge flow method itself to measure mixing in selected b events. Variation of q_b with χ_s and χ_d is shown in figure 8.19. This indicates that it is the variation of χ_d, and not χ_s, which dominates the uncertainty on q_b and hence $\sum_f q_f a_f v_f$. This is most likely as a result of tunnelling suppression of B_s^0 production during fragmentation combined with differences between the decays of B_d^0 and B_s^0 mesons.

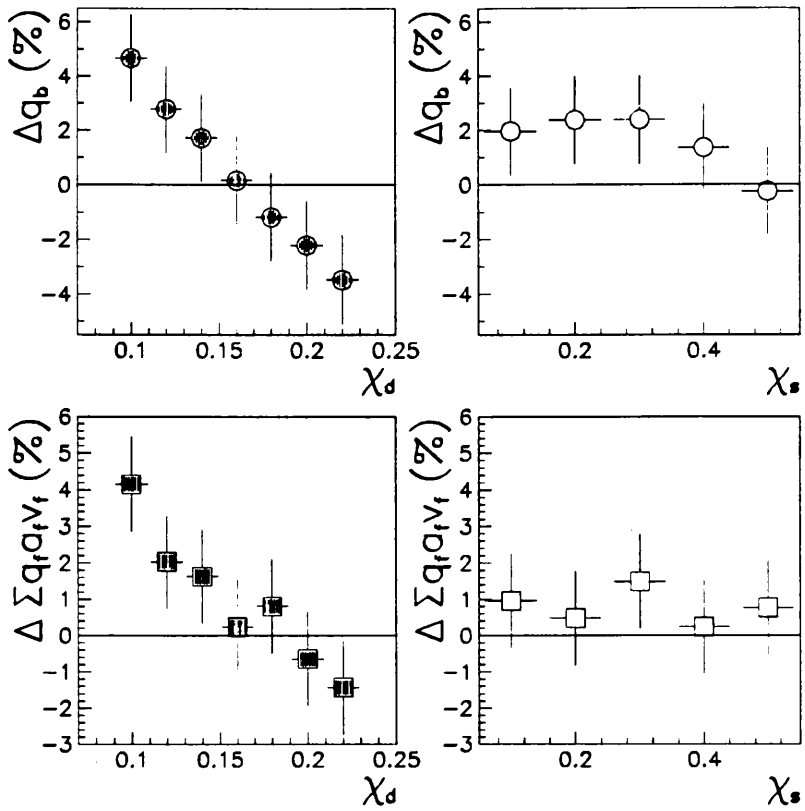

Separation changes are calculated as the percentage shift from default values at $\kappa = 1.0$ and are plotted with same scales throughout.

Figure 8.19: Variation in the b separation and its effect on $\sum_f q_f a_f v_f$ as a function of χ_d and χ_s.

8.6 Comparisons with HERWIG

For valid comparisons of quark separations between LUND and HERWIG, it is necessary to take into account some major differences which exist between them. Both models are tuned to identical event shape distributions, using bin-by-bin corrections, in ALEPH QCD analyses. This ensures that differences between separations are due to the different philosophies of the models rather than tuning of parameters. Additional conditions must be satisfied before valid comparisons are made :

(i) The ALEPH modified version of LUND[7] incorporates routines to implement $B^0 - \overline{B^0}$ mixing. This is *not* present in HERWIG, and because of the effects of the previous section, is deactivated in the LUND generator for this comparison.

(ii) The kaon rate within HERWIG, using the parameters of table A.1, results in a rate which exceeds that of LUND by more than $\sim 10\%$. So as not to introduce further $\frac{s}{u}$ contributions[8] in the comparison, the HERWIG rate is normalised to that of LUND.

[7]Referred to as the ALEPH Heavy Flavour Generator (HVFL01).

[8]Which are large in themselves (see section 8.4.5).

Two ways of normalising LUND and HERWIG kaon rates are :

- The $\frac{s}{u}$ ratio in LUND represents the combined uncertainty on light quark masses. It is possible to modify the quark masses in HERWIG to alter the rate of strangeness production.
- The probability of producing $q\bar{q}$ pairs in HERWIG during cluster formation can be directly modified from default values of unity for all light quarks. This alters strangeness production of clusters *only*, leaving the extended parton shower evolution unmodified.

The first of these is closer to the philosophy of varying the $\frac{s}{u}$ ratio within LUND but results in unacceptably large changes to the charged multiplicity. The second method is used here, where the probability of producing strange clusters is changed from 1.00 to 0.80. This preserves agreement between kaon rates to better than $\sim 2\%$ without deterioration in the agreement of charged multiplicities. After such considerations, the mean charged multiplicities and kaon rates are shown in table 8.13 and are found to agree to within 0.3% and 2% respectively. Changes to quark separations as a result of switching between

Generator	Charged Multiplicity	Kaon Rate
LUND using generator reference values	16.18 ($\pm$0.01)	1.00 ($\pm$0.01)
HERWIG using generator reference values but with $S_{prob} = 1.0$	16.13 ($\pm$0.01)	1.10 ($\pm$0.01)
HERWIG using generator reference values but with $S_{prob} = 0.80$	16.14 ($\pm$0.01)	1.02 ($\pm$0.01)

Table 8.13: Mean charged multiplicities and neutral kaon rates in LUND and HERWIG.

LUND and HERWIG are given in table 8.14 and shown in figure 8.20.

Flavour	LUND q_f	HERWIG q_f
u	0.453 ($\pm$ 0.002)	0.363 ($\pm$ 0.002)
d	0.235 ($\pm$ 0.002)	0.239 ($\pm$ 0.002)
s	0.351 ($\pm$ 0.002)	0.379 ($\pm$ 0.002)
c	0.188 ($\pm$ 0.002)	0.141 ($\pm$ 0.002)
b	0.277 ($\pm$ 0.002)	0.239 ($\pm$ 0.002)

Table 8.14: Comparison of generated LUND and HERWIG separations.

An important consideration for the selection of $\kappa = 1.0$, as the point at which an asymmetry is extracted, is optimisation of the sensitivity. The sensitivity is determined

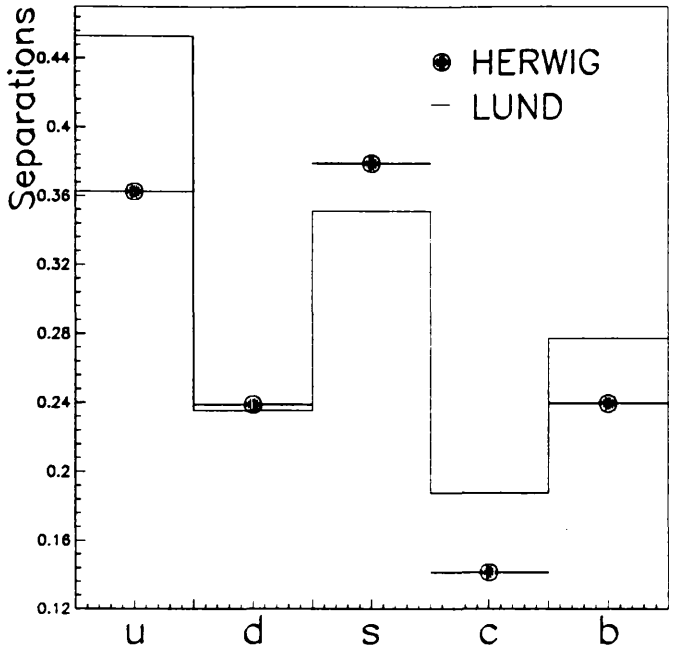

Figure 8.20: Changes to LUND separations from switching to HERWIG.

using Monte Carlo, so it is important to ensure that the optimum is not itself model dependent. Sensitivity curves for LUND and HERWIG are shown in figure 8.21 and clearly have similar positions of extreme sensitivity at around $\kappa \sim 1.0$ despite large differences in individual separations. The position of optimal sensitivity is also seen to remain stable for all LUND parameter variations discussed previously.

The total change to $\sum_f q_f a_f v_f$ at $\kappa = 1.0$ is from $\overbrace{0.352\,(\pm 0.003)\%}^{\text{LUND}}$ to $\overbrace{0.391\,(\pm 0.003)\%}^{\text{HERWIG}}$ which represents a difference of $-11.1\,(\pm 1.0)\%$. The percentage shift between LUND and HERWIG as a function of κ is shown in figure 8.22. It is clear that the percentage difference is greatest at low κ and diminishes to a stable value of $\sim -10\%$ at κ above 2.0. This is comparable with the average shift in $\sum_f q_f a_f v_f$ with κ from the variation of LUND parameters shown in figure 8.11.

The LUND model is found to give closer agreement with ALEPH data than HERWIG [48] and is selected for use when extracting physical quantities from $\overline{Q_{FB}}$ in Chapter 9 due to its proven validity over a wide range of energies and reactions. Further studies involving later versions of the HERWIG model, and various sets of tuned parameters [59] give rise to larger values of $\sum_f q_f a_f v_f$ when compared to the LUND value. These remain within a maximum range of ± 20 % which is used here as an upper limit of systematic uncertainties due to fragmentation. HERWIG also contains uncertainties in its fragmentation and decays of heavy quarks [59] [31] which remain to be investigated.

A small, additional sample of HERWIG events was generated, simulated and reconstructed with the *"Reconstructed Monte Carlo Settings"* of Appendix A. This allows an independent test of the change to generator separations after reconstruction. These are

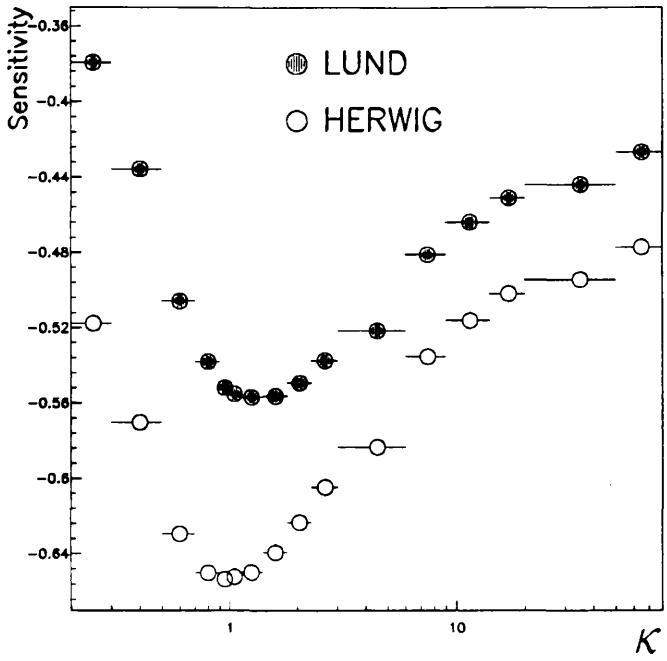

Figure 8.21: Comparison of sensitivity curves from LUND and HERWIG.

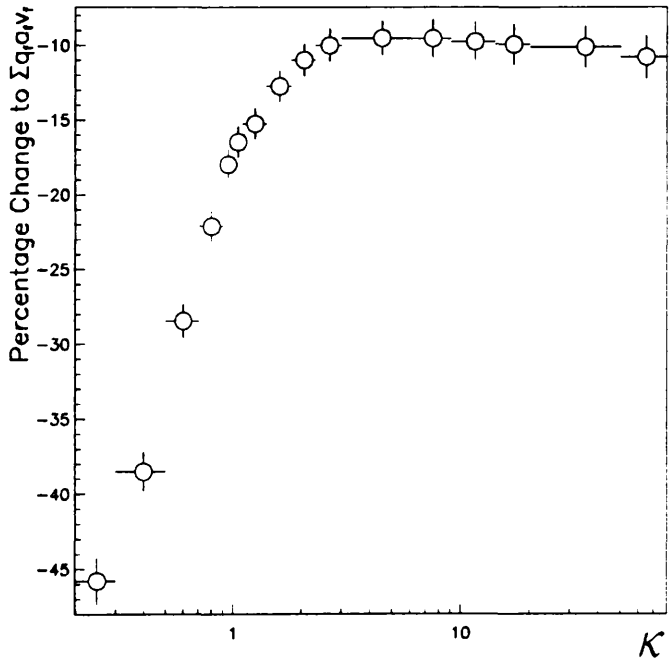

Figure 8.22: Percentage difference in $\sum_f q_f a_f v_f$ between LUND and HERWIG as a function of κ.

compared in table 8.15 and are used later to demonstrate the effects of fragmentation upon the energy dependence of an expected $\overline{Q_{FB}}$ asymmetry.

Flavour	Generated HERWIG q_f	Reconstructed HERWIG q_f
u	0.365 ($\pm$ 0.002)	0.305 ($\pm$ 0.015)
d	0.251 ($\pm$ 0.002)	0.247 ($\pm$ 0.013)
s	0.360 ($\pm$ 0.002)	0.329 ($\pm$ 0.014)
c	0.141 ($\pm$ 0.002)	0.133 ($\pm$ 0.013)
b	0.230 ($\pm$ 0.002)	0.230 ($\pm$ 0.011)

The generated sample consists of 450,000 events whereas the reconstructed sample contains 9900.

Table 8.15: Comparison of generated and reconstructed HERWIG separations.

8.7 Summary

The fragmentation systematic error, summarised below, is the total change to the generator level expected charge flow resulting from changes to LUND fragmentation and use of HERWIG as an alternative. Individual contributions are combined in quadrature and listed in table 8.16. Some values are slightly different from those of table 8.11 from larger variations in $\sum_f q_f a_f v_f$ when parameters were scanned through their respective ranges in section 8.4.5. Combining the effects of changes to $\sum_f q_f a_f v_f$ from alterations to LUND parameters and the difference between LUND and HERWIG in quadrature leads to a systematic uncertainty of $\pm$16.5 %. Taking into account further differences found when using various HERWIG versions and parameter tunings, a conservative estimate of $\pm$20 % is assigned to an expected $\overline{Q_{FB}}$ measurement at $\kappa = 1.0$.

Parameter	Range			$\frac{\Delta\overline{Q_{FB}^{ref}}}{\overline{Q_{FB}^{ref}}}$ (%)
Λ_{QCD}	0.26	-	0.40 GeV	2.9
M_{min}	1.0	-	2.0 GeV	1.6
σ	0.34	-	0.40	1.4
b	0.85	-	0.93	3.4
ϵ_c	0.002	-	0.071	4.2
ϵ_b	0.003	-	0.10	3.9
$(\frac{V}{V+PS})_{u,d}$	0.3	-	0.75	3.6
$(\frac{V}{V+PS})_s$	0.5	-	0.75	0.9
$(\frac{V}{V+PS})_{c,b}$	0.65	-	0.8	2.8
$\frac{s}{u}$	0.25	-	0.40	7.7
χ_d	0.10	-	0.22	4.1
χ_s	0.10	-	0.50	1.3
Total Combined LUND				12.2
HERWIG				11.1

Statistical error on uncertainties is ±1.2%. Uncertainties are combined in quadrature if they exceed this statistical error.

Table 8.16: Variation in expected values of $\overline{Q_{FB}}$ due to changes in fragmentation.

Chapter 9

Extraction of Physical Quantities

The magnitude and behaviour of forward-backward quark asymmetries with energy depends on the form and strength of electron and quark couplings to the intermediate particle. As described previously in chapter 1, the form of the couplings is predicted within the context of the Standard Model (SM). Their strength is governed by the value of the quantity, $sin^2\theta_w(M_Z^2)$ which can be extracted from the value of $\overline{Q_{FB}}$ in ALEPH data via the method and calculation discussed in section 5.1.4. This is the purpose of the current chapter. The particular form of the quark asymmetry makes it possible to distinguish between contributions from the initial lepton state and the final quark state. This "feature" allows information regarding the lepton couplings to be extracted when used in conjunction with measurements of quark couplings from previous experiments.

9.1 Measurement of $sin^2\theta_w(M_Z^2)$

Extracting $sin^2\theta_w(M_Z^2)$ from the measured value of $\overline{Q_{FB}}$ is most easily envisaged using a measurement close to the peak of the Z^o resonance. The on-resonance asymmetry has a particularly simple form due to the small size of the the $(s - M_Z^2)$ term in the propagator. Contributions from non-zero fermion masses and γ-exchange are small in this region [4]. This means that the lowest order, on-resonance asymmetries are determined exclusively by the measurable value of $sin^2\theta_w(M_Z^2)$. The on-resonance assumption is valid for the case of an integrated $\overline{Q_{FB}}$ measurement over all the energy points at which ALEPH has taken data. The LEP scan strategy, where a significant fraction of the run period is spent at the "peak" position, ensures that much of the data is taken close to the top of the resonance. Events from the eleven energy points may be combined together with their contributions to $\overline{Q_{FB}}$ weighted according to the number of hadronic events at that energy. This is possible due to the almost linear variation of $\overline{Q_{FB}}$ with energy[1]. $sin^2\theta_w(M_Z^2)$ is measured using the assumption that the *total* $\overline{Q_{FB}}$ for all eleven energies lies at the mean event-weighted energy atop the resonance. Contributions from off-peak positions either cancel or are negligible at the current level of statistical accuracy.

Definitions and lowest-order results for A_{FB} and $\overline{Q_{FB}}$ have been given previously in chapters 1 and 5 respectively and are assumed here. For a given value of $\overline{Q_{FB}}$, the deter-

[1]This is a good approximation as shown in figure 1.4.

mination of the corresponding value of $sin^2\theta_w(M_Z^2)$ is carried out using equation (9.1) :

$$\overline{Q_{FB}}(cos\,\theta_c) = \mathcal{A}_e \frac{cos\,\theta_c}{1+\frac{cos^2\theta_c}{3}} \times \frac{2\sum_{f=u...}^{b} q_f\, a_f\, v_f}{\sum_{f=u...}^{b}\left(a_f^2 + v_f^2\right)} \tag{9.1}$$

This can be broken into the various quantities :

(I) The correction for limited acceptance, $\frac{cos\,\theta_c}{1+\frac{cos^2\theta_c}{3}}$.

(II) The "electron term" $\mathcal{A}_e \sim 0.16$ assuming a $sin^2\theta_w(M_Z^2)$ of 0.230.

(III) The "quark terms" including the separations $\sum_{f=u,c} q_f a_f v_f \sim 0.39 \times \sum_{f=u,c} q_f$ and $\sum_{f=d,s,b} q_f a_f v_f \sim 0.69 \times \sum_{f=d,s,b} q_f$ assuming a $sin^2\theta_w(M_Z^2)$ of 0.230.

The process of calculating the expected value of $\overline{Q_{FB}}$ for each given value of $sin^2\theta_w(M_Z^2)$ is carried out iteratively until close agreement between the expected and measured value is achieved. Combining the separations (as in (III) above) assumes universality of quark couplings. The relationship between $sin^2\theta_w(M_Z^2)$ and $\overline{Q_{FB}}$ is linear to a high degree at $\kappa = 1.0$ as shown in figure 9.1. To determine the statistical and systematic uncertain-

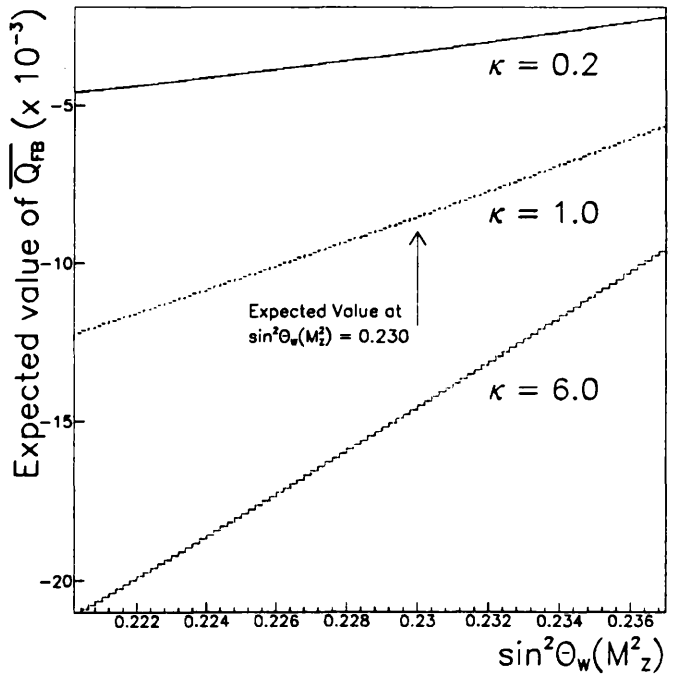

$sin^2\theta_w(M_Z^2)$ is varied during the fitting procedure and plotted with the expected value of $\overline{Q_{FB}}$ calculated using separations at the different values of κ indicated.

Figure 9.1: The linear variation of $\overline{Q_{FB}}$ with $sin^2\theta_w(M_Z^2)$

ties on $sin^2\theta_w(M_Z^2)$ the value of $\overline{Q_{FB}}$ is smeared[2] and the corresponding distribution of $sin^2\theta_w(M_Z^2)$ values is formed. The mean and width of this distribution is used to establish the measured value of $sin^2\theta_w(M_Z^2)$ and its error. The width of this distribution is

[2] According to a normal distribution of width equal to the appropriate 1σ statistical or systematic error.

found to be largely equivalent to using the 1σ error on $\overline{Q_{FB}}$ and passing it through as the percentage difference of the measured $sin^2\theta_w(M_Z^2)$ from $\frac{1}{4}$ as expected.

The sensitivity of $\mathcal{A}_e$ to $sin^2\theta_w(M_Z^2)$ relative to that of the quark summation $\sum_{f=u,...}^{b} q_f\mathcal{A}_f\Gamma_f/\Gamma_{had}$ is shown in figure 9.2. This shows that the $sin^2\theta_w(M_Z^2)$ contribution

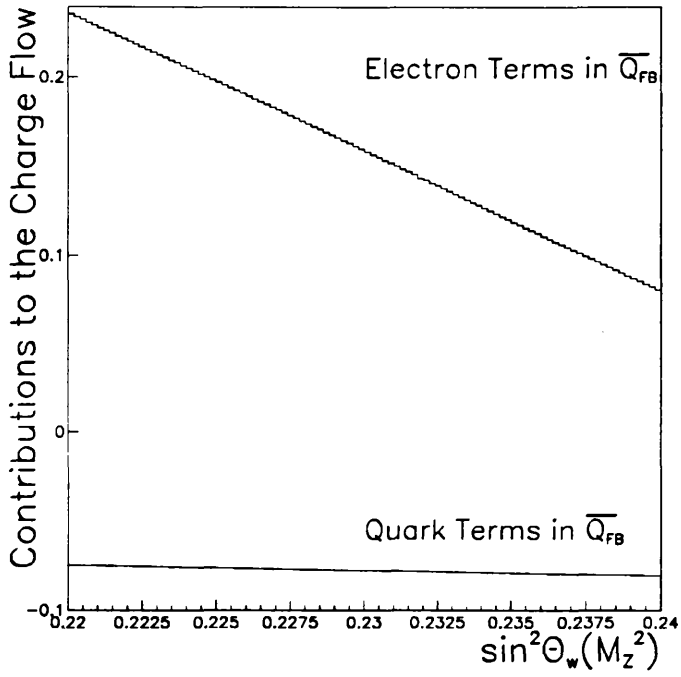

Figure 9.2: Comparison of the sensitivities of the "electron term" $\mathcal{A}_e$, and the "quark terms" in the summation $\sum_{f=u,...}^{b} q_f\mathcal{A}_f\Gamma_f/\Gamma_{had}$ of $\overline{Q_{FB}}$ to $sin^2\theta_w(M_Z^2)$.

in $\mathcal{A}_e$ can change by $\sim \pm 25\%$ within the range $0.225 \rightarrow 0.235$ while in the case of $\sum_{f=u,...}^{b} q_f\mathcal{A}_f\Gamma_f/\Gamma_{had}$ the change is less than $\sim \pm 2\%$. Thus, most of the $\overline{Q_{FB}}$ sensitivity to $sin^2\theta_w(M_Z^2)$ comes from $\mathcal{A}_e$.

9.1.1 Inclusion of Systematic Errors

Experimental and theoretical systematic errors on $sin^2\theta_w(M_Z^2)$ are determined in different ways because of the way in which they affect the method :

(i) **The Experimental Systematic Error** is considered as an additional "statistical" contribution to $\overline{Q_{FB}}$ and is treated in the same way.

(ii) **The Theoretical Systematic Error** is determined from the uncertainty on $\overline{Q_{FB}^{sum}}$ and is introduced to the $\sum_{f=u,...}^{b} q_f a_f v_f$ summation term only in equation (9.1).

In the case of (i) the effect on the $sin^2\theta_w(M_Z^2)$ distribution is small and similar to the symmetric smearing due to a larger statistical error on $\overline{Q_{FB}}$. This is expected from the linear dependence of $\overline{Q_{FB}^{sum}}$ on $sin^2\theta_w(M_Z^2)$ shown in figure 9.1. The fragmentation error of (ii) is introduced only to the quark summation and leads to a slightly asymmetric

distribution. For all cases here, 1σ errors are taken as the half width of the 68% confidence limit on the resulting distributions with the measured value taken as the centre of the interval. The small asymmetry in the distributions represents less than $\frac{1}{4}$ of the symmetric error and so remains negligible for the purposes of the current study.

Errors are determined for the following cases :

(a) The statistical uncertainty on $\overline{Q_{FB}}$ alone.

(b) The experimental systematic uncertainty on $\overline{Q_{FB}}$ alone.

(c) The fragmentation systematic uncertainty on $\overline{Q_{FB}}$ alone.

(d) The above three errors (a)→(c) combined.

The latter case is used as a cross-check to ensure consistency between the sum of the preceding cases in quadrature. The value of $sin^2\theta_w(M_Z^2)$ is taken as the central value of the 68% interval for the first case, (a). This method is used throughout the following calculations.

9.1.2 Results and Variation with κ

Using the techniques of section 9.1, the value of $sin^2\theta_w(M_Z^2)$ at a κ of 1.0 is determined to be :

$$sin^2\theta_w(M_Z^2)\ |_{\kappa=1.0} = 0.2303\ \underbrace{\pm 0.0036}_{\text{(stat.)}}\ \underbrace{\pm 0.0009}_{\text{(expt.syst.)}}\ \underbrace{\pm 0.0038}_{\text{(theor.syst.)}} \tag{9.2}$$

As $\kappa = 1.0$ is selected as the point at which the measurement is most sensitive, and least susceptible to systematics, it is of primary importance. Extracting physical quantities at other κ values provides an indication of the existence and magnitude of possible systematics. The values of $sin^2\theta_w(M_Z^2)$, determined using quark separations and measurements of $\overline{Q_{FB}}$ from data at different κ, are given in table 9.1 and shown in figure 9.3. These indicate that measurements of $sin^2\theta_w(M_Z^2)$ vary smoothly with increasing κ between the values of $\sim 0.225 \rightarrow 0.235$. The points are highly correlated (as discussed in 6.2.2) so that the quoted errors are not independent. The entire variation lies within the 1σ band indicated by combining the statistical and systematic uncertainties in quadrature at $\kappa = 1.0$. The variation of $sin^2\theta_w(M_Z^2)$ measurements with κ is expected to be due to a combination of :

1. The effects of statistics within such a highly intercorrelated sample of points.
2. The presence of differences between the Monte Carlo separations and those assumed to be present in data.

The magnitude of the variation in figure 9.3 gives confidence that the systematic errors quoted above in (9.2) represents a valid estimation of the total uncertainty on the measurement of $sin^2\theta_w(M_Z^2)$ at $\kappa = 1.0$.

κ	$sin^2\theta_w(M_Z^2)$	Statistical Uncertainty	Experimental Uncertainty
0.2	0.2370	0.0050	0.0020
0.3	0.2355	0.0044	0.0017
0.5	0.2334	0.0038	0.0013
0.7	0.2318	0.0037	0.0011
0.9	0.2308	0.0036	0.0010
1.0	0.2303	0.0036	0.0009
1.1	0.2298	0.0036	0.0009
1.4	0.2289	0.0036	0.0009
1.8	0.2278	0.0037	0.0009
2.3	0.2270	0.0039	0.0010
3.0	0.2260	0.0041	0.0010
6.0	0.2247	0.0045	0.0013
9.0	0.2242	0.0047	0.0013
14.0	0.2236	0.0049	0.0014
20.0	0.2238	0.0049	0.0013
∞	0.2244	0.0051	0.0013

Table 9.1: Measured values of $sin^2\theta_w(M_Z^2)$ as a function of κ.

9.2 Extraction of $\frac{v_e}{a_e}$

As mentioned previously, the dominant $sin^2\theta_w(M_Z^2)$ contribution to $\overline{Q_{FB}}$ is contained in $\mathcal{A}_e$. $\mathcal{A}_e$ can be isolated in equation (9.1) if the couplings a_f and v_f ($f = u, d, s, c, b$) of the quarks are known. The left and right-handed couplings of u and d quarks have been measured in neutrino-nucleon scattering as follows [60] :

$$(g_L^u)^2 + (g_L^d)^2 = 0.2996 \pm 0.0044 \tag{9.3}$$

$$(g_R^u)^2 + (g_R^d)^2 = 0.0298 \pm 0.0038 \tag{9.4}$$

$$tan^{-1}\left(\frac{g_L^u}{g_L^d}\right) = 2.47 \pm 0.04 \tag{9.5}$$

$$tan^{-1}\left(\frac{g_R^u}{g_R^d}\right) = 4.65 \pm 0.40 \tag{9.6}$$

These are used to calculate $\mathcal{A}_f$ ($f = u, d, s, c, b$) using equation (9.1) and assumes universality between the quark couplings so that :

$$\mathcal{A}_u = \mathcal{A}_c \quad \text{and} \quad \mathcal{A}_d = \mathcal{A}_s = \mathcal{A}_b \tag{9.7}$$

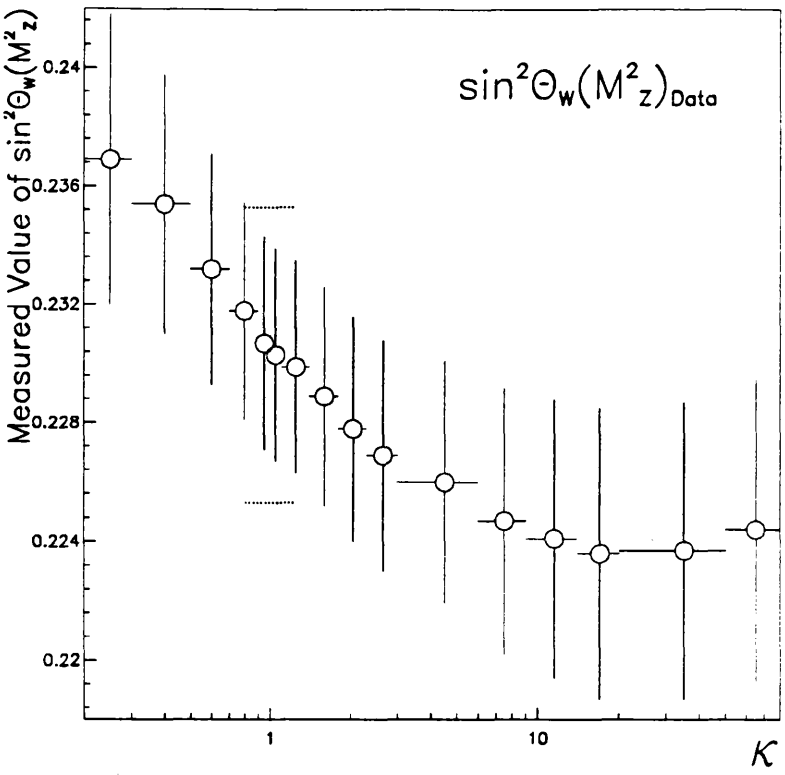

Horizontal dashed lines indicate the combined combined statistical and systematic error of the value measured at $\kappa = 1.0$. The point-by-point errors are statistical only.

Figure 9.3: Measured values of $sin^2\theta_w(M_Z^2)$ as a function of κ.

If the values of (9.3) → (9.6) are used, smeared by their corresponding errors as before, then the quark terms have value :

$$(\mathcal{A}_u, \mathcal{A}_c) = 0.64 \pm 0.07 \tag{9.8}$$

$$(\mathcal{A}_d, \mathcal{A}_s, \mathcal{A}_b) = 0.97 \pm 0.04 \tag{9.9}$$

Using the peak expression of $\sum_{f=u...}^{b} q_f \mathcal{A}_f \Gamma_f / \Gamma_{had}$ and the separations at $\kappa = 1.0$ yields :

$$\sum_{f=u...}^{b} q_f \mathcal{A}_f \frac{\Gamma_f}{\Gamma_{had}} = -0.086 \pm 0.026 \tag{9.10}$$

The error in (9.10) contains the combined statistical, detector and fragmentation systematic errors together, and combined with the measured value of $\overline{Q_{FB}}$ at $\kappa = 1.0$, gives :

$$\mathcal{A}_e = +0.148 \pm 0.047 \tag{9.11}$$

This is directly related to the ratio of the electron vector and axial couplings $\frac{v_e}{a_e}$ by the relation :

$$\frac{v_e}{a_e} = \frac{1 - \sqrt{1 - \mathcal{A}_e^2}}{\mathcal{A}_e} \tag{9.12}$$

so that $\frac{v_e}{a_e}$ is found to be :

$$\frac{v_e}{a_e} = +0.072 \pm 0.025 \tag{9.13}$$

It is clear from (9.11) and (9.13) that the *signs* of a_e and v_e are *the same*. A $sin^2\theta_w(M_Z^2)$ value of 0.232 gives an expectation that $v_e/a_e \sim +0.070$ within the context of the Standard Model.

In a similar manner, $\frac{v_e}{a_e}$ is determined for different values of κ, thus changing the values used for $\overline{Q_{FB}}$ and the separations in (9.10). The values and errors determined in this way are given in table 9.2 and shown in figure 9.4. It is clear that all measurements

κ	$\frac{v_e}{a_e}$	Statistical Uncertainty	Experimental Uncertainty
0.2	0.049	0.022	0.016
0.3	0.054	0.021	0.016
0.5	0.061	0.020	0.016
0.7	0.067	0.020	0.016
0.9	0.070	0.020	0.016
1.0	0.072	0.020	0.016
1.1	0.074	0.020	0.016
1.4	0.077	0.020	0.016
1.8	0.081	0.020	0.016
2.3	0.084	0.021	0.016
3.0	0.088	0.022	0.016
6.0	0.092	0.023	0.018
9.0	0.094	0.023	0.017
14.0	0.095	0.024	0.018
20.0	0.095	0.024	0.018
∞	0.092	0.024	0.018

Table 9.2: Measured values of $\frac{v_e}{a_e}$ as a function of κ.

of $\frac{v_e}{a_e}$ lie within the 1σ combined statistical and systematic uncertainty of the values at $\kappa = 1.0$.

This result may be used in conjunction with ALEPH results from the lepton width, Γ_{ll}, and forward-backward asymmetries to calculate the value of v_e as it is least well known experimentally. Using the measured ALEPH value [2] :

$$a_e(M_Z^2) = -1.0058\,(\pm 0.0082) \tag{9.14}$$

the above result of equation (9.13) gives :

$$v_e(M_Z^2) = -0.072\,(\pm 0.026) \tag{9.15}$$

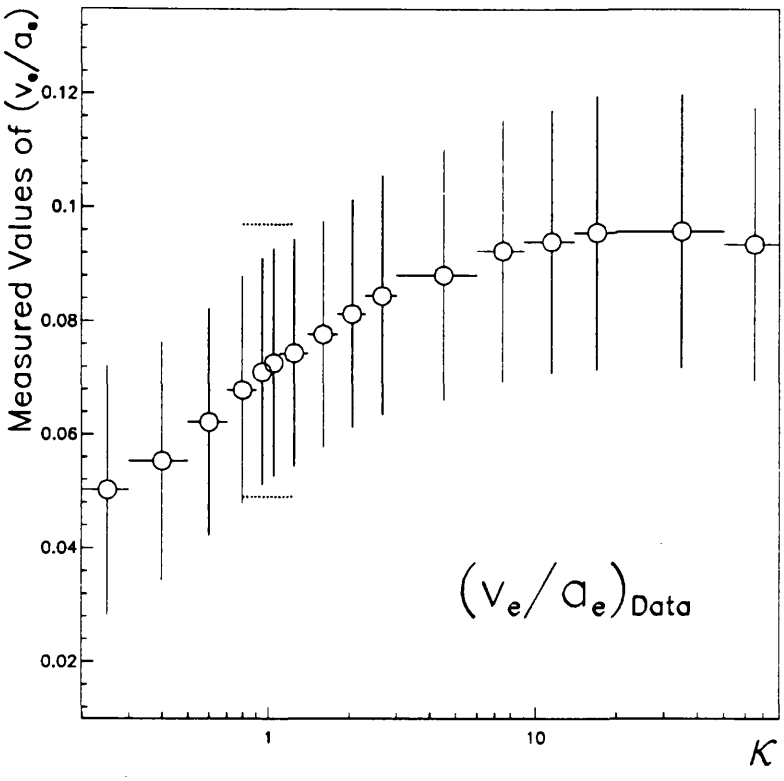

Horizontal dashed lines indicate the combined combined statistical and systematic error of the value measured at $\kappa = 1.0$. The point-by-point errors are statistical only.

Figure 9.4: Measured values of $\frac{v_e}{a_e}$ as a function of κ.

This is shown in the $v_e - a_e$ plane of figure 9.5 with more recent[3] lepton measurements and may be compared with the Standard Model expectation of $v_e = -0.080$ assuming a $sin^2\theta$ of 0.230.

9.3 Energy Dependence of $\overline{Q_{FB}}$

In the energy region around the Z^o peak the on-resonance expressions of the previous section no longer hold. Contributions from the propagator, radiative effects and γ-exchange must be considered. The expected energy dependence of the up and down-type asymmetries is shown previously in figure 1.3. Their contributions to the $\overline{Q_{FB}}$ for all quarks depend on the flavour separations.

The separations themselves are unaffected by relatively small changes in energy since they rely upon the soft effects of fragmentation. Studies at the full event level, similar to those of chapter 8, indicate that the separation dependence on energy is entirely negligible. The gradient of a single flavour contribution to the mean charge flow with energy is

[3]Lepton contours provided courtesy of E. Locci (ALEPH), Departement de Physique des Particules Elementaires, Saclay, France.

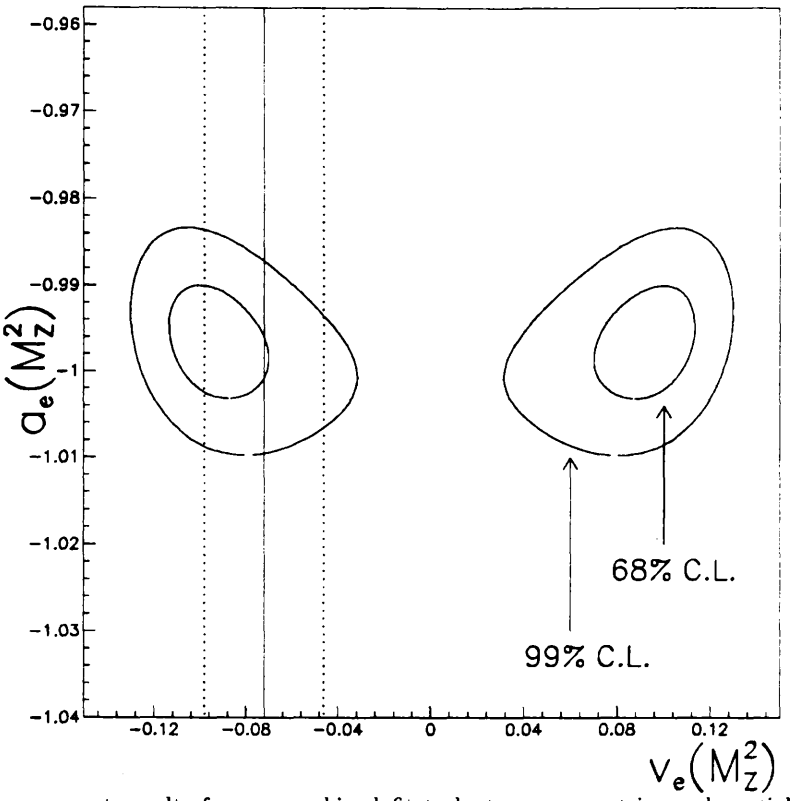

The contours represent results from a combined fit to lepton asymmetries and partial widths while the vertical lines denote the current measurement and its combined statistical and systematic 1σ error.

Figure 9.5: Probability contours for $g_a^e(M_Z^2)$ and $g_v^e(M_Z^2)$ from measured lepton widths and asymmetries compared with expectations from the current measurement.

dependent on the separation of that flavour. Thus, the gradient of the combined flavour $\overline{Q_{FB}}$ depends on the values of all the Monte Carlo separations together.

It is shown in figure 1.4 that the gradient of A_{FB} for all flavours with energy is largely insensitive to the value of $sin^2\theta_w(M_Z^2)$. So the gradient here serves only as a cross-check of general assumptions of the method, namely :

(a) It provides a large scale test of assumptions inherent in the use of Standard Model couplings and of the principle of cancellation between competing quark flavours.

(b) It represents a, currently inaccurate, test of the *degree* of cancellation between the flavours. ie. an indication of the degree of theoretical uncertainty on the quark separations.

The predicted dependence of $\overline{Q_{FB}}$ is compared with data values at three combined energy points in figure 9.6. Figure 9.6 incorporates the Monte Carlo separations from the reference reconstructed data set employing LUND fragmentation. As shown, the theoretical predictions give an acceptable description of the data behaviour. As an indication of the effect of the systematic error due to fragmentation on the gradients of such predictions, the curves are compared with those employing the HERWIG separations of table 8.15. This

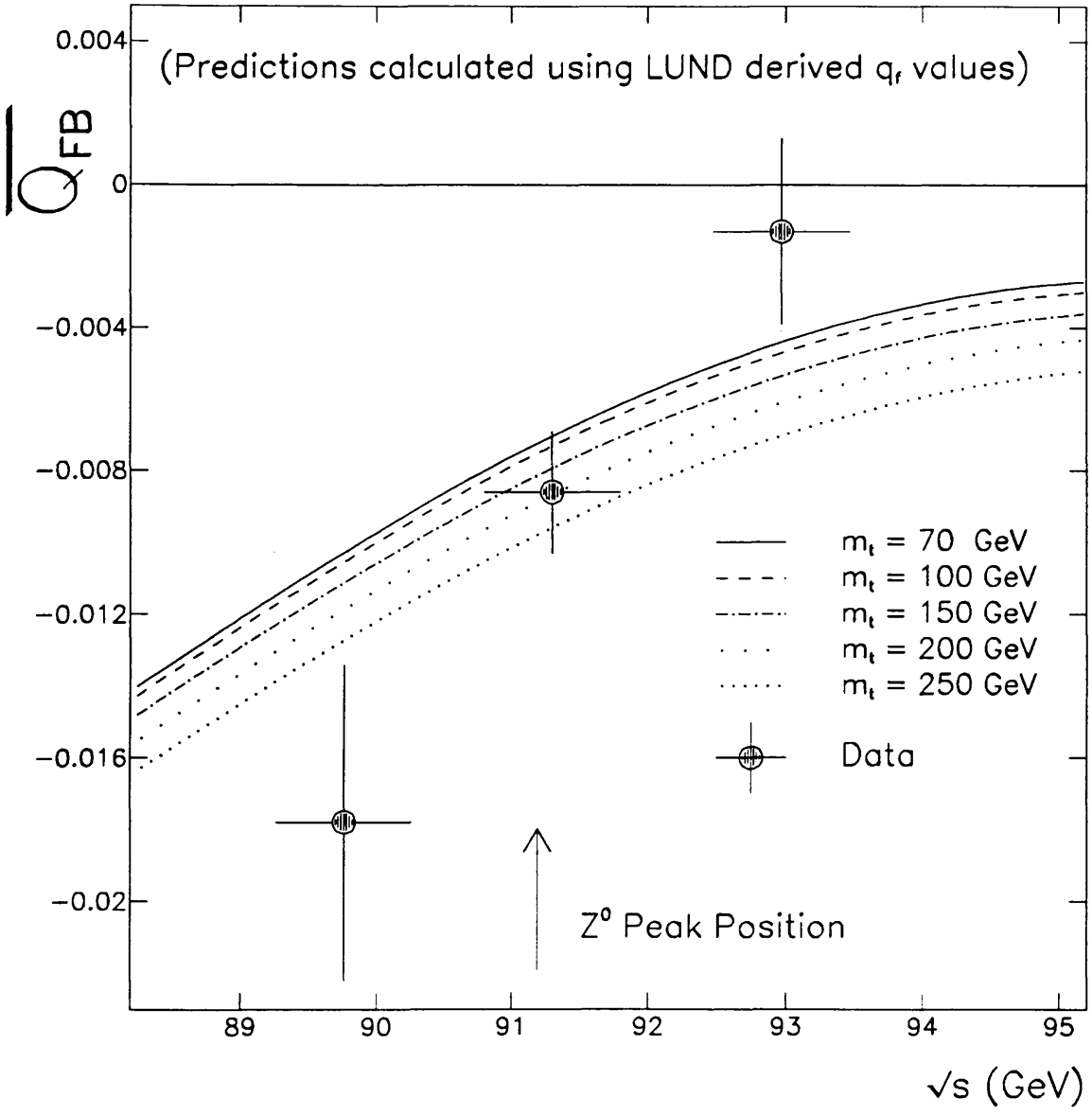

Calculations shown as curves carried out using the **EXPOSTAR** program including radiative corrections [9].

Figure 9.6: Energy dependence of $\overline{Q_{FB}}$ in data compared with that predicted using the **LUND** fragmentation scheme to derive the Monte Carlo separations.

is shown in figure 9.7 where the substantial change in gradient is apparent. The HERWIG

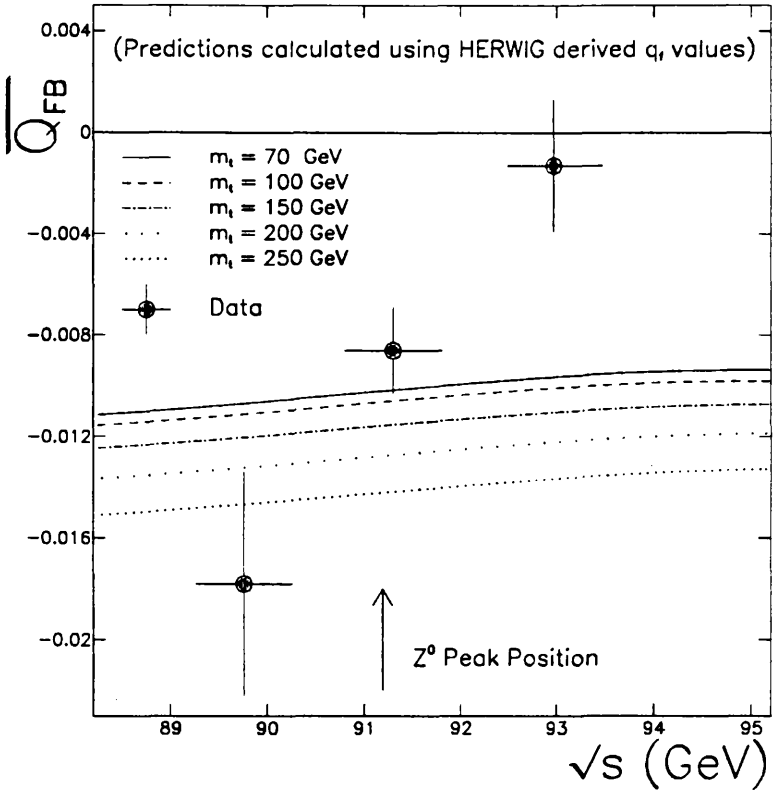

Calculations shown as curves carried out using the EXPOSTAR program including radiative corrections [9].

Figure 9.7: Energy dependence of $\overline{Q_{FB}}$ in data compared with that predicted using the HERWIG fragmentation scheme to derive the Monte Carlo separations.

separations possess a large statistical error and are only used here to show that the gradient of the predictions in figure 9.6 are significantly affected by the systematic uncertainties from fragmentation.

Chapter 10

Summary and Conclusions

An electroweak induced charge asymmetry in hadronic events has been studied using the ALEPH detector with an integrated luminosity of $8.7\,(\pm 0.2)\,\mathrm{pb}^{-1}$. The measurement of such an asymmetry relies upon charge retention effects in particle jets to tag the sign of the parent quark charge.

Monte Carlo studies (see Chapter 4) have verified that the thrust axis and weighted charge summations in each hemisphere of a hadronic event provide good estimates of the direction and sign of parent quark charges. Charge retention effects are observed in data via the fraction of oppositely signed hemispheres[1] which is measured to be $F_{\pm} = 54.1\,(\pm\,0.1)\,\%$, in good agreement with Monte Carlo expectations of 54.2 %.

The asymmetry is measured using the method of charge flow (see Chapter 5) which uses charge information from both hemispheres of each event. The asymmetry is determined from the mean shift from zero of the charge difference distribution (Q_{FB}) and is measured to be $\overline{Q_{FB}} = -0.0084\,(\pm 0.0014)\,(\mathrm{stat.})$ at $\kappa = 1.0$ (see Chapter 6). This value is ~ 6 standard deviations from zero and remains significant for all values of κ. $\overline{Q_{FB}}$ is interpreted within the framework of the Standard Model using separation factors derived from Monte Carlo charge distributions which represent the degree of charge retention in each channel. These give rise to an expected position of optimum sensitivity to an asymmetry at $\kappa = 1.0$. The distributions of $\overline{Q_{FB}}$ with angle and energy (see Chapter 6) indicate that the asymmetry is concentrated in the high $\cos\theta_{\mathrm{T}}$ region of the detector and increases with $\sqrt{s}$ as expected. Comparison of the widths of charge distributions via $\bar{q}$, which is related to the broadening of the Q_{FB} distribution due to charge retention, shows that data and Monte Carlo are in agreement to better than $\pm\,2\%$.

Detector contributions to $\overline{Q_{FB}}$ have been investigated (see Chapter 7) and found to be small when compared to the current statistical error. The dominant contribution arises from uncertainties in determining the small probability of track losses in the detector which are not simulated in a reconstructed Monte Carlo sample. Other detector effects have even smaller contributions, and the experimental systematic error is conservatively estimated to be $\pm\,0.0004$ on $\overline{Q_{FB}}$ at $\kappa = 1.0$.

The dominant systematic contribution to the interpretation of $\overline{Q_{FB}}$ is due to uncertainties in the separation factors extracted from fragmentation models. These have been studied using the LUND and HERWIG models (see Chapter 8) and are conservatively esti-

[1] Using the thrust axis and longitudinal weighting scheme with a $\kappa = 1.0$.

mated to be within $\pm 20\,\%$ of the expected asymmetry at $\kappa = 1.0$. The dependence of the expected $\overline{Q_{FB}}$ on LUND parameters is dominated by the contribution from uncertainties in strange meson production , while effects of $B^0 - \overline{B^0}$ mixing have been examined and estimated to be small. No $B^0 - \overline{B^0}$ mixing correction is applied. The fragmentation systematic is estimated using the uncertainty due to LUND parameters and differences found between the LUND and HERWIG models. The LUND separations are used to extract physical quantities due to its closer agreement with ALEPH data and proven validity at lower energies. Large parameter variations within LUND give rise to visible changes in observables which are *not* used here to constrain the systematic error due to possible correlations between parameters. Future measurements of particle production rates and jet characteristics at LEP energies are likely to constrain such ranges externally and limit the degree of variation presented in Chapter 8.

In the framework of the Standard Model, the $\overline{Q_{FB}}$ measurement is interpreted in terms of the electroweak couplings of leptons and quarks to the Z^o (see Chapter 9) and hence in terms of the single parameter, $sin^2\theta(M_Z^2)$. The systematic errors on such an interpretation are determined using the 68% interval around the central value formed when the measured value of $\overline{Q_{FB}}$ and Monte Carlo separations are varied within their errors. $sin^2\theta(M_Z^2)$ is found to be :

$$sin^2\theta_w(M_Z^2) \;=\; 0.2303 \;\underbrace{\pm 0.0036}_{\text{(stat.)}}\;\underbrace{\pm 0.0009}_{\text{(expt.syst.)}}\;\underbrace{\pm 0.0038}_{\text{(theor.syst.)}}$$

Previously extracted coupling constants from neutrino-nucleon scattering measurements give quark couplings with value $(\mathcal{A}_u, \mathcal{A}_c) = 0.64 \pm 0.07$ and $(\mathcal{A}_d, \mathcal{A}_s, \mathcal{A}_b) = 0.97 \pm 0.04$. Assuming quark universality these are used (with the measured $\overline{Q_{FB}}$) to extract the electron left-right asymmetry, $\mathcal{A}_e = +0.148 \pm 0.047$, and the ratio of lepton couplings :

$$\frac{v_e}{a_e} \;=\; +0.072 \;\pm 0.025$$

where both statistical and systematic uncertainties are combined. This measurement establishes that the signs of axial and vector lepton couplings are the same.

The method of charge flow has wide applicability in the study of jets, especially in the area of heavy flavour physics where relatively efficient tagging of single flavours is possible. The large asymmetries of individual flavours and the effects of $B^0 - \overline{B^0}$ mixing on the b jet charge represent areas into which such a method may be developed at LEP. The currently large systematic accorded to fragmentation uncertainties may be reduced in the light of future measurements of particle production in hadronic events and further understanding of comparisons between fragmented Monte Carlo and detected hadronic events.

Appendix A

Default Fragmentation Model Parameters

The choice of fragmentation parameters is fixed by agreement between event shape distributions in data and detector-corrected Monte Carlo. This has been performed for the LUND and HERWIG models by the ALEPH QCD group [48]. Parameters are derived from multi-parameter fits to event-shape distributions such as thrust, sphericity, acoplanarity etc. The method is detailed in [24]. Detector effects are corrected for using bin-by-bin factors derived from reconstructed Monte Carlo events which are compared with the generated "truth". It is important to note that the mean charged multiplicity is fixed to the data-corrected value. ie. the measured multiplicity distribution in data is used to derive the underlying generator distribution, which is held constant throughout the fit. Fitted model parameters are given in table A.1 with those used in production of the reconstructed sample. Errors on fitted parameters are statistical *only* and are consistent with

Model Parameter	Model	Reconstructed Monte Carlo Settings	Generated Monte Carlo Settings	Errors
Λ_{QCD}	LUND	0.349	0.298	0.008
M_{min}	LUND	1.46	1.5	0.12
σ	LUND	0.340	0.367	0.004
a	LUND	0.50	0.50	(fixed)
b	LUND	1.00	0.89	0.04
Λ_{QCD}	HERWIG	0.094	0.101	(fixed)
M_g	HERWIG	0.813	0.813	0.002
M_{CL}	HERWIG	3.94	3.94	0.05
S_{prob}	HERWIG	1.00	0.80	(fixed)

The LUND generator refers to version 6.3 PS. while that of HERWIG regards version 4.1 LLA.

Table A.1: Summary of model parameters.

refitting, using these parameters as input, and monitoring the scatter of output values.

When deriving the systematic uncertainty due to the parameters of the LUND model (in section 8.4), the parameters entitled *"Reconstructed Monte Carlo Settings"* are used.

When comparing quantities between LUND and HERWIG, the parameter set *"Generated Monte Carlo Settings"* are used. The two sets correspond to fits performed using distributions from different data sets. The latter corresponds to the most recent fits [48].

Appendix B

The Laser Calibration System

The TPC laser calibration system serves the twin purposes of determining the electron drift-velocity vector while providing information on the distortion of the otherwise straight tracks which it creates. The reproduction of straight tracks in the chamber, averaged over many laser shots, reduces statistical fluctuations and allows detailed studies of systematic effects. The laser tracks share many similarities with those created by passage of a charged particle.[1] During the commissioning and running of ALEPH, the system also proved to be indispensible for general track studies, development of subdetector hardware, online and offline software. Full remote control of the system from the data-taking console is necessary to make the most use of the system's power and flexibility.

B.1 Principles of Operation

The system creates up to 30 straight tracks of ionisation, using two high-powered lasers and a transport system controlled remotely by online computers. The tracks are split into two detector hemispheres of 15 beams, made up from 3 planes in ϕ containing 5 beams at different angles in θ.

The physical process responsible for the creation of the laser tracks in the chamber gas is different to that of a charged particle. Studies of the number of ions created by the laser pulses show that it depends quadratically on the laser fluence [61] indicating that resonant two-photon ionisation (R2PI) processes are responsible. This occurs in the central region of the beam, ensuring that a symmetrical trail of ionisation is created. The process occurs when large organic molecules are ionised by successive absorption of *two* laser photons. Using a gas system and proportional counter similar in manufacture to that of the ALEPH TPC, it has been shown that two of the organic compounds involved are phenol and toluene [62]. These are common constituents of plastic gas piping and organic solvents used in the construction of multi-wire proportional chambers. Their presence is inferred from the characteristic behaviour of the relative ionisation as a function of laser wavelength which displays structure at wavelengths unique to the ionisation potentials of compounds present in the gas. In the TPC gas system the R2PI structure is visible in the wavelength region around 260→278 nm, while at higher wavelengths (→320 nm) the ionisation falls by over four orders of magnitude. The presence of ionisation, without

[1] Differences due to beam focusing, intensity etc. can lead to some general differences in behaviour.

addition of seeding agents, represents a major advantage over previous experiments [63] where the obnoxious chemical properties and limited lifetime of additives severely limits their usefulness. Ionisation in the Argon-Methane gas of the TPC has been observed to persist even with gas cleaning systems used during long term operation [62].

B.2 Laser Hardware and Beam Transport System

The optical layout of the system is shown in figure B.1, indicating the various components and terminology used to describe them. The system is powered by two, externally po-

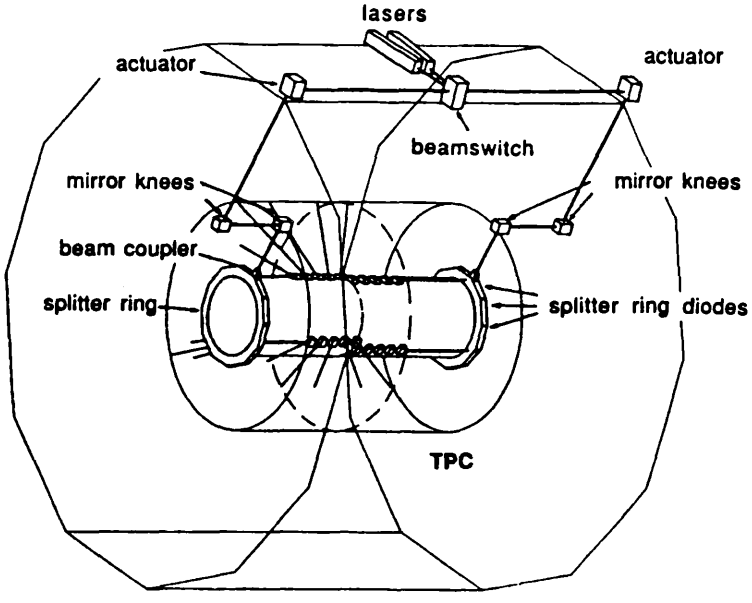

Figure B.1: General schematic layout of the laser calibration system.

sitioned, Nd-YAG lasers situated atop the magnet return yoke. These are high-powered UV pulsed lasers with operating parameters as shown in table B.1. The beam is linearly

Parameter	Specification
Maximum Energy per Pulse	$0 \rightarrow \sim 4$ mJ
Pulse Duration	5 ns (FWHM)
Pulse Repetition Rate	$0 \rightarrow 10$ Hz
Fundamental Wavelength	1064 nm (IR)
Emitted Wavelength	266 nm (UV)

Table B.1: Summary of laser specifications.

polarised on output, although the angle of its polarisation is controlled by a rotatable half-

wave plate built into the focussing telescope attached to the laser "head". The telescope shifts the beam waist into the centre of the chamber and minimises beam divergence in the ionisation region. The polarisation of the output light is important as splitting ratios of the semi-transparent mirrors of the system vary according to the relative direction of polarisation. This is demonstrated in figure B.2 where the mean pad pulse height observed after splitting the beam into three planes in ϕ are shown as a function of the angle of the half-wave plate.

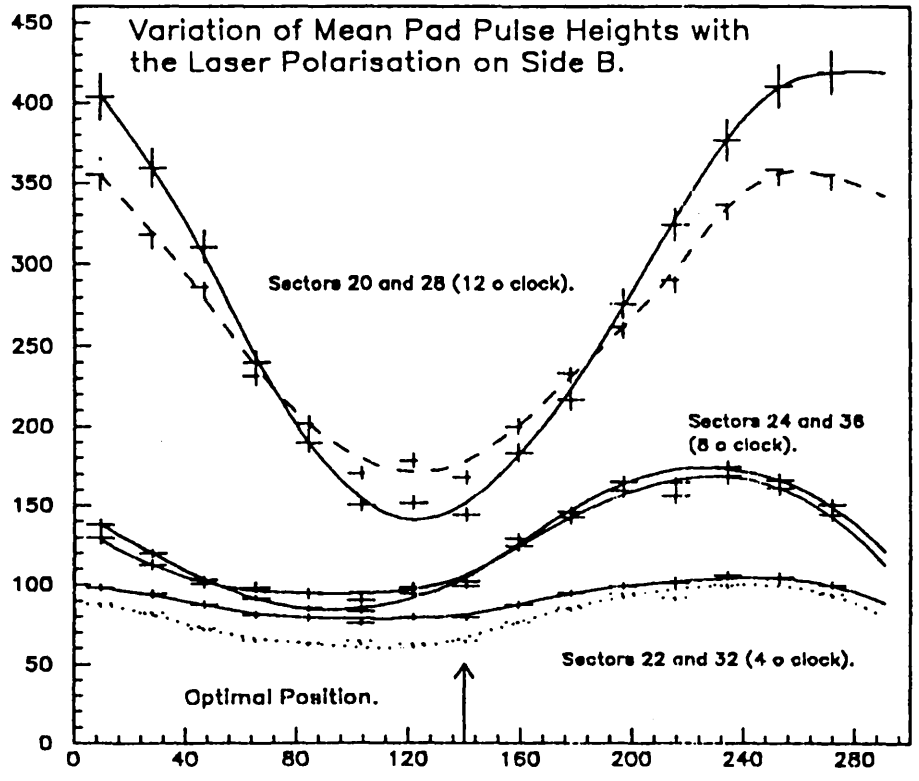

Each plane in ϕ corresponds to the beams crossing sectors $(20, 28)$, $(24, 36)$ and $(22, 32)$ at "12 o'clock", "8 o'clock" and "4 o'clock" respectively. The half-wave plate is rotated through a full 360 degrees, corresponding to the horizontal axis, with laser shots recorded at each position.

Figure B.2: Systematic variation of the mean pad pulse height in 3 pairs of TPC sectors as a function of the laser polarisation angle.

Remote energy sensing diodes are incorporated inside the lasers allowing monitoring of the output energies on a shot-by-shot basis. The laser system has a unique DAQ trigger system which fires a laser shot and starts the readout of the TPC pads and wires. Thus data is read by the DAQ in a similar fashion to Z^o interactions. Two lasers are used, firing independently into each half of the chamber, so as to allow flexible triggering and the possibility to switch each laser from side to side in case of unit failure. This is facilitated by the *beamswitch* which redirects the two beams to either side of the detector. The remainder of the transport system guides the beams using movable mirrors in the

actuator boxes before being fed past HCAL into the TPC. The actuator mirrors provide the necessary degrees of freedom to steer the three beams onto position sensitive diodes at entries and exits of the chamber.

For stable operation, the lasers are tuned and the output polarisation fixed to give equal beam intensities throughout the chamber. The transport system is initially aligned by hand so that the beams are centred on the *beam coupler* at the *splitter rings*. Subsequently the system remains under full remote control from the surface with laser guidance, control and monitoring commands available from the online VAXcluster.

B.3 The Remote Control System

The system is responsible for monitoring and controlling the operation of the two lasers. Beam position and intensities are monitored using non-magnetic diodes at several points throughout the system. The beams are controlled by stepper motors, movable mirrors and direct input to the laser power supplies. This gives full controls of the intensity, pulse-rate and alignment of the beams while ensuring reliable operation over long periods. The system is outlined schematically in figure B.3. User manipulation of the system is available via a series of software menus running within the DAQ UPI environment. This effectively "hides" the complexity of the control system from the operator and permits a largely uniform interface with other data-taking and subdetector activities. An example of the main control menus for the laser system is shown in figure B.4. The system may be realigned or *steered* in each hemisphere, using either laser, via an iterative process of scans carried out by rotating and translating the actuator mirror.

The remote control of the laser power supplies is done via TTL levels which are generated by a 16 bit input/output CAMAC register. This is also responsible for driving and determining the current position of the beamswitch. Debugging system faults is aided by the ability to monitor power supplies and the state of the fuses which connect the position diodes to their amplifiers. The on/off status of the lasers, together with cooling and interlock indicators, are also passed through the system to the operator. These are automatically surveyed on entry to the remote control program and upon activating the lasers. The laser intensity control voltage is adjustable between 0 and 1000 V by a remotely programmable DAC while the pulse rate and delay between Pockels cell release and flashlamp avalanche can also be varied.

B.4 System Performance

The system was used extensively during the commissioning phase of the ALEPH detector. The original purpose of the system, to measure the drift-velocity vector, is carried out routinely as part of chamber monitoring during LEP running. Using 100 laser shots, the statistical precision of the drift-velocity is 0.02 % with a systematic uncertainty of 0.1 % [18].

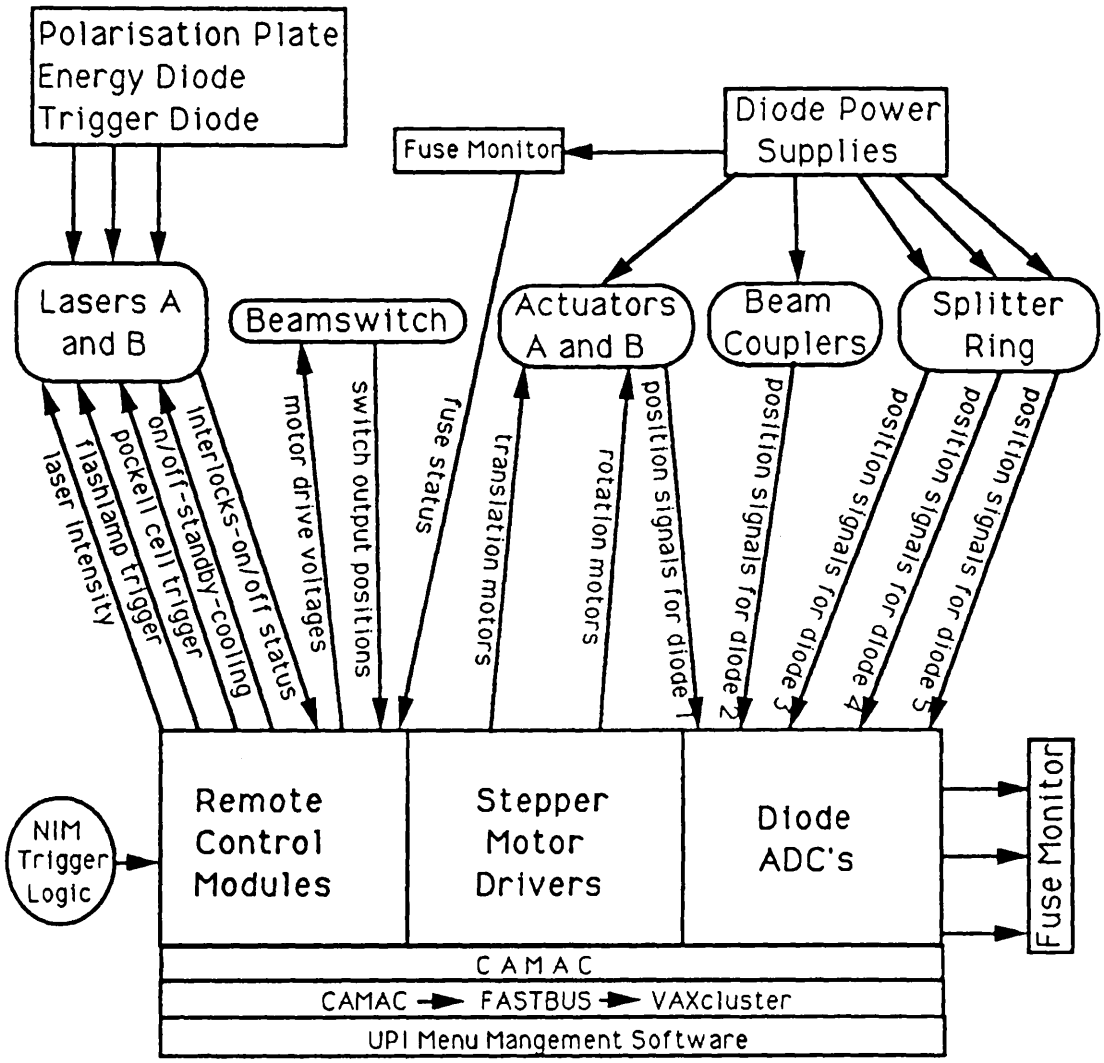

Figure B.3: Schematic of the laser remote control system.

During stable running conditions the long-term drift velocity is :

$$v_D \sim 5.2\,(\pm 0.1)\,cm\,\mu s^{-1}$$

depending on the composition of impurities in the gas[2]. The system is also used to correct for the systematic displacement of TPC coordinates due to residual inhomogeneities in the electric and magnetic fields.

After initial alignment during May of 1989, the system ran without need to open the detector until the shutdown at the end of that year. The alignment of the entire beam path is found to be slightly dependent upon the magnetic field strength, although computer steering remains sufficient to regain alignment. Full control of the system from the surface has allowed the system to be used for several purposes beyond that for which

[2]These may change for example if the detector is opened and new gas introduced.

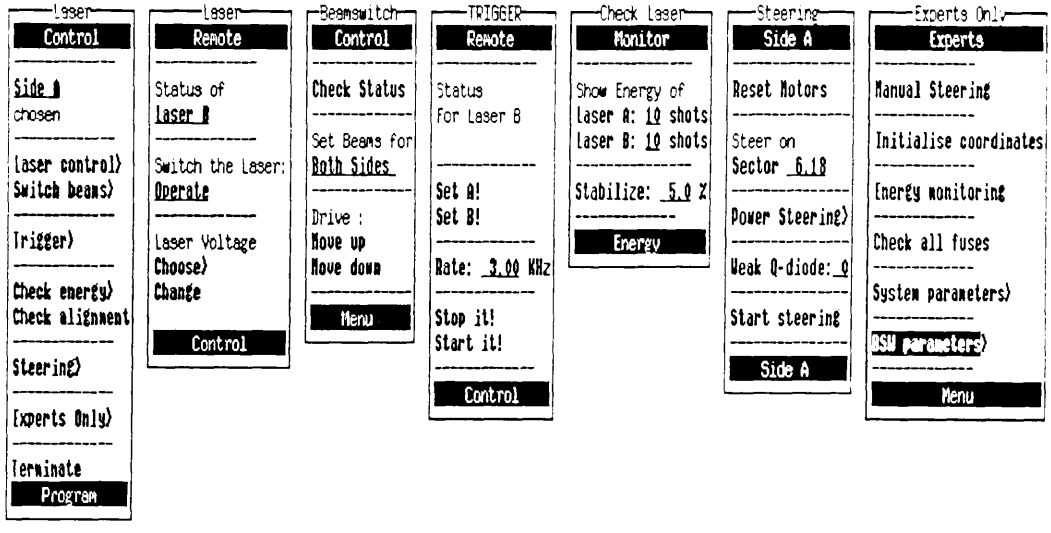

Figure B.4: Example of the user UPI interface to the laser control system.

it was designed, including the measurement of $\omega\tau$ [18].

Typically a laser run is done by shift personnel in under 30 minutes[3] and so can be interleaved with the cycle of LEP operations.

[3]Typically using ~ 200 laser shots per hemisphere at a trigger rate of $\sim 1 - 2$ Hz.

Bibliography

[1] V. Barger and R. Phillips, *Collider Physics*, Frontiers in Physics Series, Addison-Wesley Publishing, ISBN 0-201-05876-6 (1987).

[2] D. Decamp et al. (ALEPH Collaboration), *Measurement of the Electroweak Parameters from Z Decays into Fermion Pairs*, CERN Preprint EP/90-104, (July 1990), *Zeitschrift für Physik* C48 (1990) 365-391.

[3] S.L. Glashow, *Partial-Symmetyries of Weak Interactions*, Nuclear Physics 22 (1961) 579

S. Weinberg, *A Model of Leptons*, Physics Review Letters 19, (1967) 551

A. Salam, *Elementary Particle Theory*, Ed. N. Svartholm, Stockholm, Almquist and Wiksell (1968) 367.

[4] Edited by Altarelli, Kleiss and Verzegnassi, *Z Physics at* LEP *1 : Volume 1-Standard Physics*, CERN 89-08 Volume 1 (21 September 1989).

[5] Band et al. (MAC Collaboration), *A Measurement of the* $e^+e^- \rightarrow b\bar{b}$ *Forward-Backward Charge Asymmetry at* $\sqrt{s} = 29GeV$, SLAC PUB-4871, (February 1989).

[6] Greenshaw et al. (JADE Collaboration), *A Measurement of the Charge Asymmetry of Hadronic Events in Electron Positron Annihilation*, DESY 88-154, (November 1988).

[7] D. Kennedy and B. Lynn, *Electroweak Radiative Corrections with an Effective Lagrangian : Four-Fermion Processes*, Nuclear Physics B322 (1989) 1-54, (3 January 1989).

[8] Edited by Alexander, Altarelli, Blondel, Coignet, Keil, Plane and Treille, *Polarisation at* LEP *Volume 1*, CERN 88-06 (1 September 1988).

[9] Private communication and calculations courtesy of Lee Sawyer of Florida State University (ALEPH).

[10] Ash et al. (MAC Collaboration), *Observation of Charge Asymmetry in Hadron Jets from* e^+e^- *Annihilation at* $\sqrt{s} = 29GeV$, SLAC PUB-4040, (July 1986).

[11] CERN, *Large Electron-Position Storage Ring : Technical Notebook*, CERN Publications, (November 1989).

[12] Edited by W. Blum (ALEPH Collaboration), *The* ALEPH *Handbook 1989*, ALEPH 89-77 Note 89-03, (28th April 1989).

[13] D. Decamp et al. (ALEPH Collaboration), *A Detector for Electron-Positron Annihilations at* LEP, Nuclear Instruments and Methods in Physics Research, A294 (1990) 121-178, (28 February 1990).

[14] European Physical Society, *Europhysics News*, Volume 20, Number 6, (June 1989).

[15] W. von Ruden, (CERN EF Division), *The* ALEPH *Data Acquisition System*, Contributions to the Real Time '89 Conference, Williamsburg Virginia (May 1989), ALEPH 89-116 DATACQ 89-19, (July 1989).

[16] H. Albrecht, E. Blucher,ALPHA *Users Guide*, ALEPH 89-151, SOFTWR 89-22, (September 1989).

[17] L. Garrido and L. Vitale, *Extrapolation of* ITC *Tracks to* TPC, ALEPH 89-145, SOFTWR 89-21, (September 1989).

[18] W. Atwood et al. (ALEPH TPC Group), *Performance of the ALEPH Time Projection Chamber*, CERN PPE 91-24, (February 1991), Submitted to Nuclear Instruments and Methods A.

[19] Edited by J. Knobloch and P. Norton, *Status of Reconstruction Algorithms for* ALEPH, ALEPH 88-46, NOTE 88-6, (May 1988).

[20] W. Bartel et al. (JADE Collaboration), *Observation of Planar Three-Jet Events in* e^+e^- *Annihilation and Evidence for Gluon Bremsstrahlung*, DESY 79/80, (December 1979).

[21] C. Berger et al. (PLUTO Collaboration), *A Measurement of Charge Properties of Quark Jets at* PETRA, DESY 82-058, (August 1982).

[22] J. Berge et al., *Quark Jets from Antineutrino Reactions (I) Net Charge and Factorisation in the Quark Jets*, Nuclear Physics B184, (1981) 13-30.

[23] M. Arneode et al. (The European Muon Collaboration), *Strangeness Production in Deep Inelastic Muon Nucleon Scattering at 280 GeV*, Z. Phys. C, Particles and Fields, 34, 283-291(1987), (27 October 1986, Revised 21st January 1987).

[24] D. Decamp et al. (ALEPH Collaboration, *Properties of Hadronic Events in* e^+e^- *Annihilation at* $\sqrt{s}$ = *91 GeV*, Physics Letters B, Volume 234, Number 1,2, (4^{th} January 1990).

[25] R. Field and R. Feynman, *A Parameterization of the Properties of Quark Jets*, Nuclear Physics B136 (1978) 1-76.

[26] B. Webber, *A QCD Model for Jet Fragmentation Including Soft Gluon Interference*, Nuclear Physics B238 (1984) 492-528, (3 October 1983).

[27] T.Sjöstrand, *The Lund Monte Carlo for Jet Fragmentation and* e^+e^- *Physics* - JETSET *Version 6.2*, Preprint LU TP 85-10, CERN DD Long Writeup, (October 1985).

[28] G. Ballocchi and R. Odorico, *The String Effect and Independent Fragmentation Models : Lore and Facts*, CERN EP/89-162, (15 December 1989).

[29] S. Lloyd, *Test of Quark Fragmentation from* e^+e^-, Edited by B. Foster, *Topics in High Energy Physics*, Proceedings of the two day conference of the High Energy Particle Physics Group of the Institute of Physics 1-12, (April 1988).

[30] M. Arneodo et al (EMC Collaboration), *Measurements of the u Valence Quark Distribution Function in the Proton and u Quark Fragmentation Functions*, CERN EP/89-25, (January 1989).

[31] G. Marchesini and B. Webber, *Simulation of QCD Jets Including Soft Gluon Interference*, Nuclear Physics B238, 1-29, (March 1983).

[32] H. Wachsmuth, (unpublished), *Physics of Neutrino Beams : 1-Principle of neutrino experiments at proton accelrators.*

[33] D. Decamp et al. (ALEPH Collaboration), *Properties of Hadronic Events in e^+e^- Annihilation at $\sqrt{s}$ = 91 GeV*, CERN-EP/89-139, (1989).

[34] Stuart et al, (The AMY Collaboration),"Forward-Backward Charge Asymmetry in $e^+e^- \rightarrow$ Hadron jets",KEK Preprint 89-127, AMY 89-17, (October 1989), Physics Letters B, Volume 234, Number 1,2 (January 1990).

[35] J. Scarr, I. ten Have, PTCLUS*: a Jet Finding Algorithm for High Energy Hadronic Final States*, ALEPH 89-150, PHYSIC 89-60, (1989).

[36] T. Sjöstrand and M. Bengtsson, *The Lund Monte Carlo for Jet Fragmentation and e^+e^- Physics* - JETSET *version 6.3 - an Update*, LU-TP/86-22, (1986).

[37] B. Heltsly et al. (MAC Collaboration), *Results on Hadronic Events from the* MAC *Detector at* PEP *: I. Direct Photon Production, II-Precision R Measurement and Energy-Energy Correlations*, SLAC PUB-3393, (July 1984).

[38] D. Pitzl et al. (JADE Collaboration), *A Study of Photon Production in Hadronic Events from e^+e^- Annihilation*, DESY 89-129 ISSN 0418-9833, (October 1989).

[39] Minutes and transparencies of the ALEPH $q\bar{q}$ analysis group meetings (1989→1990).

[40] T. Barczewski (ALEPH), Ph.D. Thesis (unpublished), University of Mainz, (1990).

[41] Private communication with Werner Wiedemann (ALEPH), CERN Geneva.

[42] Private communication with Chris Grab (ALEPH), CERN, Geneva.

[43] Private communication with Rick St Denis (ALEPH), CERN, Geneva.

[44] D. Perkins, *Introduction to High Energy Physics (Second Edition)*, Addision-Wesley Publishing, (1982).

[45] Private communication with Andrew Belk (ALEPH), CERN, Geneva.

[46] Private communication with Eric Lancon (ALEPH), CERN, Geneva.

[47] Private communication with T. Hansl-Kozanecka and V. Sharma (ALEPH), CERN, Geneva.

[48] K. Smith (ALEPH), *Proceedings of the Singapore Conference 1990* (to be published), Plenary Talk on QCD Results from LEP and SLC, (August 1990).

[49] W. Braunschweig et al. (TASSO Collaboration), Z. Phys. C41 (1988) 359.

[50] A. Petersen et al.(Mark II Collaboration), Phys. Rev. D37 (1988) 1.

[51] Y. Li et al. (AMY Collaboration), KEK Preprint 89-149, (1989).

[52] G. Rudolph et al. (ALEPH Collaboration), *Properties of Hadronic Z^o Decays and Test of QCD Generators* (Draft), (22 February 1991).

[53] M. Akrawy et al. (OPAL Collaboration), CERN EP/90-48, (1990).

[54] D. Decamp et al. (ALEPH Collaboration), *Heavy Flavour Production in Z Decays*, CERN-EP/90-54, (24 April 1990). Physics Letters B, Volumne 244, Number 3,4 (26th July 1990).

[55] The Particle Data group, *Review of Particle Properties 1990*, Physics Letters B239, (12 April 1990).

[56] I. ten Have, (UA1), Ph.D. Thesis (unpublished), University of Nijmegen, The Netherlands, (1989).

[57] H. Albrecht et al. (ARGUS Collaboration), *Observation of $B^0 - \bar{B}^0$ Mixing*, Physics Letters B, Volume 192, Number 1,2.

[58] M. Artuso et al. (CLEO Collaboration), Physics Letters B, 62 (1989) 2233.

[59] Private communication with Gerald Rudolph (ALEPH), University of Innsbruck.

[60] U. Amaldi et al., Physics Review D36 (1987) 1385.

[61] S. Drysdale et al. (laser Ionisation Group of the University of Glasgow Department of Physics and Astronomy), *Detection of Toluene in Proportional Counter Gas by Resonant Two Photon Ionisation Spectroscopy*, Nuclear Instruments and Methods, A252 (1984) 379.

[62] M. Towrie, Ph.D. Thesis (unpublished), University of Glasgow, United Kingdom, (1987).

[63] S. Beingessner et al., *First Running Experience with the Laser Calibration System of the* UA1 *Central Detector*, CERN EP/89-62, (3rd May 1989).